THE UNIVERSITY *of* EDINBURGH

This thesis has been submitted in fulfilment of the requirements for a postgraduate degree (e.g. PhD, MPhil, DClinPsychol) at the University of Edinburgh. Please note the following terms and conditions of use:

This work is protected by copyright and other intellectual property rights, which are retained by the thesis author, unless otherwise stated.
A copy can be downloaded for personal non-commercial research or study, without prior permission or charge.
This thesis cannot be reproduced or quoted extensively from without first obtaining permission in writing from the author.
The content must not be changed in any way or sold commercially in any format or medium without the formal permission of the author.
When referring to this work, full bibliographic details including the author, title, awarding institution and date of the thesis must be given.

Palladium Catalysts for Cancer Imaging

Paul Cowling

Doctor of Philosophy with Integrated Study

Optical Medical Imaging with Healthcare Innovation and Entrepreneurship

The University of Edinburgh and The University of Strathclyde

2020

Abstract

Lung cancer is one of the most devastating diseases with a 5-year survival rate of 17 %. The reason for this poor prognosis is that the disease is often detected at a late stages because of the reliance on low accuracy/low sensitivity diagnostic techniques such as, X-rays and CT-scans. These techniques give non-specific answers as to the exact causes of a patient's symptoms; in that they can detect if an abnormality is present, but not what it is. There is a clear need for new diagnostic techniques which can deduce the presence of lung cancer in an efficient and cost-effective manner. Molecular imaging with targeted fluorescent probes has been demonstrated as a highly sensitive approach for visualising active diseases, with several probes currently in clinical trials. To image lung cancer, this work aims to recreate the concept of antibody directed enzyme prodrug therapy (ADEPT) except replacing the enzyme catalyst with a palladium catalyst. These antibody-catalyst conjugates would be able to catalyst de-propargylation reactions of protected fluorophores such as Rhodamine 110 and Dichlorofluorescein, thus giving a mechanism to "switch on" fluorescent signals that can be used to image the location of cancer cells.

To deliver this, a library of palladium-*N*-heterocyclic carbene complexes were created through novel resin-based synthetic methodologies, enabling rapid multi-reaction synthesis with one purification step. All the catalysts contained moieties that could subsequently be used for bioconjugation, therefore the catalysts developed could be attached to targeting molecules such as antibodies. The catalysts were shown to be biocompatible and catalytically active in biological environments, with a lead catalyst shown to activate a prodrug in a 3D cancer spheroid model.

Subsequently, the synthesised Pd-catalysts were for the first time, conjugated onto antibodies in a world first discovery. The Pd-antibody conjugates were shown to catalyse the activation of a fluorescent reporter, and optimisation of conjugates was performed with different Pd-loading and spacers trialled. These Pd-antibodies represent a huge step forward and could be used to ultimately image cancer cells *in vitro* and *in vivo*. In the future, these biologically targeted Pd-catalyst conjugates could highlight tumour margins by activating a range of florescent probes or activate prodrugs to help kill the tumour at the same time, representing a versatile platform technology to combat lung cancer.

Lay Abstract

Lung cancer is one of the deadliest non-infectious diseases known, and the main cause of the high mortality rate is that patients do not "identify" they have the disease until it has progressed beyond effective medical intervention. This occurs because the disease initially presents indiscernible symptoms, which are often attributed to lesser illnesses such as the common cold and flu. In addition, doctors struggle to identify lung cancer at an early stage is because the techniques used to image the chest, such as X-rays, don't have the specificity required to correctly give a definitive answer.

New technologies that use visible light would drastically improve lung cancer diagnosis. As such, fluorescent molecules are currently being developed for clinical use and offer an innovative way for doctors to identify a range of diseases with a much higher degree of confidence. If these fluorescent molecules can be "switched on" by design, they could be used *in vivo* from non-fluorescent precursors, to "tag" cancers, without harming the rest of the body. The element palladium can catalyse reactions which do not naturally occur in the body, and therefore be used to switch on the fluorescent reporters when desired.

As a part of the immune system, antibodies can distinguish between healthy and non-healthy tissue. By attaching palladium to them, the antibody will transport the palladium to the site of the cancerous tumour where it can catalyse non-natural reactions. By also delivering the relevant starting materials to the same site as the catalyst, it is possible to generate a fluorescent reporter which would identify cancerous lesions in the lung much more easily. The following work shows how such results can be achieved and looks to explore how palladium can also be used to "switch-on" toxic drugs at the cancer site.

Table of Contents

Declaration of Authorship

The research detailed within this thesis has been accumulated by the author in the duration of his PhD studentship between the dates of September 2015 and August 2019 under the supervision of Professor Mark Bradley, School of Chemistry, University of Edinburgh. The work, data, and interpretation presented here are those of the author unless there was significant collaborative contribution made, in which case it has been clearly recognised. Where published work has been consulted or quotations made, the source has been clearly cited.

This work has not been submitted for any other degrees or professional qualifications.

Parts of the work presented herein have been published as:
D. Cherukaraveedu, P. T. Cowling, G. P. Birch, M. Bradley and A. Lilienkampf, *Org Biomol Chem*, 2019, **17**, 5533-5537.

Signed

Paul Cowling

Date

Acknowledgements

In my opinion, writing a thesis is not a single person's endeavour, despite there only being one name on the front cover. There is support that comes from every corner, including the ones you didn't know you had. Without the following people I would not be where I am today and most certainly would not have completed this thesis. I could probably write pages about each individual, so I'll try to keep it brief!

First and foremost, I would like to thank my supervisor Professor Mark Bradley. Throughout the 4 years of this Ph.D. he has constantly been available to offer advice, suggestions and support both in research and beyond. His faith in my ability to complete this Ph.D. was unwavering.

Secondly, I would like to thank my parents and the rest of my family who supported me in my decision to do a Ph.D. and have always been around to offer a helping hand. Including everything from proof-reading reports to helping me move flats.

Next, I cannot thank the following people enough, most of whom I met in Edinburgh and made it a truly wonderful experience. Vikki, for being my work-wife, listening to Fleetwood Mac and supporting each other though the best and worst of times. Gavin for being a terrific flatmate and friend. Pheebs for being there with me through palladazini meetings. Sonia for being a friend to me when I needed both professional and personal advice. Hannah, who I seriously cannot thank enough for being there for me during my final year – after all what is a life without a few dramas! Dan, Yas and Antonio for also being around for the flat parties, socials and RISK games. To Matt, Kevin, Jess and Sara, Nanna and Sarah I would like to thank for always being able to offer advice for the viewpoint of; been there, done it. To everyone past and present in the Bradley group that I worked with, thank you. For all the advice, the help with equipment and the social activities.

To other people in the chemistry department, Elaine, Peter and Michael thank you for the opportunity to help develop the first-year labs and truly enhance student experience. To Colin, Jean, Sam and Kirsty for supporting me though all things OPTIMA. To all the OPTIMA student in cohorts past and present: Jamie, Anastasia and Hazel for that great weekend in Boston. Adeel, Clara, Dawn, Helen, Scott, Lana, Tom, Monica, Katie, Gillian and Kirsty for all the group projects, Christmas meals and summer school banter. Amelia for company during the brilliant club training and InterSci chats. Alisia for driving to Glasgow and listening to The XX and London Grammar.

To my friends beyond chemistry, Morgan, Rowan, Jules and Alyx thank you for the great Holyrood nights, the pubs, clubs and other events. For always being an ear to listen should I really need it. To Juppy, my oldest friend, thanks for great times in Edinburgh and hopefully to many more. To Miceala, Terri and Craig thank you for the parties, 6 Nations TV sessions, the laughs, and let's be honest, a fantastic Christmas pub crawl. A thanks to Dr. Chris Haggarty-Weir for the opportunity to do his miniMBA and really informing me of what career potential is. To Angela for everything we went through together. To older friends from Leeds, thanks for holidays and banter.

My final acknowledgement goes to Laura. Elle. Thank you, for everything. I don't know if I can adequately put it into words the thanks I owe to you but here's my best shot! I have learnt so much throughout the 4 years of my Ph.D. but with you, I was reminded that there's a whole other world out there. You helped me learn so much more about myself, about what I value, about what I find important in life. You were a rock of stability when the waters of fear and anxiety rose up. For all the wonderful evenings we spent in Edinburgh, the holidays in Verona and London, the lazy Sundays, and the stolen moments that take your breath away, thank you. But this is what I am most thankful for, for reminding me that *my Ph.D. doesn't define me*. It is a part of me but doesn't personify me. I am so much more than the contents of this thesis. Without you I genuinely don't think this thesis would've been possible. You more than anyone else inspired me to be the person that I can be, the person I'm going to be. You taught me how to fly. All I can say to you now is thank you. I hope I might get to return the favour one day L.

If I've missed your name, please know that I am still thanking you as well and there only so much space I can include here. If you read the rest, enjoy it! If you find a spelling mistake, please don't tell me! The end of this thesis signifies the ending of a major chapter of my life, and new ones will have begun, but I will not forget one day of this Ph.D., not one line, or moment.

Abbreviations

5FU	5-fluorouracil
ADC	Antibody drug conjugate
BEMP	2-*tert*-Butylimino-2-diethylamino-1,3-dimethylperhydro-1,3,2-diazaphosphorine
Boc	*tert*-Butyloxycarbonyl group
BSA	Bovine serum albumin
CuAAC	Copper catalysed azide alkyne cycloaddition
DCM	Dichloromethane
DIC	*N*,*N'*-Diisopropylcarbodiimide
DBCO	Dibenzocyclooctyne
DIPEA	*N*,*N*-Diisopropylethylamine
DMF	*N*-Dimethylformaldehyde
FBS	Fetal bovine serum
Fmoc	Fluorenylmethoxycarbonyl
FRET	Förster resonance energy transfer
HFIP	Hexofluoroisopropanol
HPLC	High-performance liquid chromatography
ICP-MS	Inductively coupled plasma mass spectrometry
LC-MS	Liquid chromatogpraphy mass spectrometry
MALDI-TOF	Matrix assissted laser desoprtion/ionisation time of flight
MeOH	Methanol
MRI	Magnetic resonance imaging
MS	Mass spectrometry
MTT	3-(4,5-Dimethylthiazol-2-yl)-2,5-diphenyltetrazolium bromide
NHS	*N*-hydroxy succinamide
NIR	Near infrared
OXYMA	Ethyl (hydroxyimino)cyanoacetate
PBS	Phosphate buffered saline
PEG	Polyethylene glycol
PET/CT	Positron emission tomography/computed tomography

*i*PrOH	Isopropan-2-ol
RFU	Relative fluorescence units
RP	Reverse phase
rt	Room temperature
SDS-PAGE	Sodium dodecyl sulfate–Polyacrylamide gel electrophoresis
SPAAC	Strain promoted azide alkyne cycloaddition
TLC	Thin layer chromatography
UV-Vis	Ultraviolet visible spectroscopy

Chapter 1 Introduction

1.1 Lung cancer

1.1.1 General

Cancer is one of the most devastating diseases worldwide with an estimated 18.4 million people affected by the disease in 2018.[1] It is believed that 1 in 2 people worldwide will get cancer at some stage in their lifetimes and this represents an enormous burden on health services around the world. Cancer is a particularly "interesting" disease as it normally originates from cells within the host through an accumulation of genetic mutations (Figure 1.1). The mutations can originate from several different sources including environmental chemicals, UV radiation, DNA replication errors and pathogens. Mutations that cause cancer lead to one of two outcomes: pathways which control and regulate cellular growth and proliferation are damaged, or pathways which activate cellular death are inhibited. Either way, the cells become "immortalised" meaning that the processes which normally regulate cellular division don't function as they should, and growth is uninhibited and uncontrolled. This often causes disease as uncontrolled growth leads to tumour masses that can protrude into other organs and thereby damaging their role/function.

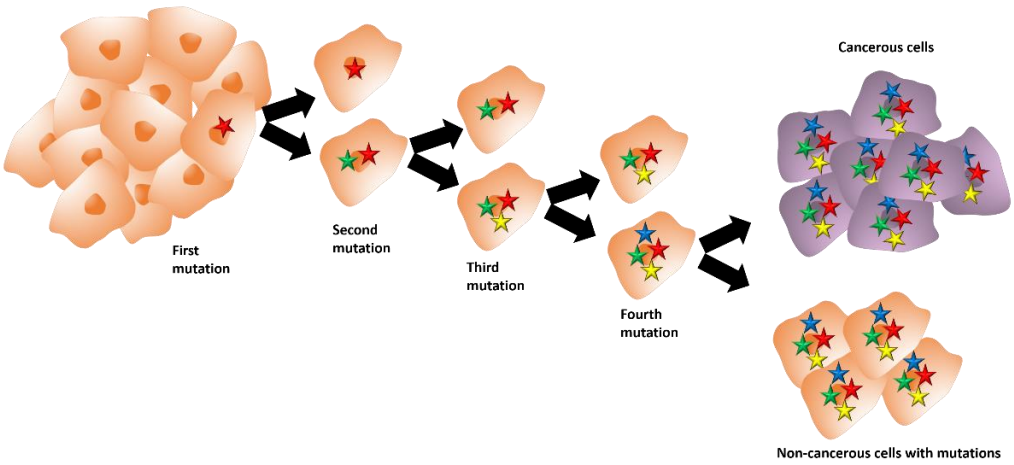

Figure 1.1 Genetic mutations in cells resulting in cancer. Each star in the nucleus represents a new mutation. Any single mutation by itself can be enough to cause a cell to become cancerous, however each additional mutation increases the likelihood of this occurring. Cells can also carry mutations and not be cancerous.

Lung cancer is particularly problematic disease representing 11 % of all cancer diagnosies,[1] while accounting for 20 % of cancer deaths;[1,2] higher than any other type. Lung cancer tumours are highly heterogeneous and can arise anywhere along the bronchoalveolar tree. It is

categorised using the internationally recognised tumour, node, metastasises (TNM) system. "T" is the primary tumour size, "N" indicates if local lymph nodes have been involved with the cancer and "M" indicates if there is metastatic spread to other organs (Table 1.1).[3] There are two sub classes of lung cancer, the first is non-small cell lung cancer (NSCLC) which accounts for 85 % of cases and the second, small cell lung cancer (SCLC) which accounts for 15 % of cases.

Table 1.1 Lung cancer TNM stages and descriptions

Stage	Description
I	Tumours are up to 5 cm in diameter with no involvement of lymph nodes or metastasis.
II	Tumours are up to 7 cm in diameter and with some involvement of regional lymph nodes.
III	Tumours over 7 cm in diameter with severe regional lymph node involvement. Secondary tumours may have begun to be established in other organs.
IV	Distant metastasis of other organs including liver, bone, brain, adrenal glands and kidneys with secondary tumours of over 5 cm.

Lung cancer has a 90 % association with tobacco smoking[4] (meaning 9 out of 10 patients are either themselves smokers or are exposed regularly to second-hand smoke) because of this, lung cancer is generally more prevalent in western countries. Smoking is also common in both India and China where, it's estimated that there could be more than 400 million smokers in the two countries combined; denoting that this is a global health issue. Moreover, as developing countries become wealthier, tobacco smoking is adopted as a "luxury" habit. This is leading to a rise in lung cancer rates in continents such as Africa and the rest of Asia. However, the number of cases in "never smokers" is also rising, stemming from people who live in cities where pollution and smog contribute to lung cancer development.[5]

The overall 5-year survival rate for lung cancer is 17 %. Breaking this down there are some interesting observations. Firstly, 70 % of lung cancer patients are diagnosed at stage III or

stage IV so, most patients are diagnosed when the cancer has already spread to lymph nodes and other organs. Secondly, the 5-year survival rate for patients diagnosed at stage III is 20 % and for patients at stage IV it is 5 %. However, the survival rate for stage I can be as high as 80 % and for stage II 50 %, so there is a clear correlation between the stage of diagnosis and the 5-year survival rate. There are important underlying reasons for these statistics, and they're rooted in the diagnosis procedures and treatment options.

1.1.2 Diagnosis and treatment

Diagnosing lung cancer is not easy. The first challenge clinicians face is getting patients suspected of having the disease to be seen by their doctor. One of the issues here is that many of the symptoms that are presented by lung cancer in the early stages are non-specific. They include:

- Chesty cough
- Persistent chest infections
- Fatigue
- Loss of appetite

Naturally these symptoms could also be caused by all sorts of other issues such as chronic obstructive pulmonary disorder (COPD), a bacterial infection, asthma or fibrosis. These symptoms also overlap with viral infections such as the common cold. As such, many patients do not recognise their own level of risk and do not refer themselves to their local doctor. During the later stages of disease progression when it becomes more serious, more obvious symptoms occurs such as:

- Coughing up blood
- Fainting
- Wheezing
- Chest and shoulder pain.

Because of this overall ambiguity, many patient referrals occur once the disease has progressed to its more serious stages (stages III and IV).

Once patients have been referred to lung respiratory specialists, they will often have an X-ray or CT scan to image the chest (Figure 1.2).[6] However, images created only show if there are abnormalities inside of the chest cavity; they do not specify what the abnormality is. The aim

of imaging is twofold: assess the extension of disease, and target the area for further biological sampling. During the CT scan, it is pertinent to scan other areas of the body (such as the brain) for metastases as they're highly common and many patients will present metastases. Iodinated contrast agents can also be used to assess invasion to local lymph nodes. In parallel to this, a biopsy to extract a sample of the abnormal tissue identified and then characterise the disease state is often performed. Once a biopsy has been taken (normally a needle biopsy), histology will be used to confirm the presence of cancer or other disease and in certain cases DNA screening to identify genotypes.

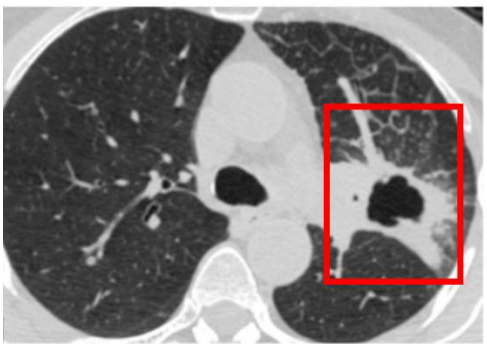

Figure 1.2 CT scan of chest cavity with suspected lung tumour (red box). Image adapted from reference 6.

Once lung cancer has been diagnosed the next step is to decide on a treatment plan. The best method to treat cancer is to remove all the cancerous cells via surgery. The presence of cancer cells in the area surrounding the resected tumour is one of the best indicators for tumour recurrence and poor patient survival. Quite often during surgery, surgeons will use the "index finger rule" to determine tumour margins. They will use one index finger width around the identified tumour and remove that tissue too. This is carried out, because it is difficult to identify tumour margins and thus certainty of where a tumour ends, and healthy tissue begins is unclear. When it comes to lung cancer, surgeons can be as extreme as to remove entire lungs.

The primary treatment for early stage (stage I and stage II) NSCLC is surgery[7] and offers the best route for survival. The 5-year survival rate after surgical resection is 60-80 % for stage I and 30-50 % for stage II NSCLC patients. Platinum based adjuvant chemotherapy is normally recommended post-surgery and has been shown in clinical trials to improve patient survival over 5 years.[8]

The primary treatment for stage III and IV NSCLC is a combined use of surgery (if possible), chemotherapy and radiotherapy. Recently, antibody-based therapies have come onto the market. Atezolizumab is a monoclonal antibody which targets the programmed death ligand 1

(PD-L1) cell surface receptor; an adaptive immune system checkpoint. The treatment was approved in 2016 for patients with metastatic NSCLC, however the treatment is only approved for stage IV of the disease. In trials is was shown to improve patient survival by 4 months with the Atezolizumab vs the control study that did not include Atezolizumab.[9]

Based on the statistics presented in the literature, diagnosis of lung cancer at the earlier stages would have a significant effect on overall patient survival, with early diagnosis more effective than improved treatment options. Whilst new treatment options will always be needed, surgery will always be the most effective treatment strategy. Furthermore, the long approval times required for new therapies means that improved diagnosis will be far more cost-effective approach in helping patients with lung cancer. In conclusion, accurate, cost effective diagnostic methods for identifying lung cancer at early stages are required in clinical settings.

1.2 Medical imaging

1.2.1 Established techniques

Diagnosis is a key step in identifying the location and type of cancer. A correct diagnosis will mean that treatments can be more specific and effective. Moreover, the identification of tumour margins is crucial for successful surgical outcomes and cancer follow-up treatments. The process of diagnosis usually begins with non-invasive medical imaging, followed by a potentially invasive biopsy that then identities the cancer more accurately via biomarkers and histological methods.

In the field of medical diagnosis one of the most powerful tools is the use of light and many different wavelengths from the electromagnetic spectrum have been utilised. One of the most important discoveries in this field was X-rays. Originally discovered by Röntgen in 1895, they revolutionised our ability to understand bone injuries. These days X-rays are simple to generate and are used pervasively due to the cost-effective information that they provide clinicians.[10] As technology evolved computed tomography (CT) X-rays were developed. This technique involves taking multiple X-rays from different positions around the same point of the body, then processing the 2D images to generate a 3D image. 3D images provide a greater detail and providing key information that affects treatment options. Naturally, a CT scan takes longer than a single X-ray though a key limitation is that they have poor soft tissue resolution,[11] though to circumvent this iodinated contrast agents can be used to improve the resolution of the images generated (Figure 1.3).[12]

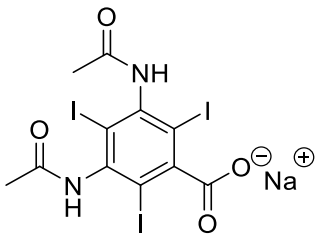

Figure 1.3 An example of an ionic iodinated CT contrast agent called diatrizoate (trade name Hypaque).

Another technology that has come to the forefront of medical diagnosis is magnetic resonance imaging (MRI). MRI works by reversing the spin of the nuclei in hydrogen atoms in water using an electromagnetic field. When the magnetic field is switched off the nuclei return to their resting state, and in doing so cause a release of electromagnetic radiation which can be detected. Hydrogen is normally the atom of choice due to its abundance in water and fats in

the human body[13] and makes MRI a powerful tool for imaging certain areas of the body such as the brain and other soft tissue areas. There are two issues with using MRI on the lungs, the first, is that lungs consist of mostly air and the lack of water gives poor contrast. The second, is that the movement caused by breathing makes calibration of the machine difficult. A CT scan is therefore likely to be the first imaging technique that would be used to try and pinpoint the location of a tumour. However, a scan that utilises nuclear imaging might be used to get a better idea of the tumour location and staging.

This includes positron emission tomography (PET), another important technique in the field of cancer diagnosis. PET works by using radioactive isotopes that undergo positron emission. These positrons collide with electrons in the surrounding tissue undergoing self-destruction generating two gamma photons that are emitted at a 180 ° angle to each other and 18-Fluorine is one such radioisotope capable of this emission. In cancer imaging, the molecule fluorodeoxyglucose ([^{18}F]FDG) (Figure 1.4) is frequently used to detect tumours.[14] Its use is based on the assumption that, because cancer cells grow faster they consume larger amounts of glucose. Thus, their uptake of FDG will be higher than normal cells.[15] Upon uptake, [^{18}F]FDG is phosphorylated by hexokinase which prevents the molecule leaving the cell, effectively trapping the molecule inside the tumour.[15]

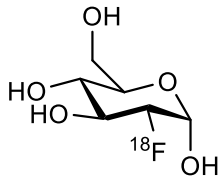

Figure 1.4 Structure of Fluorodeoxyglucose ([^{18}F]FDG).

Current medical imaging techniques all have limitations, for example CT scans and X-rays lack sufficient specificity for truly accurate diagnosis of cancer. MRI and PET have much higher specificity and can diagnose cancer. Indeed, PET and MRI imaging can reveal some of the molecular specificities of a patient; for example, the presence/activity of receptors on the surface of cells. However, PET requires the use of radioactive traces which can be expensive and difficult to synthesise, while MRI scans often take a significant amount of time and is also expensive to carry out. Crucially, none of these techniques can be used in real time (during surgery) with current equipment. As discussed before, the best survival prognosis for patients comes when they undergo surgery to remove all the cancerous tissue and ideally the imaging techniques should help guide this. Consequently, many researchers are looking to develop new technologies that aid this. Of these, a focus around the use of fluorescence is perhaps the most

common, however fluorescence-based probes need to avoid the intrinsic autofluorescence of physiologically relevant molecules such as haemoglobin. As a result, an *in vivo* imaging window has been conceptualised (Figure 1.5) and used to describe the use of light in the visible and near infra-red wavelengths that can be used to image biological tissues *in vivo.*

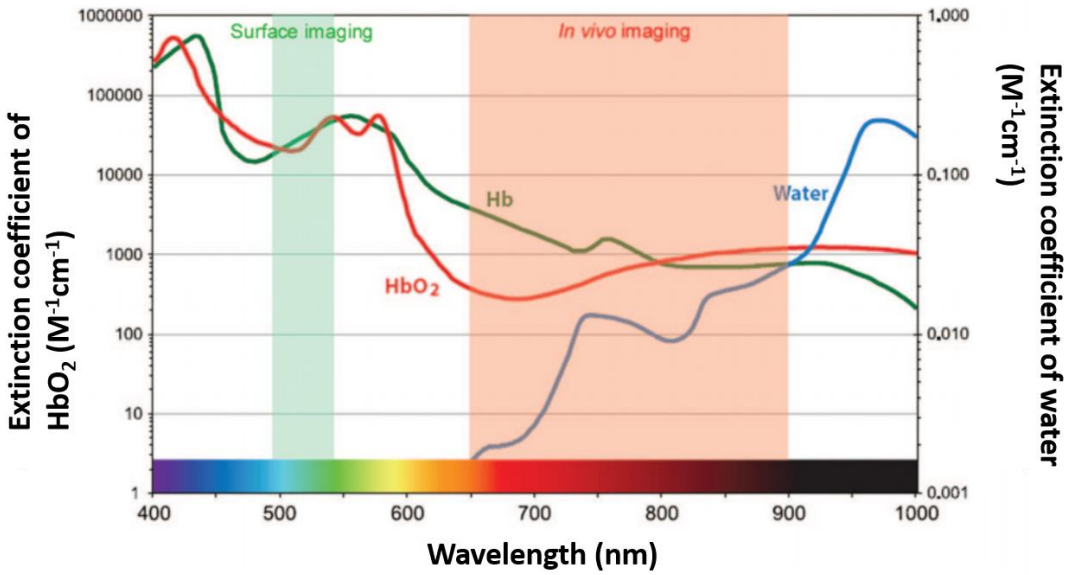

Figure 1.5 The *in vivo* imaging window. A graph plotting wavelength versus the extinction coefficients of several physiological relevant molecules. Adapted from reference 20.

1.2.2 Fluorescence and quenching

Fluorescence is a phenomenon that allows the emission of light (as photons) from a compound after the absorption of a photon. The energy of the source photon excites one of the molecular ground state electrons inducing it to an excited energy level S_1 (Figure 1.6). According to Franck-Cordon rules the electron can occupy any number of vibrational energy states. The electron will vibrationally relax to the closest semi-stable energy level, before moving down to the lowest excited state S_1 (Figure 1.6) by a process called internal conversion. Kasha's rule states that fluorescence will only occur from the lowest excited level (S_1). The electron will then transition to the ground state from the excited state, as it does it can emit the energy either as a photon (fluorescence), or through non-radiative relaxation that causes no emission.

The electron can also move to an excited triplet state T_1, in a process known as intersystem crossing (ISC, Figure 1.6). Intersystem crossing is highly unlikely as it involves a forbidden spin transition causing both electrons to have the same spin. An electron in the excited triplet

state can relax from T_1, to S_0 releasing the energy as a photon (phosphorescence), or a non-radiative relaxation.

The photon emitted is always lower in energy than the photon absorbed meaning emission wavelengths are always longer than the excitation wavelengths. The difference between the excitation and emission maxima is known as the Stokes shift, indicative of the journey travelled by the photon, with a small Stokes shift suggestive of energy loss simply through changes in vibrational energy states, whereas, a large Stokes shift implies significant energy loss due to excited state transitions. The efficiency of fluorescence can be determined through its so-called quantum yield; the percentage of photons emitted divided by the total number of photons absorbed. The quantum yield, in addition to the extinction coefficient of the fluorophore, can be used to define the 'brightness' of the fluorophore.

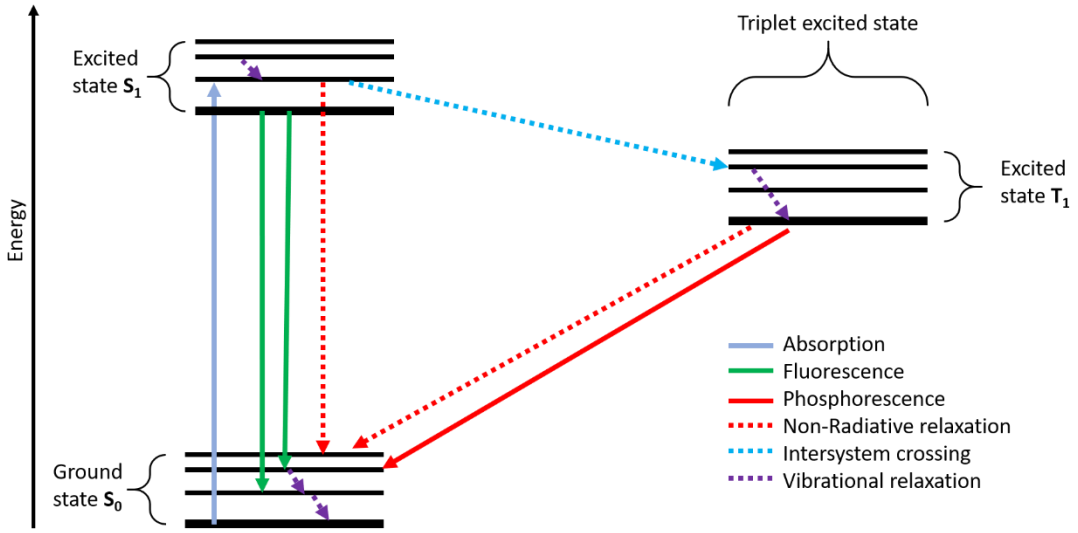

Figure 1.6 Jablonski diagram illustrating the process of fluorescence and phosphorescence. Solid arrows indicate absorption and emission routes while dashed arrows indicate methods of relaxation.

There is also a way to prevent fluorescence emission via a process known as quenching. One mechanism is when fluorescence is quenched through a process known as Förster resonance energy transfer (FRET), involving two chromophores a donor and acceptor (Figure 1.7). The donor chromophore will absorb a photon from an external source and become excited. In fluorescence this energy would be emitted, however the presence of an adjacent acceptor chromophore means that the energy can be transferred to the acceptor chromophore. This process is distance dependent and only works effectively when the two molecules are in close proximity to one another (typically less than 10 nm). Simply put, a quencher is a molecule can prevent the emission of fluorescent photons, from a fluorophore.

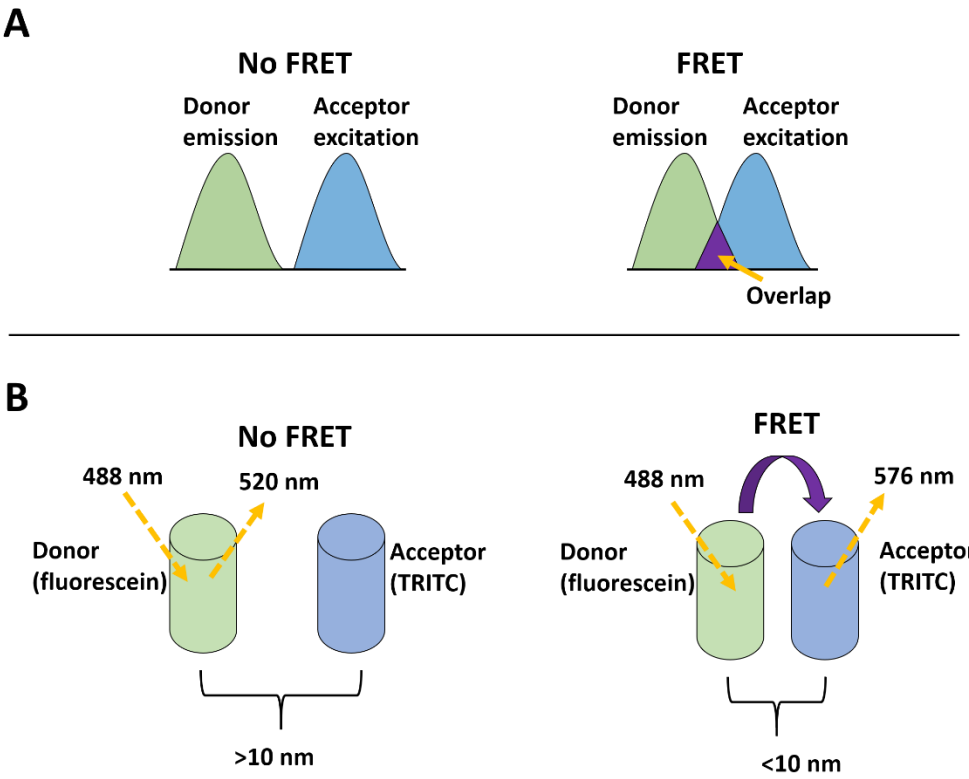

Figure 1.7 Förster resonance energy transfer. (A) The spectral overlap required between the donor's emission and the acceptors excitation spectra. If there is no overlap the acceptor cannot absorb the emitted donor photon as it has the wrong energy levels (B**)** Distance dependence of FRET, when the donor and acceptor molecules are far away from each other the efficiency of FRET is decreased, whereas molecules close to each other have a high efficiency. Fluorescein and tetramethylrhodamine (TRITC) are a common FRET pairing.

1.2.3 Fluorescence guided surgery

Surgical resection of tumours is one of the best ways to improve patient prognosis, however an issue is tumour margin identification which even today is subjective. There have been recent developments of fluorescent probes with molecular targeting moieties which can be used to image margins *in vivo* and in real time causing much more contrasted tissue boundaries. Additionally, accurate identification of tumorous margins should also result in the preservation of healthy tissue, helping patient outcomes by not damaging the body unnecessarily.

In 2011 researchers used a folate-fluorescein isothiocyanate conjugate (Figure 1.8) to image ovarian cancer during a surgical procedure.[16] Ovarian cancers are known to overexpress folate receptors, allowing the folate-FITC conjugate to selectively label these cancerous cells over healthy cells. Patients were given the compound 2-8 hours before surgery to allow time for accumulation in the cancer cells, which enabled enhanced signal to noise ratio over the healthy

surrounding tissue. The patients underwent surgery, during which fluorescent and brightfield cameras were used to image the ovaries. Interestingly the researchers found that using the fluorescent camera allowed them to find extra subsidiary cancers which could not be identified by the brightfield cameras or the surgeons' eye.

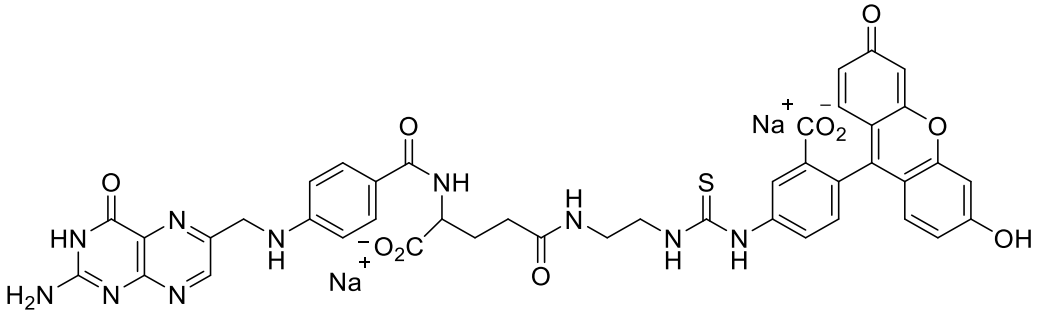

Figure 1.8 The folate FITC conjugate from reference 16. This conjugate is an example of a fluorescent molecule linked to a targeting moiety.

To improve this probe, the FITC fluorophore was changed to a cyanine dye which fluoresces (emits) at longer wavelengths (795 nm vs 520 nm). Using near infrared wavelengths of light allows for improved tissue penetration but also better contrast against the background fluorescence that tissue can have.[17] The folate-cyanine dye conjugate was first used to image lung cancer adenocarcinomas in mice[17] and then subsequently used in a phase I clinical trial on 20 patients to establish if it would improve tumour margin identification. Patients received an intravenous injection of the compound 3-6 hours before surgery.[18] The result of this trial suggested that tumour margin identification was improved and also that extra tumours were also identified that were not detected in initial scans and brightfield imaging (Figure 1.9).

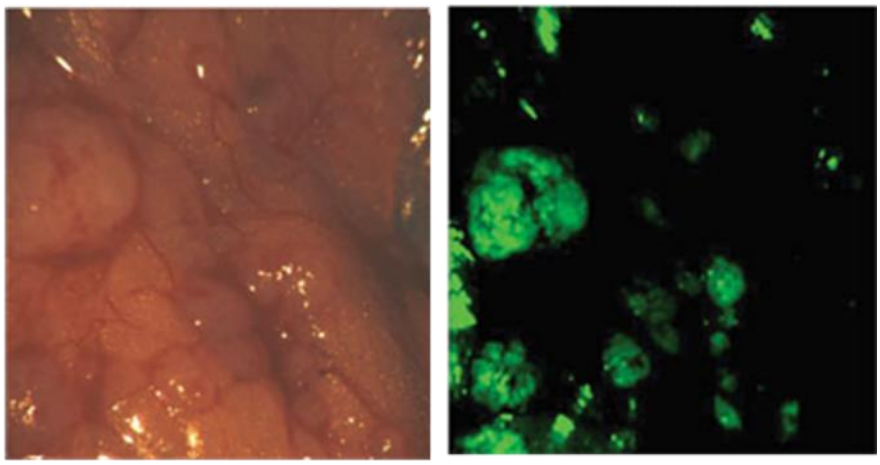

Figure 1.9 Left, brightfield images of ovarian cancer. Right, Fluorescence image of the same region, (images are taken from reference 16). The green tissue indicates binding by the Folate receptor highlighting cancerous cells. *Note: no scale bar published. The green cancer cell clusters are likely between 1-15 mm.

Another probe of note is GE-137[19] which was used to detect colorectal cancer polyps. The probe GE-137 consisted of a 26 amino acid bicyclic peptide which was able to bind to the cell surface receptor C-Met and was linked to a Cy5 cyanine dye known as Cy5** which contains multiple sulfonate groups. In a pilot study the probe was intravenously injected into patients 3 h prior to imaging and during the colonoscopy imaging process, a dual fluorescence and brightfield imaging system was used. In the first imaging pass to identify cancerous polyps, 101 were detected across the 15 patients, and in the second pass an additional 22 polyps were detected (across the 15 patients), however 17 of these 22 polyps were only detectable using fluorescence imaging i.e. they were invisible to detection under brightfield illumination. This is yet another example of fluorescence being used to image tumours during surgery to improve tumour margin detection (Figure 1.10).

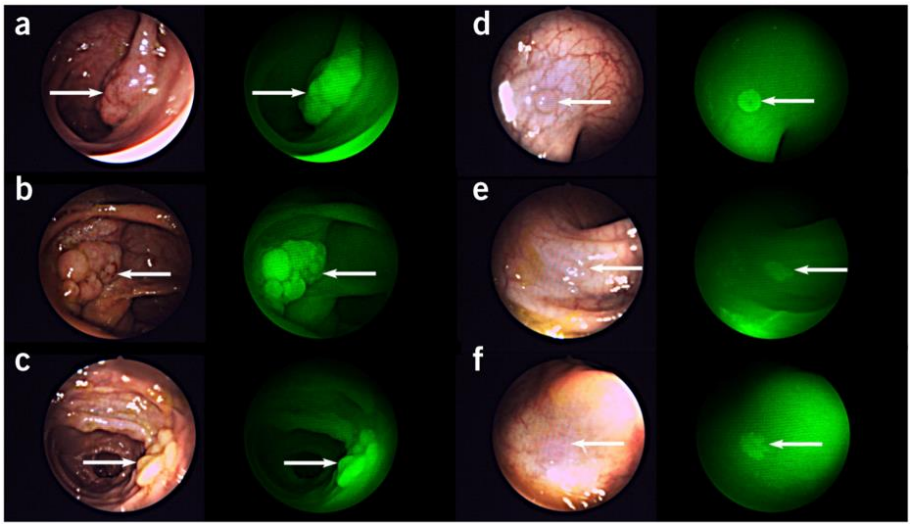

Figure 1.10 Six images of colorectal polyps taken from reference 19. Brightfield and corresponding fluorescent images are shown. Arrows indicate precise location of polyps.

The probes described above are known as "always on" since their fluorescence can always be detected which can lead to high background fluorescence levels and much work has gone into the development of "switch-on" probes. These are molecules, which, upon interaction with some environmental activator, will increase their fluorescence output. These probes can then take advantage of the unique conditions that are created by disease states, these include: pH, enzymes and metabolites.[20,21]

It is hypothesised that proteases such as matrix metallo proteins (MMPs) could be exploited to image tumours [22] as they have been implicated in the growth of tumours by remodelling the extracellular matrix. This allows the cancer cells to spread into their surrounding tissue more easily.[23] The selectivity of MMPs has been manipulated using activity-based ("switch-on") probes, by utilising a fluorophore-quencher (FRET) pairing held in proximity by a peptide sequence. These probes could then be "activated" or "switched on" by cleavage of the peptide sequence leading to an increase in florescence.

In work by Crisp, an activatable cell penetrating peptide (ACPP) probe was used to image tumours *in vivo*.[24] The ACPP would be cleaved by MMP-2, activating it and allowing the cell penetrating peptide-Cy5 probe to bind to the plasma membrane and be up-taken into cells, allowing them to be imaged (Figure 1.11). This probe extended to include an integrin binding motif (cyclic RGD peptide) which was found to greatly enhance the up-take of the probe by 10-fold into U87MG cells (*in vitro*). In MDA-MB-231 tumours the probe, gave enhanced fluorescence intensity at the core of the tumour in *in vivo* models compared to controls (Figure 1.11).

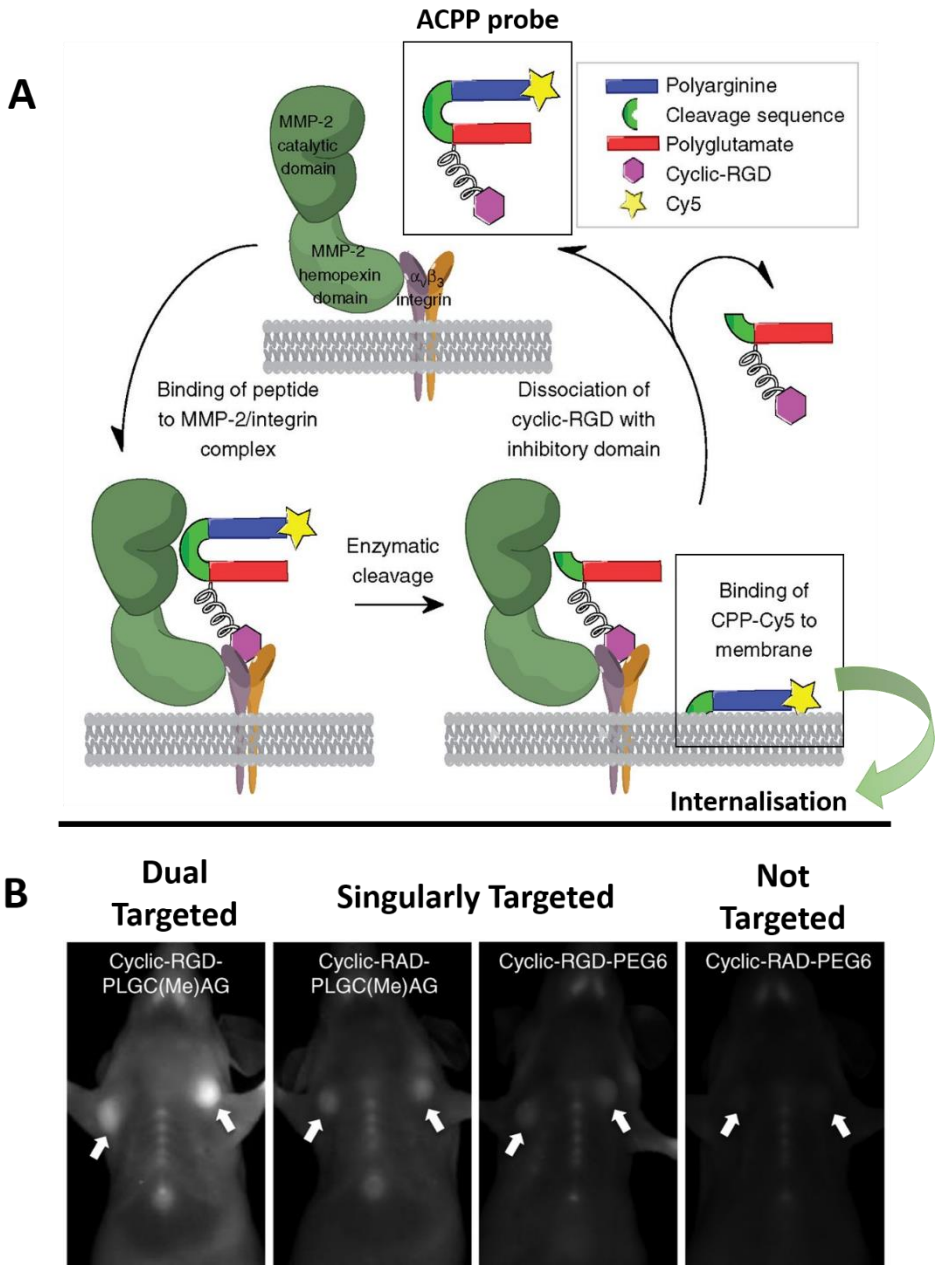

Figure 1.11 (A) The MMP-2 is linked to a membrane bound integrin. The APCC binds to this protein complex through the cyclic RGD. MMP-2 then cleaves the probe into two fragments. The CPP-Cy5 fragment then binds to the Cell membrane and is uptaken into the cell. (B) *In vivo* breast tumour imaging with dual-targeted ACPPs. Dual-targeted cyclic-RGD-PLGC(Me)AG-ACPP, single-targeted (cyclic-RAD-PLGC(Me)AG-ACPP and cyclic-RGD-PEG6-ACPP), and double-negative cyclic-RAD-PEG6-ACPP peptides were injected into mice harbouring bilateral orthotopic MDA-MB-231 breast cancer tumours. Six hours after a 10 nmol dose, mice were anesthetized and imaged for Cy5 fluorescence. Tumours are indicated with white arrows. Adapted from reference 24.

In conclusion, fluorescence based medical imaging would provide a novel, cost-effective, fast method for imaging tumour margins and potentially diagnosing the cancer itself. It also provides an opportunity to supplement existing techniques. Fluorescent probes are continuingly being improved upon by different groups – tuning fluorophores for the ideal *in*

vivo imaging qualities including brightness, stability, solubility. They can be conjugated to specific biomarkers to reveal greater details about the heterogenetic status of the cancer. This could lead to better chemotherapy treatments as cancer well be characterised to a higher specifically and therefore chemotherapy drugs with the lowest risk of encountering drug resistance mechanisms can be used. Ultimately surgeons want to move from heavy reliance on pre-operation CT scan images (Figure 1.2) to real-time imaging methods (Figure 1.9 and 1.10) that can accurately image tumour margins which would improving patient prognosis.

1.3 Cancer treatment

After Diagnosis, the patient has to undergo various treatment options and nearly all patients will have a course of chemotherpy.[25] Such agents are simply toxic compounds that kills cells with their mechanisms of action often relating to inhibiting processes related to cell division. Chemotherapy compounds can be used to treat cancer because cancer cells are dividing rapidly; a hallmark of cancer.[26] A fundamental limitation of chemotherpay drugs is that they are not targeted to the cancer cells, thus they enact their cytotoxic effects on healthy cells throughout the body and this causes the severe side effects that patients experience when undergoing chemotherpy treatment. The drug Cisplatin (Figure 1.12) has been used in chemotherapy treatment for over 50 years, and causes DNA cross linking to facilitate gross genetic damage and thus initiate cell death and is used to treat meany cancers inclding lung cancer.[27] It typifies the pros and cons of chemotherapy dugs: a highly toxic compounds which will kill most cancer cells and increase life span, but at the cost of severe side effects which may reduce quality of life and may not work for every type of cancer.

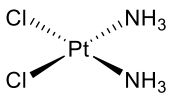

Figure 1.12 Sturcture of cisplatin.

To overcome the side effects of chemotherpay drugs, researchers have developed vairents called prodrugs. A produg is a non-toixc form of a drug which upon activation (by environmental or chemical mechanisms) becomes toxic[28] and by expoliting the unique phisological properties of tumours (like lower pH and overexproressed proteases) drugs can be activated at the tumour site. Capecitabine is a modified version of the drug 5-fluorouracil which when administered will undergo 3 enzymatic reactions to then reach its toxic form but only at the tumour site (Figure 1.13).[29]

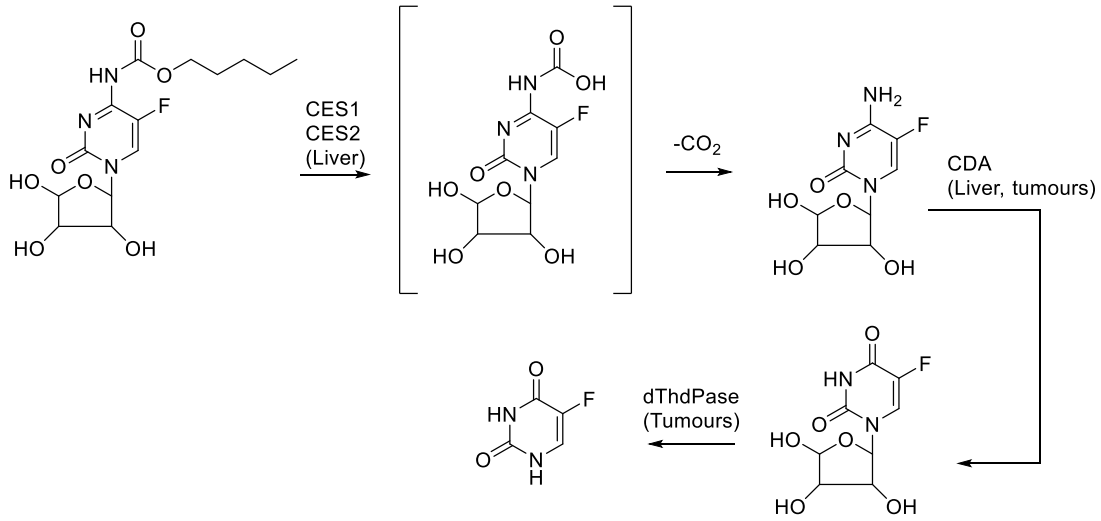

Figure 1.13 Capecitabine as an example of a prodrug that requires multiple enzymatic activation steps. The enzymatic bioconversion initiates in the liver, where human carboxylesterases 1 and 2 (CES1 and CES2) cleave the ester bond of the carbamate. This is followed by spontaneous decarboxylation reaction resulting in 5′-deoxy-5-fluorocytidine. Generation of the parent drug continues in the liver, and potentially tumours, by cytidine deaminase (CDA), which converts 5′-dFCyd to 5′-deoxyuridine. Finally, thymidine phosphorylase (dThdPase) liberates the active drug 5′-fluorouracil in tumours.[29] Adapted from reference 29.

Exciting new therapies that have come onto the market are antibody drug conjugates (ADCs) which are antibodies that have cytotoxic drugs attached to them. The concept being that the antibody can target the drug to the cancer site only, thus reducing off target toxicity. In doing so, drugs which have high toxicity (previously discarded from drug pipelines) can now be used beauase of this targeted approch since the toxicty is restricted to the cancer site. Indeed due to low amounts of antibody binding to a cell the drug must be “super toxic”, meaning that they’ve overcome a key limitation of chemotherapy. The concept has been around for several decades but only now are effective antibody drug conjugates beginning to reach the market. This topic is discussed in greater leangth at the beginning of Chapter 3.

1.4 Conclusion

There is an unmet need in being able to rapidly diagnose lung cancer and to highlight tumour margins. By increasing the number of patients diagnosed at stage I and II, more patients would qualify for surgery, tumours would be more responsive to adjuvant chemotherapy treatments, and this would lead to an overall increase in survival rates without the need for expensive immunotherapy drugs which only minimally extend a patients’ life. Developing better diagnostics methods also offers a more cost-effective than developing new treatments, while improved margin detection would enhance outcomes.

Currently diagnostic methods for lung cancer include CT, PET and biopsies; all of which have limitations from a health economics viewpoint. CT and PET are techniques which can image large areas (and potentially all) of the body which enables clinicians to identify where in the body there might be cancers; this includes potential metastasises. However, CT and PET are unable to provide information about the genetic profile of the tumour. A biopsy on the other hand, can reveal huge amounts of genetic information about the tumour as the cells extracted during the process can be profiled. The disadvantage of a biopsy, beside the invasiveness of the procedure for the patient, is that it only profiles the cells extracted. If the tumour is very large the biopsy may not capture the full heterogeneity of the tumour mass, moreover to profile any metastasises a biopsy for each one must be taken. Thus, fluorescence-based techniques may circumvent these issues.

By developing fluorescence-based imaging techniques, specific to the biomolecular signatures of tumours would allow real time analysis and detection of tumours. However, what would also be beneficial would be to have control over when fluorescent signals are activated and to be able to brightly label tumour margins. As a result, the overall aim of this thesis is to develop lung cancer targeting probes which could “switch-on” fluorescent signals or activate prodrugs, ideally applying wavelengths away from tissue autofluorescence.

1.5 Thesis aims

Examining the literature discussed above it is clear that there is a need for new lung cancer imaging methods and that the technique of fluorescence might fill this niche, moreover the fluorescence signal ideally should be activatable. In the late 1990s/early 2000s a concept called antibody directed enzyme prodrug therapy (ADEPT) was in clinical trials though ultimately failed and is discussed in further detail later in chapter 3. The following work in this thesis aims to develop a technology analogous to ADEPT, namely ADEPT but with a palladium catalyst instead of an enzyme (Figure 1.14). Antibodies with transition metals attached have been used in a variety of contexts including for the enhancement of cytotoxicity[30] and for PET imaging.[31] However, none of the metals attached to the antibodies were used for the purpose of being a catalyst. Thus, this work represents the first example a metal being attached to an antibody for the purposes of catalysis.

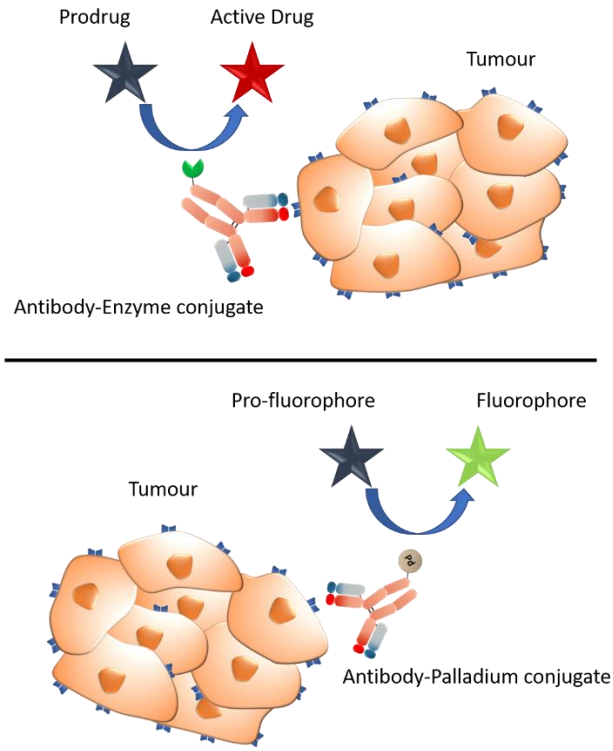

Figure 1.14 Top: Schematic of antibody directed enzyme prodrug therapy (ADEPT). Bottom: Schematic of the aims of thesis, a antibody with a palladium catalyst attached. The palladium then activates a fluorescent probe giving a detectable signal which can be used to identify cancer location.

Therefore, the goals of this thesis were to:

1. Develop a biocompatible palladium catalyst which can be used to activate fluorescent probes in cancerous cells.
2. Attach the palladium catalyst to a biological targeting molecule such as an antibody.
3. Test the ability of this targeted catalyst to generate fluorescent signals in translational models.

The long-term aim of this research would be use an antibody-targeted palladium catalyst, that could be used to diagnose, locate and treat lung cancer *in vivo*. Indeed, using these probes to image tumour margins would be a powerful tool, especially when combined with prodrug activation as tumour reductions could be visualised more easily. Whilst this thesis focused on diagnosis, the catalyst could also be used to locate tumour margins during resections and activate prodrugs. Prodrug activation at the cancer site would be a route to circumvent the detrimental side-effects of chemotherapy treatments analogous to antibody directed enzyme prodrug therapy (see Chapter 3). Finally, an antibody-metal conjugate could potentially have other applications in biotechnology, for example metal replacement with therapeutic metals (e.g. alpha particle emitters) new assays analogous to enzyme linked immunosorbent assays could be developed e.g. an palladium linked immunosorbent assay, truly with such a technology the limitation might only be imagination!

Chapter 2 Solid-phase synthesis of biocompatible *N*-heterocyclic carbene–Pd catalysts using a sub-monomer approach

The following work was carried out with Durgadas Cherukaraveedu.

Some of the following results are published in: D. Cherukaraveedu, P. T. Cowling, G. P. Birch, M. Bradley and A. Lilienkampf, *Org Biomol Chem*, 2019, **17**, 5533-5537.

2.1 Introduction

2.1.1 Bioorthogonal chemistry

The development of bioorthogonal chemistries over the last 20 years has led to a dramatic expansion of creative ways to study cellular processes. Bioorthogonal reactions have enabled the selective visualisation and manipulation of biological processes in living systems and have been widely used in a number of applications.[32–34] This includes the use of non-native chemical reactions to label biological targets or "switch-on" non-toxic/non-fluorescent compounds into their active derivatives.

Necessary features of these reactions include; the scope to be carried out in complex environments (often cellular) without side reactions and fast reaction kinetics. The term bioorthogonal chemistry was first coined by Bertozzi in 2003, during work where the Staudinger ligation was used to selectively modify cell surface membranes loaded with synthetic azidosugars.[35] Since then, the field has continued to grow and this has led to a number of concepts such as the Cu(I) catalysed azide alkyne cycloadditions (CuAAC),[36] strain promoted azide alkyne cycloaddition (SPAAC)[37,38] and the inverse electron demand Diels-Alder reaction typified by tetrazines (Figure 2.1).[39]

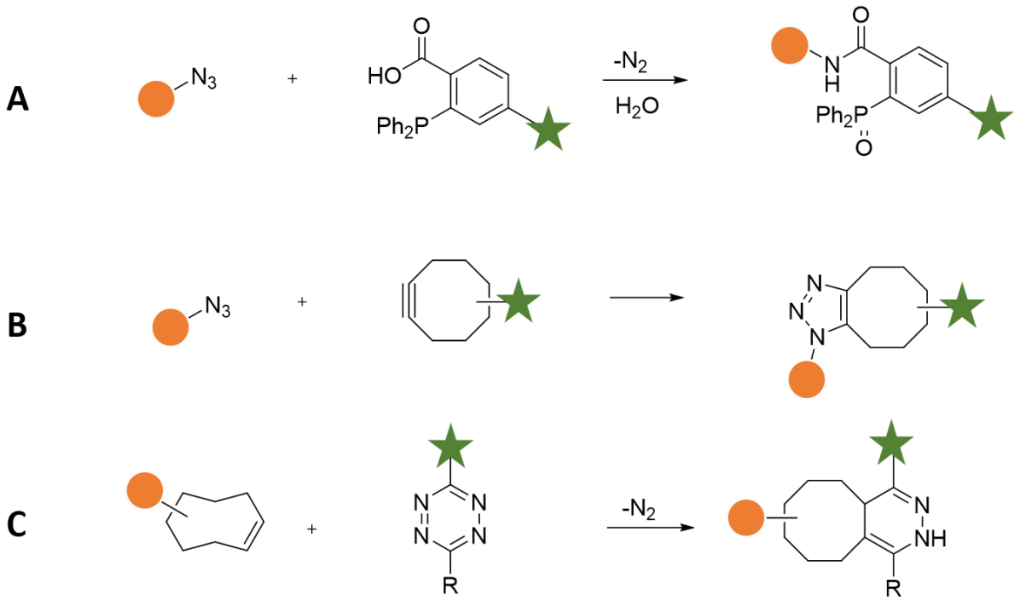

Figure 2.1 Examples of bioorthogonal reactions (A) The Staudinger ligation (B) The SPACC rection (C) The Inverse Diels-Alder tetrazine ligation. The orange circle represents the target molecule e.g. a protein. The green star represents an imaging agent e.g. a fluorophore or radioactive isotope.

Within the field of bioorthogonal chemistry, transition metal mediated bioorthogonal reactions are also of interest. This is because like the reactions in Figure 2.1 they can enable an array of non-natural chemical transformations that can be used to modulate living systems,[40–44] but can do so with much greater scope and feasibility.

2.1.2 Transition metals in bioorthogonal chemistry

Six transition metals have been used in the exploitation of bioorthogonal reactions. One of the first examples was demonstrated by Meggers who used a ruthenium catalyst to de-cage bis-allyloxycarbonyl rhodamine 110 generating fluorescence inside HeLa cells (Figure 2.2).[45]

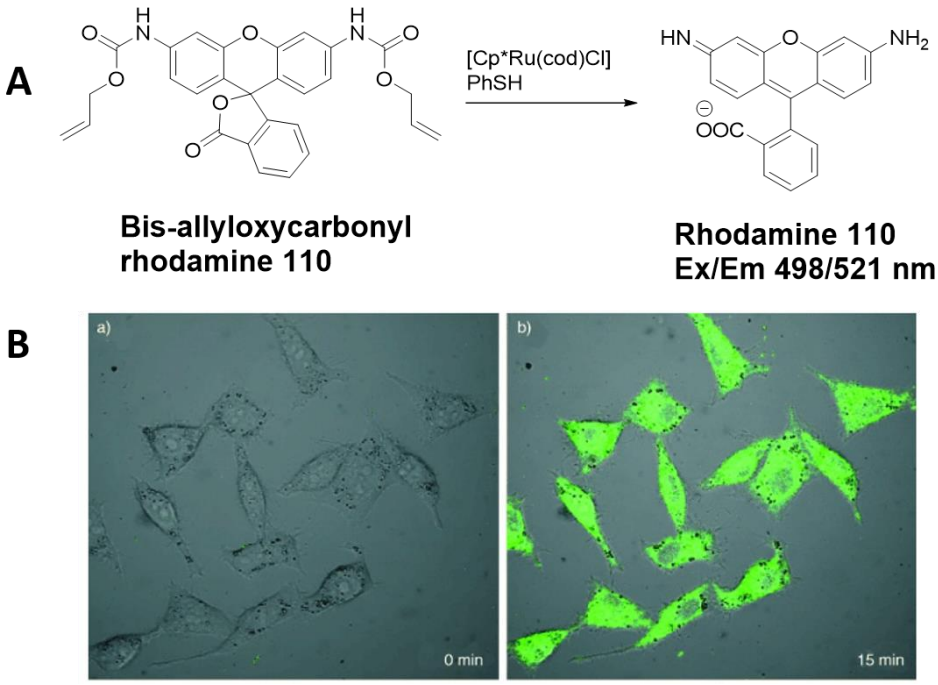

Figure 2.2 (A) Activation of bis-allyloxycarbonyl rhodamine 110 to rhodamine 110 ($\lambda_{Ex/Em}$ 498/521 nm). (B) Hela cells were incubated with bis-allyloxycarbonyl rhodamine 110 (100 µM) for 30 min. The cells were washed, and the Ru catalyst was added (20 µM) with thiophenol (500 µM). The left image was taken immediately after addition of the catalyst, the right was taken after a further 15 min. Adapted from reference 43.

Since then, a number of other ruthenium complexes (Figure 2.3) have been developed, including a series of more biocompatible ruthenium complexes for fluorophore and pro-drug activation.[46] Ruthenium has also been used in creative ways for different purposes, for example, it has been used as a catalyst to selectively activate DNA binding molecules. The molecules when bound to DNA then fluoresce, allowing imaging of the cells using methods such as flow cytometry.[47] Furthermore, ruthenium has been used to active luciferase substrates (which subsequently react with the luciferase) thus creating a real-time reporting system of catalytic activity.[48] One recent piece of work with a ruthenium catalyst showed that when conjugated to a mitochondrial targeting moiety (Figure 2.3), subcellular localisation of the catalyst occurred, allowing organelle specific catalysis.[49]

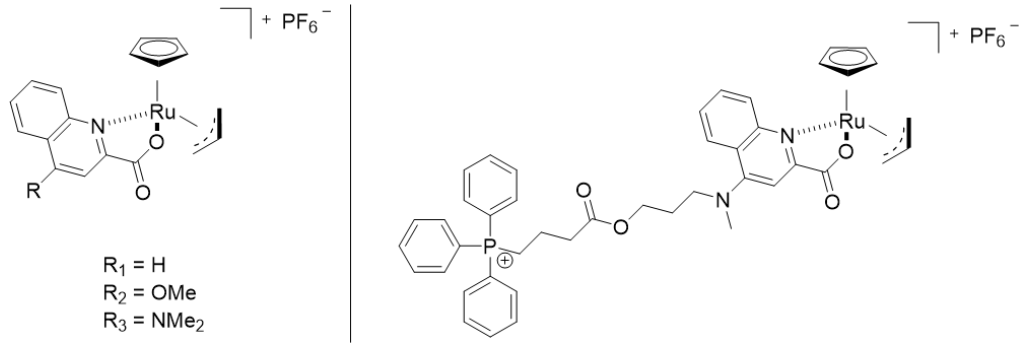

Figure 2.3 Left. Ruthenium complexes developed by Meggers that were catalytically active inside cell. Right.[46] Mitochondria targeting ruthenium catalyst developed by Mascarenas for subcellular localization of catalysis.[49]

Copper is another frequently used metal and is attractive for its catalytic role in the CuAAC reaction.[50,51] Clavadetscher functionalised TentaGel resin with amino groups, to entrap Cu onto the surface. (Figure 2.4). The Cu-nanoparticles then catalysed the synthesis of a mitochondria targeted coumarin using a coumarin azide and an alkyne linked lipophilic cation via the CuAAC. This reaction was carried out *in vivo*, the Cu-nanoparticles implanted into the yolk sac of zebrafish 24 h after fertilisation. After 3 days, with no display of toxicity, the coumarin-N_3 (5 μM) and an alkyne linked lipophilic cation (5 μM) were injected, and fluorescence measured after 24 h (see Figure 2.4).

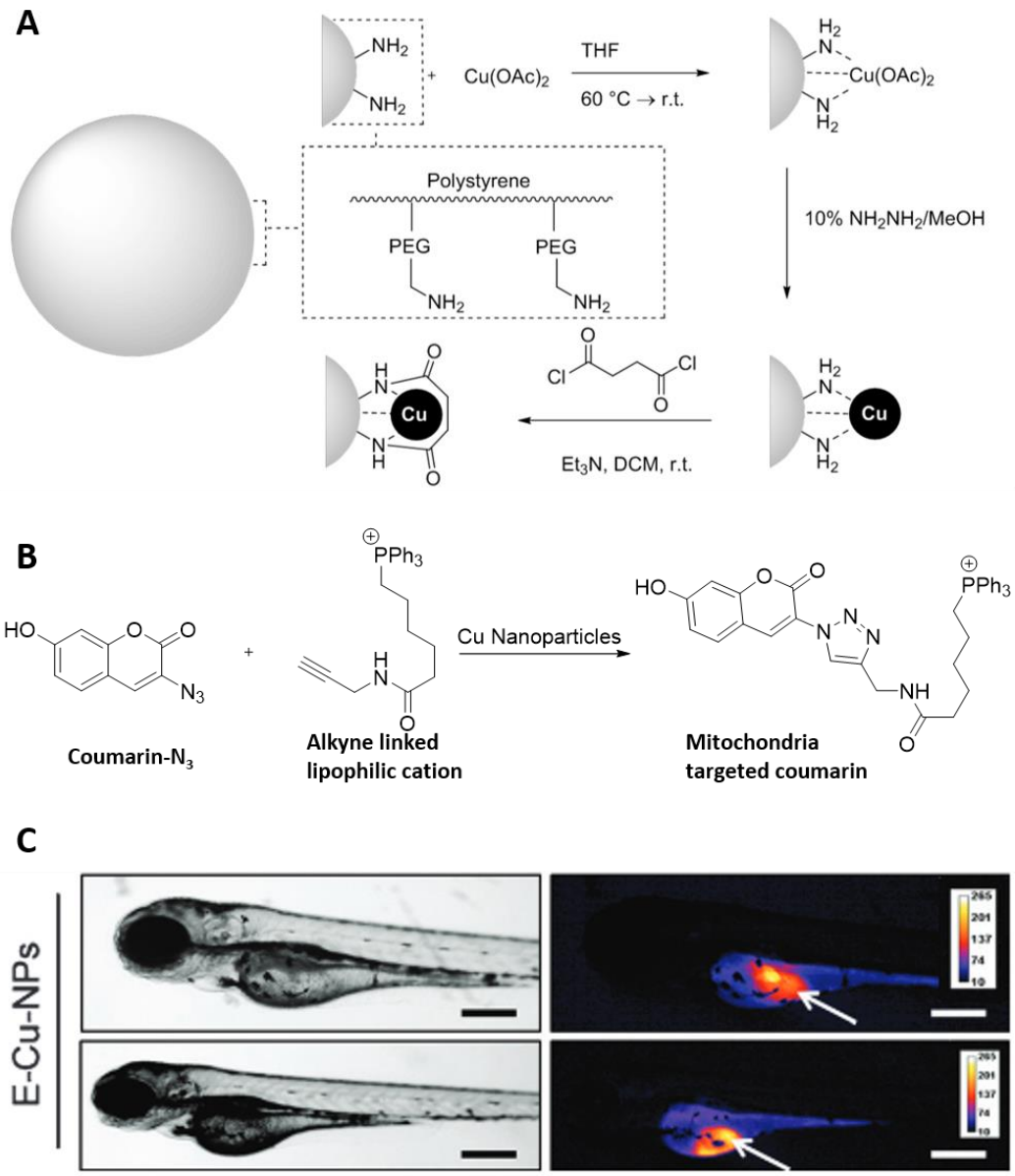

Figure 2.4 (A) Synthesis of Cu nanoparticles on Tentagel resin. (B) Synthesis of a fluorescent mitochondrial targeting compound via the CuAAC using the Cu Nanoparticles. (C) Demonstration of the reaction in the yolk sac of zebrafish, the heat map indicates levels of fluorescence indicated by the white arrow (scale bar 250 μm). Adapted from reference 49.

Gold catalysts in living systems have also gained popularity.[52–54] A prominent example by Tanaka and co-workers used a fluorescently labelled Au(III) complex (see Figure 2.5) that was coordinated to *N*-glycoalbumin through hydrophobic interactions. The *N*-glycoalbumin-Au(III) complex was administered intravenously into mice with accumulation in the liver and intestine due to the glycans present on the complex. After 30 min an *O*-propargylated cyanine dye (Cy7.5) (5 nmol) was added intravenously and the mice were imaged over the following

2 hours, with the Au(III) complex catalysing the activation of a fluorescent imaging agent. This work demonstrates an important step for gold metal catalysis *in vivo*.[54]

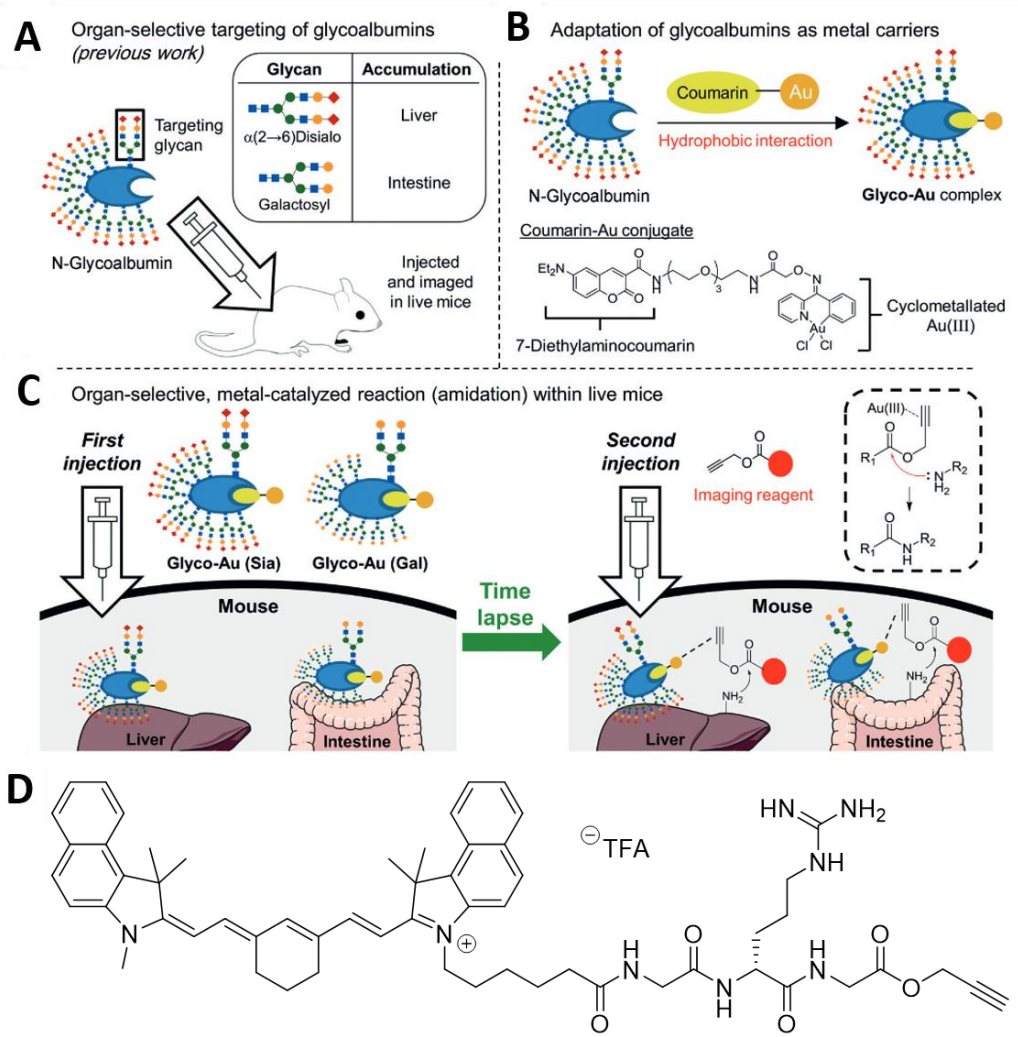

Figure 2.5 Overview of the work by Tanaka. (A) Two glycoalbumins were developed one to target the liver the other the intestine. (B) A coumarin-Au(III) complex was attached to these glycoalbumins via a hydrophobic interaction between the coumarin and albumin. (C) The glycoalbumin Au(III) complexes were injected intravenously into mice (3.4 nmol) and after 30 min a second injection with a Protected Cy7.5 imaging agent (5 nmol) was administered. (D) Structure of protected Cy7.5. Image adapted from reference 52.

Whilst ruthenium, copper and gold are interesting examples of metals used for catalytic reactions inside living systems, other metals have also been tried. Iron and iridium are two such examples, though their use in the biological settings has been limited to just one example each.[55,56] Of all the transition metals, palladium is by far the most utilised in a biological setting[57,58] and was the first that was specifically delivered into cells and used for novel carbon-carbon bond formation.

2.1.3 Palladium chemistry in biological settings

Palladium has gained popularity in bioorthogonal chemistry due its ability to perform catalytic cross-coupling reactions, enabling the generation of carbon–carbon and carbon–heteroatom bonds under mild, biological conditions.[59–61] Palladium catalysts have been used to initiate a range of intracellular reactions including dealkylation,[62,63] decaging of propargyloxycarbonyl and allyloxycarbonyl groups,[60,61,64–68] as well as Suzuki–Miyaura cross-couplings (Figure 2.6).[69,70]

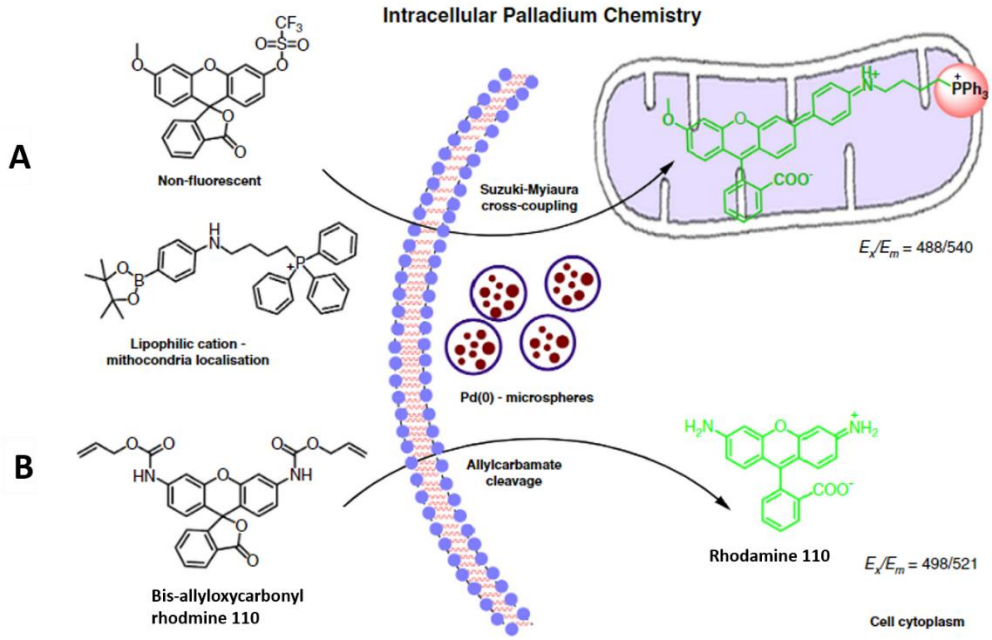

Figure 2.6 Summary of the first intracellular palladium reactions by Yusop. A nanoparticle with Pd(0) entrapped on the surface. These Pd-nanoparticle were able to catalyse: (A) A Suzuki-Miyaura cross coupling reaction that generated a fluorescent dye with a mitochondrial localising moiety. (B) The decaging of a caged fluorophore bis-allyloxycarbonyl rhodamine 110 to rhodamine 110. Adapted from reference 55.

Other work that included palladium mediated reactions in cells, have been the selective activation of enzymes through deprotection of modified amino acids within proteins[60] to the synthesis of anticancer agents *in cellulo* from two benign precursors;[61] as well as activation of prodrugs.[62,63,68] To date, the majority of examples have used Pd(0) nanoparticles entrapped within a polymeric nanoparticle support[61–63,66–69,71] (Figure 2.6), or simple palladium salts such as $Pd(OAc)_2$[60,70] although these are toxic.

There is a desire to move toward the use of small molecule homogenous palladium catalysts. Highly active homogenous palladium catalysts used in organic chemistry are often based on

stabilising ligands e.g. phosphine or *N*—heterocyclic carbene (NHC) ligands but few have been used in a biological setting.

Work to date has included the use of NHC-Pd catalysts in a biological setting with a NHC-Pd salt used to carry out a Suzuki–Miyaura cross coupling on the cell surface to label the cells with biotin.[70] Another example was the development of a water soluble NHC-Pd catalyst[65] that used a cell penetrating peptide[72] to increase uptake into cells and then catalytically activate a caged fluorophore (Figure 2.7). The most recent work was carried out by Mascarenas, who developed a series of palladium catalysts with simple phosphorous based ligands that were attached to mitochondrial targeting moieties (Figure 2.7). Though these compounds were relatively insoluble in aqueous media, they were successfully identified within mitochondria and used to switch on fluorophores in the mitochondria preferentially over the cytoplasm.[64]

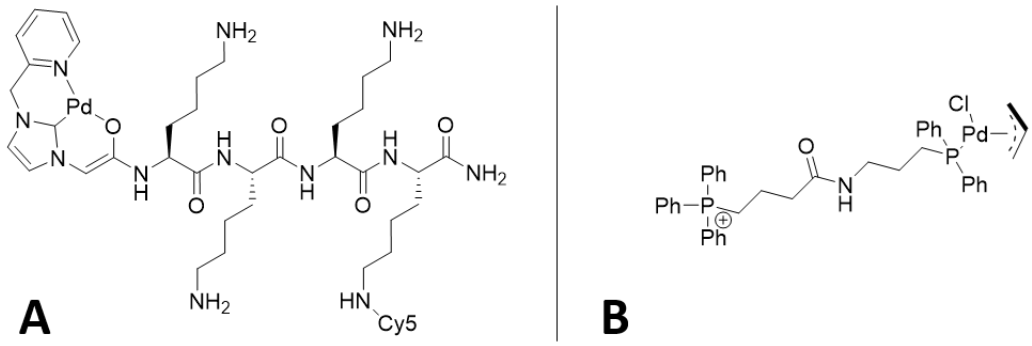

Figure 2.7 (A) The catalyst made by Indrigo with a poly-cationic sequence to enhance cellular uptake. (B) The catalyst synthesis by Mascarenas with a mitochondrial targeting moiety.

2.1.4 Chapter aims

Based on the previous work described, there is currently a niche for a homogenous Pd-catalyst that can specifically target cancer cells directly. There was a desire to synthesise a palladium catalyst designed with the express intent of having a bioconjugation handle so that it could be coupled onto a targeting molecule. This is something that has not previously been explored for any metal. The catalysts synthesised need be catalytically active inside cells given the desired application for use with antibodies *in vivo* i.e. water soluble and biocompatible.

The Pd-catalyst would follow the structure previous devised by Meldal[73] and further developed by Indrigo (Figure 2.8).[65] The final coordinating ligand is currently undefined in the literature and is presented here as Y, but would be a highly labile ligand which could be easily exchanged to convey catalytic activity (this is discuss in more detail later in this chapter). The synthesis of these ligands would incorporate solid phase peptide synthesis methodologies and the use of a chlorotrityl linker to generate a carboxylic acid moiety at the end of the molecule. This carboxylic acid could subsequently be "activated" into an NHS-ester for conjugation to biomolecules via amide bond formation.

After successfully devising a methodology for synthesising this catalyst, it could be used to explore creating catalysts with different linkers and thus build a library to validate the robustness of the synthetic strategy. These catalysts will need to be tested for their ability to catalyse a de-propargylation reaction, key for the "switch on" mechanisms desired for *in vivo* studies. be, however the catalyst can be tested on a translatable model such a 3D spheroids – model yet to be used in bioorthogonal chemistries.

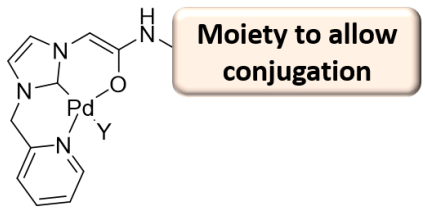

Figure 2.8 Structure of the desired NHC-Pd catalytic centre with an additional moiety for conjugation onto biological targeting molecules.

2.2 Results

2.2.1 Synthetic strategy for synthesis of *N*-Heterocyclic Carbene-Pd catalysts

A general structure for the palladium catalysts needed is shown in Figure 2.8., however the first palladium catalyst was chosen to be made is shown in Figure 2.9. This catalyst contains an amino hexanoic acid linker acting as a spacer between the palladium centre and a carboxylic acid group. The purpose of the carboxylic acid is to be activated into an *N*-hydroxysuccinamide ester. This basic catalyst structure contains all the desired properties for eventual bioconjugation to proteins.

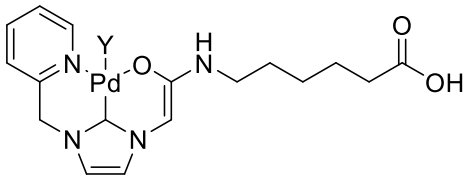

Figure 2.9 The initial palladium catalyst to be made that incorporated the features desired. The catalytic centre and a carboxylic acid for future bioconjugation strategies.

The moiety of conjugation should be able to catalyse a range of reaction but the most desired is the removal of propargyl groups from molecules such as fluorophores. The general mechanism for de-propargylation is shown in figure 2.9. The exact nature of the catalytic cycle is still debated and likely follows a variety of route. Recently, Coelho suggested that the catalytic cycle might have a bi-phasic kinetic profile.[74] The general mechanisms that they suggest for palladium catalysts of different oxidation states is shown in figure 2.10. Generally, The palladium catalyst will interact with the π-bonds of the alkyne and either use it as a ligand (Pd(II/IV) catalysts) or form a direct bond (Pd(0) catalysts). During this step the rest of the propargyl group might be released in the Pd(0) mechanism. Then the alkyne can be subjugated to a nucleophilic attack and this will likely be water in a biological system due to its abundance. The molecule then undergoes a tautomerization followed by a second nucleophilic attack and then release of the products and restoration of the original catalyst. These mechanisms are still unconfirmed and in all likelihood, there could be a variety of other things happening for example two palladium catalysts acting on the same substrate.

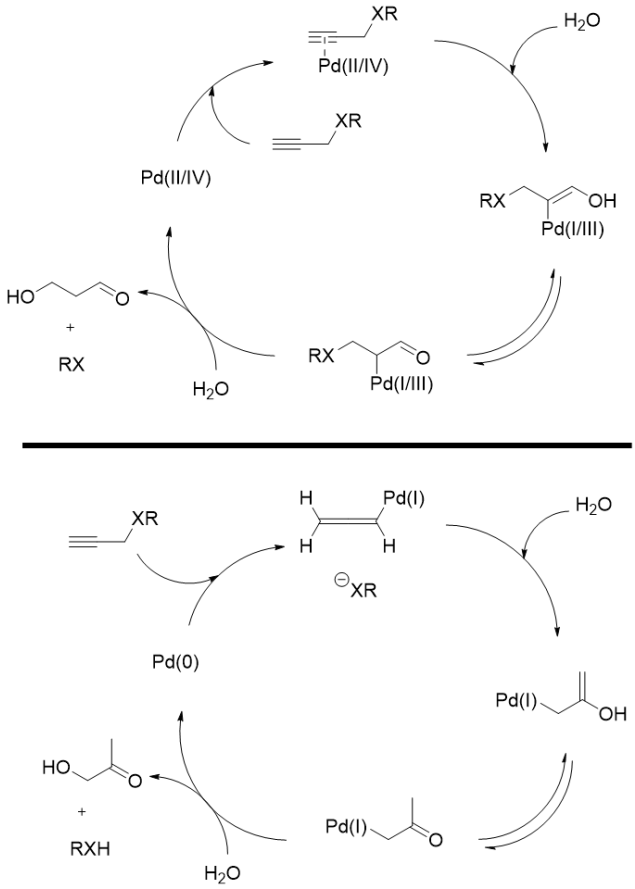

Figure 2.10 De-propargylation reaction catalysed by palladium. Top: Proposed mechanism of deprotection using a palladium II or IV catalyst. Bottom: Proposed mechanism of deprotection using a palladium 0 catalyst. Adapted from reference 74

To make the homogeneous catalyst shown in Figure 2.9, the synthesis began with a two-step synthesis of a pyridine-based imidazolium ligand (**3a**). This ligand is able to coordinate palladium through: the nitrogen lone pair on the pyridine ring, a carbene (that was) generated from the imidazolium, and the carbonyl from the carboxylic acid group. This ligand had been modified from an existing structure and was devised by Meldal.[73] The procedure followed the literature with a minor modification; step one was carried out for 18 h instead for 6 h (Scheme 2.1).

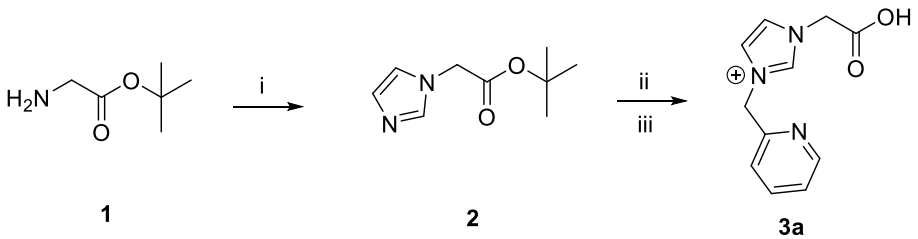

Scheme 2.1 (i) NH_3, glyoxal, formaldehyde, *i*PrOH, 80 °C, 18 h; (ii) 2-(bromomethyl)pyridine hydrogen bromide, DMF, 150 °C, 25 min, μW; (iii) TFA, 1 h.

The first reaction was a Debus-Radziszewski imidazole synthesis with the driving force behind the reaction the generation of an aromatic system through the loss of water (Scheme 2.2).

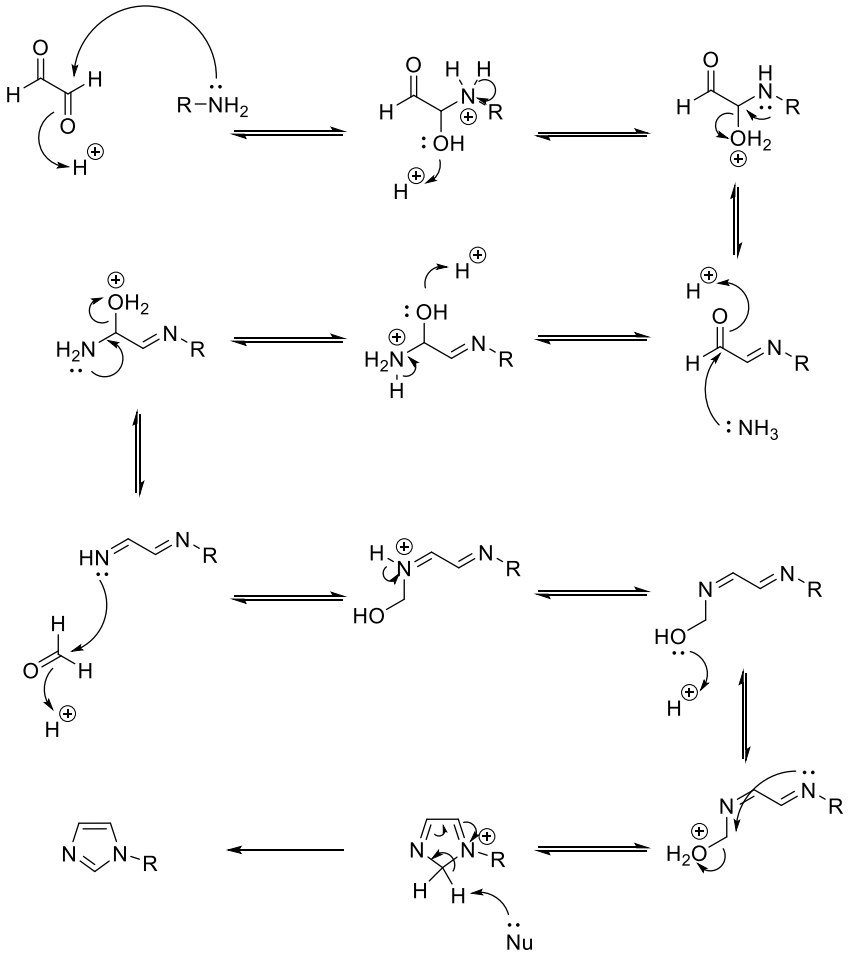

Scheme 2.2 Debus-Radziszewski imidazole synthesis proposed for the reaction in Scheme 2.1. First the primary amine from the amino acid forms and imine with glyoxal. The remaining carbonyl from the glyoxal is then attacked by ammonia to form a second imine following the loss of water. Cyclisation occurs with the loss of water again the driving force.

While the yield of this reaction was poor (30 %) by comparison to the reported literature (60 %) (Table 2.1), the starting reagents were commercially available and carried out on a multigram scale. The low yield was attributed to the multiple side products formed, including imidazole, formed by the addition of two ammonia groups (Table 2.1). Minor alterations to the method were attempted but did not increase the yield significantly.

Table 2.1 Reaction conditions explained to give compound **2**.	
Conditions and (reaction scale)	**Yield (%)**
Literature procedure (0.5 g), 6 h	40
Literature procedure, reaction time 18 h (0.5 g)	33
Literature procedure, time 24 h (2 g)	30

Following isolation of the imidazole product, it was *N*-alkylated through an S_N2 substitution using 2-(bromomethyl)pyridine hydrogen bromide. The reaction was carried out under microwave irradiation before removing the *tert*-butyl group with TFA (Scheme 2.1). Whilst the conversion of **2** to generate **3a** was typically 30 % the isolated yield was often only 5 % (isolation was carried out by preparative reverse phase high pressure liquid chromatography (RP-HPLC)). Multiple attempts to purify the compound using different methods (such as de-activated silica, alumina) did not result in higher yields. Using RP-HPLC gave the highest purity of the compound and was thus favoured, but gave low yields, yielding only 20 mg of **3a** from 350 mg of **2**.

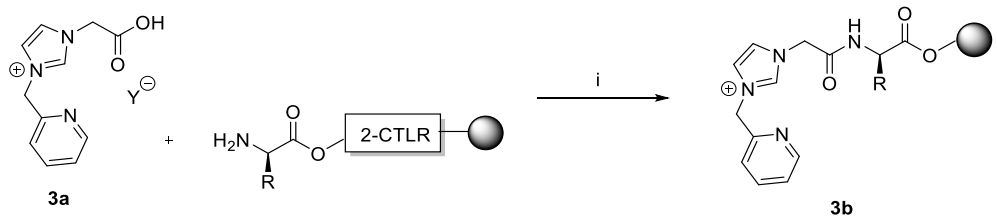

Scheme 2.3 Coupling of **3a** on to an amino acid attached to a solid phase support via a linker; (i) TBTU, NEM, DMF, 20 min, 60 °C, μw.

3a was then coupled onto an amino acid via solid phase synthesis (see Scheme 2.3) with 2-(1H-Benzotriazole-1-yl)-1,1,3,3-tetramethylaminium tetrafluoroborate (TBTU) used as a coupling agent with the base *N*-ethyl morpholine (NEM) in DMF. The solution was heated to 60 °C for 20 minutes with the coupling confirmed by a negative Kaiser test (absence of primary amine groups). With the successful coupling, palladium could then be loaded to generate the final catalyst **3c** (Scheme 2.4).

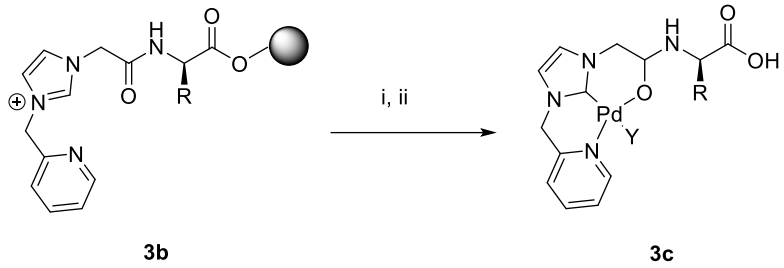

Scheme 2.4. Palladium loading into the ligand; (i) Ar, BEMP, 45 mins r.t.; (ii) DMF, $Pd(COD)Cl_2$ O/N, r.t.

Due to the poor yield and time taken to generate **3a**, a new methodology was devised based on the retrosynthesis proposed in Figure 2.11. Given the availability of starting reagents it was hypothesised that the organic ligand in compound **3a** could be synthesised using a sub-monomer type approach first devised by Zuckerman for the synthesis of *N*-alkylated peptoids.[75,76]

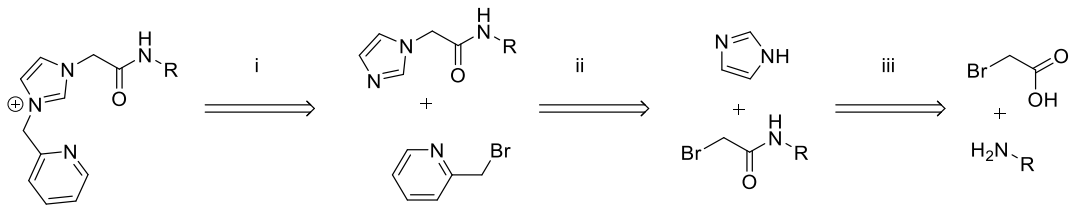

Figure 2.11 Retrosynthesis of the palladium coordinating ligand. (i) *N*-alkylation with Bromomethyl pyridine; (ii) *N*-alkylation with imidazole; (iii) Amide bond formation.

Using this synthetic route, bromoacetic acid could be coupled onto a primary amine (attached to a solid support via a linker) by activating the carboxylic acid with DIC. Next imidazole could substitute the bromine group via S_N2 substitution. Finally, an *N*-alkylation using 2-bromomethyl pyridine could be carried out (Scheme 2.1). This synthetic route was used so that all reactions were carried out using solid-phase synthesis methods thus reducing the number of purifications step, increasing the efficiency and giving an overall simpler synthetic route.

The palladium catalyst was thus created using the overall synthesis shown in Scheme 2.5. 6-Aminohexanoic acid was used a model amino acid spacer to test different reaction conditions when synthesising the ligand.

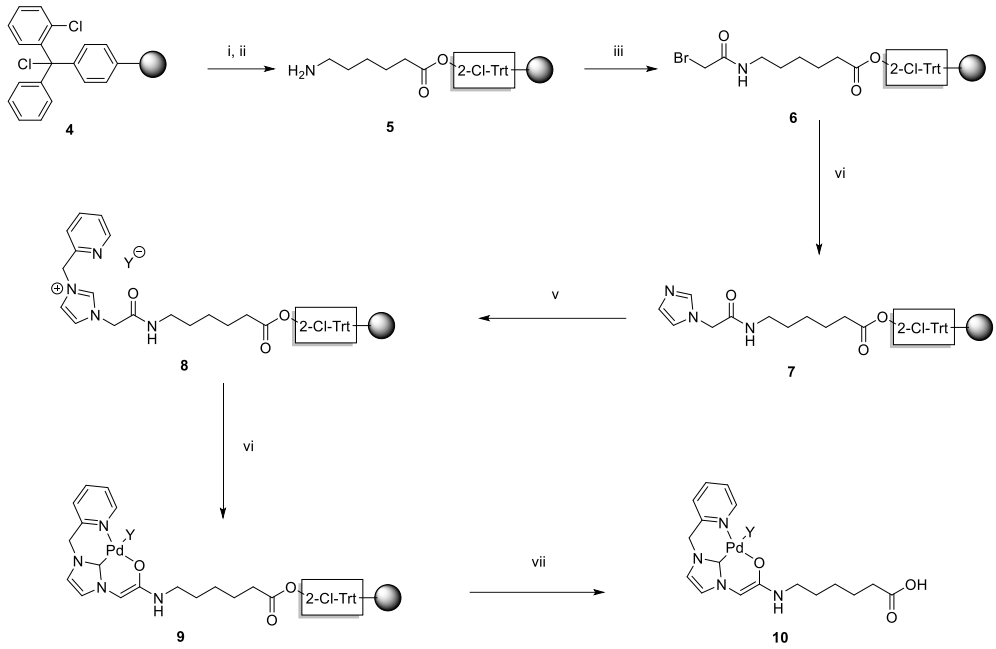

Scheme 2.5 Synthetic pathway for the model NHC-Pd catalyst. (i) Fmoc-Ahx-OH (0.3 M), DIPEA (0.6 M), dry DMF, 1 h; (ii) 20 % piperidine in DMF, 2 × 10 min; (iii) Bromoacetic acid in DMF (2 M), DIC (1 M), µw, 20 min, 60 °C; (vi) Imidazole (2 M), $AgNO_3$ (0.5 M), DMSO, µw, 40 min, 60 °C; (v) 2(bromomethyl)pyridine hydrogen bromide (1.5 M), $AgNO_3$ (0.5 M), Et_3N (1 M), dry DMF, µw 90 min 60 °C; (vi) Ar, BEMP, dry DMF, 45 min, r.t., $Pd(COD)Cl_2$ in DMF,18 h.; (vii) 30 % HFIP in DCM.

Using a 2-chlorotrityl linker on a polystyrene resin (mesh 100-200), Fmoc protected 6-aminohexanoic acid in the presence of DIPEA in anhydrous DMF was attached to the resin through an S_N1 reaction Scheme 2.6.

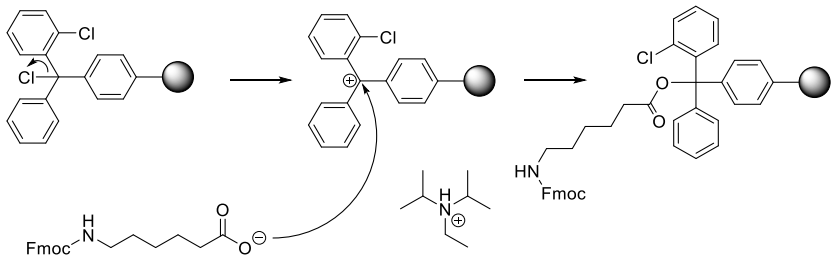

Scheme 2.6 Mechanism for first amino acid coupling to the chlorotrityl linker.

Following Fmoc deprotection using 20 % piperidine in DMF, the synthesis of the ligand was carried out. Starting with the free primary amine, an amide bond was created by adding bromoacetic acid (2 M) with the coupling agent DIC (1 M) to create an anhydride susceptible to nucleophilic attack by the primary amine (Scheme 2.7).

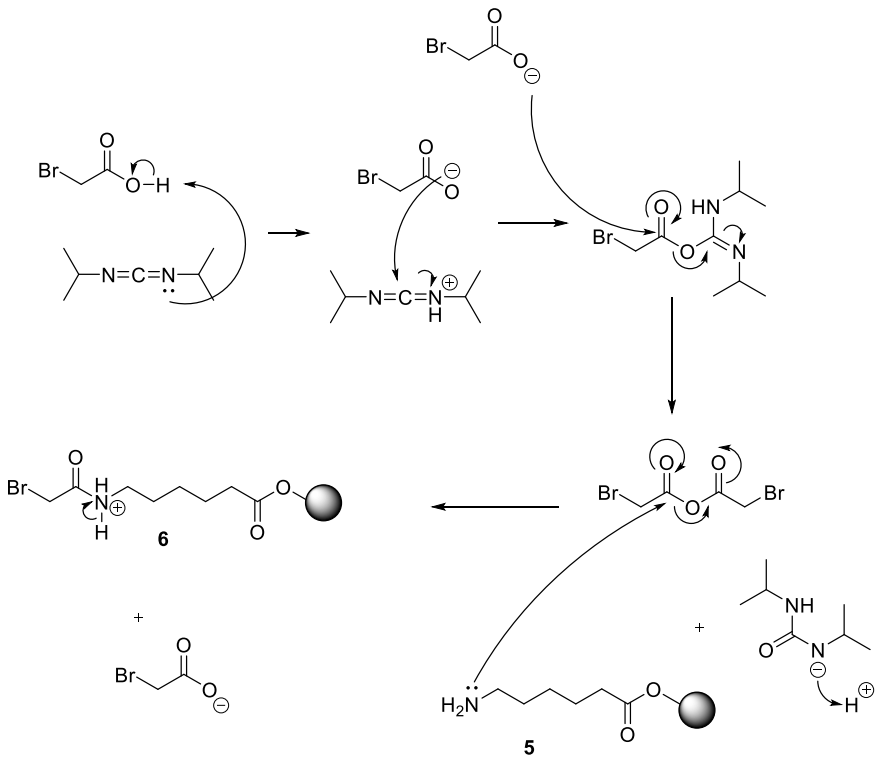

Scheme 2.7 Mechanism of amide bond formation using DIC as a coupling agent that generates the symmetrical anhydride.

The reaction to generate compound **6** from **5** was monitored by the Kaiser test. Following the successful coupling, the bromine group from compound **6** was then displaced by imidazole to generate **7**. Several reaction conditions were trialled, and it was found that the presence of silver nitrate improved the conversion (Table 2.2 and Figure 2.12) with DMSO as the optimal solvent. It is known that silver nitrate reacts with haloalkanes (often forming silver-halogen salt precipitates). It was hypothesised that the silver ion interacts with the bromine to polarise the bond and promote attack (Scheme 2.8).

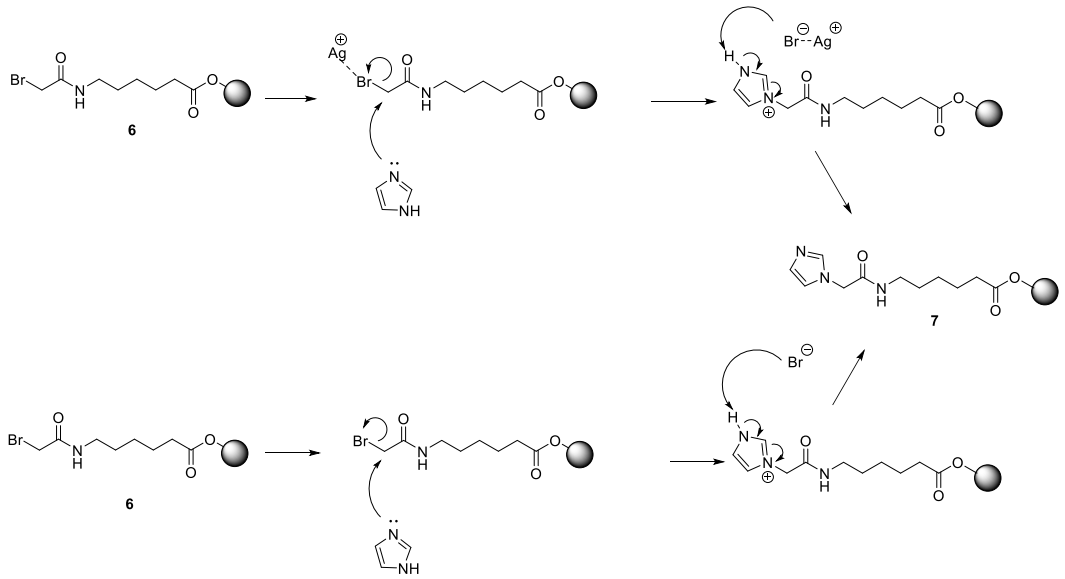

Scheme 2.8 Generation of **7**. (Top) Proposed mechanisms of imidazole substitution using silver ions improving the bromines atom's ability to act as a leaving group. (Bottom) The mechanism without the silver ions.

The optimisation of the on-resin alkylation of **6** was carried out under microwave heating (60 °C, 25W, 40 min). At the end of the reaction, **7** was cleaved off the resin with 30 % HFIP in DCM (45 min) and the purity analysed by HPLC and ^{1}H NMR.

Table 2.2 Different reaction conditions used to substitute the bromide by an imidazole group. (generating **7** from **6**) [a] Determined by HPLC (ELS detection). [b] Determined by ^{1}H NMR.

Entry	**Imidazole (M)**	**Additive**	**Solvent**	**Conversion (%)**
1	1	None	DMF	50[a]
2	1	Et_3N 1 eq.	DMF	60[b]
3	1.5	Et_3N 1 eq.	DMSO	75[b]
4	1.5	None	DMSO	77[b]
5	2	$AgNO_3$ (0.5 M)	DMSO	97[a]

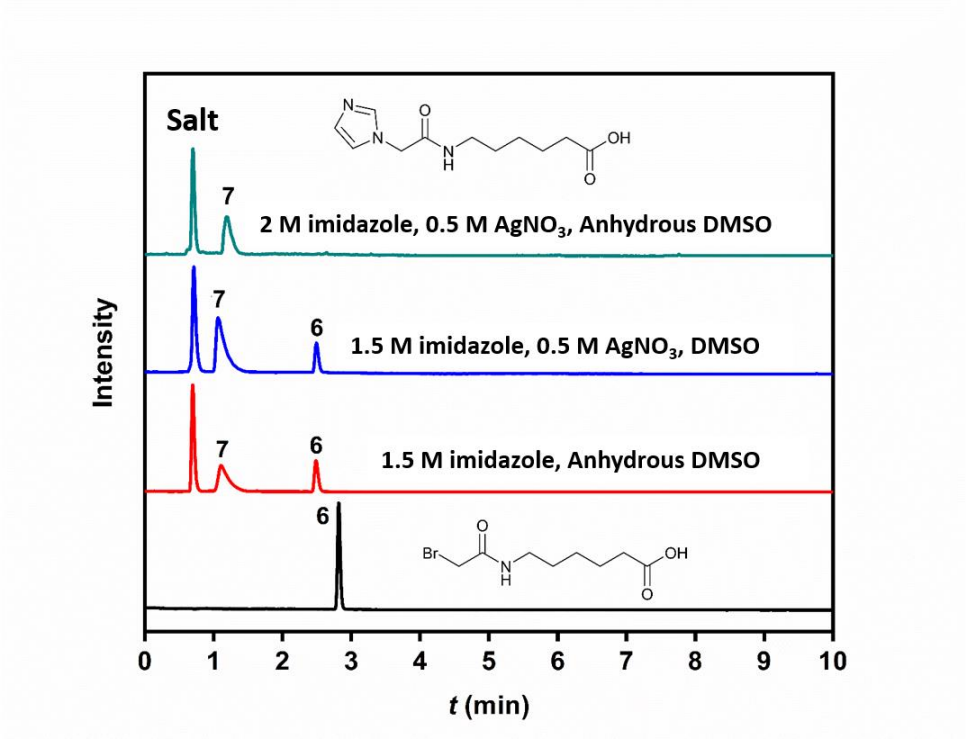

Figure 2.12 Normalised HPLC chromatograms (detection by an evaporative light scatting detector) of the alkylation of **6** after 40 min at 60 °C with μw irradiation. Complete conversion to product **7** was observed when DMSO was used as solvent with $AgNO_3$ as an additive. Peak at 0.8 min is salts.

It can be seen from Figure 2.9 that full conversion to **7** from **6** was achieved with imidazole (2 M), $AgNO_3$ (0.5 M) in dry DMSO with 40 min of microwave irradiation (60 °C). The peak with retention time of 0.8 min are salts/DMSO traces carried through from the cleavage protocol.

Following successful substitution (confirmed by HPLC and ^{1}H NMR) the imidazole on compound **7** was then *N*-alkylated with 2-(bromomethyl)pyridine to form **8** (Scheme 2.9). All the reactions listed in Table 2.3 were carried out in DMF under microwave irradiation (60 °C, 25W, 90 min). After the completion of the reaction, the compound was cleaved off the resin with 30 % HFIP in DCM for analysis by HPLC and ^{1}H NMR.

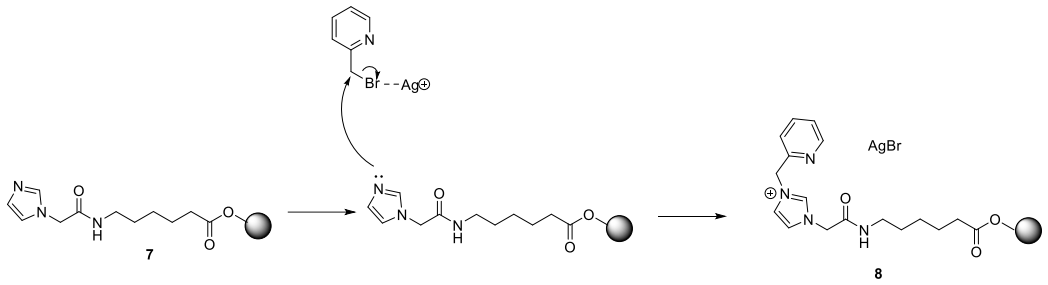

Scheme 2.9 Mechanism for *N*-alkylation of imidazole on the resin.

Table 2.3. Different reaction conditions for the *N*-alkylation using 2(bromomethyl)pyridine · hydrogen bromide to give **8**. [a] Determined by HPLC (ELSD and 254 nm). [b] Determined by ^{1}H NMR.

Entry	**2-(Bromomethyl) pyridine HBr**	**Additives**	**Time (min)**	**Solvent**	**Conversion (%)**
1	1.5 M	2 eq. Et_3N	30	DMF	50[a]
2	1.5 M	2 eq. Et_3N	60	DMF	70[a]
3	1.5 M	3 eq. Et_3N	60	DMF	70[a]
4	2 M	3 eq. Et_3N	60	DMF	80[b]
5	2 M	3 eq. Et_3N	90	DMF	96[a]
6	2 M	0.5 M Et_3N + 0.5 M $AgNO_3$	90	DMF	96[a]

Again, it was found that the presence of silver nitrate helped improve the conversion. In addition, the presence of Et_3N was critical in neutralising HBr salts from the starting material as well as HBr generated during the reaction. The purity of **8** is shown in two different HPLC traces in Figure 2.13, representative of the conversion following the optimised conditions (Entry 6, Table 2.3).

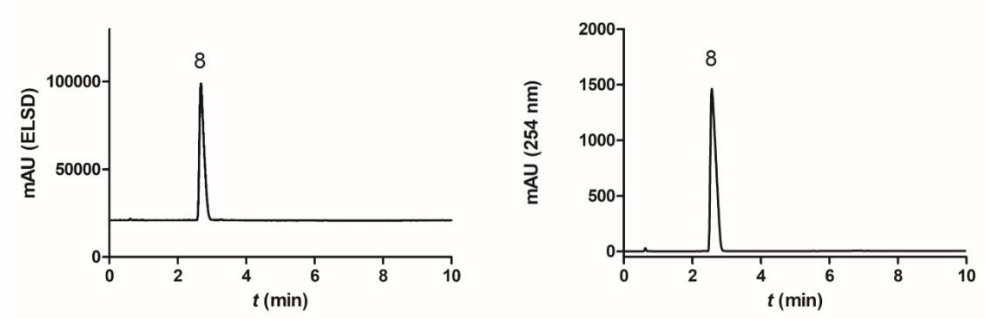

Figure 2.13 HPLC chromatograms of crude **8** after cleavage off the resin (crude purity > 95 %). Left: detection by ELSD. Right: detection at 254 nm.

Following complete conversion of compound **8**, palladium was then loaded into the ligand. BEMP (pK ~24) in DMF was added to the resin bound ligand and stirred for 45 minutes. The base deprotonates the NHC-imidazole proton to generate the carbene (Scheme 2.10) while the other equivalent of BEMP was used to generate the enolate from the α-carbonyl carbon. After, the resin was drained and palladium cyclooctadiene chloride in DMF was added, the reaction was stirred overnight and coordinated to the ligand complex to give **9** (the resin bound catalyst).

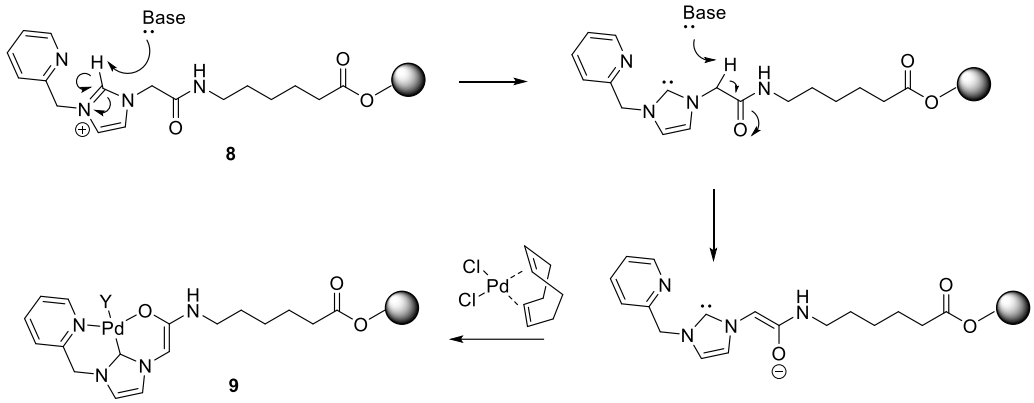

Scheme 2.10 Mechanism for the generation of the *N*-heterocyclic carbene and palladium coordination.

With **9** in hand, the resin was repeatedly washed with DMF and DCM, with cleavage from the resin achieved using a mixture of TFA, DCM and H_2O. The crude product was purified via preparative RP-HPLC to give **10** (yield 15 %, purity >95 %). The purity of **10** is shown in Figure 2.14 with the HRMS shown in Figure 2.15. To calculate purity, first ELSD channels were used to check for no other contaminants such as palladium salts (data not shown), then the major peak in the 254 nm channel was integrated and compared to the total integral of all other peaks found.

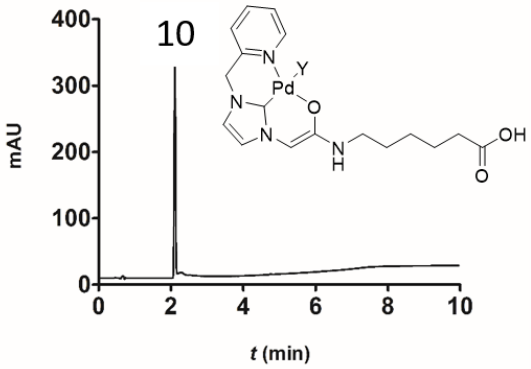

Figure 2.14 RP analytical HPLC of compound **10** after purification at 254 nm wavelength.

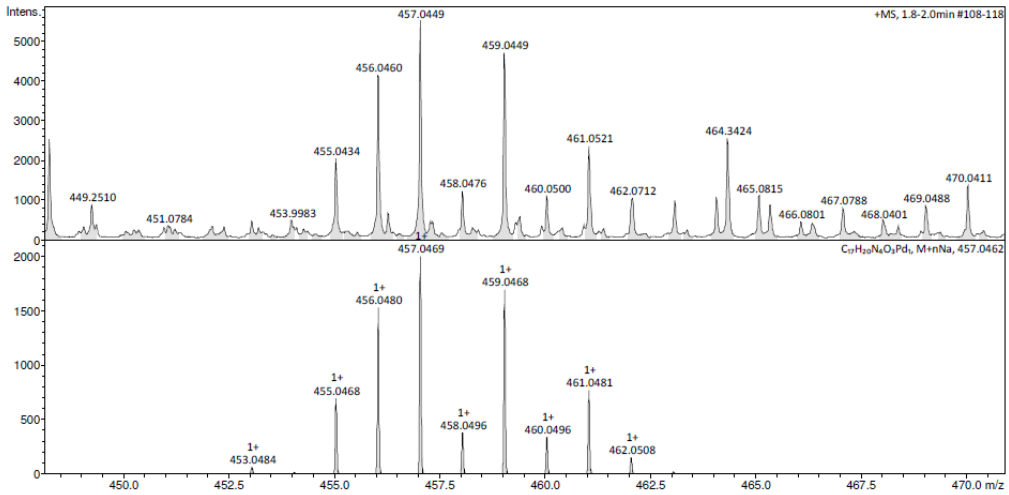

Figure 2.15 Measured (top) and predicted (bottom) HRMS (ESI) spectra for compound 10 [M+Na] (calculated 457.0469 for $C_{17}H_{20}O_3N_4Na_1{}^{106}Pd$; found 457.0624).

With compound **10** purified and isolated, the next step was to assess the scope of the synthetic methodology to determine if it could be replicated for more complex amino acids. Overall, the new synthesis route was hugely more efficient than the original approach based on the solution synthesis of the ligand (**3a**) and its purification.

2.2.2 Development of a catalyst library

Having established that the methodology worked, the solid-phase synthesis route was used to generate an NHC–Pd catalyst library. The amino hexanoic acid spacer was therefore substituted with a range of amino acids with all catalysts synthesised using the chloro-2-chlorotrityl linker on a polystyrene resin.

The range included hydrophobic, aromatic, and charged amino acids to compare the potential effect on catalytic activity, as well as the robustness of the synthetic method (Figure 2.16). ranging from single amino acids e.g. **11** to compound **17**. Furthermore, the synthetic methodology was also successfully applied to create a tripeptide using an amino methyl polystyrene resin functionalised with a Rink-amide linker that generated a terminal amide upon cleavage. **18** was cleaved from the Rink-amide linker using mixture of TFA and H_2O (19:1) with the NHC-Pd centre stable to these more extreme acid conditions.

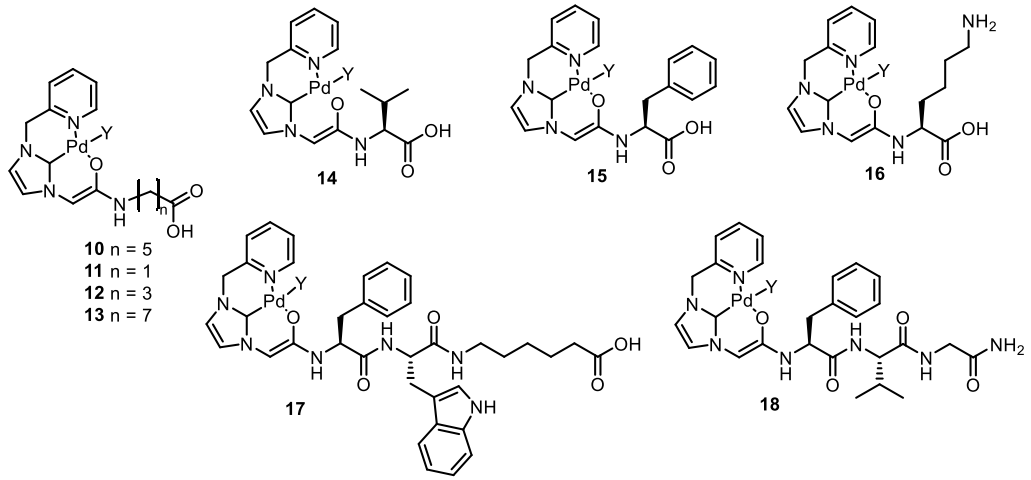

Figure 2.16 Library of catalysts synthesised using the synthetic methodology.

For characterisation, the ligands of each catalyst were fully characterised before loading with palladium using NMR, HPLC (ELS and 254 nm detection), and HRMS with the final catalysts (**10** – **18**) characterised by HPLC and HRMS. Using compound **11** as an example, the "naked ligands" and the Pd-loaded ligands displayed different retention times sufficient for separation by HPLC (Figure 2.17). Pleasingly this enabled a consistent purification strategy for all the catalysts.

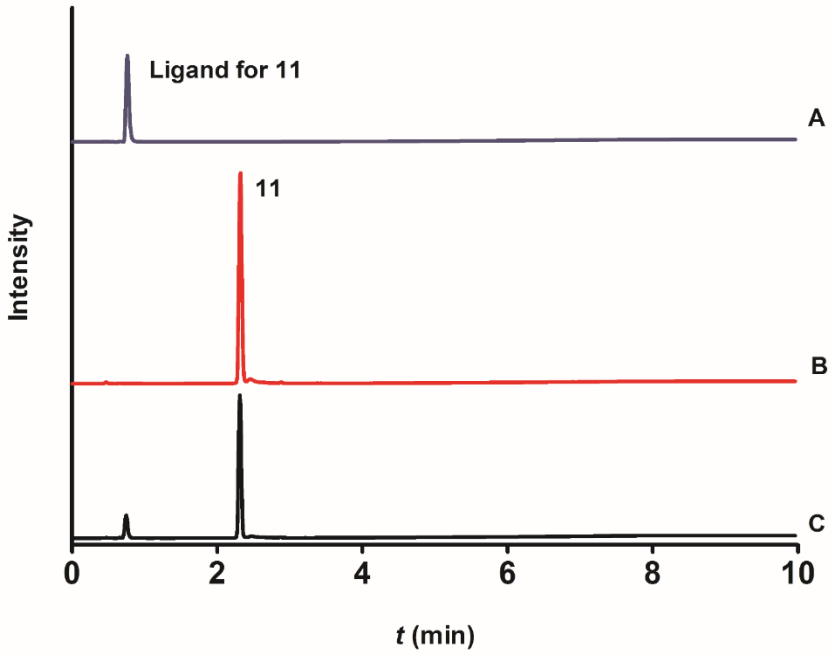

Figure 2.17 HPLC analysis (detection at 254 nm) of the ligand and catalyst 11. (A) The Ligand **11**. (B) Catalyst **11**. (C) A sample of catalyst 11 spiked with the ligand, showing the difference in retention time upon palladium loading.

Fascinatingly, it was found when examining the H^1 NMR of some of the ligands prior to palladium loading in CD_3OD, the N-C**H**-N imidazole proton was missing (expected chemical shift approximately 9.17 ppm). After changing solvent to d_6-DMSO both the NHC proton and the NH proton from the amide bond became visible, showing that these protons were exchanging with the acidic deuterium in CD_3OD. This is shown for compound **8** in Figure 2.18.

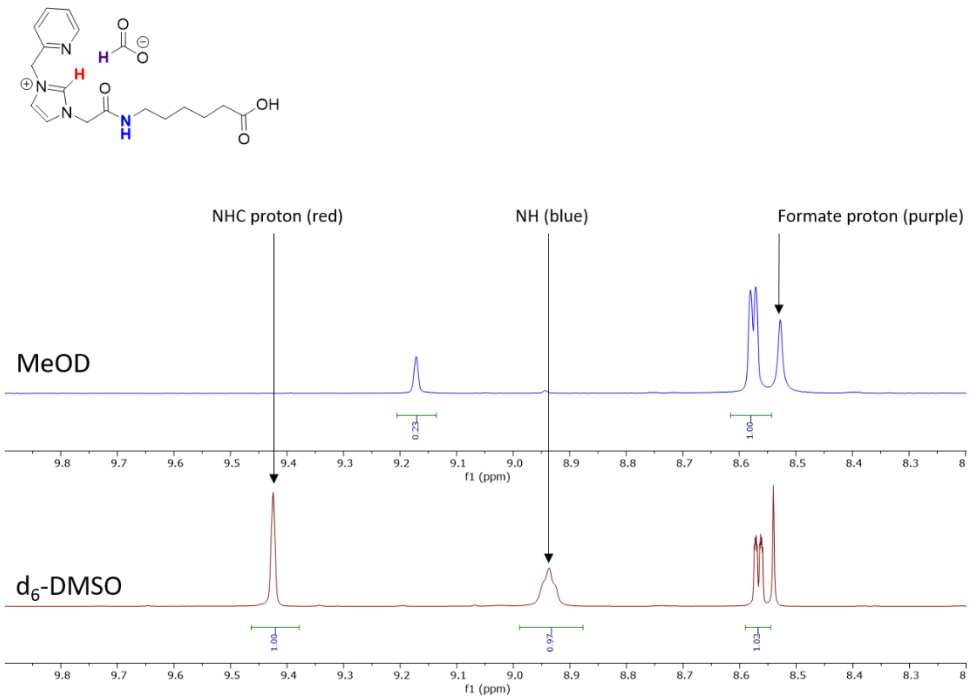

Figure 2.18 NMR spectra of compound **8** in CH_3OD (Blue) and d_6-DMSO (red). In d_6-DMSO the NHC and NH protons are clearly visible at 9.43 and 8.94 ppm respectively. The proton from a formate counter ion is also visible as a singlet at 8.54 ppm. In CH_3OD the peaks are no longer visible. The carboxylic acid proton was also not observed in CH_3OD and beyond the scale at 11.8 ppm in d_6-DMSO.

This proton deuterium exchange might suggest that the phosphazene base, BEMP, used in this reaction may not be necessary to generate the carbene, though further experiments would be required to test this. The reason why this exchange might be easier could be due to the presence of the amide bond. The donation of the nitrogen lone pair into the amide bond likely helps form a resonance structure of a 6 membered ring containing: the carbonyl oxygen and carbon atoms, the α-carbonyl carbon and imidazole nitrogen, N-**C**-N carbon and the exchangeable hydrogen atom in question. Furthermore, the lone pair from the pyridine ring is likely also contributing some bonding which might make a proton-deuterium exchange more likely. However, these hypothesises are purely speculation. The ligands for each of the catalysts are characterised in methods section (Chapter 5).

Once palladium was loaded, the catalysts were cleaved off the resin using 30 % HFIP in DCM and purified. The purity of the catalysts was analysed by analytical HPLC (Figure 2.19). The purity, yields and HRMS data for **10** – **18** are shown in Table 2.4.

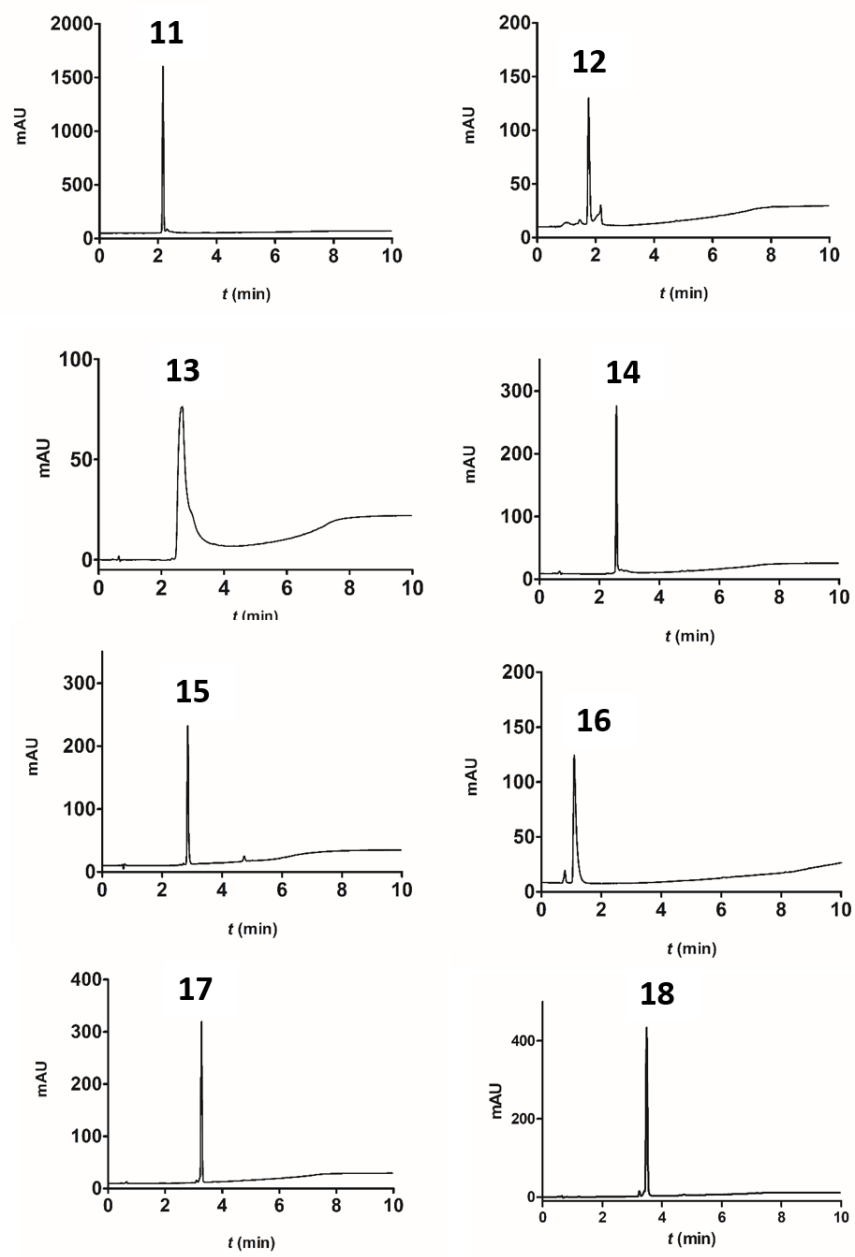

Figure 2.19 HPLC purity traces of compounds **11** – **18**, with detection at 254 nm.

Table 2.4. Summary table of the yields, purity by HPLC (ELSD and 254 nm) and HRMS of the catalysts **10** – **18**.				
Compd.	**Yield (%)**	**Purity (%)**	**Mass Calcd.**	**Mass Observed**
10	11	94	435.0643	435.0640
11	8	94	379.0017	379.0025
12	8	90	407.0330	407.0332
13	9	82	463.0963	463.0956
14	13	93	421.0486	421.0491
15	11	94	469.0486	469.0488
16	7	95	450.0752	450.0750
17	7	96	768.2136	768.2120
18	14	96	624.1545	624.1556

These catalysts (10 mM in CH_3CN/H_2O (3:7)) were found to be stable for two weeks at room temperature, and ≥ 8 weeks at 4 °C (Figure 2.20). This was another satisfying finding as in the clinical setting these catalysts could remain in the body for a significant period of time if attached to an antibody. Antibodies are known for their long half-life's (>2 months) and thus anything that might be attached to them in the future must factor in this consideration.

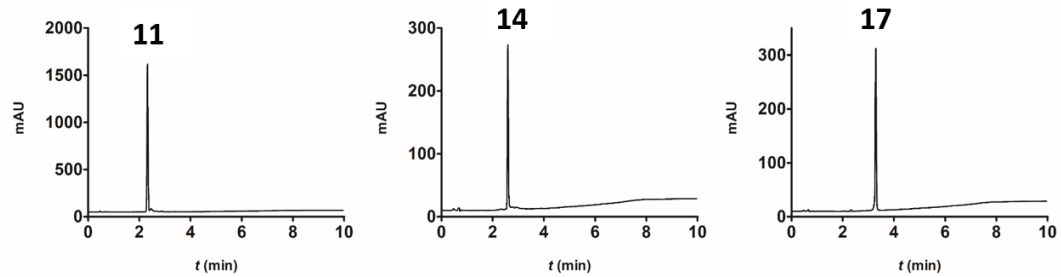

Figure 2.20 Stability of NHC-Pd catalysts **11**, **14** and **17** (*t* is retention time).

A caveat with the purity analysis is that it was only carried out by HPLC methodology. In this analysis both evaporative light scattering (ELS) (data not shown) and 254 nm wavelength detections were used. The ELS will detect any molecule including impurities such as potential palladium salts and other small molecules with no double bond conjugation moieties while the 254 nm wavelength detection was used to confirm where the desired product was eluting due to the presence of conjugated moieties. The methodologies were set up to ensure that all products were eluted after 2 minutes thus allowing the molecule time to separate from any

impurities. Moreover, eluting near the injection peak of the sample was also avoided as this causes issues with the ELS detection. To calculate the purity of signal deemed to be the product (suggested by low resolution mass analysis), the peak was integrated (on the 254 nm channel). All other peaks observed were also integrated and the comparison between the two was used to calculate the purity (table 2.4). Finally, it is known that the non-palladium bound ligands have separate retention times thus their presence could be easily detected if present. Anecdotally it also seemed that the catalysts with palladium seemed to have more absorbance at 282 nm compared to their non-palladium counterparts, though this was not used as any confirmation and is merely an observation. An issue with this methodology, there is no certainty that a second compound is not co-eluting with the desired product. However, if there was a contaminating product, we would likely have observed this in the mass spectrometry analysis. Molar extinction coefficients were not calculated for the compounds and this data may have been useful, though this would be calculated via known concentrations which would be subject to pipetting errors.

In conclusion a catalyst library was successfully synthesised with 9 different catalysts synthesised, purified and isolated. Whilst the yields were low, much of this can be attributed to reactivity of the carbene, as any water in the reaction system could revert it back to it protonated precursor thus will not generate the palladium containing product. More importantly with the new synthetic methodology, these catalysts can be made from scratch rapidly, the Pd ligands can be readily purified. With this success, the compounds were screened for their catalytic activity.

2.2.3 Screening of catalytic activity

Following the successful synthesis of these catalysts, their catalytic activity was evaluated against a protected version of the fluorophore 2,7-dichlorofluorescein (**DCF**). **DCF** was *O*-propargylated to create the protected version of the fluorophore (**Pro-DCF**) (synthesised by Durgadas Cherukaraveedu). **Pro-DCF** was converted back to the fluorescent derivative **DCF** ($\lambda_{Ex/Em}$ = 500/530 nm) upon Pd-catalysed cleavage of the propargyl group (Figure 2.21). The absorption maximum of **DCF** was found to be 500 nm with emission at 530 nm in accordance with the literature.[77]

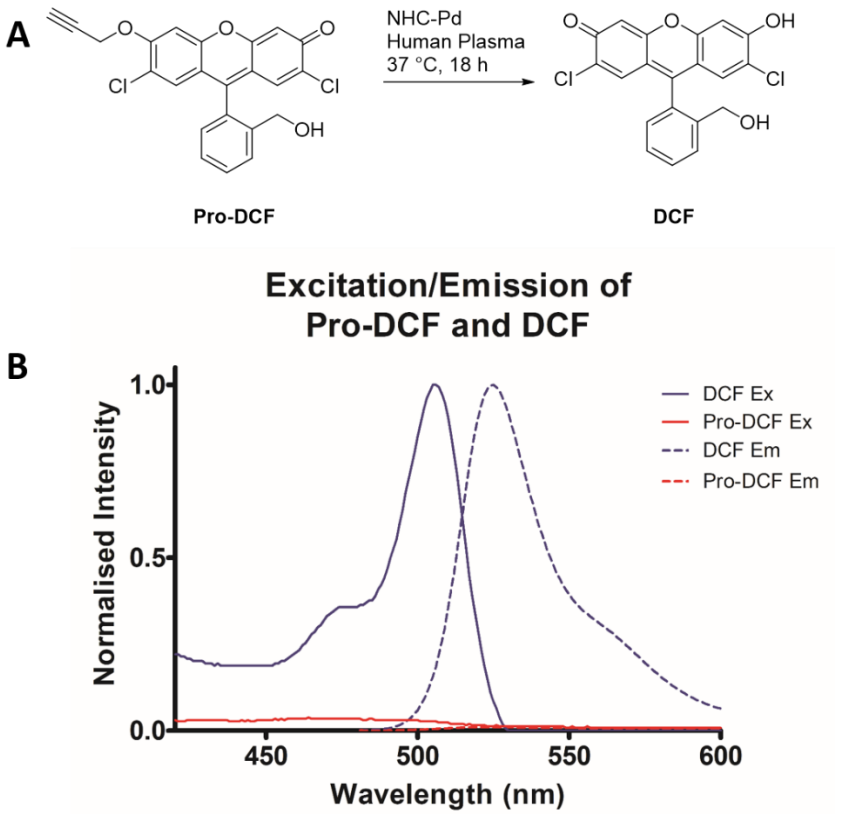

Figure 2.21 (A) Pd catalysed depropargylation reaction of **Pro-DCF** to give fluorescent **DCF** ($\lambda_{Ex/Em}$ 500/530 nm). In the presence of palladium the compound **Pro-DCF** loses its propargyl group resulting in conjugation of the aromatic rings being restored and its fluorescence being "switched-on". (B) Absorption (Solid lines) and emission spectra (dashed lines) of **Pro-DCF** (red) and **DCF** (blue). All spectra were measured at 10 µM in PBS.

The mechanism of deprotection is suggested in figure 2.22 which was based on the mechanism suggested in figure 2.10. The first thing to note is that de-propargylation will not happen without the presence of the palladium catalyst, this is observed in figure 2.23 control experiments. Initially the palladium catalyst has a highly labile ligand "Y" attached to it. To this point Y has not been discussed as it is not clear what it is from mass spectrometry data, however that is also indicative about its nature of being labile. It is speculated that Y is likely to be a solvent ligand, or some ion found in the solvent to which the compound has been exposed to during synthesis and purification. The most likely candidates are as follows with an explanation as to where they come from: water, from solvent systems and in biological media water is the most abundant molecule in any buffered system; acetonitrile (ACN) from HPLC purification systems; chloride ion, sodium chloride is often found in biological solutions, it may have also arisen form the palladium chloride source used in the synthesis; bromide ion, from the reagents used to synthesise the organic ligand (2-bromomethyl pyridine); formate ion, from the HPLC solvent system, formate is used to adject the pH in the

HPLC purification systems used; TFA ion, TFA was used in the cleavage of the compound from the solid phase resin support. Given the commonality and stability of Palladium II catalysts the remaining ligand Y is likely to be neutral i.e. water or acetonitrile. In the mechanism this ligand is exchanged with the propargyl group which utilises π-bonding. There is then a nucleophilic attack from water (although any nucleophile is possible) as this will be the most abundant nucleophile in a biological system, followed by an isomerisation. Finally, a second nucleophilic attack occurs with the release of the OR group (the fluorophore). The oxidised propargyl group is then released regenerating the catalyst. This description of the mechanism is purely speculative and is open to discussion.

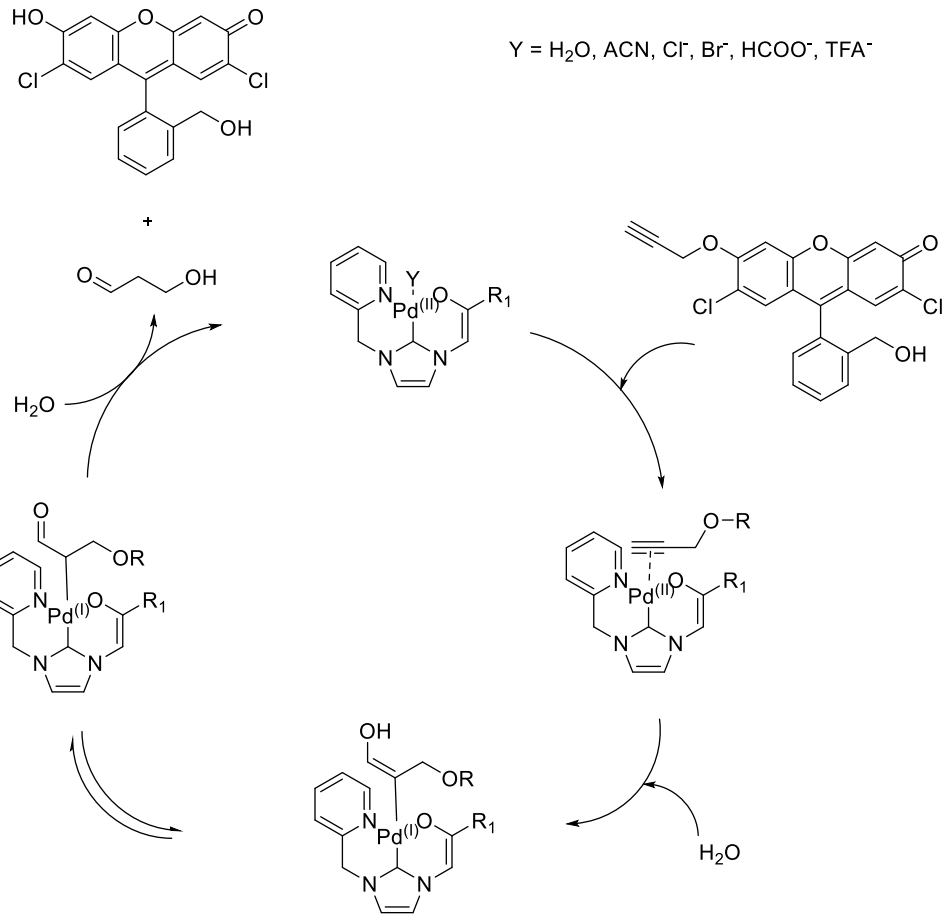

Figure 2.22 Proposed mechanism for propargylation of the compound **Pro-DCF**. Mechanism includes the palladium catalyst and suggestions of the identity of the unknown ligand Y.

It is also likely that the nature of side chain R_1 also plays some part in the efficiency of the catalyst underlining the importance of a screening process to understand which side chain give the highest activity. Catalyst screening was carried out at 37 °C in PBS (Figure 2.20) to evaluate their catalytic activity under biologically relevant conditions. Catalysts **10** – **17** (0.8

mol %) were incubated with **Pro-DCF** (10 μM) and an increase in fluorescence measured over 4 h.

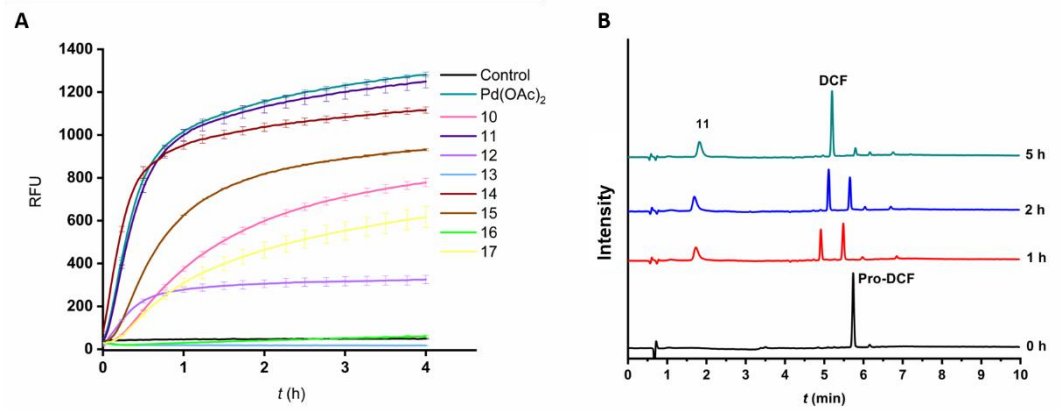

Figure 2.23 (A) Screening of catalysts **11**–**17** (0.8 mol %) for the activation of **Pro-DCF** (10 μM) in PBS (n = 3). The reactions were monitored over 4 h and an increase in fluorescence recorded over time and compared to the blank (no catalyst) and 0.8 mol % $Pd(OAc)_2$. (B) The catalytic decaging of **Pro-DCF** (50 μM) with catalyst **11** (2 mol %) was monitored by HPLC (detection at 282 nm) over time with the reaction carried out in PBS, showing > 92% conversion.

With the exception of **16** and **13**, all the catalysts were active in PBS with **11** and **14** (ligands containing glycine and valine amino acids respectively) showing comparable activity to 0.8 mol % $Pd(OAc)_2$ (Figure 2.23). This was a pleasing result given how versatile $Pd(OAc)_2$ is. Catalyst **11** (2 mol %) was further evaluated by monitoring the decaging of **Pro-DCF** by RP-HPLC, with the experiments performed in PBS, giving 92 % conversion to **DCF** after 5 h (Figure 2.23).

Next, the catalysts were screened for their activity in plasma to mirror a cellular environment rich in proteins. The decaging reactions were notably slower in cell lysate, but **11** and **14** again showed the best catalytic efficiency under these conditions and outperformed Pd $(OAc)_2$ (Figure 2.24). In plasma, **11** (2 mol %) resulted in a 97 % conversion over 5 h (Figure 2.24). The overall trend suggested that the smaller spacers such as **11** and **14** were more active whilst larger more hydrophobic spacers like **17** were less catalytically efficient.

It is clear from these result that the amino acid R groups influence activity. One reason for the low activity of compound **16** (lysine linker), **10**¸**12** and **13** could be related to intermolecular interactions with the palladium centre. In compound **16** it is highly possible that the ε-amine group on the side chain could interact with the Pd centre and become ligand "Y". The proximity of this group and its ability to bind to the metal may explain why its activity is so low. Compounds **10**, **12** and **13** are carbon chain of 6, 4 and 8 respectively. At the end of these carbon chains is a carboxylic acid moiety. It is hypothesised that these carboxylic acid groups could be able to interact with the palladium centre due to the flexibility present in the carbon

chain. The reason why 13 presents nearly no activity is due to the chain length being a "perfect" length to bend round and interact with minimal steric hinderance. Compounds 10 and 12 might just be too short for and thus their interactions with the palladium centre are not as constant enabling some catalytic activity. The two groups discussed here are very important as they are the most common moieties found on the surface of proteins used for water solubility and this may be an important point when considering the efficiency of a Pd-antibody conjugate.

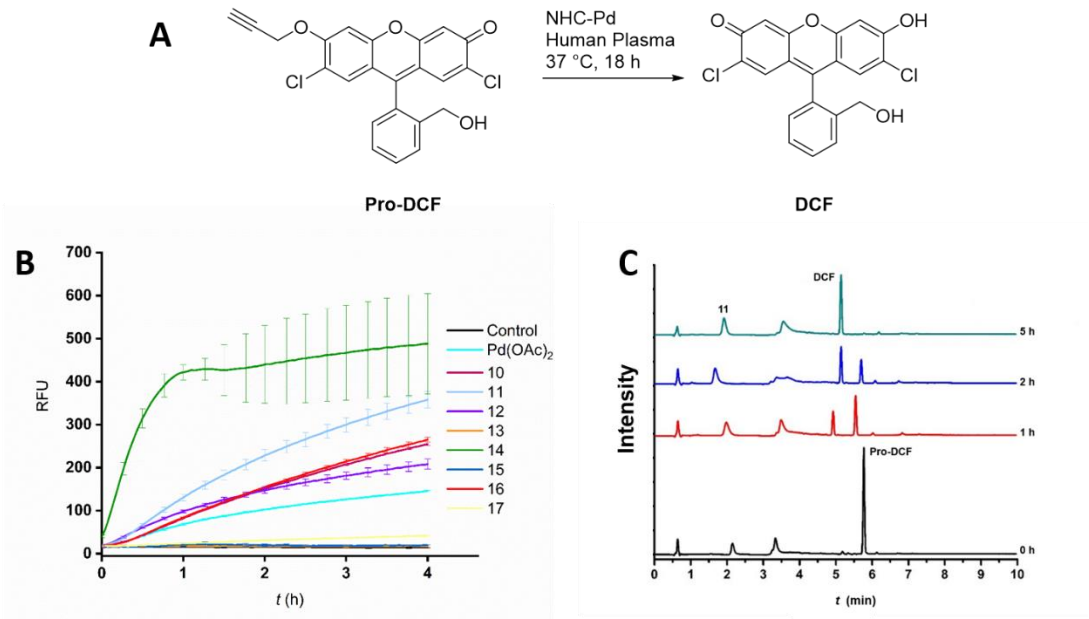

Figure 2.24 (A) Pd catalysed depropargylation reaction of **Pro-DCF** to give fluorescent **DCF** ($\lambda_{Ex/Em}$ 500/530 nm). (B) Fluorescence based screening of NHC–Pd catalysts **5–12** (0.8 mol %) for depropargylation of the probe **Pro-DCF** (10 μM) in cell lysate (n = 3). (C) The depropargylation of **Pro-DCF** (50 μM) with catalyst **11** (2 mol %) in plasma monitored by HPLC (detection at 282 nm).

The library of compounds created does have limitations and should be expanded to obtain a clearer picture of the effect of amino acids of the catalytic activity, with the sub-monomer methodology developed at the start of this chapter allowing this.

2.2.4 Prodrug activation in cancer cells and in cancer cell spheroids

Currently most of the work on bioorthogonal metal catalysts is *in vitro* with only a few examples of studies *in vivo*. Given the often-poor translation between 2D cell culture testing and clinical studies we sought to move to a more representative model of cancer growth; namely 3D cancer spheroids.

The catalyst **11** was evaluated for its efficiency to activate the caged anticancer drug 5-fluoro-1-propargyluracil (**Pro-5-FU**) (synthesised by Durgadas Cherukaraveedu) into its active drug form 5-fluorouracil (**5-FU**) (Scheme 2.11 and Figure 2.25). **5-FU** has been in medical use as a clinically approved anticancer agent for 40 years.[78] In PBS, **11** converted **Pro-5-FU** into the active drug **5-FU** within 48 h, as monitored by HPLC (Figure 2.25) which was a highly satisfying conversion. In MCF-7 cells, co-treatment with catalyst **11** (10 mol %) and **Pro-5-FU** (100 µM) for 5 days resulted in comparable cytotoxicity (MTT assay) to **5-FU** (Figure 2.25). Catalyst **11** showed only mild toxicity (>87 % cell viability) at 10 µM which suggested cell cytotoxicity was due to the activation of the drug.

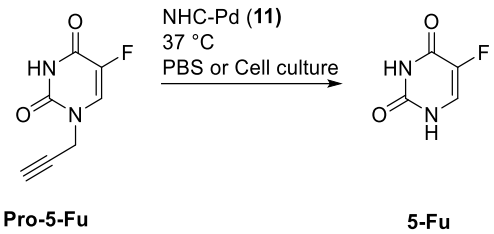

Scheme 2.11 The Pd-catalysed decaging of the prodrug 5-fluoro-1-propargyluracil (**Pro-5-FU)** into the active anticancer drug 5-fluorouracil (**5-FU**).

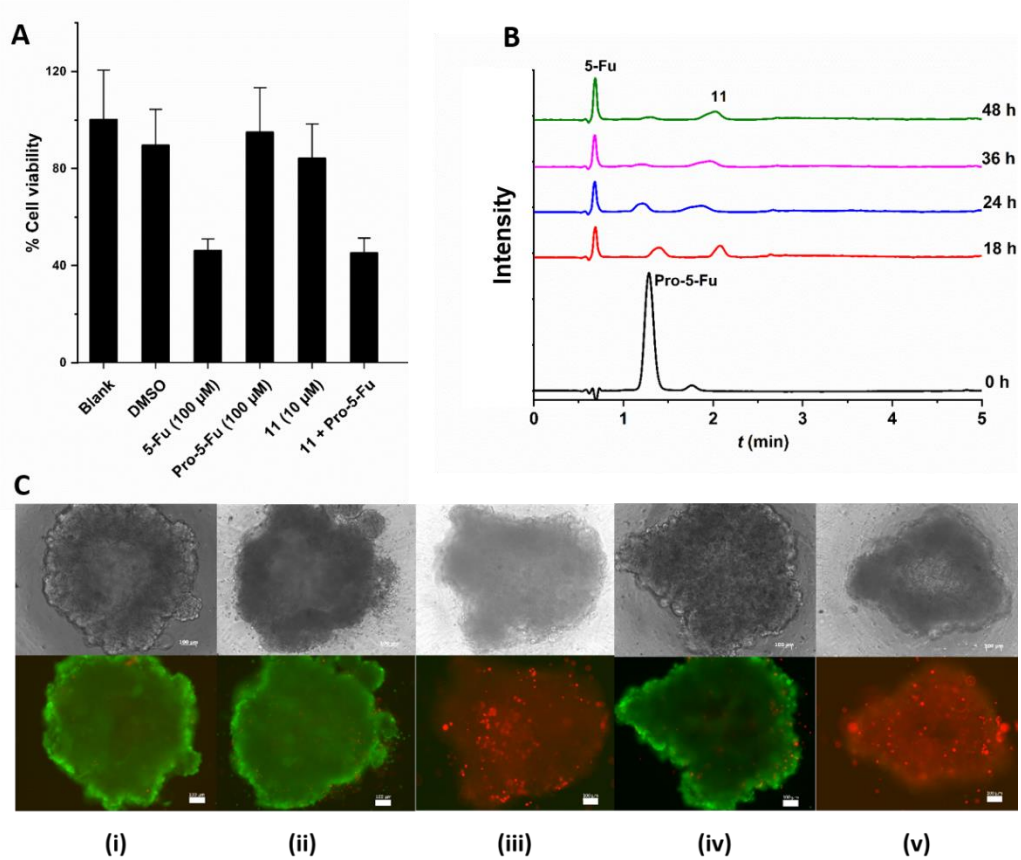

Figure 2.25 (A) MTT cytotoxicity assay for prodrug activation in MCF-7 cells. The prodrug **Pro-5-FU** did not induce cytotoxicity at 100 µM and the NHC–Pd catalyst **11** only showed moderate toxicity (13 %) at 10 µM, after 5 days incubation (untreated control cells were defined as 100 % viable). Co-treatment with catalyst **11** (10 mol %, 10 µM) and **Pro-5-FU** (100 µM) for 5 days resulted in comparable cytotoxicity to **5-FU**. Error bars are standard deviation (n=3) (B) Decaging of **Pro-5-FU** (100 µM) with catalyst **11** (5 mol %) in PBS (pH 7.4, 37 °C) monitored by HPLC with detection at 282 nm. (C) *in situ* activation of prodrug **Pro-5-FU** by catalyst **11** in 3D MCF-7 spheroids. The spheroids were imaged for live/dead status, Green cells ($\lambda_{Ex/Em}$ 495/520 nm) are live whilst the red cells ($\lambda_{Ex/Em}$ 595/615 nm) are dead. (i) Untreated spheroid (control); (ii) Spheroid treated with (10 µM) of catalyst **11**; (iii) Spheroid treated with **5-FU** (100 µM) resulting in cell death; (iv) Spheroid treated with prodrug **Pro-5-FU** (100 µM) showing good viability; (v) Spheroid co-treated with the **Pro-5-FU** (100 µM) and catalyst **11** (10 µM) showing cell death equivalent to that seen with 100 µM of **5-FU**. Scale bar 100 µm.

Next, MCF-7 spheroids were treated with the prodrug **Pro-5-FU** and catalyst **11** for 5 days, stained with a LIVE/DEAD™ Cell Imaging Kit ($\lambda_{Ex/Em}$ = 488/570 nm), and analysed by fluorescence microscopy. The spheroids treated with both the prodrug and catalyst satisfyingly resulted in cell death comparable to cells treated with **5-FU**, whereas treatment with only the catalyst or the prodrug **Pro-5-FU** had no effect on the viability of the 3D spheroids (Figure 2.25). These results appeared to be extremely encouraging for the 3D cancer model. It was assumed that the reaction was happening extracellularly, irrespectively these results demonstrated that the catalyst was able to de-cage the protected prodrug in a 3D cancer model.

2.3 Conclusions

The aim was to develop a biocompatible, water soluble NHC-Pd catalyst. Through the development of a highly efficient microwave assisted solid-phase synthesis based on a 'sub monomer' approach biocompatible NHC-Pd catalysts were generated on scale. The catalysts developed had a range of spacers including alkyl chains, hydrophilic and hydrophobic amino acids. The catalysts could be made using both a 2-chlorotrityl and Rink linkers to generate different C-terminal groups. Overall, the results present provide a solid platform for further work to explore a fuller range of amino acids and spacers to be used. By expanding the library, the effect of the juxtaposing amino acid to the catalytic centre can be studied to fully understand the kinetics and stability of the palladium centre. Finally, building the catalyst onto biomolecules with targeting abilities e.g. the cyclic RGD sequence, is an avenue for more biological research. For example, perhaps anchoring the catalyst to the cell surface via sugars/lipids/peptides and then carrying out bioorthogonal reactions on the cell surface to study membrane dynamics could be of interest.

Nearly all catalysts produced were able to activate a protected fluorophore **Pro-DCF** in both PBS and plasma with **11** and **14** demonstrating comparable activity to palladium acetate. This allows questions to be asked about how the different spaces affect the catalytic activity. Though no clear trend is observed it would appear that spacers that contain multiple amino acids seem to have lower activity compared to spacers that are single amino acids, however to deduce fuller conclusions, more catalysts would need to be made for more accurate comparisons.

Catalyst **11**, comprising of the NHC–Pd moiety linked to glycine, was the most catalytically active in the series. **11** was able to activate **Pro-DCF** in a biological setting with comparable activity to Pd $(OAc)_2$. Moreover **11** could de-cage the protected anticancer drug (**Pro-5-FU**) in a 3D cancer cell culture model resulting in comparable cell death to **5-FU**. This successful activation inside a more representative cancer model is of most interest given the overall aims of this thesis and the context of applying the catalysts in a clinical setting. Whilst *in vivo* models have been used for other metals, 3D *in vitro* models have not been studied. This is particularly important point as the *in vivo* models so far have only included zebra fish and murine models. In the context of lung cancer these models are not translatable. The best models will be the use of ovine (sheep) since their lung size are the most comparable to humans. To supplement this, *ex vivo* human lungs would also provide a powerful model. Considering this, the use of 3D cancer spheroids is likely to be a closer translation than using a xenographed murine models for the testing of compounds. Ideally if the spheroid could be grown from

primary lung cancer cells extracted from real patients this might also enable to the simulation of the tumour heterogeneity, again this is a more representative model as it can illustrate potential drug resistance that tumours can acquire.

These robust NHC-Pd catalysts with a carboxylic acid can be readily converted to a stable active ester. This provides a handle for bioconjugation and offers applications for both specific cell targeting ligands and bioorthogonal prodrug activation. Overall, it presents a step forward in the synthesis of conjugatable homogenous NHC-Pd catalysts.

Chapter 3 Cancer-targeting palladium catalysts

3.1 Introduction

3.1.1 Antibody drug conjugates overview

Monoclonal antibodies (mAbs) have become an integral part of modern-day research and medicine since their discovery due to their high specificity and affinity for their target antigens. Over the past few decades the use of mAbs in disease therapeutics has increased and their use is often glamorised with analogy to the "magic bullet" concept proposed by Ehrlich and Metchnikoff since they can specifically target a biomolecule and induce a therapeutic effect. Monoclonal antibodies can impart a therapeutic effect though complement-dependent cytotoxicity or antibody-dependent cell-mediated cytotoxicity,[79,80] with both requiring interaction with the host's immune system. They can also have therapeutic effect by inhibiting the function of the target antigens, for example, trastuzumab, bevacizumab and ceruxitmab have such an effect.[80,81] However, few monoclonal antibodies have significant therapeutic activity against cancer and in clinical trials most only increase patient survival rates by a few months.[80,82]

To improve the therapeutic potency of mAbs and reduce the side effects of common chemotherapy drugs the two have been combined to create antibody-drug conjugates (ADCs). ADCs aim to overcome the issues of chemotherapy side effects by targeting the delivery of the drug to cells that present the target antigen i.e. the cancerous cells. Often these antigens are over-expressed receptors on the surface of cancer cells, and once bound to the cancer cell, it can be internalised, with drug release able to enact its cytotoxic effect (see Figure 3.1).

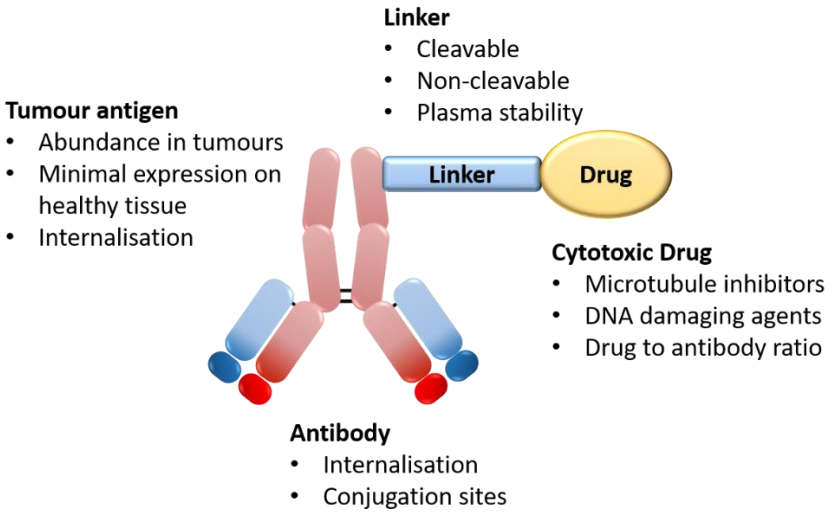

Figure 3.1 Important design features of an antibody drug conjugate.

There are currently three Food and Drug Administration (FDA) approved ADCs. Brentiuximab vedotin (Adcetris®)[83] was the first ADC is be approved in 2011. Under an accelerated approval regulations for patients with relapsed or refractory CD30-positive Hodgkin's lymphoma after autologous stem-cell transplantation (ASCT) or when multiagent chemotherapy was not an option.[84] It is a CD30-targeting mAb coupled with a microtubule disrupting agent monomethyl auristatin E (MMAE). MMAE cannot be used a drug by itself due to its high toxicity. A cathepsin-cleavable linker was used to link the drug and antibody together, and after binding to the CD30 receptor and internalisation into lysosomes, cathepsin proteases cleave this linker. The release of MMAE arrests the cell cycle between the gap 2 phase and mitosis, resulting in cell apoptosis.[85]

The second was Ado-trastuzumab emtansine (approved in 2013, Kadcyla®).[86] It is composed of the mAb trastuzumab, the drug Mertansine (also called DM1) with the two linked via a non-cleavable thioether. DM1 is a maytansine derivative and binds tubulin, inhibiting its formation. Upon binding to the HER2 receptor, and internalisation it undergoes proteolytic digestion, releasing three molecules of maytansine within the cells. Furthermore, the binding of trastuzumab to the HER2 receptor blocks the HER2-mediated signalling pathway, triggering antibody-dependent cell-mediated cytotoxicity.

The third approved ADC Inotuzumab ozogamicin (Besponsa®), was approved for the treatment of acute lymphoblastic leukaemia (ALL) by the FDA in 2017. The mAb targets CD22 cell receptors and upon internalisation a hydrazone chemical linker is cleaved via

hydrolysis, releasing a Calicheamicin. These examples demonstrate that ADCs have had clinical success and there are over 65 ADCs in clinical trials suggesting that more will soon become available.[87–91]

When designing ADCs there are three key things to consider (see figure 3.1):

1. The antibody of choice (including amino acid sites for potential drug conjugation).
2. The type of linker to be used: cleavable or non-cleavable.
3. The drug to be conjugated.

3.1.2 Selection of antibody and labelling sites

The choice of antibody depends on the tumour antigen. Ideally, the antigen would be localised to the cell surface to allow for selective ADC binding. In addition, the antigen should be overexpressed on the surface of cancers cells and minimally expressed on healthy cells. If ADCs are taken into healthy tissue this would result in off-target toxicity lowering the amount that reaches the cancerous tissue. For maximum release of the drug, the ADC needs to be endocytosed into the cell upon which the antibody is degraded and would result in the drug being released freely into the cell (Figure 3.2).

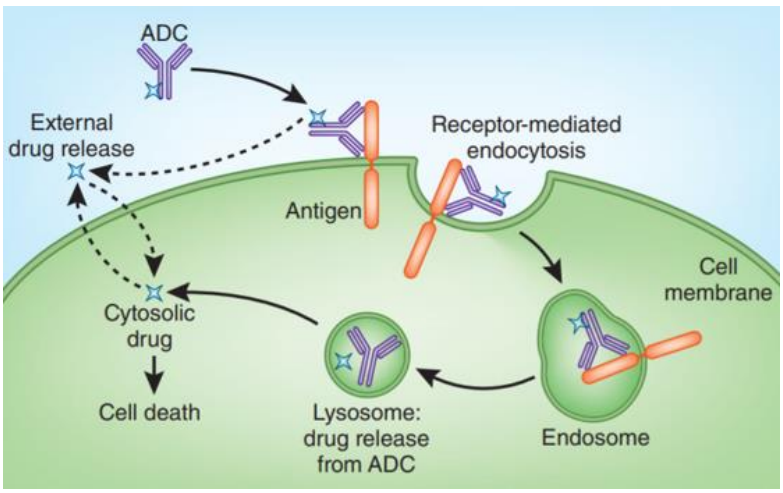

Figure 3.2 ADC processing. The ADC binds to its target antigen on the cell surface. The ADC-antigen complex is internalised into endosomes and then lysosomes. In the lysosome the antibody is digested by proteases, releasing the cytotoxic drug inside the cell. Adapted from reference 83.

When attaching the cytotoxic drug to the antibody, the site of attachment is an important consideration.[92] Generally lysine and cysteine residues are the preferred for bioconjugation,

due to the nucleophilicity of the amine or thiol moieties (Figure 3.3).[93] The numerous lysines can result in heterogeneous labelling of the ADC which results in pharmacokinetic variability and difficulty in purification. Homogeneous ADC mixtures can be produced by genetically engineering unnatural amino acids into the antibody structure for specific labelling (Figure 3.3). Homogenous ADC mixtures compared to heterogeneous mixtures, have a higher stability and better activity *in vivo*.[92,94,95]

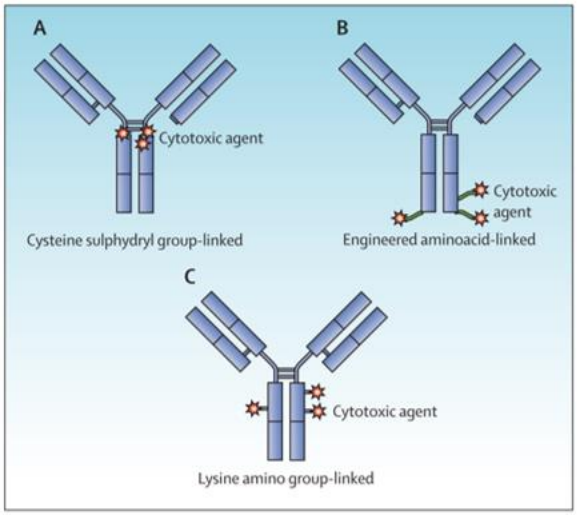

Figure 3.3. Different ways which drugs can be loaded onto a monoclonal antibody. (A) Using native cystine residues after reduction of disulphide bridges. (B) Using engineered amino acids for highly specific labelling (C) Linkage through native lysine residues. Adapted from reference 87.

When using lysines as a site for conjugation, the primary ε-amines can be easily reacted with *N*-hydroxysuccinamide (NHS) activated esters to form the stable amide bond with a number of commercial linkers based on this approch.[96,97] However, it is estimated that there are 40 to 80 available lysine residues on mAbs, and without any specificity of which sites are labelled, the number of ADC variations can reach millions once the degree of labelling is >5 i.e.$(40 – 80)^5$ and this explains why such heterogenous mixtures are impossible to purify to a single compound.

Cysteine residues on antibodies are used to help maintain the quaternary structure of the antibody by linking the protein subunits together through disulphide bridges. It has been suggested that reducing these disulphide bridges rarely affects the function of the antibody.[98] Under controlled conditions, disulphide bridges can be reduced to provide reactive thiol groups whilst maintaining the overall structure of the antibody. Most often, the thiol is then reacted with a maleimide group through a 1, 4 addition, though other chemistries are possible

e.g. reactions with haloalkanes, or activated disulphides. A major discussion point with maleimide chemistry is the ADCs have been reported as losing their payload through retro-1, 4 additions initiated by existing thiols present in plasma.[99] The hydrolysis of the succinimide ring is a potential method to circumvent the retro-1,4 addition chemistry, as the ring-opened product is more stable[100,101] but gives two product regioisomers.

3.1.3 The ADC linker

The linkers used in ADCs can vary greatly and there are two main classes: cleavable and non-cleavable.[102,103] The choice is important as it can have effects on the pharmacokinetic properties, therapeutic index, overall antibody specificity and affects the overall strategy for drug choice. To deliver their drug payload, cleavable linkers often rely on high levels of reducing agents (such as glutathione), low pH, and enzymes. On the other hand, non-cleavable linkers are dependent on the mAb degradation upon internalisation into endosomes and lysosomes for their activity. This generates metabolites containing the active drug with or without a portion of the linker. These differences should be considered when creating the ADC and their potential effect on the overall characteristics of the therapy.[104]

Non-cleavable linkers have the benefit over cleavable linkers of being more stable in plasma, and generally, non-cleavable linkers have lower off-target toxicity. Yelena et. al. synthesised an ADC that linked the monoclonal antibody huC242 (a humanised anti-MUC1 monoclonal antibody) to the drug DM1 via an N-succinimidyl-4-(*N*-maleimidomethyl)cyclohexane-1-carboxylate (SMCC) linkage (Figure 3.4). This utilised a “non-cleavable thioether” linker and its toxicity was tested against the COLO 205 and Namalwa cells aimed at targeting the mucin glycoprotein (MUC1) which is overexpressed in these cell lines. This ADC was compared directly against huC242-DM1 (Figure 3.5) that utilised a disulphide cleavable linker. It was found that off-target toxicity caused by the by-stander effect was lower in xenograft tumour models with huC242-SMCC-DM1 i.e. the non-cleavable linker compared to huC242-DM1.

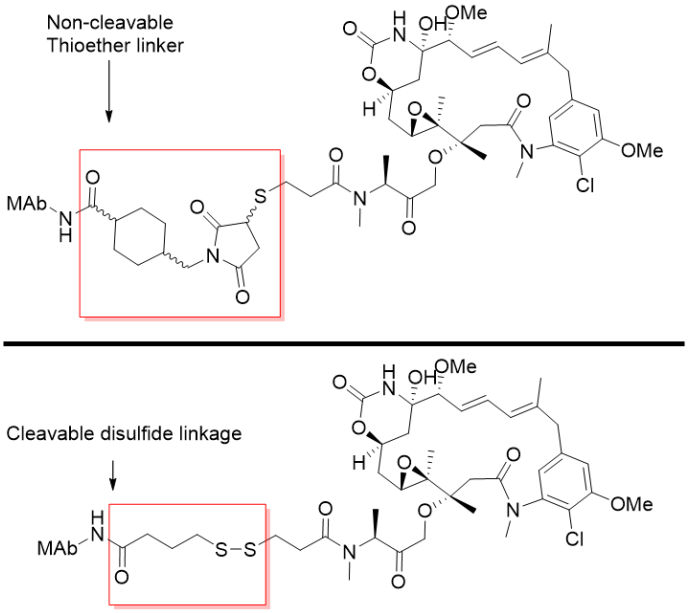

Figure 3.4 Top; Structure of huC242-SMCC-DM1. Bottom; Structure of huC242-DM1.

There are a variety of cleavable linkers which exploit different types of chemistry. Hydrazone groups are semi-acid labile linkers designed to be stable in the body at pH 7.4 during circulation in the blood. Upon internalisation of the ADC into lysosomes the environment will be approximately pH 5.0. This lower pH will allow the linker to undergo hydrolysis and release the cytotoxic drug; BR96-Dox (Figure 3.5) is an example of this strategy. BR96 is a mAb which targets the Lewis-Y antigen. It was shown by Firestone that after binding to the target tumour cells, the ADC is endocytosed into lysosomes.[105] In clinical trials BR96-Dox was found to not be associated with the typical side effect profile of native doxorubicin and could therefore increase the therapeutic window for treating antigen-expressing tumours.[106,107] However, in one study it was found that the hyrdazone linker was unstable with free drug being found prematurely released into the bloodstream[108] raising questions about its potential use in the clinic.

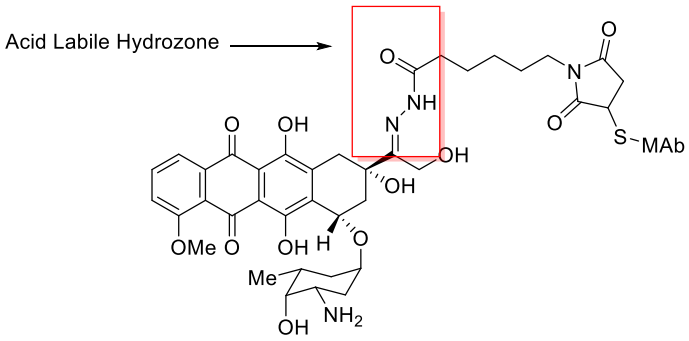

Figure 3.5 Structure of BR96-Box with an acid labile hydrazone linker.

Reducible linkers are another attractive proposition in ADC generation, because reduced glutathione in tumour cells can be up to 1000-fold higher than in normal cell cytoplasm.[109] It has also been suggested that tumour cells contain more enzymes in the protein disulphide isomerase family, which may contribute to the reduction of disulphide bonds in tumour cellular compartments.[109,110] A development analogous to the huC242-SPCC-DM1 is shown in Figure 3.6 which made it to phase II clinical trials, indeed IMGN901 has shown promising results. It contains the highly potent maytansinoid attached to a novel CD56-binding monoclonal antibody.

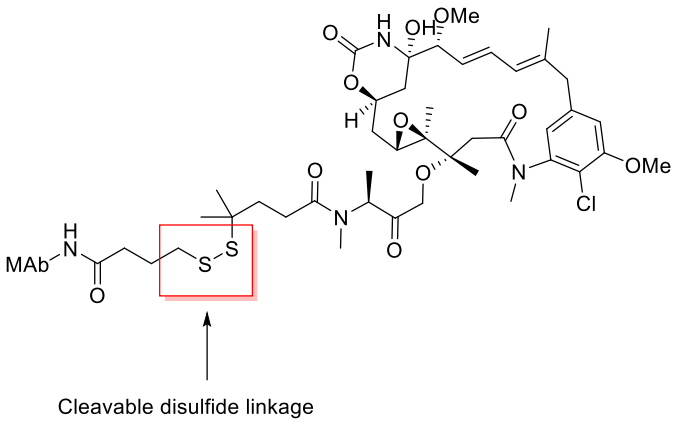

Figure 3.6 Structure of IMGN901 with a disulphide bridge to link maytansinoid to a monoclonal antibody.

Enzyme cleavable linkers present one of the more attractive options since they take advantage of the numerous enzymes available in cells. Peptide-cleavable linkers are the most widely used, and the linkers are designed to be stable in blood circulation and then be cleaved by intracellular proteases such as cathepsin B.[111] The linkers for cathepsin B centre around the use of valine-citrulline dipeptides and the phenylalanine-lysine (Phe-Lys) dipeptide linker. These linkers have shown a good balance between plasma stability and intracellular protease

cleaveage.[112] The best example of the dipeptide in the clinic is brentuximab vedotin (Adcetris®) shown in Figure 3.7.

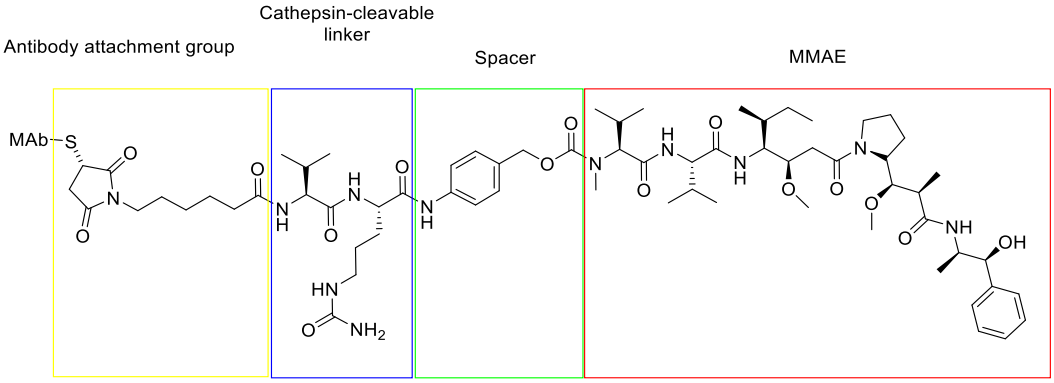

Figure 3.7 Structure of brentuximab vedotin with a valine-citrulline linker.

There are several different linkers to choose from when creating an ADC. Each linker has its own pros and cons, but the choice will have a profound effect on the ADC and its viability in the clinic. The final factor to consider for ADCs is the drug which is attached to it.

3.1.4 The drug choice

The choice of drug is important as it is the primary method of killing and reducing tumour size. It is key to know what the drug's mode of action is, and if there is known methods of resistance and its overall potency. Most drugs used in ADCs are highly potent cytotoxic agents which target either microtubule formation or DNA structures with the IC_{50} values in the nanomolar range. Typically, they're too toxic to be administered alone. The highly toxic agents are preferred, because of their effectiveness in combination with mAbs which requires only a limited number of antigens on the surface of a cell. By combining with mAbs the therapeutic window and selectivity of these drugs may increase such that they are clinically viable. Despite the specificity of ADCs, only a fraction of an administered dose will reach the intracellular target. Other things to be considered are the chemical structure such that there are moieties for conjugation to the linker. There should be some water solubility and stability in blood plasma because of the way which ADCs are prepared and administered intravenously.

Maytansines and dolstatin analogues (Figure 3.8) target tubulin and fragment microtubules,[113] and are seen as promising drugs.[114] Dolstatins originally failed at stage II clinical trials due to

toxic effects on non-malignant tissue, that prevented dose escalaltion.[115] Maytansine was also assessed in clinical trials in the 1970s, though during Phase II trials there were concerns of its off target effects on the central nervous system.[116]

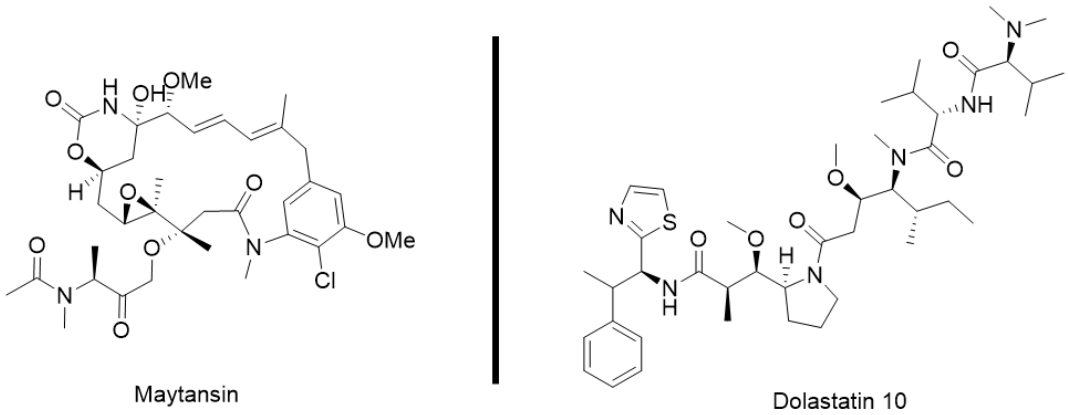

Figure 3.8 Structures of the cytotoxic drugs Maytansinoid and dolstatin 10.

There are also drugs which target the minor groove of DNA. Duocarmycins, and calicheamicins which cause irreversible alkylation and lead to cell death. Duocarmycins are a class of compounds which target A-T rich regions of DNA; these compounds have progressed to clinical trials but, due to dose-limiting effects, dosages were too low to achieve anti-tumour activity.[117,118] Recently a trastuzumab and duocarmycin ADC has been developed known as SYD985 which is currently being tested in clinical trials.[119,120]

Calicheamicins bind to the DNA minor groove and cause double strand breaks but has narrow therapeutic indices and serious toxic effects.[121,122] In 2017 the ADC , Inotuzumab ozogamicin (Besponsa®), was approved for the treatment of acute lymphoblastic leukaemia (ALL) by the FDA (Figure 3.9). The mAb targeted CD22 cell receptors and upon internalisation a hydrazone chemical linker would be cleaved via hydrolysis, releasing Calicheamicin.

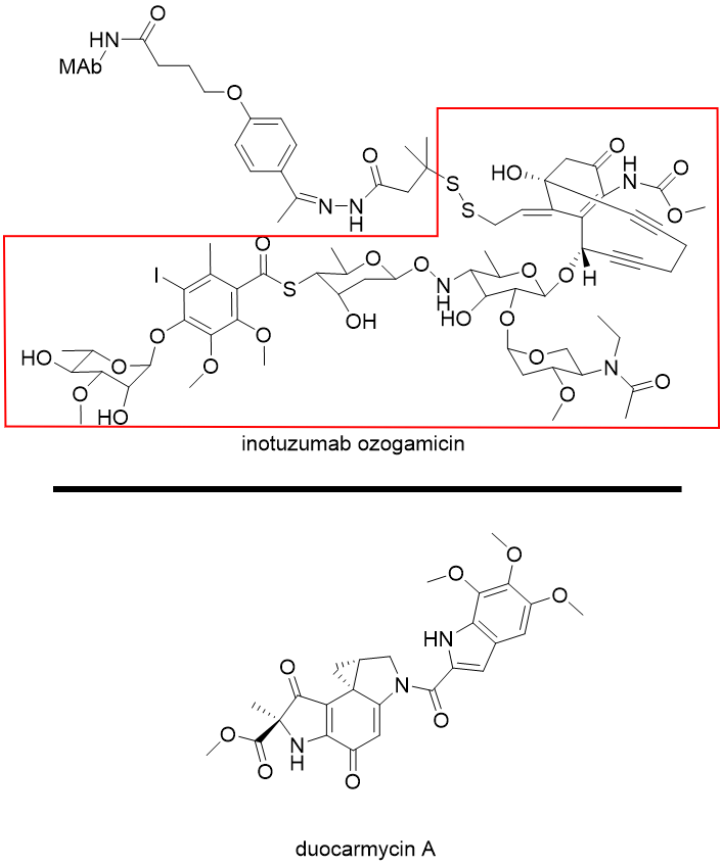

Figure 3.9 Structures of inotuzumab ozogamicin (Besponsa) with the calicheamicin highlighted (top), and the structure of the drug duocamycin A (bottom).

There are a wide variety of features to consider when designing an antibody drug conjugate. Given the importance of finding new cancer therapies and excitement in the field around ADC numerous reviews have been published that consider all the aspects previously discussed,[90,95,103,123,124] such that ADCs have come a long way, and possibly represent the next generation of cancer treatments. There also are other approaches for cancer therapy that can be taken that also use antibodies. One such approach is the antibody directed enzyme prodrug therapy (ADEPT).

3.1.5 Antibody Directed Enzyme Prodrug Therapy (ADEPT)

ADEPT[125–127] was a popular concept due to its simplicity; a mAb is linked to an enzyme to create a conjugate. This conjugate binds to cell surface receptors that are overexpressed on cancerous cell but minimally expressed on healthy cells. After accumulation of the conjugate, a pro-drug is then administered to the body where upon interaction with the mAb-Enzyme

conjugate, the prodrug is chemically activated by the enzyme. The active drug can now be taken up into cancer cells via small molecule mechanisms and cause cellular death. The overall effect is like that of ADCs, a cytotoxic drug is delivered with spatial control to cancer cells preferentially over healthy cells. This reduces side effect of the drugs and potentially allows for higher doses to be administered (Figure 3.10).

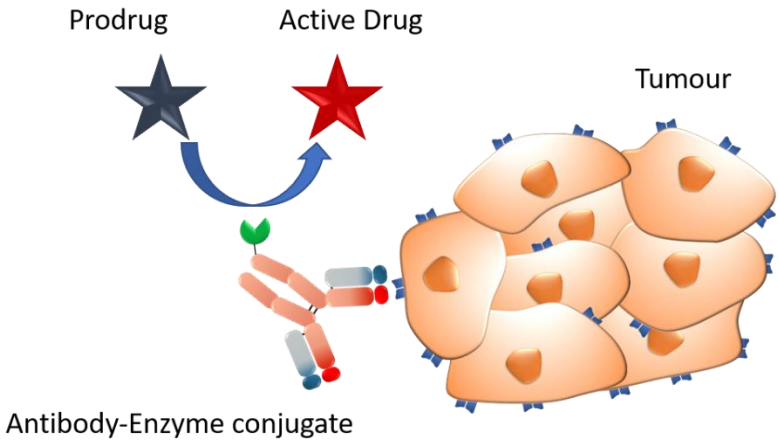

Figure 3.10 The concept of antibody directed enzyme prodrug therapy. An antibody enzyme conjugate binds to an overexpressed receptor on a tumour. A prodrug is added to the system, and only at the tumour site will the prodrug be activated into the active drug derivative. The active drug would then be taken inside the tumour cells.

The problem for ADEPT was that whilst some candidates made it to stage II clinical trials,[125,126] they ultimately failed due to the immunogenicity of the treatment. The only conjugate to have been studied in a clinical setting used carboxypeptidase G2 (CPG2). This enzyme originates from the *Pseudomous* sp. and had no known human analogues, and catalyses the cleavage of reduced and non-reduced folates.[128] This allowed specific prodrugs to be designed which would not be activated by the host's own enzymes, thus increasing specificity. It was because this enzyme was non-human that an immunogenic response was elicited causing a halt to progression in clinical trials. This, in combination with the need for repeat dosages to sustain the therapeutic effect, ultimately led to the requirement of co-administration of cyclosporine to suppress the immune response.[129]

It is possible that this approach could be more powerful than ADCs as the linker would always be non-cleavable and once site specificity had been optimised this could be applied to a range of different antibodies providing a therapeutic strategy with less variables than ADCs.

Changing the enzyme to another catalytic entity could be the key to progressing this technology forward since the immunogenicity of the enzyme was the biggest issue.

3.2. Chapter aims

The aim of this chapter was the synthesis an antibody palladium-catalyst conjugate capable of binding to cells and activating fluorophores (Figure 3.11). The considerations that were made for the generations of ADCs also need to be considered in this antibody-palladium conjugate.

First a model system would be used to test the conjugation strategies with fluorophores. BSA would be used as a protein initially and carboxyfluorescein-NHS to test amide bond formation on the proteins. Following this, strained alkyne molecules could be added via the NHS-conjugation (based on the result from the carboxyfluorescein-NHS conjugation). Then a fluorescein azide could be attached via strain promoted azide alkyne cycloaddition (SPAAC). With the SPAAC synthesis established, an *N*-heterocyclic carbene Pd catalyst was conjugated using the same methodology. This mAb-Pd conjugate would then be tested for its catalytic activity.

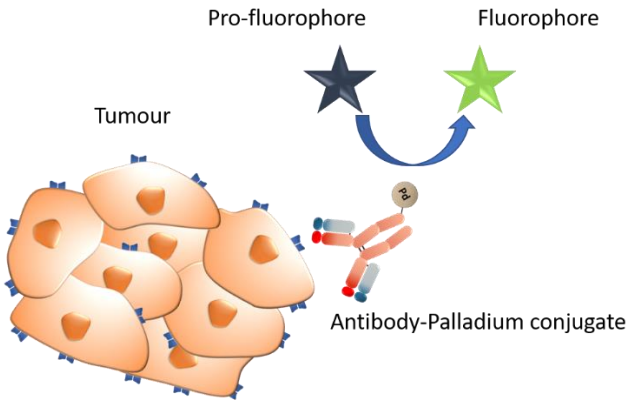

Figure 3.11 A mAb-Palladium conjugate binds to an over expressed receptor on the surface on a tumour cell. A pro-fluorophore is administered to the system and upon interaction with palladium, it is activated into a fluorescent derivative. The activation of the fluorophore at the cancer site would potentially enhance the imaging of the cells.

3.3 Results

3.3.1 Synthesis and evaluation of palladium catalysts with bioconjugation handles

Following the successful development of a methodology of palladium catalysts described in chapter 2. A small sub-library of palladium catalysts with bio-conjugation handles were synthesised. Based on the results from chapter 2, it was decided to use the NHC-Pd centre with a valine attached. This conferred catalytic activity whilst also providing stability (Figure 2.18, Figure 2.20 and Figure 2.21). The spacer separates the catalytic centre and the bioconjugation handle and the amino acid; amino hexanoic acid served this purpose. Finally, the handle was either lysine, glutamic acid or lysine-ε-azide. This provided either an amine, carboxylic acid or an azide group respectively for conjugation reactions. Using this methodology, the following three catalysts were synthesised (Figure 3.12).

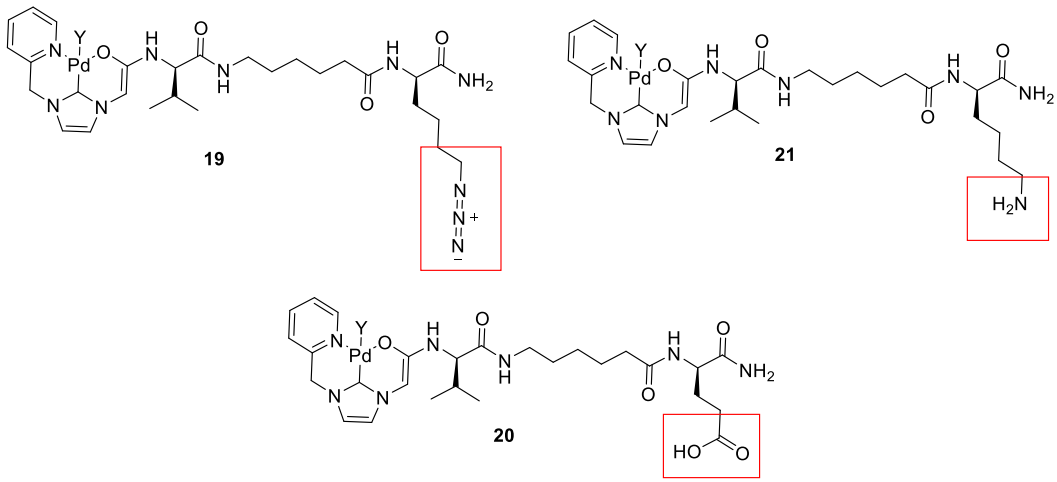

Figure 3.12 Structures of the catalytic units synthesised **19**, **20** and **21**.

Of the catalysts, the most objectively interesting was the catalyst containing the azide (**19**). To date, it is the first catalyst which contains a catalytically active transition metal and an azide moiety within the same compound. There are examples of azide-transition metal complexes[30] however, these have not been used to catalyse reactions. Delightfully, the azide also tolerated microwave synthesis and palladium loading conditions as previously utilised, further enhancing the credentials of the synthetic route's versatility.

The three catalysts were all assessed for their catalytic activity, using both **PROC-Rh 110** and **Pro-DCF** as model pro-fluorophores for propargyl deprotection reactions. The reactions were

carried out with 10 mol % of catalyst and 100 µM of the fluorophores in PBS overnight (Figure 3.13).

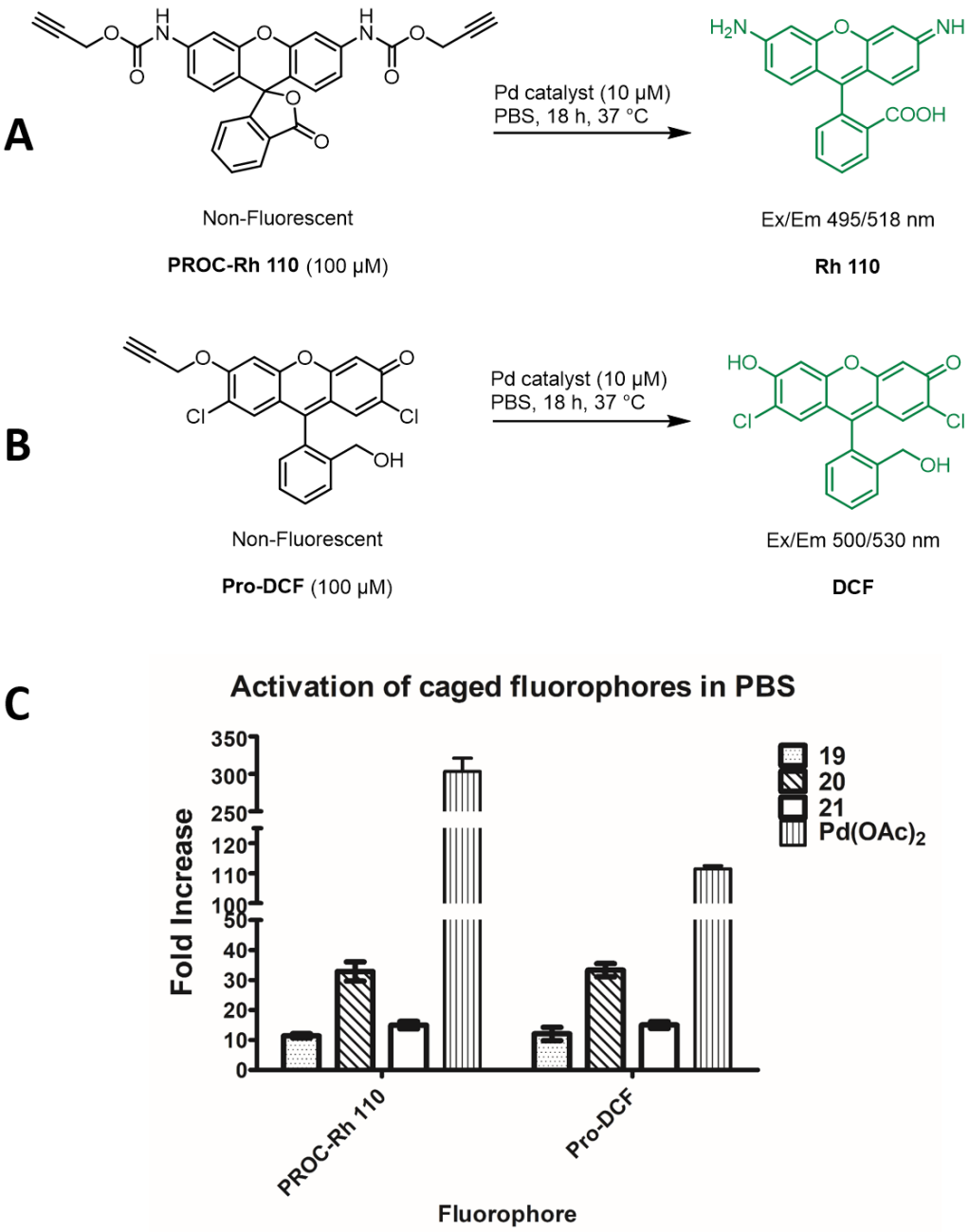

Figure 3.13 (A) **PROC-Rh 110** activation by Pd catalyst (B) **Pro-DCF** activation by Pd-catalysts. (C) Fluorescence fold increase. For all experiments n = 3 and error bars represent standard deviation.

All three catalysts (**19, 20** and **21**) were able to generate a 10-fold increase in fluorescence. However, this was significantly less than the increase shown by $Pd(OAc)_2$, at the same mol % of catalyst, with each fluorophore (~100 – 300 fold). It was thought that these catalysts would

be highly active due to the valine, so these results were underwhelming and surprising. Nevertheless, it was shown in chapter 2 that NHC-Pd catalyst with longer amino acid chains had reduced catalytic activity compared to those with a single amino acid linker. Why exactly this happened is unclear, but these results are consistent with those found in chapter 2.

It can be deduced from the results in Figure 3.13 is that all three catalysts (**19, 20** and **21**) were able to "switch-on" fluorescence. Knowing that the catalysts were active, they were tested for any potential cytotoxicity against cells. Cells were incubated for 24 h with each compound at 0.1, 1, 10 and 100 µM. the negative control for cytotoxicity was simply regular DMEM media and the positive control for cytotoxicity was 100% DMSO.

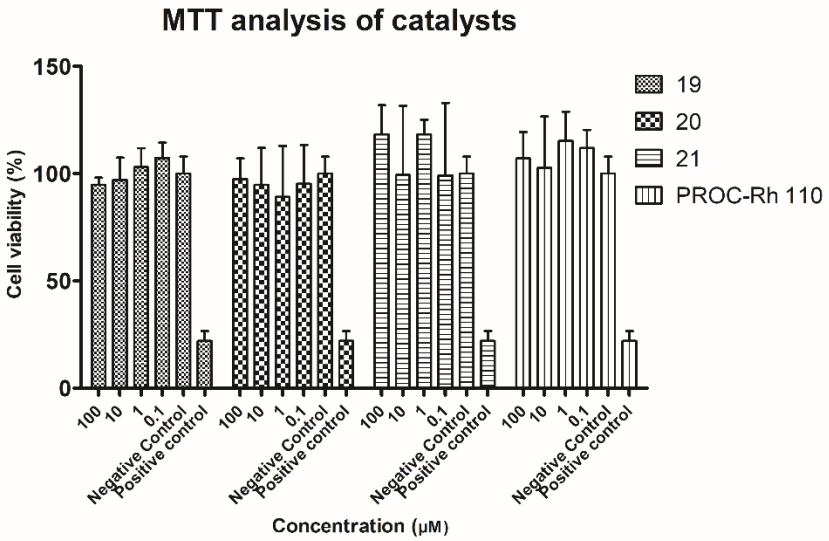

Figure 3.14 MTT analysis of **19, 20, 21** and **PROC Rh-110** against HeLa cells. Cell were incubated with different concentrations of each catalyst. The positive control for cell death was 100 % DMSO. for all experiments n = 3 and error bars are the standard deviation.

It can be seen from Figure 3.14 that the catalysts exhibited no cytotoxicity (up to 100 µM) compared to a positive control for cytotoxicity. Whilst this result was expected, it is worth noting that given these would be targeted to cancer cells a degree of toxicity might be tolerated or even beneficial in a clinical setting.

19 was also tested to see if it could also carry out Suzuki-Miyaura coupling. **19** (0.1 mol %) was incubated with phenyl boronic ester (75 µmol) and iodobenzene (37.5 µmol) with caesium carbonate (75 µmol) in water/acetonitrile (1:1, 1 mL) (Scheme 3.1). The reaction was monitored by HPLC (Figure 3.15) over the course of 7 days for the appearance of the product biphenyl.

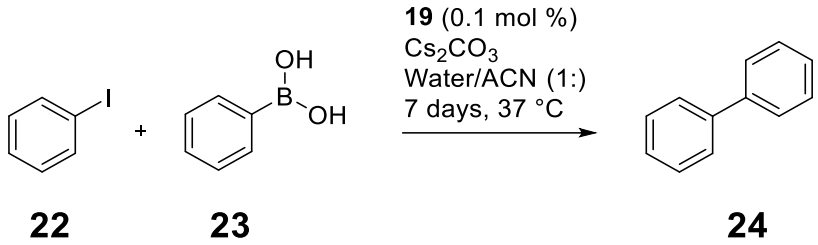

Scheme 3.1 Synthesis of biphenyl using iodobenzene and phenyl boronic acid and an NHC-Pd catalyst.

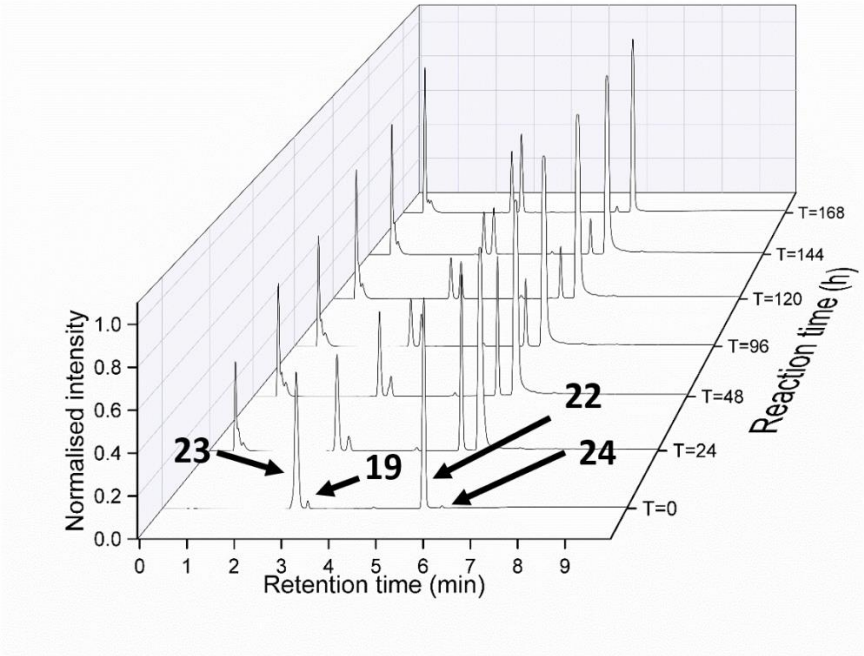

Figure 3.15 Analytical HPLC analysis of Suzuki Coupling over time. The retention time of the catalyst is 3.1 min, with the retention of phenyl boronic ester at 3.0 min and iodobenzene at 5.9 min. Pure biphenyl was measured as a reference and has a retention time of 6.1 min. Measurements taken at the 254 nm wavelength.

After 24 h a new peak for biphenyl could be seen, with conversion (based on the reduction of the iodobenzene peak) shown in Table 3.1.

Table 3.1 Conversion to **24** over time by measurement of reduction of **22** at 254 nm.

Reaction time (h)	24	48	96	120	144	168
Conversion (%)	30	50	70	80	90	>95

This reaction shows that this type of cross coupling chemistry is possible with the catalysts and is also one of the first examples of a Suzuki-Miyaura coupling in water using a homogenous catalyst whereas previous examples have used heterogeneous catalysts.

To conclude **19** catalysed both de-propargylation reactions and Suzuki-Miyaura couplings. These features mean that it could be a feasible catalyst to carry forward for protein conjugation experiments. However, should difficulties occur the other two catalysts could also potentially be used.

3.3.2 BSA modelling

Within the field of protein conjugation there are a variety of strategies that can be used.[102,124,130] It was decided the first approach to conjugation would be by using free amines present on lysine residues on the protein. Whilst this type of labelling is non-specific, if a strained alkyne could be conjugated onto a protein (via an NHS-activated ester), this would allow subsequent specific labelling via SPAAC using compound **19**. Therefore, so long as the initial conjugations via the NHS-ester did not inhibit protein function it could be a viable route of labelling (Figure 3.16).

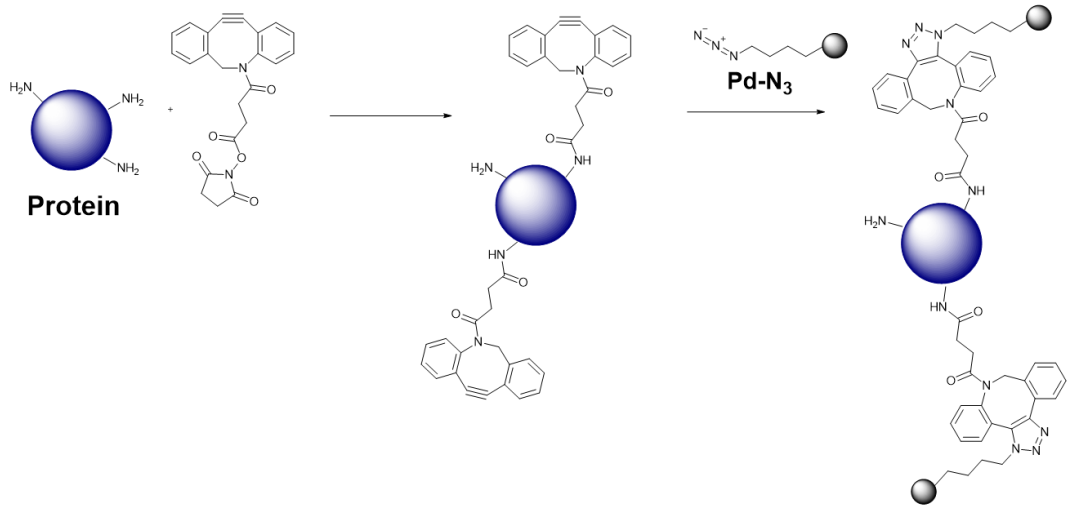

Figure 3. 16 Overall strategy for conjugating palladium onto a protein.

To conjugate a pallidum catalyst on to an antibody a methodology was first devised using BSA as a model protein. To begin, the commercial fluorophore isomer mix 5(6)-carboxyfluorescein was converted into the active NHS esters using EDC and NHS (synthesised by Daniel Norman). It was chosen due to availability and low cost of materials. Given that the following reactions were to be used as a model for understanding protein conjugation techniques, the isomers were not separated.

Initially BSA was reacted with the fluorescein-NHS ester (scheme 3.2). Using five equivalents of the fluorescein-NHS (0.2 mM), the solution was heated to 37 °C for 4 h. The excess fluorophore was removed using Amicon® centrifugal filters using a molecular weight cut off (MWCO) membrane of 10 kDa. The reaction was carried out at two different pHs; 7.0, and 8.0 to give products **25a** and **25b** respectively.

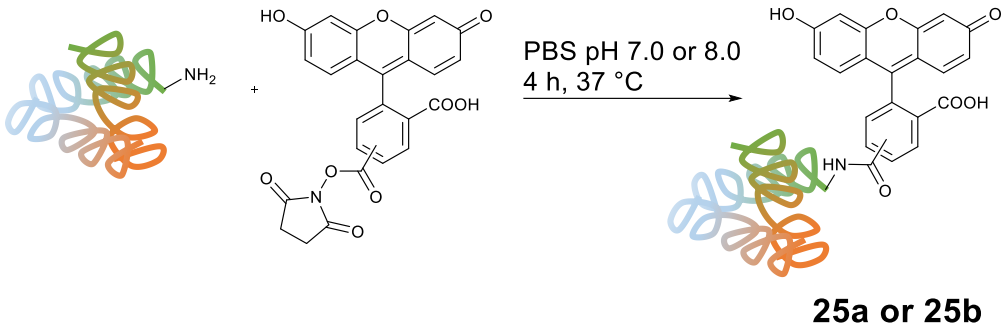

Scheme 3.2 Carboxyfluorescein coupling to BSA.

Following purification of the products they were analysed by MALDI-TOF MS, SDS-PAGE and UV-Vis spectroscopy techniques to calculate the degree of labelling.

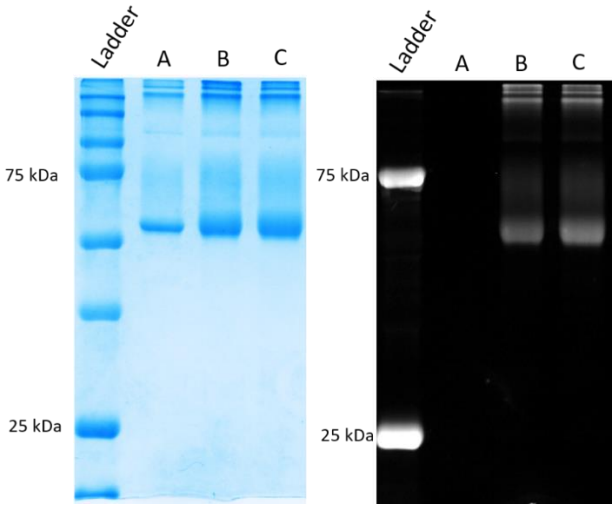

Figure 3.17 (Left) SDS-PAGE (10 %) after Coomassie staining; (Right) SDS-PAGE under irradiation at 480 nm. Each lane represents the following: Precision Plus Protein Kaleidoscope ™ standards, with 25 and 75 kDa labelled; (A) Pure BSA; (B) **25a** from a reaction at pH 7.0; (C) **25b** from a reaction at pH 8.0.

An SDS-PAGE gel was run to check for the presence of protein and confirm fluorescent labelling had occurred (Figure 3.17). As can be seen from the Coomassie blue staining, BSA-fluorophore conjugates are present, though the resolution is too low to see any increase in molecular weight. Illumination under 480 nm was more informative where the reaction carried out in both pH 7.0 (Lane B) and 8.0 (lane C) had a fluorescent band. The reaction at pH 8.0 appeared to have labelled the protein as evidenced by the higher intensity of the fluorescent band.

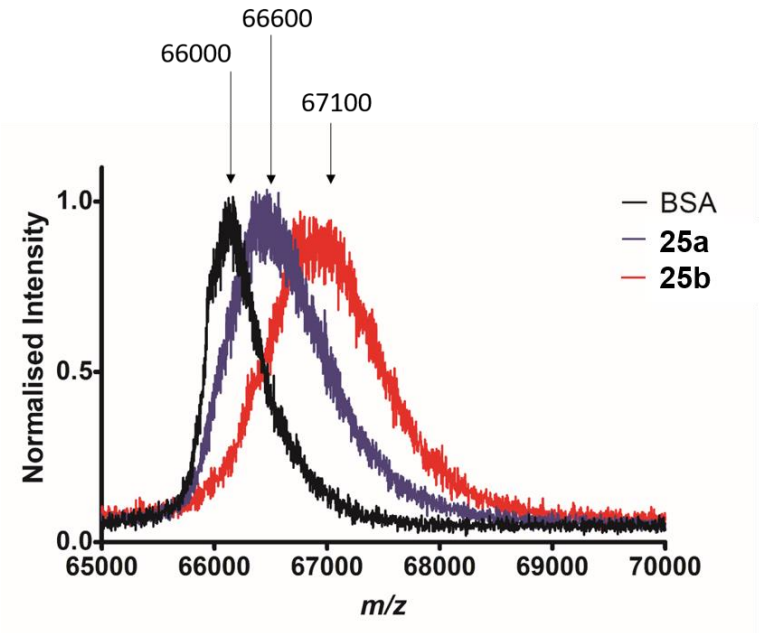

Figure 3.18 MALDI-TOF MS analysis of BSA reaction with fluorescein to generate **25**. Native BSA is shown in black. **25a** in blue; **25b** in red (Using 2,5-dihydroxybenzoic acid as a matrix).

With the confirmed isolation of **25a**, the reactions were then analysed by MALDI-TOF MS (Figure 3.18). It can be seen the molecular weight increased upon the reaction at pH 7.0 compared to the native BSA by around 600 g/mol. Since the molecular weight of the fluorophore added each time is approximately 344 g/mol this would suggest a degree of labelling of around 1.8 – 2. The reaction at pH 8.0 showed an increase in molecular weight of 1100, suggesting that there is a degree of labelling of around 3.9 moles of fluorophore per mole of protein.

One of the issues with using MALDI-TOF MS analysis is that the spectra tend to be broad due to the abundance of natural isotopes present the protein. This makes recording a precise measurement of the *m/z* subjective. Furthermore, the methodology means that there will be a heterogeneous mix of proteins labelled with different amounts of the fluorophore giving labelling ratios of 1:1, 2:1, 3:1 and 4:1 etc. Therefore, the degree of labelling will not likely be a whole number and accounts for this heterogeneity, as a result, the degree of labelling will be an **average**. To confirm the level of labelling two equations can be used from the calculation shown in Equation 3.1 and Equation 3.2 (Thermo Scientific: Tech Tip #31).

$$(\mathbf{1})\ Protein\ concentration\ (M) = \frac{A_{280} - (A_{max} \times CF)}{\varepsilon} \times dilution\ factor$$

Equation 3.1. Equation used to calculate the protein concentration after conjugation with a fluorophore. Where A_{280} is the absorbance at 280 nm of the protein-fluorophore conjugate. A_{max} is the absorbance value at the maximum absorbance wavelength of the fluorophore (for example FAM = 492 nm). CF is the correction factor (correcting for the absorbance of the fluorophore at 280 nm). ε is the molar extinction coefficient of the protein and the dilution factor is any dilution applied to the sample.

$$(\mathbf{2})\ Moles\ of\ dye\ per\ mole\ of\ protein = \frac{A_{max}\ of\ the\ labelled\ protein}{\varepsilon' \times protein\ concentration\ (M)} \times dilution\ factor$$

Equation 3.2. Equation to calculate the degree of labelling (DoL) from using equation 3.1. "A_{max} of the labelled protein" is the absorbance value at the maximum absorbance wavelength of the fluorophore; ε' is the molar extinction coefficient of the fluorophore; Protein concentration (M) is found from Equation 3.1.; Dilution factor is any dilution that may have been applied to the sample.

The ε values for the fluorophore and BSA at 280 nm are 68,000 $cm^{-1}\,M^{-1}$ and 43,824 $cm^{-1}\,M^{-1}$ respectively. The degree of labelling calculated from these values are shown in Table 3.2.

Table 3.2 Absorbance values of products **25a** and **25b** used to determine the degree of labelling based on equations 3.1 and 3.2.

Reaction (**product**)	Absorbance at 280 nm	Absorbance at 492 nm	Degree of labelling (average)
pH 7.0 (**25a**)	0.94	1.42	1.8
pH 8.0 (**25b**)	0.87	1.87	3.9

The degree of labelling for the reactions at pH 7.0 and 8.0 are 1.8 and 3.9 respectively. These data are supported by the results from the MALDI-TOF MS analysis. Satisfyingly, these results support the theory that as the pH increases, the degree of labelling increases, since more lysine resides on the protein surface have been converted from NH_3^+ to NH_2, thus making them available to react as nucleophiles. Based on the results, it was decided to keep the pH at 7.0 as this would be more beneficial to the proteins – increasing the pH could lead to denaturing effects. Secondly, it means that the pH of the labelling reactions can be adjusted if the degree of labelling needs to be increased in future experiments. Finally, it was also important not to react too many lysine sites since they are used to help keep the protein soluble in aqueous

environments and this would reduce the risk of modifying the protein at functionally sensitive sites.

Following the success of fluorophore-labelling, a strained alkyne was then attached to BSA. Five equivalents of DBCO-NHS (0.2 mM) were reacted with BSA at pH 7.0 for 4 h at 37 °C. The excess DBCO-NHS was removed using Amicon centrifugal units, MWCO 10 kDa. And the reacted BSA-DBCO product **26,** was concentrated to a final volume of 50 µL. A 5 µL sample was retained for analysis and the remaining solution diluted to 100 µL. To this, 5 equivalents of commercial 5-FAM-N_3 was added (0.2 mM). The solution was heated to 37 °C for 4 h, purified and concentrated as previously described to give **27** (BSA-DBCO-5-FAM).

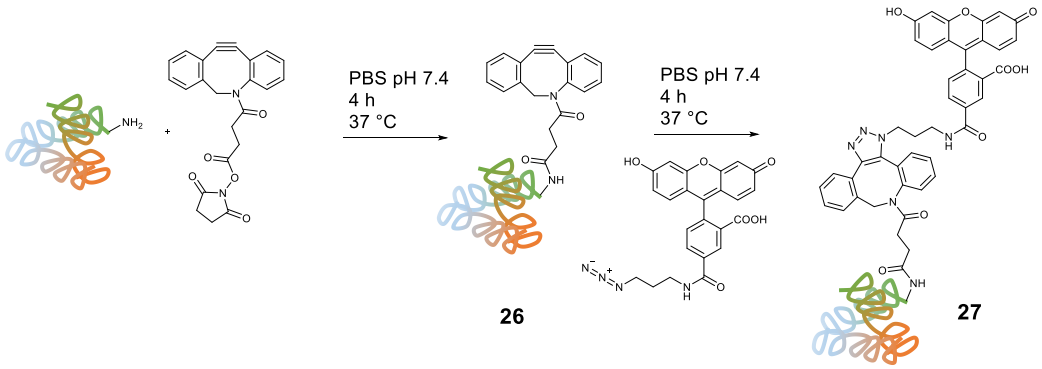

Scheme 3.3 BSA reaction with DBCO-NHS to give **26** and then cycloaddition with 5-FAM-N_3. to give **27.**

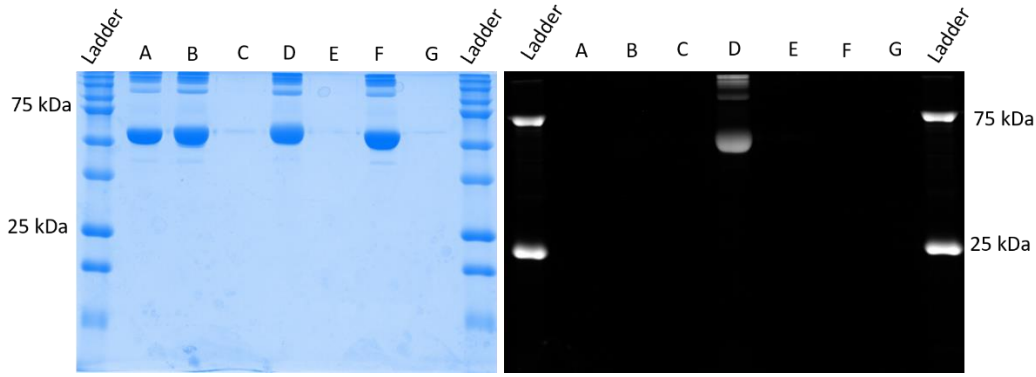

Figure 3.19 SDS-PAGE gel of the reactions in scheme 3.3. (Left) Coomassie staining for proteins; (Right) gel exposed to 480 nm light prior to Coomassie staining. Lanes are as follows: Precision Plus Protein Kaleidoscope ™ standards; (A): pure BSA; (B) **26**; (C) **26** wash steps from purification; (D) **27**; (E) **27** wash steps from purification; (F) pure BSA mixed with 5-FAM-N_3 control; (G) BSA-5-FMA-N_3 control wash from purification.

From the SDS-PAGE gel (Figure 3.19), the reactions were clearly successful. Firstly, products **26** and **27** were successfully isolated confirmed by the presence of bands in Lanes B and D and the absence of bands in lanes C and E. There also appears to be a small shift up the gel when comparing Lanes, A and D indicating an increase in molecular weight. The fluorescence

in Lane D also confirms the attachment of a fluorescent molecule. Reaction with BSA and 5-FAM-N_3 as a control did not result in a fluorescent band (lane F). This suggests that the bands in Lane D are due to the covalent bonds formed via SPAAC reactions

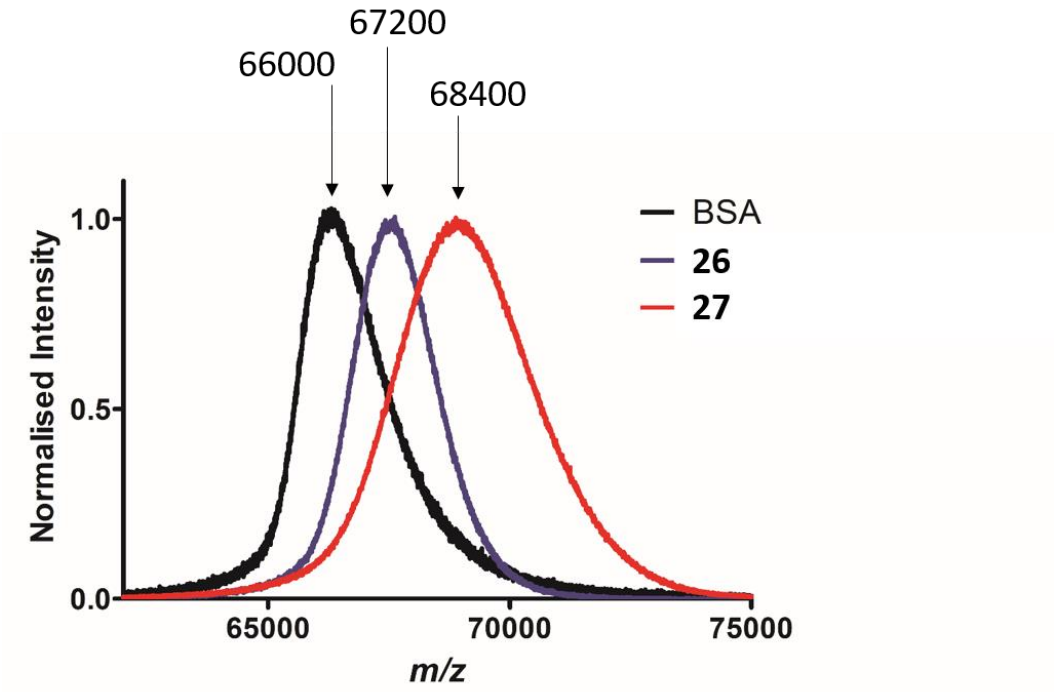

Figure 3.20 MALDI-TOF MS analysis of the reaction from Scheme 3.3. Pure BSA is in black, **26** in blue and **27** in red.

From the MALDI TOF MS analysis (Figure 3.20), a clear shift in the protein molecular weight could be seen. The product of the BSA-DBCO reaction gave an increase of molecular weight of 1200. Since the increase in molecular weight per DBCO added is approximately 300 g/mol, approximately 4 equivalents of DBCO were added to each mole of BSA. There was an observed increase in molecular weight of 1200 after the 5-FAM-N_3 (458 g/mol) coupling, to give a degree of labelling of approximately 3 fluorophores per molecule of BSA, and showed that approximately 75 % of the available strained alkyne sites had reacted though the SPAAC reaction. The absorbance of **27** was measured at 280 nm (protein concentration) and 495 nm (wavelength of maximum absorbance of fluorescein) and used in equations 3.1 and 3.2 to give the degree of labelling (Table 3.3).

Table 3.3 Absorbance values and level of labelling of **27** used to determine the degree of labelling based on equations 3.1 and 3.2.

Product	Absorbance at 280 nm	Absorbance at 492 nm	Degree of labelling (average)
27	0.80	1.51	2.9

Following the results of the experiments described, it was concluded that the methodology would be sound to attempt to label antibodies with fluorophores and then move onto attaching palladium to the antibody. However, the antibody-fluorophore conjugate had to be validated to ensure that binding was not hampered by the addition of the conjugates.

3.3.3 Labelling of Herceptin with a fluorophore

With a successful simple strategy for labelling proteins using SPAAC the same methodologies were carried out on the antibody Herceptin; a clinically approved mAb used to treat breast cancer.[131,132] Herceptin binds to the epidermal growth factor receptor (EGFR, also known as the Her2 receptor) and prevents receptor dimerisation. Consequentially, this prevents the epidermal growth factor (EGF) binding to the receptor (Figure 3.21) and as a result there is no downstream signalling to induce cellular growth and proliferation. Herceptin was chosen as a model antibody due to its availability and cost compared to other antibodies.

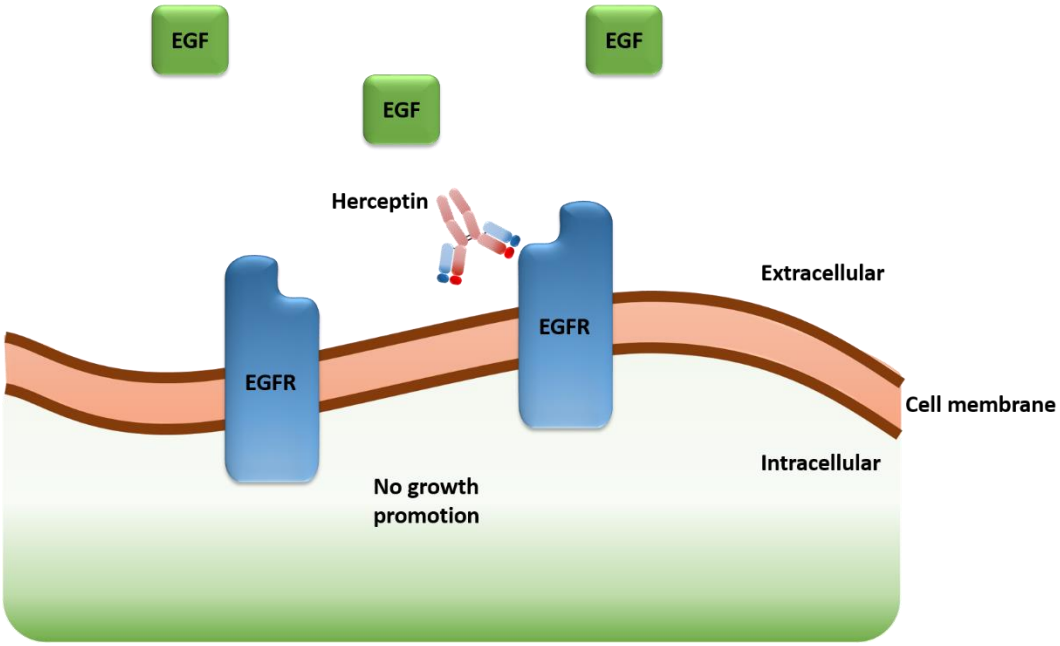

Figure 3.21 Overview for Herceptin function. Herceptin binds to the epidermal growth factor receptor (EGFR). Binding prevents dimerisation of the EGFR and thus prevents binding of the epidermal growth factor. This ultimately leads to the prevention of downstream signalling of cellular growth and proliferation.

Firstly, Herceptin was reacted with 5 equivalents (0.2 mM) of DBCO-NHS at 37 °C for 4 h. The excess DBCO-NHS was removed using Amicon centrifugal spin units (MWCO 10 kDa). **28** was then incubated with 5 equivalents of 5-FAM-N_3 (0.2 mM) at 37 °C for 4 h and then purified and concentrated as before to give **29**.

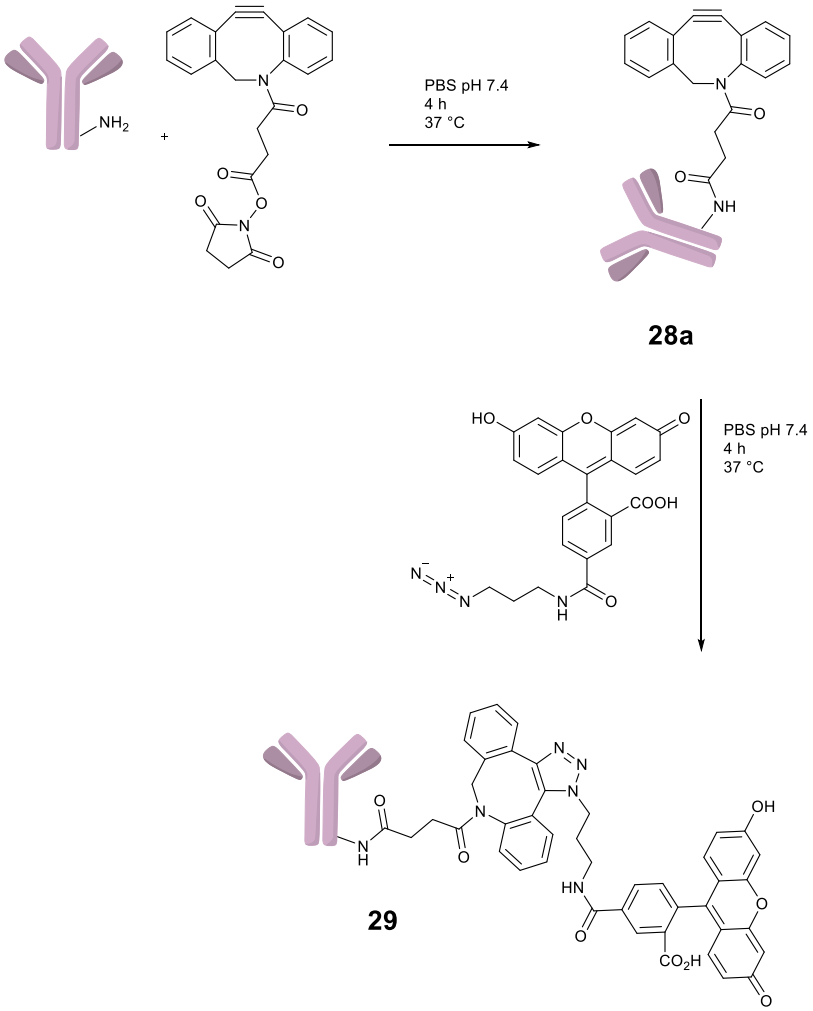

Scheme 3.4 Attachment of fluorescein to Herceptin via the SPAAC reaction using DBCO as the strained alkyne to make **28a** and followed by 5-FAM-N_3 to give **29.**

As before, the reactions were analysed by SDS-PAGE, MADI-TOF MS and UV-Vis absorbance. It can be seen clearly from the SDS-PAGE (Figure 3.22) that Herceptin has been successfully labelled. Products **28a** and **29** were both isolated successfully as shown on the Coomassie stained gel (Figure 3.22). Comparing lanes, A and C it can be seen the band at 25 kDa in Lane C is slightly higher suggested that conjugation has increased molecular weight. Most tellingly, in the fluorescent image of the same gel (Figure 3.22). Only **29** in lane C had any fluorescence indicating that the conjugation reactions were successful.

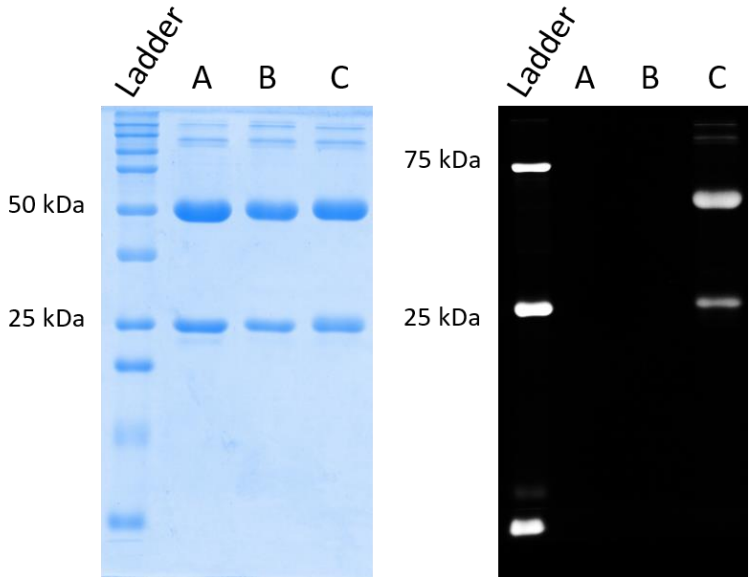

Figure 3.22 Labelling of Herceptin with a fluorophore (Scheme 3.4) analysed by SDS-PAGE (Left) Coomassie staining. (Right) Gel imaged under 480 nm light prior to Coomassie staining. Lanes are as following; Kaleidoscope ladder with key markers identified; (A) Pure Herceptin; (B) **28a**; (C) **29**.

Next, the conjugates were analysed by MALDI-TOF MS (Figure 3.23). From the data it can be seen there was an average increase in molecular mass of 1000 Da between the native Herceptin and product **28a**. This suggests that there are approximately 3 equivalents of DBCO added to Herceptin (300 da per DBCO molecule). After the addition of 5-FAM-N_3 to **28a** to give **29**, the increase in molecular weight was approximately 1200 from 146000 to 147200 (458 g/mol per fluorophore). This suggested that there is an average degree of labelling of 2.5 equivalents of 5-FAM-N_3 attached to the antibody.[133]

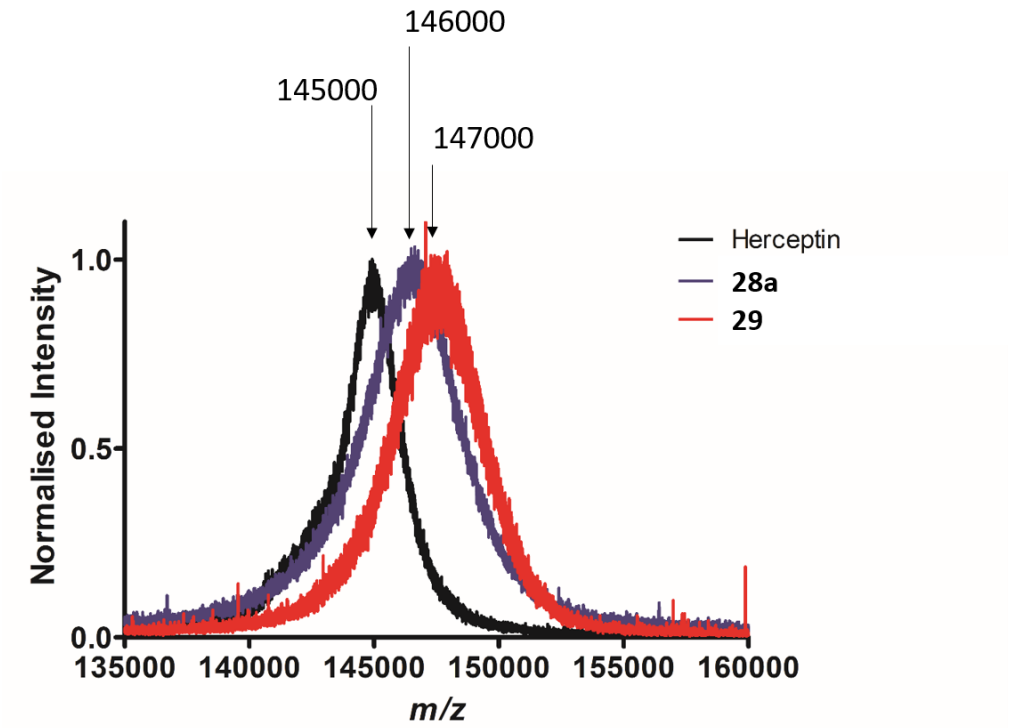

Figure 3.23 MALDI-TOF MS analysis of the reactions from Scheme 3.4. Unmodified Herceptin is in black; **28a** is in blue; **29** in red.

Finally, the Herceptin product **29** was analysed by absorbance to determine the degree of labelling (Table 3.4). The ε values for the fluorophore and Herceptin at 280 nm are 68,000 cm^{-1} M^{-1} and 210000 cm^{-1} M^{-1} respectively.

Table 3.4 Absorbance values and level of labelling of **29** used to determine the degree of labelling based on equations 3.1 and 3.2.

Product	Absorbance at 280 nm	Absorbance at 492 nm	Degree of labelling (average)
29	1.41	0.97	2.7

Having successfully labelled the antibody it was imperative to test if it had retained its binding functionality. Due to the number of lysine sites and the non-specific nature of the labelling technique, it needed to be confirmed that there wasn't any labelling in the crucial binding site of the antibody (Figure 3.24).

While it has been stated before, it is important to reiterate that because of the non-specific labelling technique, and that the MALDI-TOF peaks are so broad, that the degree of labelling

is an **average** of the whole sample; this is true for all previous and future experiments. Therefore, there will be some conjugates within the "product" that are only singularly labelled and some which may have up to 5 or even 10 labelling. This is important when we consider antibody binding functionality as the antibodies that have the lowest conjugation numbers (i.e. only 1 or 2 fluorophores per antibody) are most likely to have retained their binding functionality since the probability of labelling the binding site will be lower. Following this, the antibodies in the sample with the highest labelling numbers (5 and above) will also have the high probability of a fluorophore being conjugated at or near the binding site thus reducing or even inhibiting binding functionality. The issue with this is that when analysing fluorescence these antibodies will give off the highest signal. The top 20 % of the MALDI-TOF peak may account for 50 % of the fluorescence in the sample. The conclusion from these points is that in a clinical setting the majority of antibody binding will be with the lowest level of labelling and thus the lowest fluorescent signals or lowest amount of palladium catalyst loaded assuming that binding is an analogue concept and not strictly "on/off". Naturally, this issue could have major implications with imaging diseases *in vivo*. In addition, it could mean that the calculated binding affinity does not correlate with the degree of labelling i.e. that because only 70 % of the product population are binding to the target, the average degree of labelling of will likely be lower than that of the whole population. To assess binding, other assays could be used, for example an ELISA assay might be devised which can give a more definitive/quantitative analysis of the $K_{d.}$ To check that even the most heavily labelled antibodies are binding a simple binding experiment that is then analysed by mass spectrometry might also be possible though this is just hypothetical.

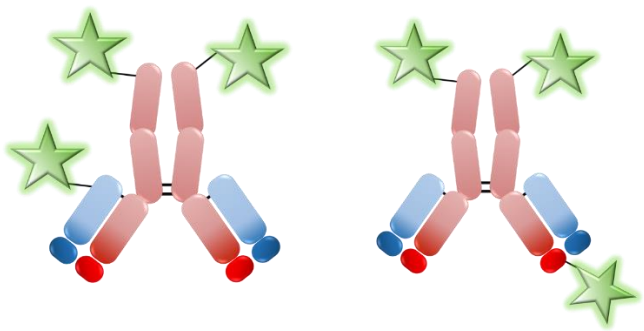

Figure 3.24 Labelling of the antibody. (Left) Desired labelling on the antibody on the heavy chains or the light chain. (Right) Undesired labelling with a fluorophore located in the binding site of the antibody which would impair function.

Analysing the structure of the binding site, there were no lysine residues in or close to the binding site of the antibody (protein data bank code: 1N8Z).[133] This implies that the risk of conjugation inhibiting binding capabilities should be low. **29** was incubated with two breast

cancer cell lines; SK-BR-3 and MCF-7. Both cell lines express the EGFR receptor on to their cell surface, however the SK-BR-3 cells have a significant over-expression of the receptor compared with MCF-7 cells. Both cell lines were incubated with **29** for 4 hours at a range of concentrations, and the cells were washed and analysed by flow cytometry.

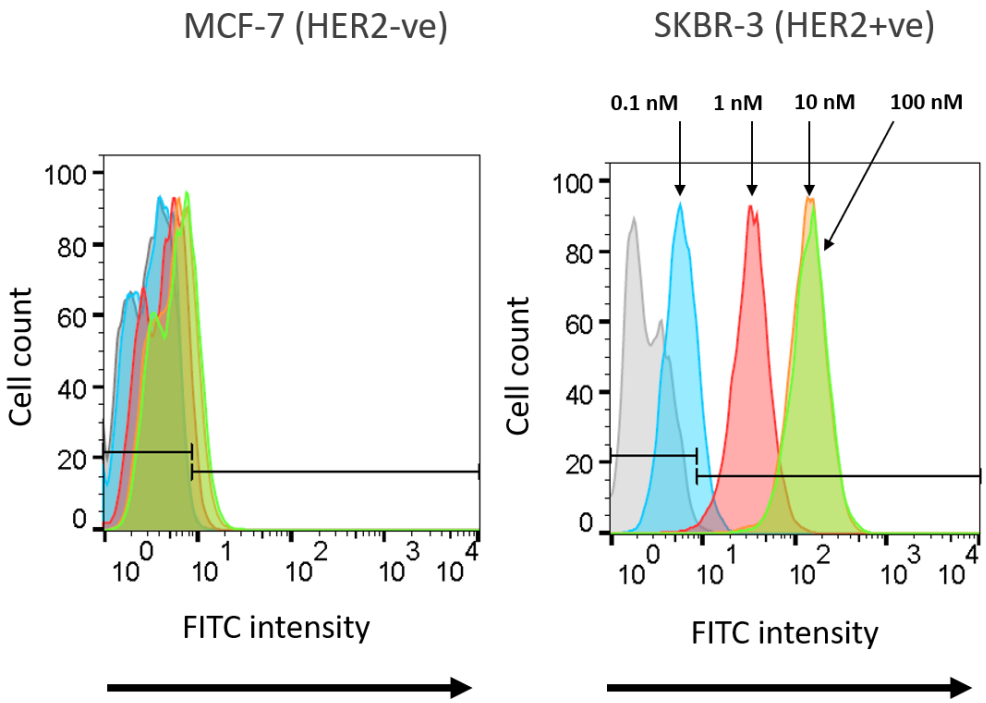

Figure 3.25 Flow cytometry of cell lines incubated with **29**. (Left) Incubation with MCF-7 cells. (Right) Incubation with SKBR-3 cells. Cell population colours are as follows; Grey, control cells with no antibody; blue, 0.1 nM of **29**; Red, 1 nM of **29**; Yellow, 10 nM of **29**; Green 100 nM of **29**.

The flow cytometry data in Figure 3.25 shows that when **29** was incubated with the MCF-7 cell line, there was no significant shift in the populations. This was true for all concentrations used (0.1 nM – 100 nM). Contrastingly, when **29** was incubated with the SKBR-3 cell line, there was a moderate shift in the population at 0.1 nM (approximately. 30 %), and a clear shift at 1 nM (>95 % compared to the control). Interestingly at 10 nM and 100 nM the cell population shifts were the same, this suggests that even at 10 nM, all available cell surface receptors have already been saturated with **29**. This suggests that the K_d of **29** is within the same order of magnitude as the native drug Herceptin which the FDA states as 5 nM.[134,135]

As discussed above the fact that the degree of labelling is an average does mean that this interpretation of the K_d is debatable. Whilst the antibodies with the lowest levels of labelling will likely be binding securely, the issue is with antibodies with higher levels of labelling loosely binding. A $K_{d\ within}$ the "same order of magnitude" may not be sufficient for *in vivo* scans

These results suggest that the antibody had retained its binding ability (Figure 3.25) and pleasingly was found to be in the same order of magnitude as native Herceptin (>10 nM) however, as discussed earlier this is very much a crude measurement and should be suject to further testing. Overall, this suggested that this method of conjugation would be viable for attaching a palladium catalyst since the only change in methodology would be changing 5-FAM-N_3 for **19**.

3.3.4 Labelling of Herceptin with Palladium

With the success of labelling Herceptin with a fluorophore the next step was to try and label Herceptin with a Pd catalyst. Following the previous methodologies described above, **19** was attached to Herceptin as follows. Pure Herceptin was incubated with 5 equivalents of DBCO-NHS (0.2 mM) at 37 °C for 4 h as before to generate **28a**. Then 5 equivalents (0.2 mM) of **19** was then added to the **28a** for 4 h at 37 °C and purified using the Amicon centrifuge units (Scheme 3.5) to give **30a**. The conjugation was confirmed by MADLI-TOF MS, SDS-PAGE and ICP-MS analysis.

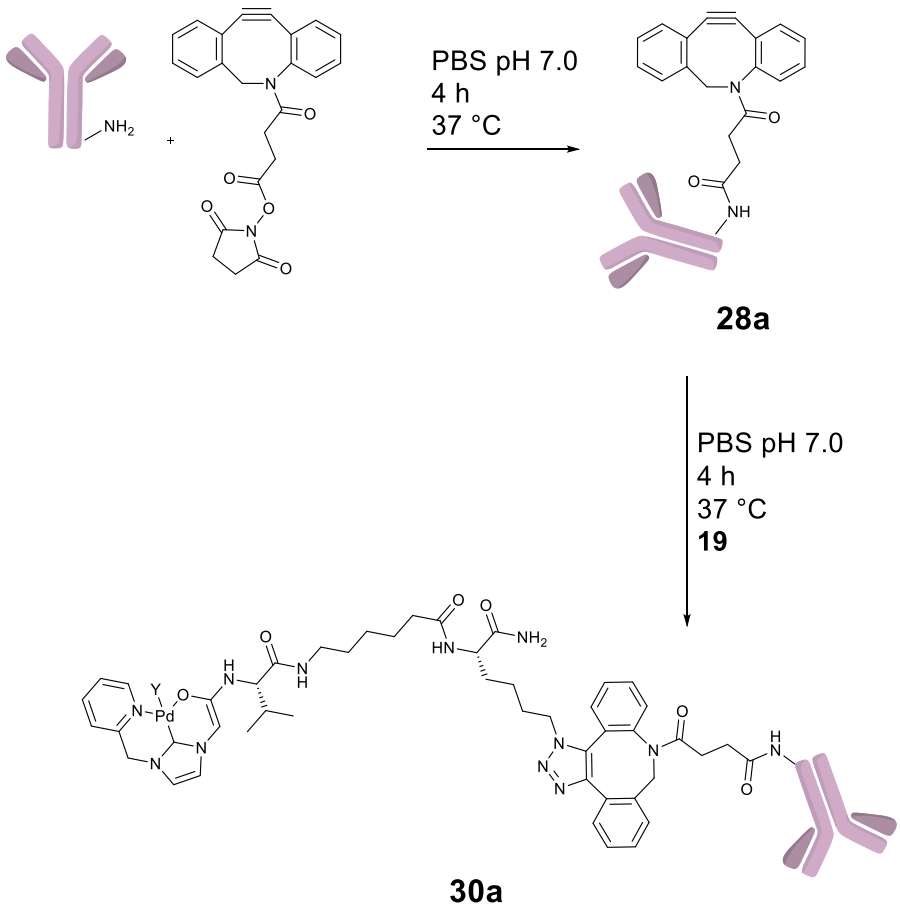

Scheme 3.5. Labelling of Herceptin with palladium via the SPACC.

From the SDS-PAGE gel (Figure 3.26) it can be seen that the isolation and purification of **28a** and **30a** were successful. The resolution was not high enough to discern an accurate molecular weight shift.

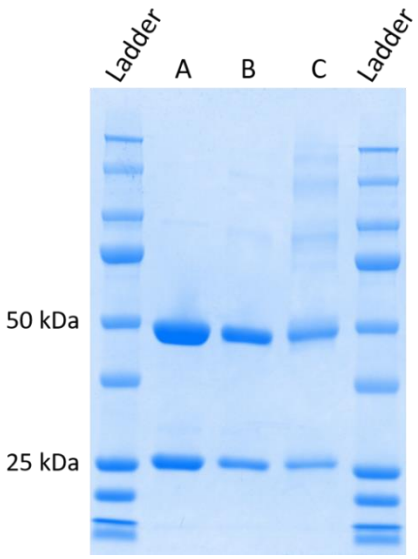

Figure 3.26 SDS-PAGE of Palladium coupling onto Herceptin. Kaleidoscope ladder. (A) pure Herceptin; (B) **28a**; (C) **30a**.

From the MALDI-TOF MS spectra (Figure 3.27) it can be seen that Herceptin was successfully labelled with DBCO with results consistent with those seen in Figures 3.24 and 3.25. The shift in molecular weight from **28a** to **30a** was 2000 Da. Since the molecular weight of **19** is 687 Da, this would suggest approximately 3 moles of **19** have been attached onto the antibody. It also suggests that close to 100 % of the available strained alkynes on **28a** were converted to the triazole containing product.

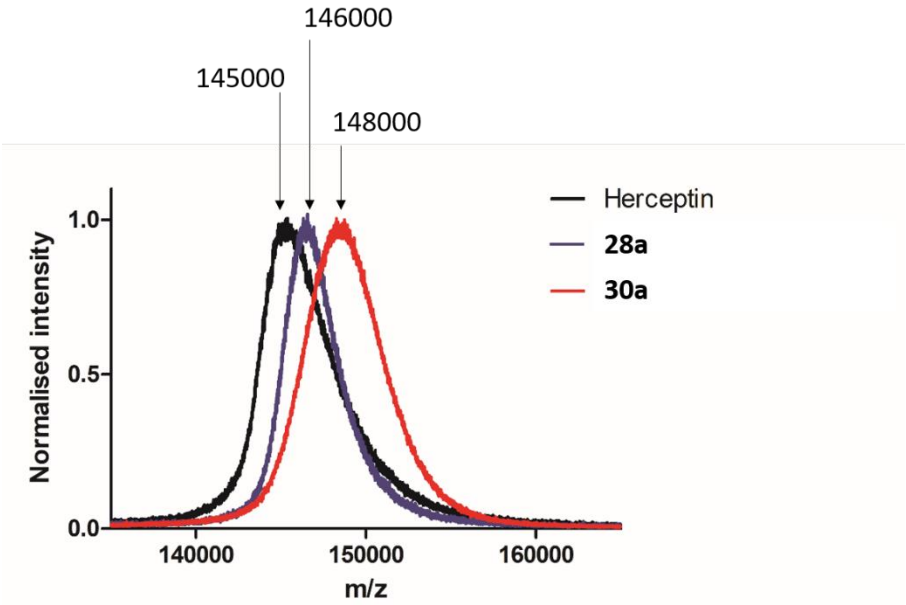

Figure 3.27 MALDI-TOF MS analysis of the palladium conjugation to Herceptin. Unmodified Herceptin in black; **28a** in blue; **30a** in red.

These analyses confirmed that the level of labelling was between 2.5-3 equivalents of palladium per antibody; consistent with the previous labelling experiments. It is assumed that the labelling will not have impaired the binding capabilities of the antibody based on the flow cytometry data previously discussed. Though to confirm this more complex biological assays would be required. At this stage it was of more importance to confirm that the antibody-palladium conjugate **27** still retained its catalytic activity. Absorbance at 280 nm and ICP-MS confirmed concentration for protein and the presence of palladium, respectively in **30a** (Table 3.5).

Table 3.5 Protein concentration (based on absorbance at 280 nm) and palladium content (ICP-MS measurements) of Pd-antibody conjugate **30a**.

Compound	Pd (ppm)	Pd (nmol/ mg antibody)	Protein concentration (mg/mL)	Pd (μM)	Protein concentration (μM)	Pd/antibody ratio (average)
30a	4.22	18.6	2.21	39.8	15.2	2.6

With confirmation that palladium had been attached to Herceptin, it was then evaluated for its ability to catalyse the deprotection of a caged fluorophore. Thus, the palladium catalyst was

incubated with **PROC-Rh 110** (Scheme 3.6). 3.3 µM of **30a** was incubated with 100 µM of **PROC-Rh 110** for 18 h at 37 °C, this equated to 10 µM of catalyst being in the reaction. This assumption was based on the MADLI-TOF MS data suggesting there are approximately 3 moles of Pd per mole of Herceptin.

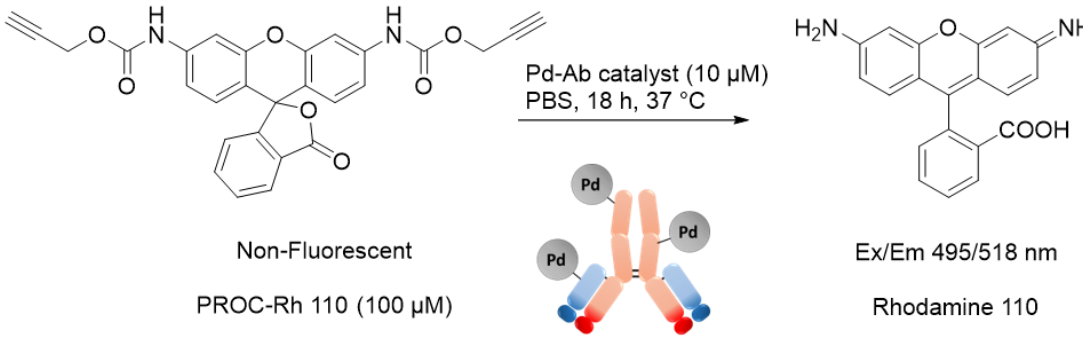

Scheme 3.6 Activation of PROC-Rh 110 with **30a**.

Several experiments were set up for analysis. **19** (an NHC-Pd catalyst with an N_3 moiety) was incubated with the **PROC-Rh 110** substrate as a positive control. The native Herceptin antibody was incubated with **PROC-Rh 110** as a control to ensure that it did not cause any activation of the substrate. Finally **PROC-Rh 110** was incubated with no other additives as a negative control. The fluorescence outputs measured after 18 h.

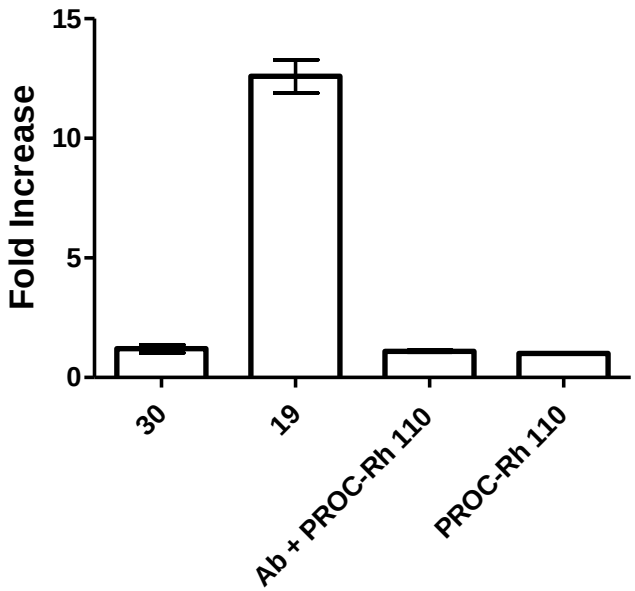

Figure 3.28 PROC-Rh 110 activation by palladium catalysts. Fluorescence readings were measured as a fold increase compared to the **PROC-Rh 110** negative control which is represented as 1. 19 was reacted with the substrate as a positive control. Reactions were carried out at 37°C, for 18 h in PBS. Pd concentrations were at 10 µM and **PROC-Rh 110** at 100 µM. n = 3 error bars are standard deviation.

Figure 3.28 shows that The Ab-Pd conjugate appeared not to be active compared to the control reactions. The fold increase was no higher than the substrate without any catalyst, and the positive control reaction shows that in theory the catalyst should have had an activity close to **19** since the concentrations were equal (10 µM). The antibody by itself did not cause an increase in fluorescence. It was decided to incubate **19** with the antibody freely in solution to see if the antibody inhibits catalytic activity in any way without the conjugation steps. The concentration of Herceptin used in all the following reactions was 10 µM and the pro-fluorophore at 100 µM.

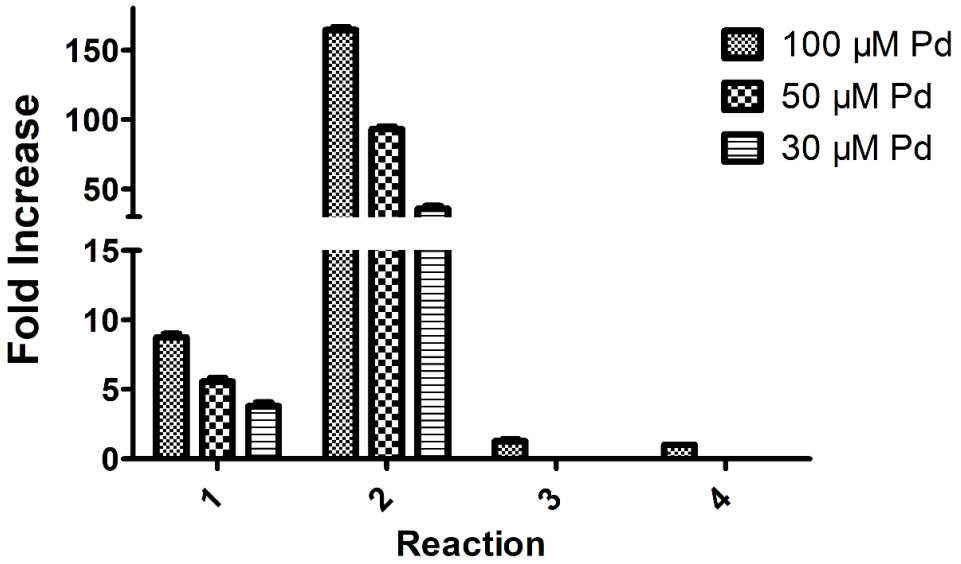

Figure 3.29 Incubation of Palladium with Herceptin in solution. *Reaction 1,* **19** with free Herceptin and **PROC-Rh 110**; *Reaction 2,* **19** and **PROC-Rh 110** only. *Reaction 3* is Herceptin and **PROC-Rh 110** (no Pd). *Reaction 4* is **PROC-Rh 110** only. Reactions were carried out at 37 °C, for 18 h in PBS. Pd concentrations are at either 100 µM, 50 µM, or 30 µM. **PROC-Rh 110** at 100 µM. Herceptin was a concentration of 10 µM. n = 3 errors bars are standard deviation.

These results (Figure 3.29) suggest that the presence of Herceptin alone reduced the catalytic activity of **19**. This was consistent at a range of concentrations. There is no clear hypothesis as to why this reduction in activity is so drastic. It is possible that the catalyst has been inactivated by thiols on the protein surface, however other Pd-catalysts were shown to be active in DMEM and in cells in Chapter 2, so this would seem inconsistent. One possibility could be that the Pd centres are "stuck" onto the surface of the antibody through non-covalent interactions. This prevents access of the pro-fluorophore to the Pd centre thus reducing the activity. Another possibility is that the free amine and carboxylic acid groups on the protein surface are binding to the catalytic centre inhibiting it; assuming the role of ligand "Y". Based

on these results, it was decided that increasing the levels of palladium loading onto the antibody could help improve the catalytic efficiency. Should this also fail to confer catalytic activity other ideas would need to be explored such as extending the linker between the catalytic centre and the mAb.

To increase the palladium loading on Herceptin, the antibody was reacted with DBCO-NHS to generate **28b** and subsequently **19** to give **30b** (Scheme 3.5). To increase the degree of labelling, 25 eq. (1 mM compared to 0.2 mM previously) of DBCO-NHS was used. After purification and isolation, 25 eq. of **19** were added. After the reactions the products were analysed by SDS-PAGE, MALDI-TOF and ICP-MS.

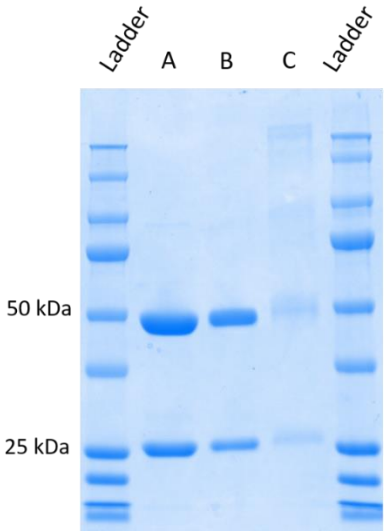

Figure 3.30 SDS-PAGE gel of **28b** and **30b**. Lanes are as following; Kaleidoscope ladder with key markers identified; (A) Pure Herceptin; (B) **28b**; (C) **30b**.

The SDS PAGE (Figure 3.30) showed distinct shifts in the protein bands when comparing lanes, A, B and C indicating increased molecular weight and thus conjugation. This is most easily seen with the antibody light chain at 25 kDa. When comparing lanes B and C there was a further increase in the protein bands as the catalyst was added.

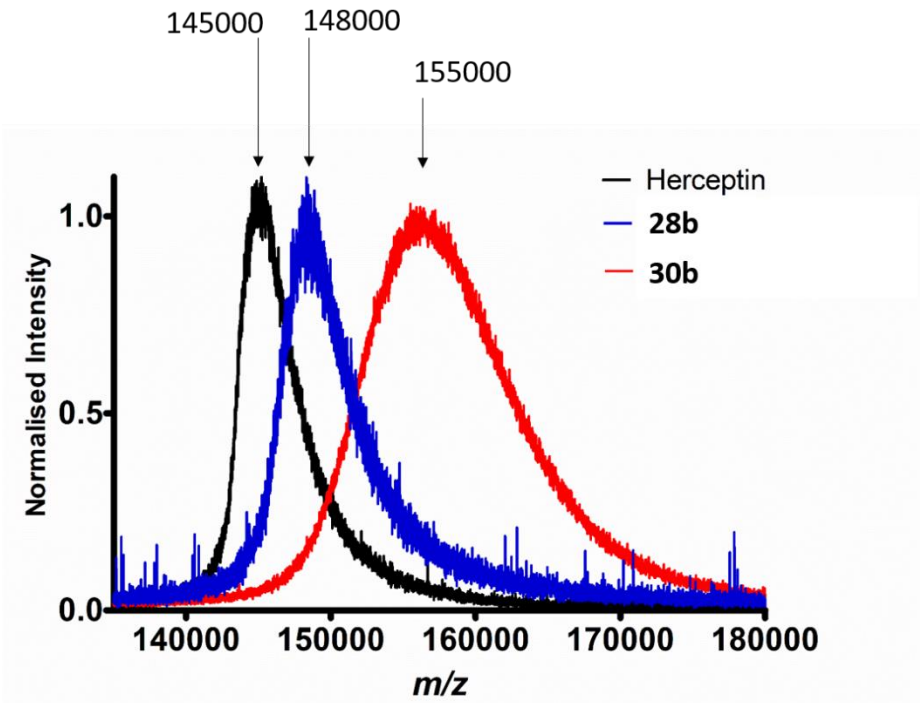

Figure 3.31 MALDI-TOF MS of the reaction in Scheme 3.8. Pure Herceptin in black. **28b** in blue. **30b** in red.

The MALDI-TOF MS data (Figure 3.31) showed significant shifts in the m/z of products **28b** and **30b**. The shift from the native Herceptin after reacting with the strained alkyne DBCO was 3000 Da. Given that the increase is 300 g/mol per DBCO added this suggests that there are now 10 equivalents of the strained alkyne attached. The increase after the palladium was added was 7000 Da the molecular weight **19** is 687 Da, suggesting an increase of around 10-11 catalysts per antibody. The peaks became very broad, highlighting the heterogenicity of antibody-conjugates produced. Once again Absorbance at 280 nm and ICP-MS were also used to confirm the protein concentration and the palladium content, respectively of **30b** (Table 3.6).

Table 3.6 Protein concentration (based on absorbance at 280 nm) and palladium content (ICP-MS measurements) of Pd-antibody conjugate **30b**.

Product	Pd (ppm)	Pd (nmol/ mg antibody)	Protein concentration (mg/mL)	Pd (μM)	Protein concentration (μM)	Pd/antibody ratio (average)
30b	5.91	75.7	0.96	55.7	6.2	9.0

With confirmation of increased loading via MALDI-TOF MS and the palladium content confirmed via ICP-MS, this new conjugate (**30b**) was then assessed for its ability to activate **PROC-Rh 110**. The palladium catalyst was incubated with **PROC-Rh 110** with 1 µM of **30b** incubated with 100 µM of **PROC-Rh 110** for 18 h at 37 °C; the equivalent of 10 µM of Pd in the reaction.

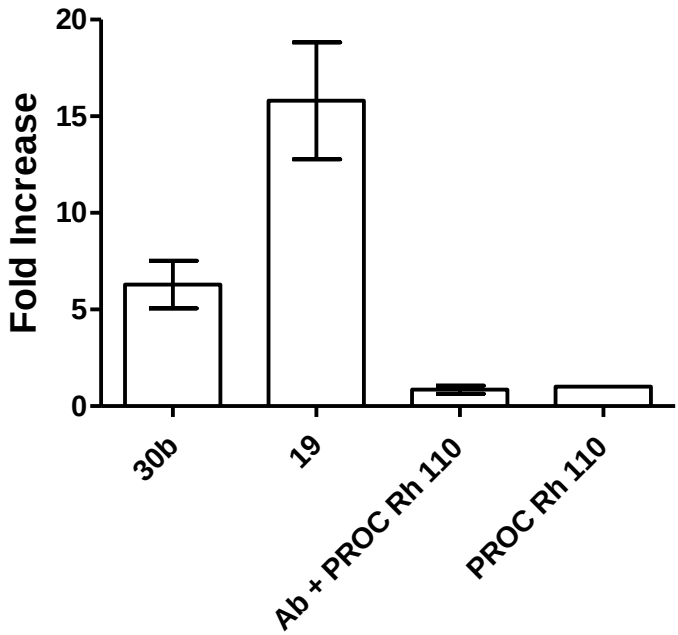

Figure 3.32 Activation of **PROC-Rh 110** with palladium catalysts. Reactions were carried out at 37 °C, for 18 h in PBS. Pd concentration of 10 µM, **PROC-Rh 110** at 100 µM. n = 3 error bars are standard deviation.

The results in Figure 3.32 showed **30b** did cause some increase in fluorescence with its higher levels of Pd. It is notable that even though the concentrations of palladium in the reactions with **30b** and **19** are the same, the absence of the antibody conjugation (and thus the lack of inhibition of the catalyst) means that fluorescence output was higher for the reaction with **19**. Regardless, this shows that the concept of a catalytically active Pd-antibody "ADC" is viable. The key issue is that the turn-over of these catalysts were very low and practically a higher turnover would be beneficial. It was therefore decided to try and increase the length of the linker between the protein and the antibody to see if that would improve the activity.

3.3.5 Changing the spacer

It was hypothesised that extending the spacer between the antibody and the palladium catalyst might allow the palladium to be more active. DBCO-PEG$_{12}$-NHS was chosen as a spacer due to the PEG chains allowing for more hydrophilicity; important for clinical applications by improving aqueous solubility (Scheme 3.7). The reactions were carried out and products purified using the same conditions as previously described. To generate two products with different degrees of labelling.

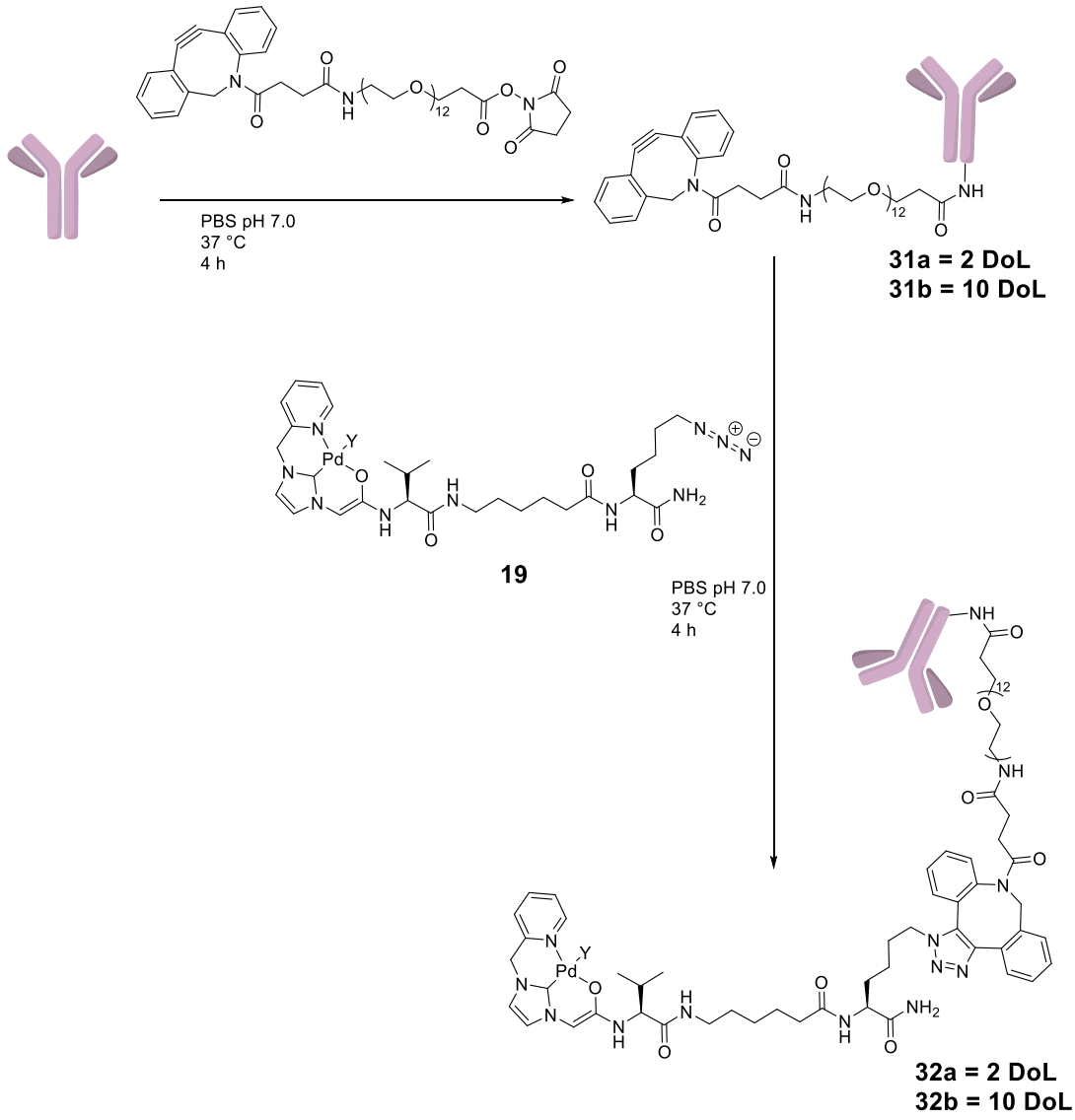

Scheme 3.7 Coupling of **19** onto Herceptin via DBCO-PEG$_{12}$-NHS chemistry (DoL = degree of labelling).

Initially, 5 Equivalents of DBCO-PEG$_{12}$-NHS (0.2 mM) were added to Herceptin at 37 °C for 4 h to generate **31a**. To this, 5 equivalents (0.2 mM) of **19** was added at 37 °C for 4 h and

purified using Amicon centrifugal spin columns to give **32a**. To generate **31b** and **32b** the same procedure was carried out except using 25 equivalents (1 mM) of the reagent DBCO-Peg_{12}-NHS and **19**.

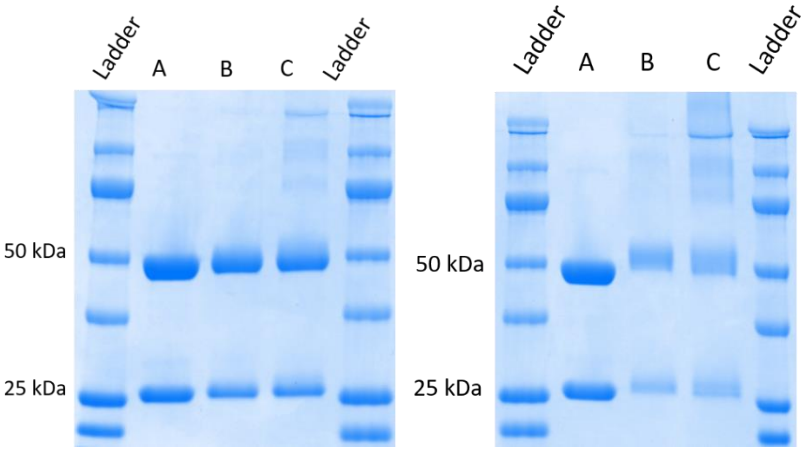

Figure 3.33 SDS PAGE gel of the reactions in scheme 3.9: (Left gel) Lanes are as follows; Kaleidoscope ladder with key markers identified; (A) Pure Herceptin; (B) **31a**; (C) **32a**. (Right gel) Lanes are as following; Kaleidoscope ladder with key markers identified; (A) Pure Herceptin; (B) **31b**; (C) **32b**.

The SDS-PAGE in Figure 3.33 shows that both **31a** and **32a** showed an increase in the molecular weight of the protein, reducing their mobility and causing them to appear higher up the gel. The bands also widened due to the heterogeneous nature of the products. The same can be also seen for products **31b** and **32b**. These shifts together with the MS analysis (Figure 3.34 and Figure 3.35) clearly indicated that conjugation of the linker and the palladium catalyst had been successful.

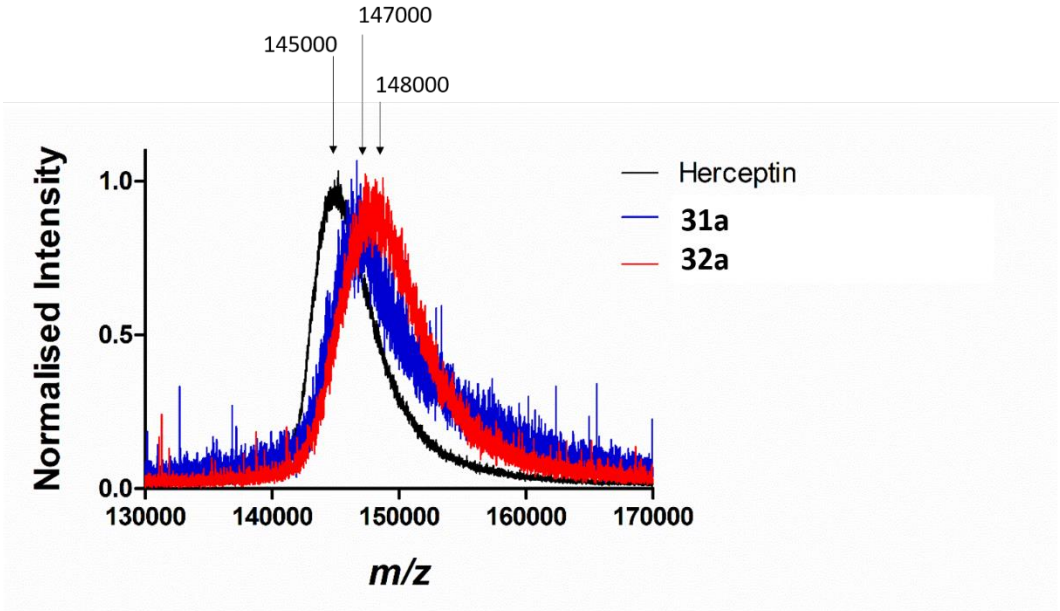

Figure 3.34 MALDI-TOF MS of the reaction in Scheme 3.7. Pure Herceptin in black. **31a** in blue and **32a** in red.

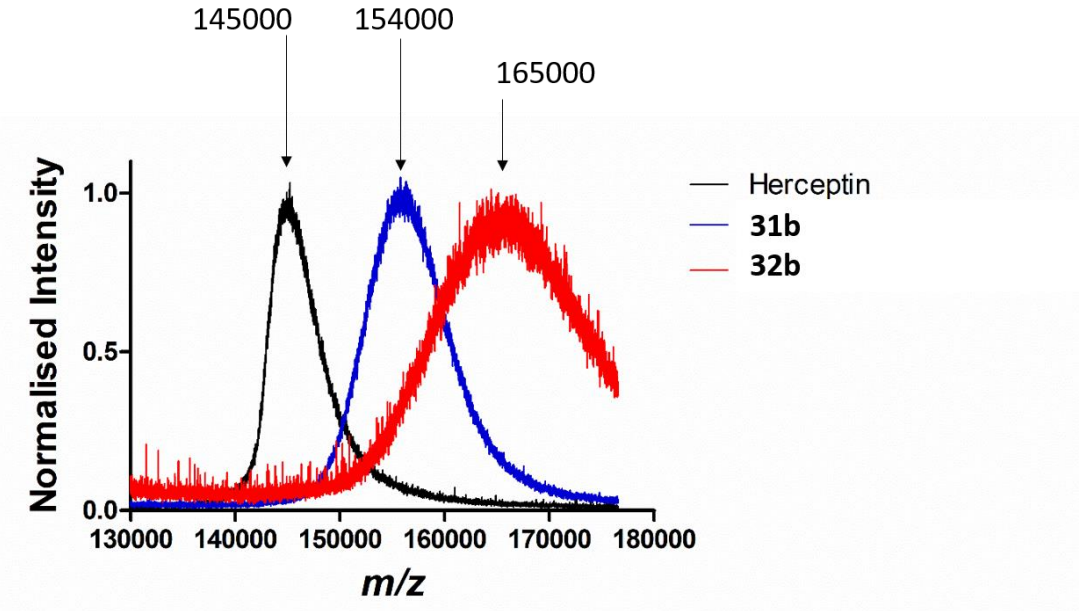

Figure 3.35 MALDI-TOF MS of the reaction in Scheme 3.7. Pure Herceptin in black. **31b** in blue and **32b** in red.

Further to the SDS-PAGE gels, the products were then analysed by MALDI-TOF MS (shown in Figures 3.34 and 3.35). Figure 3.34 shows that the increase in molecular weight was 2000 from Herceptin to **31a** (indicative to 2 molecules of DBCO-PEG attached) and then approximately 1000 Da more from **31a** to **32a** showing there are approximately 1 to 1.5

molecules of Pd per antibody. In figure 3.35, the MALDI-TOF analysis of **31b** and **32b** showed a molecular weight increase of about 9000 (for **31b**) and then a further 10000 Da (for **32b**). Suggesting that an average of 9 DBCO-PEG_{12} molecules were added to the antibody with 10 molecules of Pd subsequently added. Finally, **32a** and **32b** were analysed by absorbance at 280 nm and ICP-MS to determine the protein concentration and palladium content respectively of **32a** and **32b** (Table 3.7).

Table 3.7 Protein concentration (based on absorbance at 280 nm) and palladium content (ICP-MS measurements) of Pd-antibody conjugate **32a** and **32b**.

Product	Pd (ppm)	Pd (nmol/ mg antibody)	Protein concentration from Absorbance at 280 nm (mg/mL)	Pd (μM)	Protein concentration (μM)	Pd/antibody ratio (average)
32a	1.02	12.5	0.77	9.6	5.2	1.8
32b	4.61	50.0	0.87	35.5	5.0	8.7

The discrepancy between the number of DBCO-PEG_{12} (9) and Pd (10) molecules added is likely due to the heterogeneous nature of the conjugates. Since the MALDI peaks are so broad definition becomes more subjective. These new antibody conjugates were evaluated for their ability to activate the pro-fluorophore **PROC-Rh 110**.

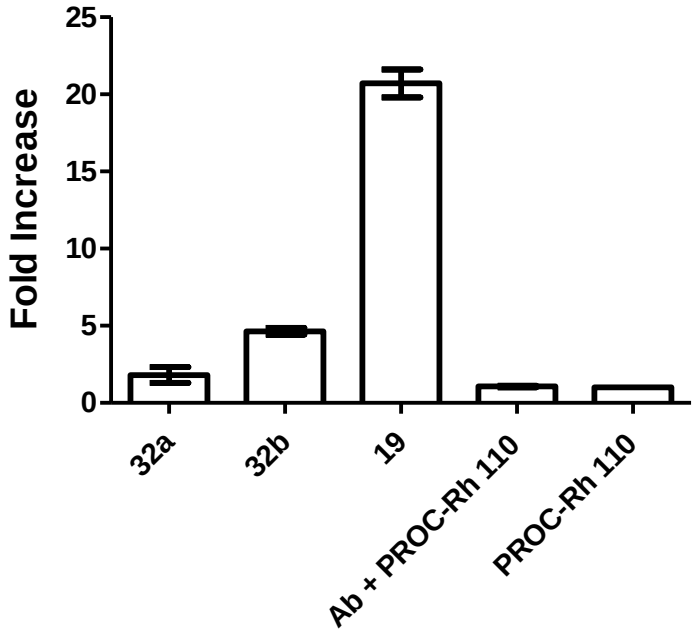

Figure 3.36 Activation of **PROC-Rh 110** with palladium catalysts. Reactions were carried out at 37 °C, for 18 h in PBS. Pd concentrations were 10 µM, in all cases with **PROC-Rh 110** at 100 µM. (antibody in the controls was also 10 µM). n = 3, error bars are standard deviation.

The results of the fluorophore activation with the new antibody-Pd conjugates (**32a** and **32b**) is shown in Figure 3.36 and compared to the negative control reactions with no Pd. **32a** and **32b** showed a small increased in fluorescence (2-fold and 5-fold respectively). Comparable to the activity of conjugate **30b.** This suggests changing the length of the spacer did not have a significant effect on improving the catalytic activity of the Pd-catalyst.

Overall, these results show that Herceptin was successfully loaded with the palladium catalyst via the strained alkyne DBCO with a longer PEG spacer and it was possible to label Herceptin with different ratios by modifying the concentration of reagents used. When the Pd-Herceptin conjugates were incubated with **PROC-Rh 110**, there was some turnover compared to controls although this was the same as when the linker was shorter, and in both cases limited. At this point any potential immunoreactivity was not tested however, this would need to be done regardless of the level of labelling and would likely be carried out in a phase I clinical trial. Given the widespread use of Herceptin and the knowledge that these catalysts are not cytotoxic, it is hoped that systemic immunogenicity *in vivo* would not be an issue.

3.4 Conclusions and future work

In conclusion, this work demonstrates that it was possible to conjugate a palladium catalyst onto an antibody, a world first. This was accomplished by first evaluating BSA as a model for establishing reaction conditions for conjugation of fluorophores to the proteins. Then translated to labelling Herceptin with a fluorophore using SPAAC chemistry. Vitally, this fluorescent-Herceptin conjugate could still bind to its target HER2 receptor on SK-BR3 cells. Finally, an *N*-heterocyclic carbene palladium catalyst was conjugated onto the antibody and then evaluated for its catalytic activity.

This antibody-Pd conjugate was the first of its kind and represents a step forward in the field of targeted palladium catalysts. The first conjugate synthesised **30a** was not catalytically active, however it was shown that simply the presence of the antibody decreases the catalytic efficiency of catalyst **19**. The reduction in catalytic activity is likely to be related to the mechanism and potentially what the ligand Y is. As speculated in chapter two Y could be any number of ligands from the solution but could also be a moiety from within the same molecule (e.g. carboxylic acid or amine). Moreover, in the context of the Pd-antibody the proximity of amine and carboxylic acid groups (from lysine and glutamic acid residues respectively) found on proteins may also be the source of inhibition to the catalyst and go some way to explaining the results found in figure 3.29.

Thus, there needs to be a thorough investigation into the reasons for why the addition of an antibody decreases the catalytic activity of catalyst **19**. Such an investigation could include spiking the catalysts with a ligand that will bind strongly to the Pd atom, then analysis by mass spectrometry. The spiking could include a range of different ligands including imidazole (which binds strongly to metals), or small molecules to simulate amines or carboxylic acids. The subsequent "products" might be then analysed with other structural studies like X-ray crystallography (if possible) to see if these ligand are bound as well as assaying the catalytic activity of the palladium using previously described substrates.

Initially other NHC-Pd synthesised in Chapter 2 could be tested to see if the presence of an antibody decreases their activity too. Moreover, different antibodies might have a less profound effect – this might be unlikely if the issue is cause by some general factor such as thiols or the protein structure.

From the initial results, it was decided that increasing the level of palladium on the conjugate might improve the catalytic efficiency of the conjugate. Delightfully, this higher Pd loaded catalyst (10 moles of Pd per antibody), showed greater conversion of the pro-fluorophore

PROC-Rh 110 to the fluorescent product Rhodamine 110. One key limitation was that the conversion was lower than that of the free catalyst though this is somewhat mitigated by the findings that the antibody reduces activity even in solution. The analysis in this chapter lacked quantitative conversion analysis by techniques such as HPLC and it would be desirable data to support this work. However, in a clinical setting, low conversion may not matter if the reporter fluorophores are bright enough and there is a large enough signal-to-noise ratio. If higher conversion were needed one option would be to change the catalyst to one that demonstrated higher activity from Chapter 2. For example, the catalyst that had just a valine residue was both highly active and stable. Since all those catalysts had carboxylic acids they could be converted into active NHS-esters and be attached to proteins via and amide bond. Changing the catalyst might be preferable in future work anyway to allow for better catalytic responses to give greater control over clinical procedures.

During this work different levels of palladium were loaded on to catalyst after their validation of the conjugation methodology. The linker between the catalyst and the protein was also varied to see if that this would have any effect on the catalytic activity, but in the end, it did not. In this work only 2 different linkers were explored, a short four-carbon chain and a longer PEG_{12} chain. With regards to improving the catalytic efficiency of the Pd-antibody conjugate other linkers could also be trialled, for example branched linkers might allow for a higher loading of the palladium catalysts and PEG might decompose the Pd. In this work the linkers tested had flexible chains, however having rigid linkers should also be explored to see if they help to improve catalytic efficiency. However, given the that the two options already explored did not cause any difference in the catalytic turnover, it suggests that the chemistry of the linker is not crucial. Ultimately, it is important that the linker is kept as a “non-cleavable” linker so that in clinical setting there would not be any undue loss of palladium before the conjugate reached its intended target.

Extra research that might be of interest would be X-ray crystallography to determine the crystal structure of the Pd-antibody conjugate. This might be best attempted once a more consistent method of labelling has been created such that there is a homogenous product. A crystal structure would also be another way to validate that the conjugation of the Pd catalyst was not in any crucial binding site of the antibody.

Once a Pd-antibody conjugate has been made which is sufficiently catalytically active, the next experiments would be to begin testing this type of system *in vitro* then *in vivo* using translatable models. Should those be successful however, the technology could be a basis for transformative change not only in medical diagnosis, but also in therapeutics. Palladium with

its catalytic activity and range of chemical reactions could also be used to switch on prodrugs such as those demonstrated at the end of Chapter 2 in the 3D cancer spheroid models. In a clinical setting it could be feasible to use one administration of an antibody-Pd conjugate, that could diagnose (using fluorescence activation) and treat the disease (pro-drug activation). The ligand developed could also be explored with other metals (for example Ru) or perhaps radioactive metals for alternative therapeutic approaches. Ultimately, with the range of antibodies available these bio-conjugatable catalysts could become a powerful platform technology with their use pervasive in biotechnology.

Chapter 4 Thesis conclusions

The original aims of this thesis were to:

1. Develop a biocompatible catalyst which can be used to activate fluorescent probes in cancerous cells.
2. Attach the catalyst to a biological targeting molecule such as an antibody.
3. Test the ability of this targeted catalyst to generate fluorescent signals in translational models.

The first aim was successfully achieved in Chapter 2, where a new synthetic methodology was used to create a library of biocompatible Pd catalysts. Not only was this methodology robust to generate a range of different catalysts, but also significantly reduced the time taken to synthesise them. The catalysts were shown to activate a caged fluorophore in biologically relevant conditions with **11** then used to activate a prodrug inside a 3D cancer spheroid model. This was important, as 3D cancer models are more representative than 2D when trying to replicate results in a clinical setting. These catalysts also had a carboxylic acid moiety which could be activated for conjugation purposes.

The next aim was to attach Pd catalysts to a targeting molecule such as an antibody. Following the success in Chapter 2, Chapter 3 began with the synthesis of three more catalysts which had distinct handles for bioconjugation methods, with a particularly interesting catalyst containing an azide moiety. These were then successfully conjugated onto antibodies after model reactions were used to determine suitable conjugation reaction conditions. With a successful Pd-antibody conjugate, the first known, this conjugate was then tested for its ability to activate a caged fluorophore. It was only when the levels of palladium had been increased (from 3 to 10 molecules of Pd per antibody) that catalytic activity was observed, though the turnover was disappointingly low. Moreover, changing the linker did not improve the activity of the conjugate. This leaves the chapter somewhat at a crossroads but leaves lots of potential to explore new avenues. These avenues include:

1. Changing the catalyst for one which is more active.
2. Find brighter/more responsive fluorophores so that minimal signals can be detected. This includes changing the fluorophores wavelengths to NIR that could be more clinically relevant.
3. Design amplification probes that release multiple fluorophores so that one activation “event” generates brighter signals.

The third aim of this thesis was untimely not achieved, it would be the next step in the development of the Pd-Antibody conjugates in their pathway to the clinic. Looking forward once a more functionally viable Pd-antibody has been made, the first step would be to test its ability to activate caged fluorophore whilst its attached to cells. This activation could also include prodrugs to show enhanced cell death. Next the conjugate can be tested on 3D cell culture or *ex vivo* models that are more representative of lung cancer before potentially moving to *in vivo* models. The beauty of this design is that it could be highly transferable where the changing of the antibody could allow the same concept to be used to diagnose other cancers or diseases.

Chapter 5 Experimental

5.1 General Experimental

Amino acids, aminomethyl polystyrene resin and 2-chlorotrityl polystyrene resin were purchased from GL Biochem (Shanghai) Ltd and NovaBiochem, all other chemicals were from Sigma Aldrich, Acros and Fluorochem and used without purification unless otherwise stated. Solvent removal was carried out under reduced pressure on a Büchi rotary evaporator, or overnight in a Heraeus vacuum oven at 40 °C. PBS used was Dulbecco's phosphate buffered saline. Dibenzocyclooctyne *N*-hydroxysuccinamide ester (DBCO-NHS), dibenzocyclooctyne-polyethylene glycol *N*-hydroxysuccinamide ester (DBCO-PEG_{12}-NHS) and 5-fluorescein azide (5-FAM-N_3) were purchased from Jena Bioscience. Poly acrylamide SDS-PAGE gels 10 % were purchased from Bio-Rad. Herceptin was purchased from Carbosynth (Berkshire) Ltd.

^{1}H and ^{13}C NMR spectra were recorded on an automated Bruker AVA 500 (500 and 126 MHz respectively) in the indicated solvents at 298 K. Chemical shifts (δ) are quoted in parts per million (ppm) using the deuterated solvent as an internal standard and all coupling constants (J) were measured in Hertz (Hz). Resonances are specified as singlets (s), doublets (d), triplets (t), multiplets (m), broad singlets (br s) or aromatics (Ar). Low Resolution Mass Spectra (LRMS) were obtained using an Agilent LCMS 1100 ChemStation with a G1946B quadrupole mass detector. High Resolution Mass Spectra (HRMS) were performed on a Bruker 3.0 T Apex II spectrometer. All HRMS data is quoted in positive mode unless specified. All compounds have been reported as $[M+H]^+$ though for many $[M+Na]^+$ was also observed. MALDI-TOF mass spectra were obtained with a Bruker UltraflexExtreme MALDI TOF/TOF instrument and analysed using the Bruker Daltonics flexAnalysis software. All MALDI data was acquired in positive mode unless specified. Analytical RP-HPLC was performed on an Agilent 1100 Chemstation equipped with a Kinetex 5 µm XB-C18 100A (50 mm × 4.6 mm) column eluting with a gradient of water/formic acid (0.1 %) to MeCN/formic acid (0.1 %) over 10 minutes with a flow rate of 1 mL/min, with compounds detected by an ELS detector and a multi-wavelength detector. Preparative RP-HPLC purifications were performed on an Agilent Technologies HP1100 Chemstation eluting with water and MeOH (5 % MeOH to 95 % over 25 min) with 0.1 % formic acid on a Kinetex 5 µm XB-C18 100A (150 mm × 21.2 mm) column with a flow rate of 10 mL/min, or on an Eclipse XDB-C18 5 µm (9.4 mm × 250 mm) column with a flow rate of 1 mL/min. Microwave assisted heating was carried out in a Biotage initiator at 2.45 GHz. All melting points were obtained using a SMP10 melting point

apparatus from Bibby Scientific Ltd. Absorbance and fluorescence spectra were obtained using either a Shimadzu RF-6000 spectrofluorometer, or a Synergy Biotek plate reader and analysed using the Gen5 software. Fluorescent kinetic assays were read on a BioTek synergy HT plate reader. Absorbance values for protein conjugates were measured on a Thermo Scientific NanoDrop 2000c.

ICP-MS Pd content were obtained on an Agilent 7500ce ICP-MS suitable for the trace analysis of metals between 0.001-10.0 ppb. Gel electrophoresis was carried out on buffered gels and analysed on a Bio-Rad Gel Doc XR+ system and analysed on Image Lab V6 software. Flow cytometry was carried out on a Becton Dickinson (BD) FACSAriaTM and analysed using the FlowJo software (version 7.2.4). Confocal images were obtained on a Leica SP5 confocal microscope and ImageJ version 1.52i was used for analysis.

5.2 Solid phase synthesis

Resin Activation

2-Chlorotrityl polystyrene resin (300 mg, 1 mmol/g) was swollen in dry DCM for 30 min and drained. To the resin, a solution of thionyl chloride (2.5 eq.) in DCM (3 mL) was added. The resin was shaken for 1 hour before being drained and washed with dry DMF (3 × 5 mL) and dry DCM (3 × 5 mL).

First amino acid couplings

All amino acids and linkers were coupled according to standard Fmoc SPPS protocols. Quantities were based on the use of 300 mg of resin (1 mmol/g loading).

For coupling to 2-chlorotrityl linker, the first appropriate amino acid (1 mmol) was dissolved in dry DMF (3 mL). To this, DIPEA (314 µL, 1.8 mmol) was added and the mixture was added to the resin and shaken for 1 h before being drained and washed with DMF (3 × 5 mL) and DCM (3 × 5 mL) and MeOH (3 × 5 mL). The resin was then capped with a mixture of DCM/MeOH/DIPEA (80:15:5) for 10 min (2 × 3 mL).

For aminomethyl polystyrene resin (300 mg 0.675 mmol/g), Fmoc Rink linker (5 eq., 1 mmol) was dissolved in DMF (3 mL) and mixed with Oxyma (5 eq., 1 mmol) for 5 min. To this, DIC (5 eq., 1 mmol, 157 µL) was added and mixed for 5 mins further. The solution was added to the resin and stirred for 2.5 h. The resin was then washed with DMF (3 × 5 mL), DCM (3 × 5 mL) and MeOH (3 × 5 mL).

Fmoc deprotection

Pre-swollen peptidyl resin (300 mg, 1 mmol/g) was treated with piperidine in DMF 20 % (*v*/*v*) (2 × 10 min) and washed with DMF (3 × 5 mL) and then DCM (3 × 5 mL).

Subsequent amino acid couplings

Appropriate Fmoc-protected amino acids (5 eq., 1 mmol), were dissolved in DMF (3 mL) and mixed with Oxyma (5 eq., 1 mmol) for 5 min. To this, DIC (5 eq., 1 mmol, 157 µL) was added and mixed for 5 min further. The solution was added to the resin and stirred for 45 min. The resin was then washed with DMF (3 × 5 mL), DCM (3 × 5 mL) and MeOH (3 × 5 mL).

Bromoacetic acid coupling

The resin (300 mg, 1 mmol/g) was washed with DMF (2 × 5 mL) and a solution of bromoacetic acid (830 mg, 6 mmol) and DIC (460 µL, 3 mmol) in DMF (3 mL), pre-mixed for 20 s, was added. The mixture was heated under microwave irradiation in an SP Wave (Biotage) for 20 min at 60 °C. The resin was subsequently washed with DMF (3 × 5 mL), and DCM (3 × 5 mL).

Imidazole coupling

To resin (300 mg, 1 mmol/g) washed with DMF (2 × 5 mL), a solution of imidazole (413 mg, 6 mmol) in DMSO (2 mL) was added and shaken for 5 min. A solution of $AgNO_3$ (254 mg, 1.5 mmol) in DMSO (1 mL) was added. The mixture was heated under microwave irradiation in an SP wave for 40 min at 60 °C. The resin was subsequently washed with DMF (3 × 5 mL), and DCM (3 × 5 mL).

Imidazole alkylation coupling

To resin (300 mg, 1 mmol/g) washed with DMF (2 × 5 mL) trimethylamine (139 µL, 1 mmol) was added followed by a solution of 2-bromomethyl pyridine (759 mg, 3 mmol) in DMF (2 mL) and shaken for 5 min. A solution of $AgNO_3$ (254 mg, 1.5 mmol) in DMF (1 mL) was added and shaken for 2 min. The mixture was heated under microwave irradiation in an SP wave for 90 min at 60 °C. The resin was subsequently washed with DMF (3 × 5 mL), then piperidine in DMF 20 % (v/v, 3 × 5 mL) and DCM (3 × 5 mL).

Palladium loading to ligands on resin

Resin (300 mg, 1 mmol/g) was swollen for 30 min under Ar in anhydrous DCM. The resin was then washed with anhydrous DMF (2 × 5 mL) under Ar. The resin was swollen with a minimal amount of anhydrous DMF after which 2-*tert*-butylimino-2-diethylamino-1,3-dimethylperhydro-1,3,2-diazaphosphorine (173 µL 0.6 mmol) was added and stirred for 30 min under Ar. The solution was then removed and dichloro(1,5-cyclooctodiene)palladium (127 mg, 0.45 mmol) in anhydrous DMF (1 mL) was added to the resin and stirred overnight under inert atmosphere at room temperature. The resin was washed with DMF (2 × 5 mL) and DCM (2 × 5 mL) and 95 % TFA/DCM was added for 2 h to cleave the product. The solution was drained from the resin and the solvent was removed under reduced pressure. The crude mixture was then re-dissolved in H_2O/ACN (95:5) and purified by preparative RP-HPLC.

5.3 Compounds

5.3.1 Solution synthesis

***tert*-Butyl (imidazol-1-yl)acetate 2**

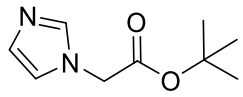

2

Glyoxal (40 wt% solution in water, 580 mg, 10 mmol) and formaldehyde (37 wt% solution in water, 300 mg 10 mmol) in *i*-PrOH (10 mL) were added dropwise to a stirred solution of glycine *tert*-butyl ester hydrochloride (1.68 g, 10 mmol), ammonia (28 wt% solution in H_2O, 11 mmol, 552 µL) and *i*-PrOH (35 mL). After complete addition the reaction was heated to 80 °C overnight. The dark red solution was allowed to cool to room temperature and diluted with DCM (25 mL). The organic layer was separated, washed with NaOH (1.0 M, 25 mL), dried over $MgSO_4$, filtered and concentrated *in vacuo*. The crude was purified by silica gel column chromatography (ethyl acetate/hexane = 4:1, then DCM/methanol = 19:1). Purification was monitored by thin layer chromatography, to yield a yellow solid (703 mg, 3.8 mmol), 39 %.

Mp 110-112 °C; **^{1}H NMR** (500 MHz, $CDCl_3$): δ ppm 7.48 (1H, s), 7.08 (1H, t, J = 1.1), 6.94 (1H, t, J = 1.3), 4.58 (2H, s), 1.47 (9H, s); **^{13}C NMR** (126 MHz, $CDCl_3$): δ ppm 166.3 (C), 137.8 (CH), 129.5 (CH), 119.8 (CH), 83.1(CH_2), 48.7 (C), 27.9 (CH_3); **HRMS (ESI)**: calculated. for $C_9H_{15}O_2N_2$, 183.1128; found 183.1113 $[M+H]^+$. Spectral data are consistent with the literature.[73]

3-(Carboxymethyl)-1-[(pyridin-2-yl)methyl]-3*H*-imidazol-1-ium 3a

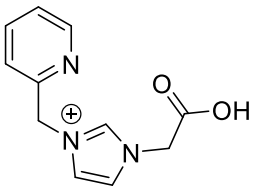

3a

2-(Bromomethyl)pyridine hydrogen bromide (505 mg, 2 mmol) was added to a solution of **2** (364 mg, 2 mmol) dissolved in DMF (8 mL). The solution was heated to 150 °C for 25 min

under microwave irradiation. The solvent was removed *in vacuo*, and the crude was dissolved in DCM/TFA (1:1, 10 mL) and stirred for 2 h after which the solvent was removed *in vacuo*. The concentrated solution was dissolved in water and purified by preparative RP–HPLC to yield the title compound as a dark red oil (20 mg, 0.09 mmol, 5 %).

^{1}H NMR (500 MHz, CD_3OD): δ ppm 9.10 (1H, s), 8.57 (1H, ddd, J = 4.9, 1.9, 1.0 Hz), 7.88 (1H, td, J = 7.7, 1.8 Hz), 7.62 (1H, t, J = 1.8 Hz), 7.58 (1H, t, J = 1.8 Hz), 7.50 (1H, d, J = 7.8 Hz), 7.40 (1H, ddd, J = 7.7, 4.8, 0.9, Hz), 5.58 (2H, s), 4.84 (2H, s); **^{13}C NMR** (126 MHz, CD_3OD): δ 171.1 (C), 154.5 (C), 150.9 (CH), 139.2 (CH), 138.4 (CH), 125.2 (CH), 125.1 (CH), 124.1 (CH), 123.4 (CH), 54.9 (CH_2), 53.3 (CH_2); **HRMS** (ESI): Calculated for $C_{11}H_{12}O_2N_3$, 218.0924; found 218.093 $[M+H]^+$. Spectral data are consistent with the literature.[73,136]

Bis-propargyloxycarbonyl-protected Rhodamine 110 (PROC-Rh 110)

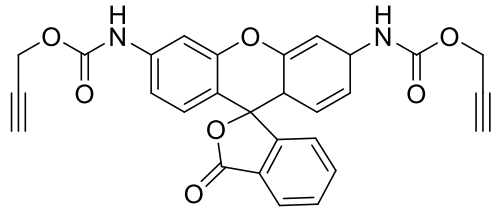

PROC-Rh 110

Rhodamine 110 (200 mg, 0.55 mmol) was dissolved in anhydrous DMF then cooled to 0°C. Propargyl chloroformate (129 µL, 1.1 mmol), and triethylamine (228 µL, 1.64 mmol) were added dropwise, followed by 4-dimethylaminopyridine (3.3 mg, 0.03 mmol). The cooled solution was allowed to warm to room temperature stirred for 24 h. The pink solution was dissolved in ethyl acetate (5 mL) and washed with 1 mM HCl (2 × 20 mL). The aqueous phase was then extracted with ethyl acetate (2 × 20 mL). The organic phase was washed and dried over $MgSO_4$, filtered and concentrated. The resultant crude was purified by silica gel chromatography (hexane/ethyl acetate = 1:2) and monitored by thin layer chromatography to yield the title compound as a white solid (25 mg, 51 µmol, 9 %).

^{1}H NMR δ (500 MHz, Chloroform-*d*): 8.02 (1H, d, J = 7.5 Hz), 7.66 (1H, td, J = 7.4, 1.1 Hz), 7.62 (1H, td, J = 7.5, 1.1 Hz), 7.51 (2H, s), 7.13 (1H, dt, J = 7.6, 1 Hz), 6.96 (2H, dd, J = 8.6, 2.2 Hz), 6.78 (2H, br s), 6.73 (2H, d, J = 8.6 Hz), 4.80 (4H, d, J = 2.5 Hz), 2.53 (2H, t, J = 2.5 Hz); **^{13}C NMR** (126 MHz, Chloroform-*d*): 169.5 (C × 2), 153.3 (C × 2), 152.2 (C × 2), 152.0 (C × 2), 139.7 (C × 2), 135.3 (CH), 130.0 (CH), 129.5 (CH × 2), 125.3 (CH), 124.0 (CH),

114.5 (CH × 2), 106.7 (CH × 2), 82.2 (C × 2), 75.5 (CH_2 × 2), 53.2 (CH_2 × 2); $\mathbf{R_f}$ (EtOAc:hexane, 2:1) = 0.76; ***m/z*** (LC/MS ESI, MeCN) 495.1 $[M+H]^+$. Spectral data are consistent with the literature.[62] HPLC was used to confirm lack of peaks at 495 nm indicating no fluorescence material was in the product which could generate false positive results in fluorescence studies. ELS and 254 nm channels were also checked to assess purity by integration of peaks.

5.3.2 Ligands for palladium catalysts

The following section contains characterisation data of compounds **8**, and **33** to **43**. These compounds are the ligands to which palladium was subsequently added. As a result, they were not explicitly described in the main text but their characterisation prior to palladium loading was vital.

Each compound was synthesised according to the general methodologies described in Section 5.2 (Solid phase synthesis). All were synthesised on a resin scale of 300 mg, using either a 2-chlorotrityl (**8** and **33**-**39**) or Rink linker (**39-43)** on polystyrene resin. Samples of each ligand were cleaved off the solid support with 30 % HFIP in DCM (for 2-chlorotrityl linker) or 95 % TFA in water (for Rink linker) and purified by semi-preparative RP-HPLC (unless otherwise specified). Formate counterions are from purification by HPLC systems and their peaks can be seen in NMR spectra as shown in chapter 2. Where no counter ion was clearly found through any analysis (MS or NMR) the compound has been shown in its zwitterionic form. It is possible that other counter ion are possible such as Bromide ions (originating from synthesis reagents used) or TFA ion from resin cleavage protocols.

"Purity by HPLC" was measured by ELS detection and 254 nm wavelength detector unless otherwise specified. ELS detection was used to check for any impurities while the major peak at 254 nm was then integrated against all other peaks found in the system (at 254 nm). This peak was then confirmed as the product by NMR and mass spectrometry. All HRMS data was acquired in positive mode and calculation are for $[M+H]^+$ though $[M+Na]^+$ was some time observed.

3-[2-[(5-Carboxypentyl)amino]-2-oxoethyl]-1-(2-pyridinylmethyl)-1*H*-imidazolium formate 8

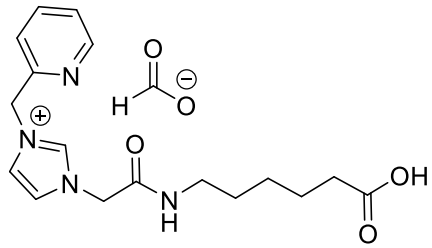

8

Purity by HPLC: 96 %; **Yield**: 65 %; **^{1}H NMR** (500 MHz, Methanol-d_4): δ 8.58 (1H, d, J = 4.8 Hz), 7.93 – 7.85 (1H, m), 7.68 (1H, d, J = 1.6 Hz), 7.63 (1H, d, J = 1.6 Hz), 7.51 (1H, d, J = 7.8 Hz), 7.42 (1H, dd, J = 7.5, 4.9 Hz), 5.58 (2H, s), 5.02 (2H, s), 3.26 (2H, t, J = 6.8 Hz), 2.22 (2H, t, J = 7.2 Hz), 1.67 – 1.51 (4H, m), 1.44 – 1.34 (2H, m); **^{13}C NMR** (126 MHz, Methanol-d_4): δ 180.5 (C), 169.9 (C), 154.2 (C), 151.0 (CH), 139.2 (CH), 125.2 (CH), 125.1 (CH), 124.1 (CH), 123.8 (CH), 54.9 (CH_2), 51.9 (CH_2), 40.6 (CH_2), 37.1 (CH_2), 29.7 (CH_2), 27.5 (CH_2), 26.4 (CH_2); **HRMS (ESI)**: calculated 331.1765 for $C_{17}H_{23}O_3N_4$; found 331.1748 $[M+H]^+$; **HPLC**: t_R 2.7 min (254 nm).

3-[2-[(Carboxymethyl)amino]-2-oxoethyl]-1-(2-pyridinylmethyl)-1*H*-imidazolium 33

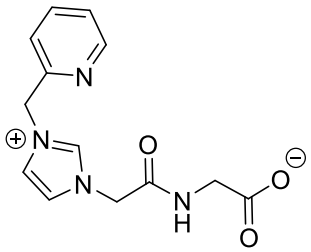

33

Purity by HPLC: 91 %; **Yield**: 57 %; **^{1}H NMR** (600 MHz, Methanol-d_4): δ 9.19 – 9.13 (m, 1H), 8.58 (ddd, J = 4.9, 1.8, 0.9 Hz, 1H), 7.89 (td, J = 7.7, 1.8 Hz, 1H), 7.69 (t, J = 1.9 Hz, 1H), 7.64 (t, J = 1.8 Hz, 1H), 7.51 (d, J = 7.8 Hz, 1H), 7.42 (ddd, J = 7.7, 4.9, 1.1 Hz, 1H), 5.57 (s, 2H), 5.10 (s, 2H), 3.94 (s, 2H); **^{13}C NMR** (151 MHz, Methanol-d_4): δ 179.9 (C), 169.8 (C), 154.2 (C), 151.0 (CH), 139.5 (CH), 139.2 (CH), 125.3 (CH), 125.2 (CH), 124.1 (CH), 123.8 (CH), 54.9 (CH_2), 51.9 (CH_2), 42.6 (CH_2); **HRMS (ESI)** calculated 276.1217 for $C_{13}H_{15}O_3N_4$; found 276.1209 $[M+H]^+$; **HPLC** t_R 0.7 min (254 nm).

3-[2-[(3-Carboxypropyl)amino]-2-oxoethyl]-1-(2-pyridinylmethyl)- 1*H*-imidazolium formate 34

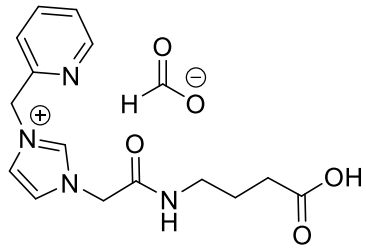

34

Purity by HPLC: 94 %; **Yield**: 62 %; **^{1}H NMR** (500 MHz, Methanol-d_4): δ 8.60 – 8.54 (m, 1H), 7.89 (td, J = 7.7, 1.7 Hz, 1H), 7.68 (d, J = 1.8 Hz, 1H), 7.63 (d, J = 1.7 Hz, 1H), 7.51 (d, J = 7.8 Hz, 1H), 7.42 (dd, J = 7.3, 5.1 Hz, 1H), 5.57 (s, 2H), 5.02 (s, 2H), 3.28 (d, J = 6.8 Hz, 2H), 2.29 (t, J = 7.3 Hz, 2H), 1.83 (m, 2H); **^{13}C NMR** (126 MHz, Methanol-d_4): δ 179.4 (C), 169.5 (C), 154.2 (C), 151.0 (CH), 139.2 (CH), 125.3 (CH), 125.1 (CH), 124.2 (CH), 123.9 (CH), 54.9 (CH_2), 51.9 (CH_2), 40.7 (CH_2), 34.3 (CH_2), 26.2 (CH_2); **HRMS** (ESI) calculated 303.1452 for $C_{15}H_{19}O_3N_4$; found 303.1445 $[M+H]^+$; **HPLC** t_R 0.8 min (254 nm).

3-[2-[(7-Carboxyheptyl)amino]-2-oxoethyl]-1-(2-pyridinylmethyl)-1*H*-imidazolium formate 35

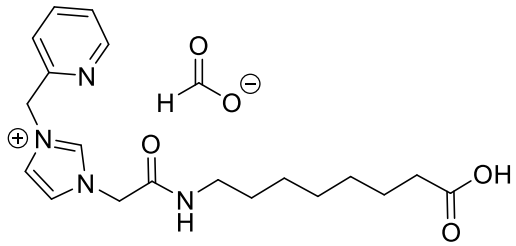

35

Purity by HPLC: 96 %; **Yield**: 46 %; **^{1}H NMR** (500 MHz, Methanol-d_4): δ 8.57 (d, J = 4.2 Hz, 1H), 7.89 (td, J = 7.7, 1.7 Hz, 1H), 7.69 (d, J = 2.0 Hz, 1H), 7.62 (d, J = 2.0 Hz, 1H), 7.51 (d, J = 7.8 Hz, 1H), 7.45 – 7.38 (m, 1H), 5.58 (s, 2H), 5.03 (s, 2H), 3.25 (t, J = 6.9 Hz, 2H), 2.23 (t, J = 7.4 Hz, 2H), 1.65 – 1.57 (m, 2H), 1.57 – 1.50 (m, 2H), 1.40 – 1.30 (m, 6H); **^{13}C NMR** (126 MHz, Methanol-d_4): δ 179.9 (C), 169.8 (C), 154.3 (C), 151.1 (CH), 139.2 (CH), 125.3 (CH), 125.1 (CH), 124.1 (CH), 123.9 (CH), 54.9 (CH_2), 52.0 (CH_2), 40.8 (CH_2), 36.7 (CH_2), 30.2 (CH_2), 30.1 (CH_2), 29.9 (CH_2), 27.6 (CH_2), 26.6 (CH_2); **HRMS** (ESI) calculated 359.2078 for $C_{19}H_{27}O_3N_4$; found 359.2078 $[M+H]^+$; **HPLC** t_R 3.5 min (254 nm).

3-[2-[(Carboxyisopropyl)amino]-2-oxoethyl]-1-(2-pyridinylmethyl)-1*H*-imidazolium formate 36

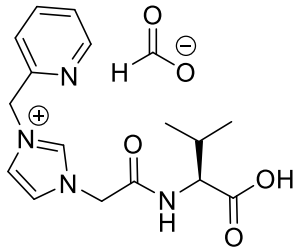

36

Purity by HPLC: 92 %; **Yield**: 51 %; **^{1}H NMR** (500 MHz, Methanol-d_4): δ 8.57 (1H, d, J = 5.0 Hz), 7.92 – 7.85 (1H, m), 7.67 (1H, d, J = 1.6 Hz), 7.63 (1H, d, J = 1.5 Hz), 7.50 (1H, d, J = 7.7 Hz), 7.44 – 7.38 (1H, m), 5.56 (2H, s), 5.15 – 5.04 (2H, m), 4.25 (1H, d, J = 4.7 Hz), 2.31 – 2.21 (1H, m), 0.96 (6H, dd, J = 7.3, 1.2 Hz); **^{13}C NMR** (126 MHz, Methanol-d_4): δ 177.7 (C), 169.2 (C), 154.3 (C), 151.0 (CH), 139.2 (CH), 125.3 (CH), 125.1 (CH), 124.1 (CH), 123.7 (CH), 61.7 (CH), 54.9 (CH_2), 52.1 (CH_2), 32.0 (CH), 20.1 (CH_3), 18.0 (CH_3); **HRMS** (ESI) calculated 318.1686 for $C_{16}H_{22}O_3N_4$; found 318.1686 $[M+H]^+$; **HPLC** t_R 2.7 min (254 nm).

***N*-[2-[1-(2-Pyridinylmethyl)-1*H*-imidazolium-3-yl]acetyl]-L-phenylalanine formate 37**

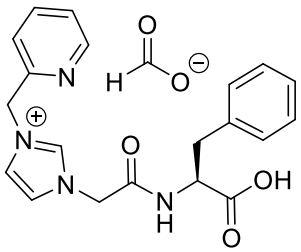

37

Purity by HPLC: 93 %; **Yield**: 36 %; **^{1}H NMR** (500 MHz, Methanol-d_4): δ 8.60 – 8.53 (1H, m), 7.88 (1H, td, J = 7.7, 1.8 Hz), 7.63 (1H, d, J = 2.0 Hz), 7.51 – 7.46 (2H, m), 7.41 (1H, dd, J = 7.6, 4.9 Hz), 7.28 – 7.21 (4H, m), 7.20 – 7.12 (1H, m), 5.54 (2H, s), 4.99 (1H, d, J = 16.2 Hz), 4.88 (1H, d, J = 16.4 Hz), 4.55 (1H, dd, J = 9.3, 4.3 Hz), 3.29 – 3.27 (1H, m), 2.92 (1H , dd, J = 14.0, 9.3 Hz); **^{13}C NMR** (126 MHz, Methanol-d_4): δ 177.6 (C), 169.1 (C), 154.2 (C),

151.0 (CH), 139.7 (CH), 138.0 (C) 130.4 (CH), 129.2 (CH × 2), 127.4 (CH × 2), 125.3 (CH), 124.9 (CH), 124.1 (CH), 123.7 (CH), 57.8 (CH), 54.9 (CH_2), 52.1 (CH_2), 39.3 (CH_2); **HRMS** (ESI) calculated 366.1686 for $C_{20}H_{22}O_3N_4$; found 366.1669 $[M+H]^+$; **HPLC** t_R 3.6 min (254 nm).

***N*-[2-[1-(2-Pyridinylmethyl)-1*H*-imidazolium-3-yl]acetyl]-L-lysine 38**

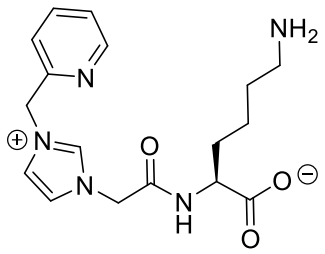

38

Purity by HPLC: 93 %; **Yield**: 32 %; **^{1}H NMR** (500 MHz, Methanol-d_4): δ 9.18 – 9.15 (1H, m), 8.60 – 8.55 (1H, m), 7.89 (1H, td, J = 7.7, 1.8 Hz), 7.70 (1H, t, J = 1.8 Hz), 7.63 (1H, t, J = 1.8 Hz), 7.53 – 7.50 (1H, m), 7.43 – 7.40 (1H, m), 5.58 (2H, s), 5.12 (2H, s), 4.46 – 4.39 (1H, m), 2.93 (2H, t, J = 7.7 Hz), 2.01 – 1.90 (1H, m), 1.80 (1H, dt, J = 13.5, 7.5 Hz), 1.74 – 1.65 (2H, m), 1.58 – 1.47 (2H, m); **^{13}C NMR** (126 MHz, Methanol-d_4): δ 175.0 (C), 166.8 (C), 154.2 (C), 151.0 (CH), 139.6 (CH), 139.2 (CH), 125.3 (CH), 125.1 (CH), 124.2 (CH), 123.9 (CH), 54.9 (CH_2), 54.0 (CH), 51.8 (CH_2), 40.4 (CH_2), 32.2 (CH_2), 28.0 (CH_2), 23.8 (CH_2); **HRMS** (ESI) calculated 346.1873 for $C_{17}H_{24}O_3N_5$; found 346.1858 $[M+H]^+$; **HPLC** 0.6 min (254 nm).

***N*-[2-[1-(2-Ppyridinylmethyl)-1*H*-imidazolium-3-yl]acetyl]-L-phenylalanyl-L-tryptophan-5-carboxypentylic acid 39**

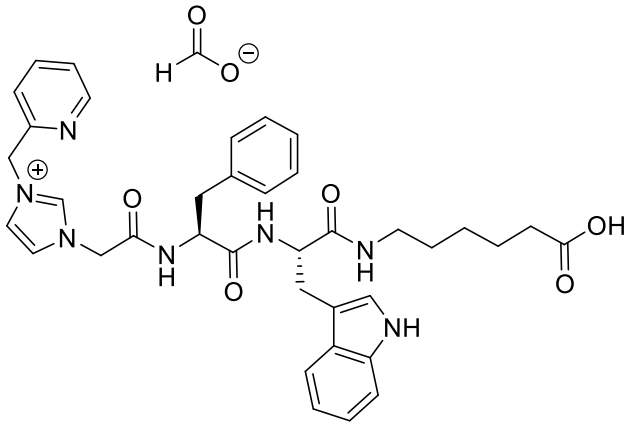

39

Purity by HPLC: 96 %; **Yield**: 37 %; **^{1}H NMR** (500 MHz, Methanol-d_4): δ 8.56 – 8.54 (1H, m), 7.86 (1H, td, J = 7.7, 1.8 Hz), 7.65 (1H, d, J = 2.0 Hz), 7.55 (1H, d, J = 7.9 Hz), 7.49 (1H, d, J = 7.8 Hz), 7.40 (1H, d, J = 2.0 Hz), 7.40 – 7.37 (1H, m), 7.35 – 7.32 (1H, m), 7.28 – 7.16 (5H, m), 7.11 – 7.05 (2H, m), 7.04 – 6.99 (1H, m), 5.54 (2H, s), 4.92 (2H, d, J = 3.7 Hz), 4.62 (1H, dd, J = 9.1, 5.5 Hz), 4.57 (1H, t, J = 7.1 Hz), 3.21 – 3.15 (1H, m), 3.15 – 3.10 (2H, m), 3.08 – 3.03 (1H, m), 3.00 – 2.95 (1H, m), 2.88 (1H, dd, J = 14.0, 9.2 Hz), 2.15 (2H, t, J = 7.4 Hz), 1.49 (2H, p, J = 7.5 Hz), 1.31 – 1.20 (2H, m), 1.14 – 1.05 (2H, m); **^{13}C NMR** (126 MHz, Methanol-d_4): δ 180.5 (C), 173.2 (C), 172.7 (C), 169.9 (C), 154.1 (C), 151.1 (CH), 139.2 (CH), 138.0 (CH), 138.0 (C), 130.3 (CH × 2), 129.6 (CH × 2), 128.8 (C), 127.9 (CH), 125.3 (CH), 124.9 (CH), 124.7 (CH), 124.1 (C), 123.8 (CH), 122.5 (CH), 119.8 (CH), 119.4 (CH), 112.4 (CH), 110.7 (C), 56.7 (CH), 55.9 (CH), 54.9 (CH_2), 51.4 (CH_2), 40.3 (CH_2), 38.6 (CH_2), 37.1 (CH_2), 29.7 (CH_2), 29.1 (CH_2), 27.5 (CH_2), 26.5 (CH_2); **HRMS** (ESI) calculated 665.3310 for $C_{37}H_{43}O_5N_7$; found 665.3320 $[M+H]^+$; **HPLC** t_R 4.4 min (254 nm).

***N*-[2-[1-(2-Pyridinylmethyl)-1*H*-imidazolium-3-yl]acetyl]-L-phenylalanyl-L-valine-L-glycine amide 40**

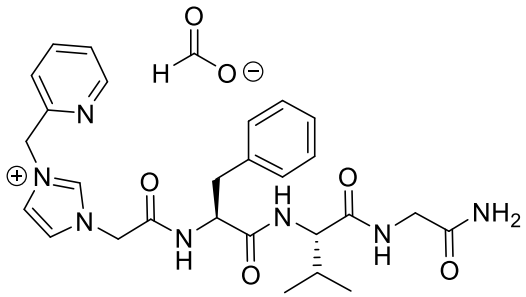

40

Purity by HPLC: 95 %; **Yield**: 75 %; **^{1}H NMR** (500 MHz, Methanol-d_4): δ 9.10 (1H, t, J = 1.6 Hz), 8.61 (1H, ddd, J = 4.9, 1.8, 1.0 Hz), 8.27 (1H, d, J = 7.7 Hz), 7.93 (1H, td, J = 7.7, 1.8 Hz), 7.70 (1H, t, J = 1.8 Hz), 7.53 (1H, t, J = 1.8 Hz), 7.46 (1H, ddd, J = 7.7, 4.9, 1.1 Hz), 7.34–7.30 (4H, m), 7.27 (1H, dd, J = 4.8, 3.8 Hz), 5.59 (2H, s), 5.08 (1H, d, J = 16.5 Hz), 5.01 (1H, d, J = 16.6 Hz), 4.77 (1H, dd, J = 9.4, 5.4 Hz), 4.20 (1H, d, J = 2.4 Hz), 3.95 (1H, dd, J = 16.9, 5.2 Hz), 3.79 (1H, dd, J = 16.9, 5.3 Hz), 3.24 (1H, dd, J = 14.0, 5.4 Hz), 2.96 (1H, dd, J = 14.0, 9.4 Hz), 2.15–2.10 (1H, m), 1.00 (3H, d, J = 1.8 Hz), 0.98 (3H, d, J = 1.8 Hz); **^{13}C NMR** (126 MHz, Methanol-d_4): δ 210.0 (C), 173.9 (C), 173.8 (C), 166.7 (C), 154.2 (C), 151.0 (CH), 139.4 (CH), 139.2 (CH), 138.1 (C), 130.3 (CH × 2), 129.6 (CH × 2), 127.9 (CH), 125.3 (CH), 125.1 (CH), 124.2 (CH), 123.9 (CH), 60.9 (CH), 56.5 (CH_2), 55.0 (CH), 51.8 (CH_2),

43.1 (CH_2), 38.9 (CH_2), 31.7 (CH), 19.7 (CH_3), 18.8 (CH_3); **HRMS** (ESI) calculated 520.2667 for $C_{27}H_{34}O_4N_7$; found 520.2673 $[M+H]^+$; **HPLC**; t_R 3.3 min (254 nm).

***N*-[2-[1-(2-Pyridinylmethyl)-1*H*-imidazolium-3-yl]acetyl]-L-valine-(5-carboxypentyl)-L-lysine(azide) amide 41**

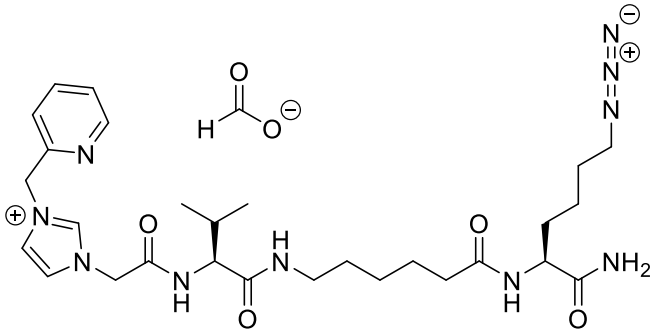

41

Purity by HPLC: 95 %; **Yield**: 60 %; **^{1}H NMR** (500 MHz, Methanol-d_4): δ 8.57 (1H, dt, J = 4.7, 1.6 Hz), 7.89 (1H, td, J = 7.7, 1.7 Hz), 7.69 (1H, d, J = 2.0 Hz), 7.62 (1H, d, J = 2.1 Hz), 7.51 (1H, dt, J = 7.8, 1.2 Hz), 7.42 (1H, ddd, J = 7.7, 4.9, 1.1 Hz), 5.57 (2H, s), 5.11 (2H, s), 4.32 (1H, dd, J = 9.0, 5.2 Hz), 4.13 (1H, d, J = 7.1 Hz), 3.30 – 3.27 (2H, m), 3.19 (2H, td, J = 6.9, 3.0 Hz), 2.25 (2H, t, J = 7.4 Hz), 2.07 (1H, h, J = 6.5 Hz), 1.85 – 1.77 (1H, m), 1.71 – 1.57 (5H, m), 1.55 – 1.40 (4H, m), 1.39 – 1.31 (2H, m), 0.98 (6H, t, J = 6.4 Hz); **^{13}C NMR** (126 MHz, MeOD): δ 177.1 (C), 176.1 (C), 173.1 (C), 166.8 (C), 154.2 (C), 151.1 (CH), 139.2 (CH), 125.3 (CH), 125.1 (CH), 124.2 (CH), 123.9 (CH), 60.9 (CH), 54.9 (CH_2), 54.2 (CH), 52.3 (CH_2), 51.9 (CH_2), 40.2 (CH_2), 36.6 (CH_2), 32.8 (CH_2), 32.0 (CH), 30.0 (CH_2), 29.5 (CH_2), 27.5 (CH_2), 26.5 (CH_2), 24.2 (CH_2), 19.7 (CH_3), 18.7 (CH_3); **HRMS** ESI-MS calculated 583.3463 for $C_{28}H_{43}O_4N_{10}$; found 583.3483 $[M+H]^+$; **HPLC**; t_R 2.6 min (254 nm).

***N*-[2-[1-(2-Pyridinylmethyl)-1*H*-imidazolium-3-yl]acetyl]-L-valine-(5-carboxypentyl)-L-glutamaic acid amide 42**

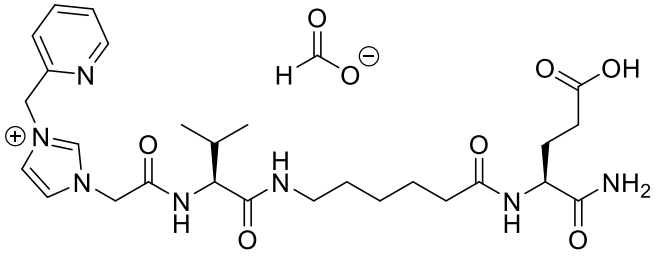

42

Purity by HPLC: 93 %; **Yield**: 61 %; **^{1}H NMR** (500 MHz, Methanol-d_4) δ 8.60 (1H, dt, J = 4.7, 1.3 Hz), 7.92 (1H, td, J = 7.7, 1.8 Hz), 7.72 (1H, d, J = 2.0 Hz), 7.66 (1H, d, J = 2.0 Hz), 7.55 (1H, dt, J = 7.8, 0.9 Hz), 7.45 (1H, ddd, J = 7.7, 4.9, 1.1 Hz), 5.61 (2H, s), 5.18 (1H, d, J = 16.4 Hz), 5.14 (1H, d, J = 16.5 Hz), 4.36 (1H, dd, J = 9.4, 4.8 Hz), 4.18 (1H, d, J = 7.0 Hz), 3.31 – 3.26 (1H, m), 3.19 – 3.13 (1H, m), 2.41 – 2.35 (2H, m), 2.27 (2H, t, J = 7.2 Hz), 2.16 – 2.07 (2H, m), 1.98 – 1.88 (1H, m), 1.65 (2H, p, J = 7.3 Hz), 1.58 – 1.51 (2H, m), 1.42 – 1.33 (2H, m), 1.01 (6H, dd, J = 6.8, 5.2 Hz); **^{13}C NMR** (126 MHz, MeOD) δ 184.6 (C), 176.9 (C), 175.5 (C), 173.2 (C), 166.9 (C), 154.3 (C), 151.1 (CH), 139.2 (CH), 125.3 (CH), 125.2 (CH), 124.2 (CH), 123.8 (CH), 61.0 (CH), 55.0 (CH_2), 54.2 (CH), 51.9 (CH_2), 40.2 (CH_2), 36.6 (CH_2), 31.9 (CH_2), 30.7 (CH_2), 29.9 (CH), 28.9 (CH_3), 27.3 (CH_2), 26.4 (CH_2), 19.7 (CH_3), 18.7 (CH_3); **HRMS** ESI-MS calculated 558.3035 for $C_{27}H_{40}O_6N_7$; found 558.3042 $[M+H]^+$; **HPLC**; t_R 1.8 min (254 nm).

***N*-[2-[1-(2-Pyridinylmethyl)-1*H*-imidazolium-3-yl]acetyl]-L-valine-(5-carboxypentyl)-L-lysine amide 43**

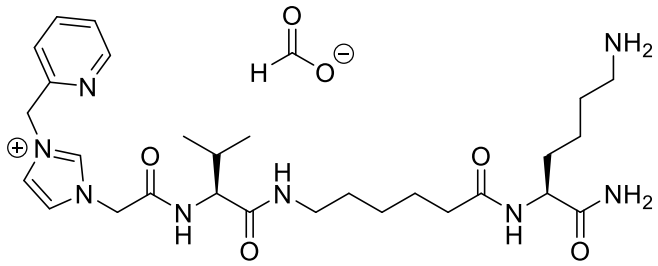

43

Purity by HPLC: 91 %; **Yield**: 66 %; **^{1}H NMR** (500 MHz, Methanol-d_4): δ 8.60 (1H, dt, J = 4.9, 1.4 Hz), 7.92 (1H, td, J = 7.7, 1.8 Hz), 7.72 (1H, d, J = 2.1 Hz), 7.65 (1H, d, J = 2.0 Hz), 7.54 (1H, dd, J = 7.8, 1.2 Hz), 7.45 (1H, ddd, J = 7.7, 4.9, 1.2 Hz), 5.60 (2H, s), 5.15 (2H, d, J = 2.8 Hz), 4.36 (1H, dd, J = 8.8, 5.5 Hz), 4.17 (1H, d, J = 7.0 Hz), 3.25 (1H, dt, J = 13.8, 7.0 Hz), 3.18 (1H, dt, J = 13.6, 7.0 Hz), 2.98 – 2.92 (2H, m), 2.28 (2H, t, J = 7.3 Hz), 2.11 (1H, h, J = 6.9 Hz), 1.93 – 1.81 (1H, m), 1.78 – 1.58 (5H, m), 1.57 – 1.43 (4H, m), 1.43 – 1.34 (2H, m), 0.98 (2H, d, J = 5.7 Hz) 0.97 (2H, d, J = 5.7 Hz); **^{13}C NMR** (126 MHz, MeOD): δ 176.9 (C), 176.1 (C), 173.1 (C), 166.8 (C), 154.2 (C), 151.1 (CH), 139.2 (CH), 125.3 (CH), 125.1 (CH), 124.2 (CH), 123.9 (CH), 60.92 (CH), 54.9 (CH_2), 54.0 (CH), 51.9 (CH_2), 40.51 (CH_2), 40.23 (CH_2), 36.64 (CH_2), 32.59 (CH_2), 32.00 (CH_2), 30.04 (CH), 28.17 (CH_2), 27.58 (CH_2), 26.43 (CH_2), 23.86 (CH_2), 19.69 (CH_3), 18.63 (CH_3); **HRMS** ESI-MS calculated 557.3558 for $C_{28}H_{45}O_4N_8$; found 557.3555 $[M+H]^+$; **HPLC**; t_R 0.7 min (254 nm).

5.3.3 Palladium catalysts

The following Section describes the characterisation of the palladium catalysts synthesised. The catalysts were synthesised using the procedure outlined in Section 5.2. As in section 5.3.2., the purity by HPLC was analysed by ELS and 254 nm detection. The ELS confirmed the presence of no impurities such as salts or other non-UV absorbing molecules. The 254 nm detection confirm the product and its purity was calculated by the comparing the integral of the product peak against the integral of all other peaks observed. All HRMS data was acquired in positive mode and products are referenced as $[M+H]^+$. For some compounds $[M+Na]^+$ was also observed though has not be quoted.

All the catalysts have been presented with an unspecified ligand "Y". The identity of Y has been speculated in both chapters 2 and 3 and is likely to be one of the following: H_2O, ACN, Cl^-, Br^-, Formate anion, TFA anion. These originate from the additives and solvent systems used during synthesis and purification and in PBS from biological studies. "Y" could also be a moiety from the same compound, for example the carboxylic acid or amine group that bends round to interact or from another molecule of the same compound. Mass spectrometry analysis sometimes showed the appearance of dimers though this data is anecdotal and was not found consistently for each molecule. Furthermore, none of these ligands were observed in the HRMS spectra.

These catalysts were not analysed by NMR due to the palladium caused a broadening of the spectrum making it difficult to identify individual peaks. Thus, the structure of the Pd centre is yet to be confirmed. Ideally X-ray crystallography would be the best way to determine the structure and confirm that it is the oxygen atom from the amide bond coordinating and not the nitrogen (NMR confirmation of the presence of an enol would also support this if possible). However, yields of the compound during this this were not significant enough to begin the process of attempting crystallisation. Other form of spectroscopy such as UV or IR might also provide information about the nature of the bonding within the molecule (anecdotally it is known that the Pd-loaded catalysts absorb more at 282 nm). ICP is useful for determining the presence and levels of palladium, however this gives no structure insights. Revisiting the mass spectrometry and different techniques available there and designing experiments to probe the ligand structure may be one of the best initial routes.

Some of these structures have been published with equivalent amounts of data, however this does not prevent the accumulation of more data where possible. Much more data is need about

the structure of the Pd as in all the papers in which the structure has been published, none make an attempt to confirm it with structural techniques.

3-[2-[(5-Carboxypentyl)amino]-2-oxoethyl]-1-(2-pyridinylmethyl)-1*H*-imidazol-2-ydiene palladium(II) 10

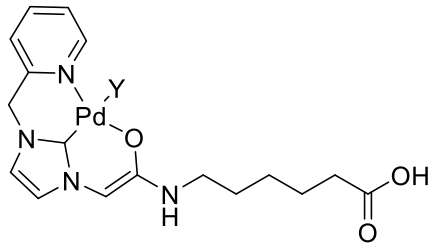

10

Synthesised from **8**. The product was isolated as a white solid (14 mg, 32.2 µmol, 11 %).

Purity by HPLC: 94 %; **HRMS (ESI)** calculated 435.0629 for $C_{17}H_{21}O_3N_4{}^{106}Pd$; found 435.0640 $[M+H]^+$; **HPLC** t_R 2.1 min (254 nm).

3-[2-[(Carboxymethyl)amino]-2-oxoethyl]-1-(2-pyridinylmethyl)-1*H*-imidazol-2-ydiene palladium(II) 11

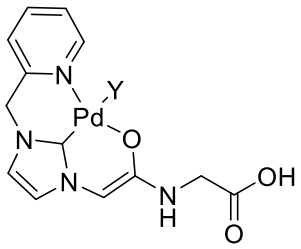

11

Synthesised from **33**. The product was isolated as a white solid (9 mg, 23.7 µmol, 8 %).

Purity by HPLC: 94 %; **HRMS (ESI**) calculated 379.0017 for $C_{13}H_{13}O_3N_4{}^{106}Pd$; found 379.0025 $[M+H]^+$; **HPLC** t_R 2.0 min (254 nm).

3-[2-[(3-Carboxypropyl)amino]-2-oxoethyl]-1-(2-pyridinylmethyl)- 1*H*-imidazol-2-ydiene palladium(II) 12

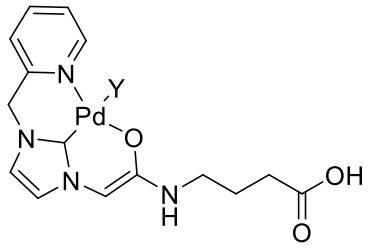

12

Synthesised from **34**. The product was isolated as a white solid (10 mg, 24.6 µmol, 8 %).

Purity by HPLC: 90 %; **HRMS** (ESI) calculated 407.0323 for $C_{15}H_{17}O_3N_4{}^{106}Pd$; found 407.0332 $[M+H]^+$; **HPLC** t_R 1.8 min (254 nm).

3-[2-[(7-Carboxyheptyl)amino]-2-oxoethyl]-1-(2-pyridinylmethyl)-1*H*-imidazol-2-ydiene palladium(II) 13

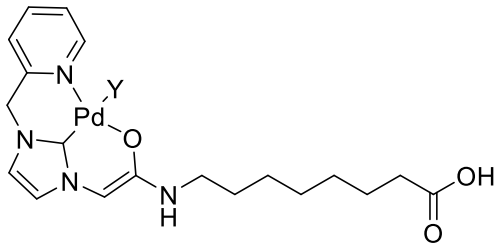

13

Synthesised from **35**. The product was isolated as a white solid (13 mg, 28.0 µmol, 9 %).

Purity by HPLC: 82 %; **HRMS** (ESI) calculated 463.0956 for $C_{19}H_{25}O_3N_4{}^{106}Pd$; found; 463.0963 $[M+H]^+$; **HPLC** t_R 2.6 min (254 nm).

3-[2-[(Carboxyisopropyl)amino]-2-oxoethyl]-1-(2-pyridinylmethyl)-1*H*-imidazol-2-ydiene palladium(II) 14

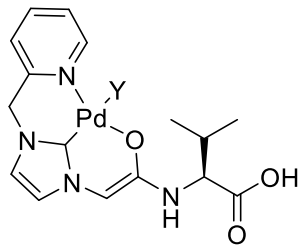

14

Synthesised from **36**. The product was isolated as a white solid (17 mg, 40.4 μmol, 13 %).

Purity by HPLC: 93 %; **HRMS** (ESI) calculated 421.0486 for $C_{16}H_{19}O_3N_4{}^{106}Pd$; found 421.0491; $[M+H]^+$ **HPLC** t_R 2.4 min (254 nm).

***N*-[2-[1-(2-Pyridinylmethyl)-1*H*-imidazol-2-ysiene-3-yl]acetyl]-L-phenylalaine palladium(II) 15**

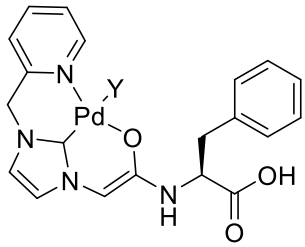

15

Synthesised from **37**. The product was isolated as a white solid (15 mg, 32.0 μmol, 11 %).

Purity by HPLC: 94 %; **HRMS** (ESI) calculated 469.0486 for $C_{20}H_{19}O_3N_4{}^{106}Pd$; found 469.0488 $[M+H]^+$; **HPLC** t_R 2.9 min (254 nm).

***N*-[2-[1-(2-Pyridinylmethyl)-1*H*-imidazol-2-ydiene-3-yl]acetyl]-L-lysine palladium(II) 16**

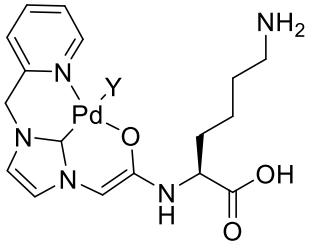

16

Synthesised from **38**. The product was isolated as a white solid (10 mg, 22.2 µmol, 7 %).

Purity by HPLC: 95 %; **HRMS** (ESI) calculated 450.0752 for $C_{17}H_{22}O_3N_5{}^{106}Pd$; found 450.0750 $[M+H]^+$; **HPLC** t_R 1.1 min (254 nm).

***N*-[2-[1-(2-Pyridinylmethyl)-1*H*-imidazol-2-ydiene-3-yl]acetyl]-L-phenylalanyl-L-tryptophan-5-carboxypentylic acid palladium(II) 17**

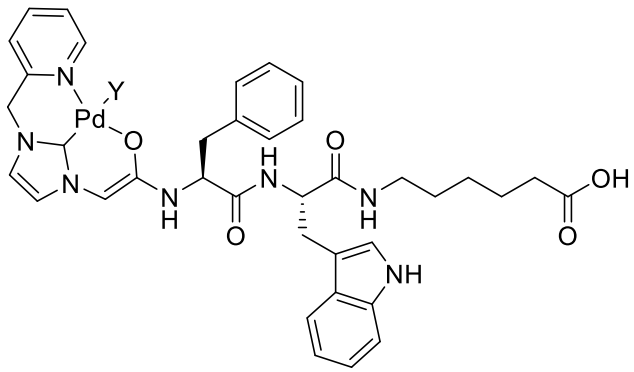

17

Synthesised from **39**. The product was isolated as a white solid (21 mg, 27.3 µmol, 7 %).

Purity by HPLC: 96 %; **HRMS** (ESI) calculated 768.2120 for $C_{37}H_{40}O_5N_7{}^{106}Pd$; found; 768.2136 $[M+H]^+$; **HPLC** t_R 3.5 min (254 nm).

***N*-[2-[1-(2-Pyridinylmethyl)-1*H*-imidazol-2-ydiene-3-yl]acetyl]-L-phenylalanyl-L-valine-L-glycine palladium(II) 18**

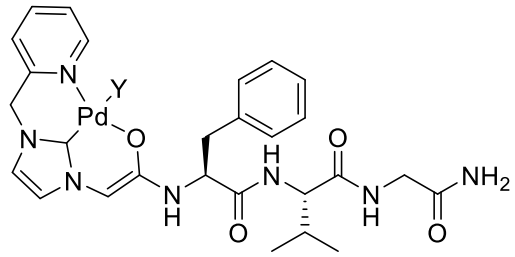

18

Synthesised from **40**. The product was isolated as a white solid (18 mg, 28.0 µmol, 14 %).

Purity: 96 %; **HRMS** ESI-MS calculated 624.1545 for $C_{27}H_{32}O_4N_7{}^{106}Pd$; found 624.1556 $[M+H]^+$; **HPLC**; t_R 3.5 min (254 nm).

***N*-[2-[1-(2-Pyridinylmethyl)-1*H*-imidazol-2-ydiene-3-yl]acetyl]-L-valine-(5-carboxypentyl)-L-lysine(azide) amide palladium(II) 19**

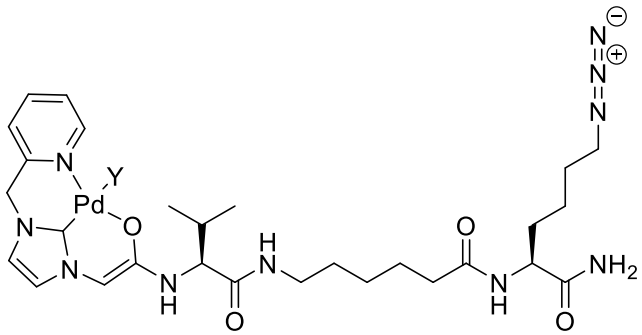

19

Synthesised from **41**. The product was isolated as a white solid (25 mg, 36.4 µmol, 18 %).

Purity by HPLC: 95 %; **HRMS** ESI-MS calculated 687.2342 for $C_{28}H_{41}O_4N_{10}{}^{106}Pd$; found 687.2384 $[M+H]^+$; **HPLC**; t_R 3.0 min (254 nm).

***N*-[2-[1-(2-Pyridinylmethyl)-1*H*-imidazol-2-ydiene-3-yl]acetyl]-L-valine-(5-carboxypentyl)-L-glutamaic acid amide palladium(II) 20**

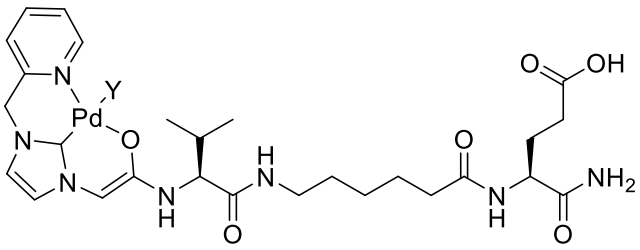

20

Synthesised from **42**. The product was isolated as a white solid (29 mg, 42.8 µmol, 22 %).

Purity by HPLC: 97 %; **HRMS** ESI-MS calculated 662.1913 for $C_{27}H_{38}O_6N_7{}^{106}Pd$; found 662.1932 $[M+H]^+$; **HPLC**; t_R 2.6 min (254 nm).

***N*-[2-[1-(2-Pyridinylmethyl)-1*H*-imidazol-2-ydiene-3-yl]acetyl]-L-valine-(5-carboxypentyl)-L-lysine amide palladium(II) 21**

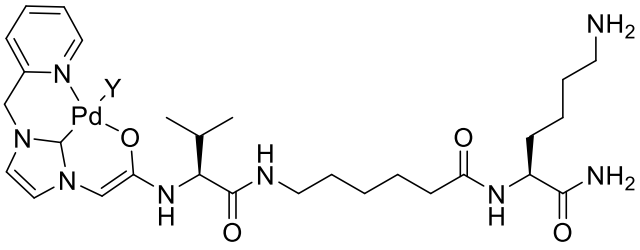

21

Synthesised from **43**. The product was isolated as a white solid 18 mg (27.2 µmol, 13 %).

Purity by HPLC: 96 %; **HRMS** ESI-MS calculated 661.2437 for $C_{28}H_{43}O_4N_8{}^{106}Pd$; found 661.2469 $[M+H]^+$; **HPLC**; t_R 2.4 min (254 nm).

5.4 Protein conjugation experiments

Analysis by absorbance measurements

The degree of labelling for protein-fluorophore conjugates was calculated using the equations described in Chapter 3 (repeated below). In all cases a dilution factor of 10 was used, and the correction factor for fluorescein was 0.3. The wavelength for A_{max} was 492 nm. ε vales for BSA, Herceptin and fluorescein were 43,824 cm^{-1} M^{-1} (AAT bioquest), 210,000 cm^{-1} M^{-1} (Thermofisher tech tip #31), 68,000 cm^{-1} M^{-1} (Thermofisher tech tip #31) respectively.

$$(3.1)\ Protein\ concentration\ (M) = \frac{A_{280} - (A_{max} \times CF)}{\varepsilon} \times dilution\ factor$$

Equation 3.1. Equation used to calculate the protein concentration after conjugation with a fluorophore. Where A_{280} is the absorbance at 280 nm of the protein-fluorophore conjugate. A_{max} is the absorbance value at the maximum absorbance wavelength of the fluorophore (for example FAM = 492 nm). CF is the correction factor (correcting for the absorbance of the fluorophore at 280 nm). ε is the molar extinction coefficient of the protein and the dilution factor is any dilution applied to the sample.

$$(3.2)\ Moles\ of\ dye\ per\ mole\ of\ protein = \frac{A_{max}\ of\ the\ labelled\ protein}{\varepsilon' \times protein\ concentration\ [M]} \times dilution\ factor$$

Equation 3.2. Equation to calculate the degree of labelling from using equation 3.1. "A_{max} of the labelled protein" is the absorbance value at the maximum absorbance wavelength of the fluorophore; ε' is the molar extinction coefficient of the fluorophore; protein concentration [M] is found from Equation 3.1.; Dilution factor is any dilution that may have been applied to the sample.

Analysis of proteins by SDS-PAGE

Protein samples (1 mg/ml, 10 µl) were diluted with 2 × sample buffer (10 µl) and heated to 95 °C for 5 min. The samples were then loaded into a precast 10 % poly acrylamide gel and run at 80 V (30 min) followed by 160 V (90 min). The gel was submerged in Coomassie staining solution (~100 mL) for 4 h and then de-stained for 24 h (de-staining solution (100 mL) replaced every 6 h). The gel was then viewed under white light in a GelDoc imaging system and analysed on Image Lab software.

Analysis by MALDI-TOF MS

The spectra of protein conjugate products were compared to native Herceptin. 2,5-Dihydroxybenzoic acid was used a matrix and the machine calibrated to native Herceptin. The

MADLI-TOF was analysed in positive mode. The difference in mass between the highest intensity peaks was determined and then divided by the molecular weight of the molecule added to get a degree of labelling by MALDI-TOF MS.

Analysis by ICP-MS

For ICP-MS analysis (Pd content), Pd-antibody conjugates (1 µl) was added to concentrated nitric acid (75 µL). The resulting solution was diluted to 5 % HNO_3 with water (1.5 mL), and Pd analysis was carried out by ICP-MS with calibration against Pd standard solutions (n = 3). The Pd content per antibody was quantified using the two equations below.

$$(5.1)\ \frac{[ppm]}{molecular\ mass\ of\ palladium} \times sample\ volume = mole\ of\ Pd\ per\ sample$$

$$(5.2)\ (Antibody\ concentration \times sample\ volume) = mass\ of\ Antibody\ per\ sample$$

$$(5.3)\ \frac{Equation\ 5.1}{Equation\ 5.2} = mole\ Pd\ per\ mass\ of\ antibody$$

Sample calculation using data for compound **30a**

$$\frac{(4.22\ [\frac{mg}{L}] \times 1.5\ mL)}{106.42\ [\frac{g}{mol}]}\ x\ 1000 = 59.7\ nmol\ of\ Pd\ per\ sample$$

$$2.21\ [\frac{mg}{ml}] \times 1.5\ mL = 3.32\ mg\ of\ Antibody$$

$$\frac{119.4\ nmol}{6.63\ mg} = 18.6\ nmol\ of\ Pd/mg\ of Antibody$$

Alternatively, the Pd content can be calculated by as follows:

$$(5.1)\ \frac{[ppm]}{molecular\ mass\ of\ palladium} = concentration\ of\ Pd\ per\ sample$$

$$(5.4)\ \frac{Antibody\ [\frac{mg}{mL}]}{Molecular\ mass\ of\ Antibody\ [\frac{g}{mol}]}$$

$$(5.5)\ \frac{Equation\ 5.1}{Equation\ 5.4}$$

Sample calculation using data for compound **30a**

$$\frac{4.22\ [\frac{mg}{mL}]}{106.42\ [\frac{g}{mol}]} = 39.8\ \mu M\ of\ Pd$$

$$\frac{2.21\ [\frac{mg}{mL}]}{145000\ [\frac{g}{mol}]} = 15.2\ \mu M\ of\ antibody$$

$$\frac{39.8\ [\mu M]}{15.2\ [\mu M]} = 2.6\ mol\ of\ Pd\ per\ mol\ of\ antibody$$

5(6)-Carboxyfluorescein BSA 25a

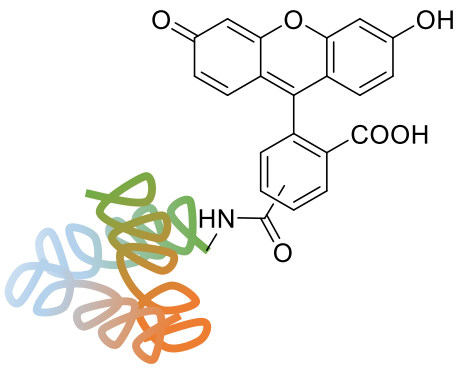

25a

BSA (5 mg) was dissolved in PBS (250 µL, pH 7.0) and a solution of 5(6)-carboxyfluorescein-NHS (11 µL, 10 mg/mL) was added. The solution was shaken at 37 °C for 4 h in an Eppendorf ThermoMixer®. The solution was diluted in PBS (200 µL) and purified using Amicon centrifugal spin columns (0.5 mL, MWCO 10 kDa) using a Thermo Scientific Heraeus Pico 17 benchtop centrifuge (13200 rpm, 10 min) and washed with PBS (10 × 0.5 mL) to elute unreacted carboxyfluorescein-NHS. The concentrated protein solution (50 µL) was collected in an Eppendorf tube by centrifugation (1 min, 13200 rpm).

SDS-PAGE: Broad band at 66,000 Da; **MALDI-TOF MS**: Intensity max at 66,600 Da; **Absorbance**: 0.94 at 280 nm, 1.42 at 492 nm; **Degree of labelling**: 1.8 moles of fluorophore per mole of BSA.

5(6)-Carboxyfluorescein BSA 25b

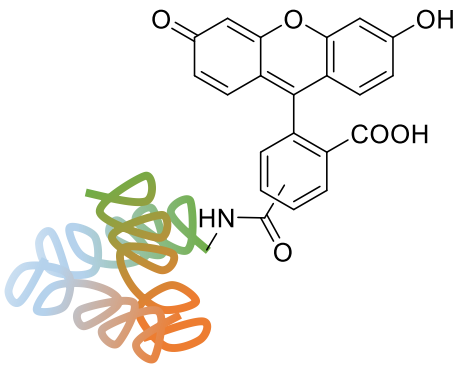

25b

25b was synthesised using the same methodology as **25a** except using pH 8.0.

SDS-PAGE: Broad band at 67,000 Da; **MALDI-TOF MS**: Intensity max at 67,200 Da; **Absorbance**: 0.87 at 280 nm, 1.87 at 492 nm; **Degree of labelling**: 3.9 moles of fluorophore per mole of BSA.

BSA-dibenzocyclooctyne 26

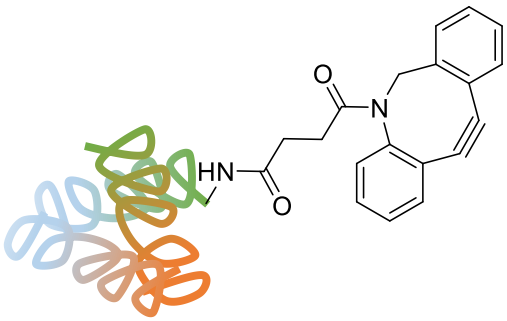

26

BSA (5 mg) was dissolved in PBS (250 µL, pH 7.0) and a solution of DBCO-NHS dissolved in DMSO (30.8 µL, 5 mg/mL) was added. The solution was shaken at 37 °C for 4 h in an Eppendorf ThermoMixer®. The solution was diluted in PBS (200 µL) and purified with Amicon centrifugal spin columns (0.5 mL, MWCO 10 kDa) using a Thermo Scientific Heraeus Pico 17 benchtop centrifuge (13200 rpm, 10 min) and washed with PBS (10 × 0.5 mL) to elute unreacted DBCO-NHS. The concentrated protein solution (50 µL) was collected in an Eppendorf tube by centrifugation (1 min, 13200 rpm).

SDS-PAGE: Band at 67,000 Da; **MALDI-TOF MS**: Intensity max at 67,200 Da; **Degree of labelling**: 4 moles of DBCO per mole of BSA.

BSA-dibenzocyclooctyne-fluorescein azide 27

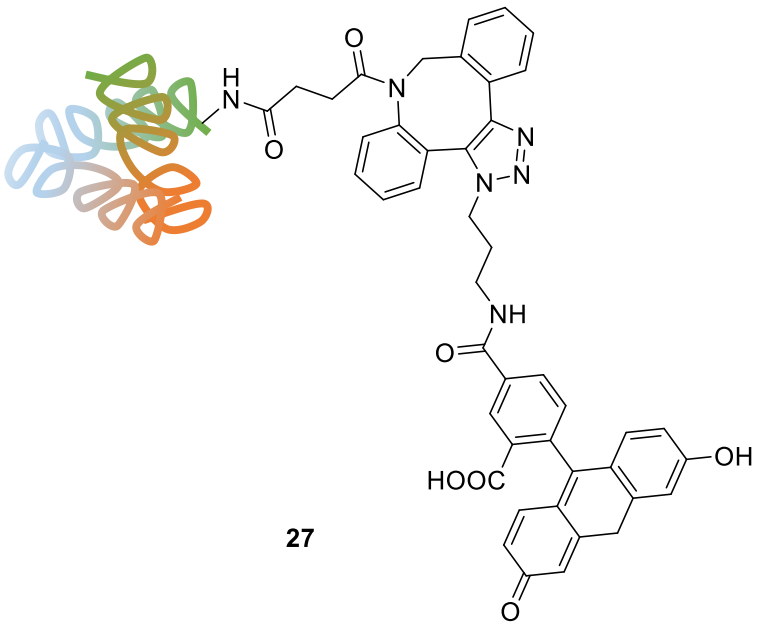

27

To **26** (45 µL, 20 mg/mL) a solution of 5-carboxyfluorescein-azide dissolved in PBS (169 µL, 1 mg/mL) was added. The solution was shaken at 37 °C for 4 h in an Eppendorf ThermoMixer®. The solution was diluted in PBS (200 µL) and purified using Amicon centrifugal spin columns (0.5 mL, MWCO 10 kDa) using a Thermo Scientific Heraeus Pico 17 benchtop centrifuge (13200 rpm, 10 min) and washed with PBS (10 × 0.5 mL) to elute unreacted 5-carboxyfluorescein azide. The concentrated protein solution (50 µL) was collected in an Eppendorf tube by centrifugation (1 min, 13200 rpm).

SDS-PAGE: Broad band at 66,000 Da; **MALDI-TOF MS**: Intensity max at 68,400 Da; **Absorbance**: 0.8 at 280 nm, 1.51 at 492 nm; **Degree of labelling**: 2.8 moles of fluorophore per mole of BSA.

Herceptin-dibenzocyclooctyne, *low loading* **28a**

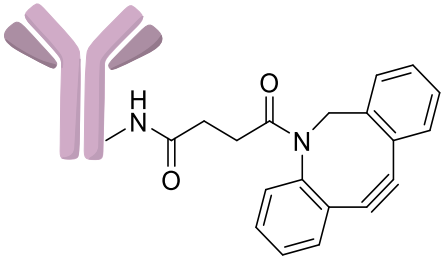

28a

To Herceptin (50 µL, 20 mg/mL), PBS (150 µL) was added. To this a solution of DBCO-NHS dissolved in DMSO (2.79 µL, 5 mg/mL, 5 eq.) was added. The solution was shaken at 37 °C for 4 h in an Eppendorf ThermoMixer®. The solution was diluted in PBS (200 µL) and purified using Amicon centrifugal spin columns (0.5 mL, MWCO 10 kDa) using a Thermo Scientific Heraeus Pico 17 benchtop centrifuge (13200 rpm, 10 min) and washed with PBS (10 × 0.5 mL) to elute unreacted DBCO-NHS. The concentrated protein solution (50 µL) was collected in an Eppendorf by centrifugation (1 min, 13200 rpm).

SDS-PAGE: Bands at 25,000 and 50,000 Da; **MALDI-TOF MS**: Intensity max at 146,000 Da; **Degree of labelling**: 2.8 moles of DBCO per mole of Herceptin.

Herceptin-dibenzocyclooctyne-5-carboxyfluorescein 29

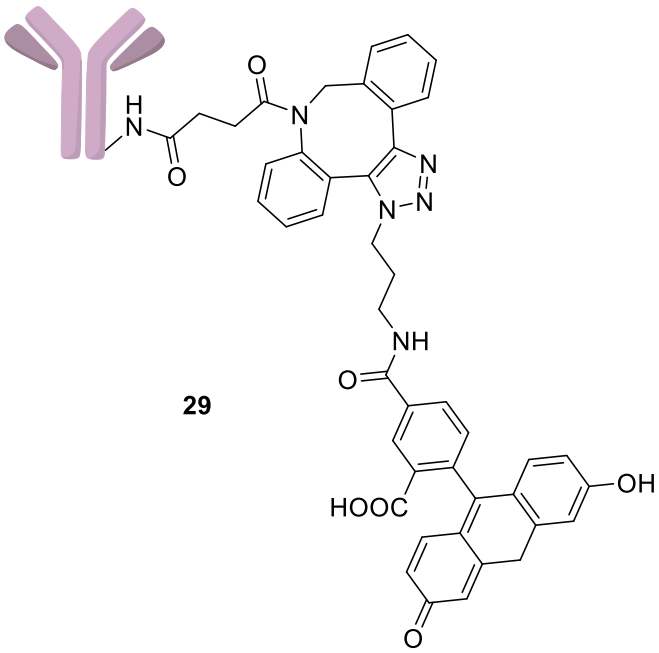

29

To **28a** (45 µL, 20 mg/mL), a solution of 5-carboxyfluorescein-azide (15.8 µL, 1 mg/mL, 5 eq.) was added. The solution was shaken at 37 °C for 4 h in an Eppendorf ThermoMixer® C. The solution was diluted in PBS (200 µL) and purified using Amicon centrifugal spin columns (0.5 mL, MWCO 10 kDa) using a Thermo Scientific Heraeus Pico 17 benchtop centrifuge (13200 rpm, 10 min) and washed with PBS (10 × 0.5 mL) to elute unreacted DBCO-NHS. The concentrated protein solution (50 µL) was collected in an Eppendorf by centrifugation (1 min, 13200 rpm).

SDS-PAGE: Bands at 25,000 and 50,000 Da; **MALDI-TOF MS**: Intensity max at 147,000 Da; **Absorbance**: 1.41 at 280 nm, 0.97 at 492 nm; **Degree of labelling**: 2.8 moles of fluorophore per mole of Herceptin.

Herceptin-dibenzocyclooctyne-19 30a

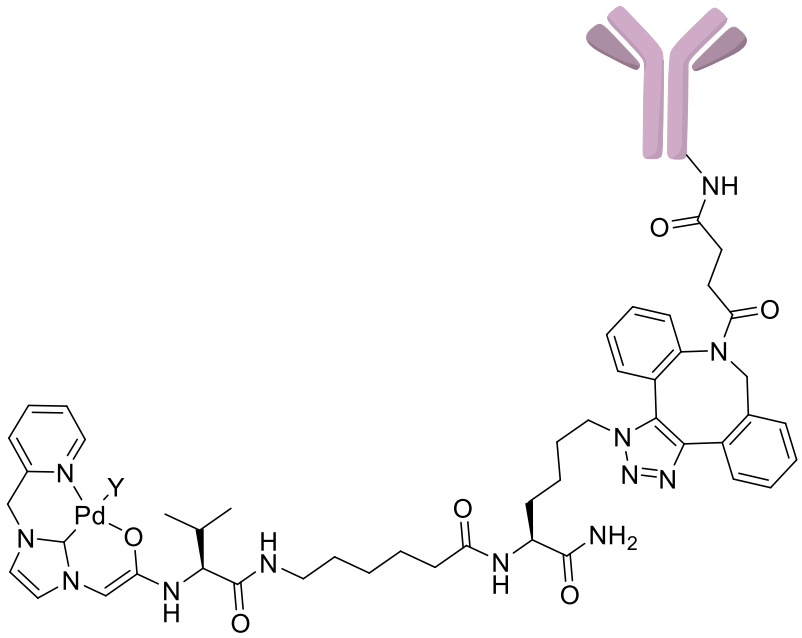

30a

To **28a** (45 µL, 20 mg/mL), a solution of **19** (3.45 µL,10 mM) was added. The solution was shaken at 37 °C for 4 h at 1000 rpm in an Eppendorf ThermoMixer®. The solution was diluted in PBS (200 µL) and purified using Amicon centrifugal spin columns (0.5 mL, MWCO 10 kDa) using a Thermo Scientific Heraeus Pico 17 benchtop centrifuge (13200 rpm, 10 min) and washed with PBS (10 × 0.5 mL) to elute unreacted **19**. The concentrated protein solution (50 µL) was collected in an Eppendorf by centrifugation (1 min, 13200 rpm).

SDS-PAGE: Bands at 25,000 and 50,000 Da; **MALDI-TOF MS**: Intensity max at 148,000 Da; **ICP-MS**: 4.22 ppm (15.2 µM); **Degree of labelling**: 2.7 moles of Palladium per mole of Herceptin.

Herceptin-dibenzocyclooctyne, *high loading* (**28b**)

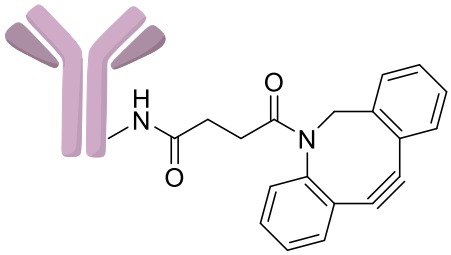

28b

For **28b** the reaction was repeated using the same conditions as those used to make **28a** but with a larger quantity of DBCO-NHS dissolved in DMSO (154 µL, 5 mg/mL, 25 eq.).

SDS-PAGE: Bands at 25,000 and 50,000 Da; **MALDI-TOF MS**: Intensity max at 148,000 Da; **Degree of labelling**: 10 moles of DBCO per mole of Herceptin.

Herceptin-dibenzocyclooctyne-19 30b

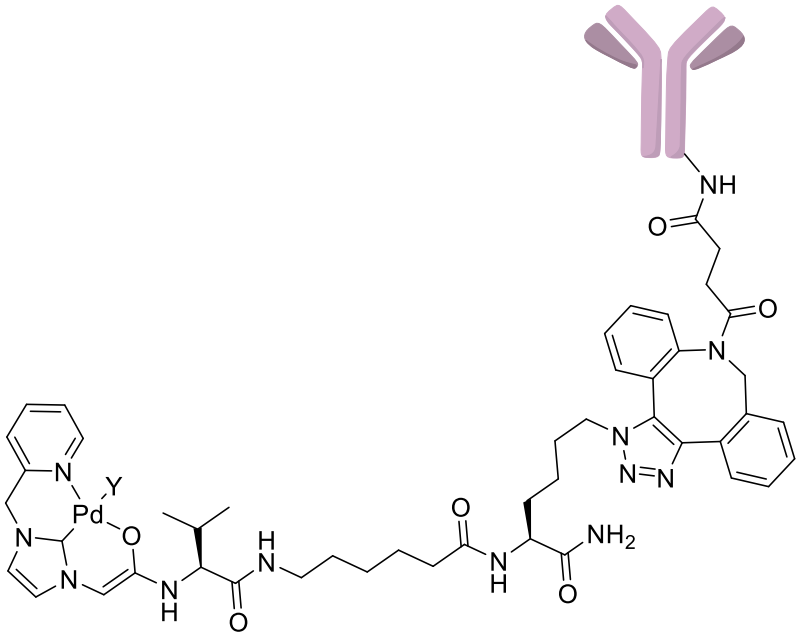

30b

For **30b** the rection was repeated using the same conditions as compound **30a** except using **28b** as a starting molecule and higher quantities of **19** (17.3 µL, 10 mM).

SDS-PAGE: Bands at 25,000 and 50,000 Da; **MALDI-TOF MS**: Intensity max at 155,000 Da; **ICP-MS**: 5.91 ppm (55.7 µM); **Degree of labelling**: 10 moles of Palladium per mole of Herceptin.

Herceptin-(Peg)$_{12}$-dibenzyocyclooctyne 31a

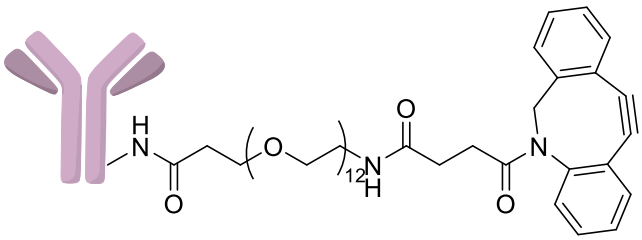

31a

To Herceptin (50 µL, 20 mg/mL), PBS (150 µL) was added. To this a solution of DBCO-(Peg)$_{12}$-NHS dissolved in PBS (3.4 µL, 10 mg/mL) was added.

SDS-PAGE: Bands at 25,000 and 50,000 Da; **MALDI-TOF MS**: Intensity max at 147,000 Da; **Degree of labelling**: 2 moles of DBCO-PEG$_{12}$ per mole of Herceptin.

Herceptin-(Peg)$_{12}$-dibenzyocyclooctyne 31b

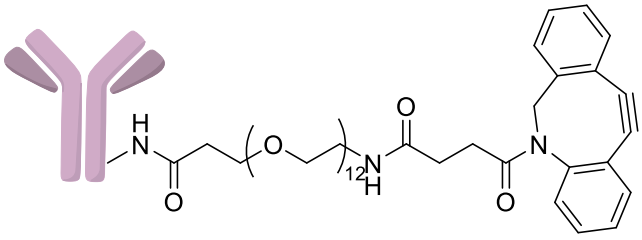

31b

31b was synthesised using the same protocol as **31a** except using a larger amount of DBCO-(Peg)$_{12}$-NHS (17 µL, 10 mg/mL).

SDS-PAGE: Bands at 25,000 and 50,000 Da; **MALDI-TOF MS**: Intensity max at 154,000 Da; **Degree of labelling**: 9 moles of DBCO-PEG$_{12}$ per mole of Herceptin.

Herceptin-(Peg)$_{12}$-dibenzocyclooctyne-19 32a

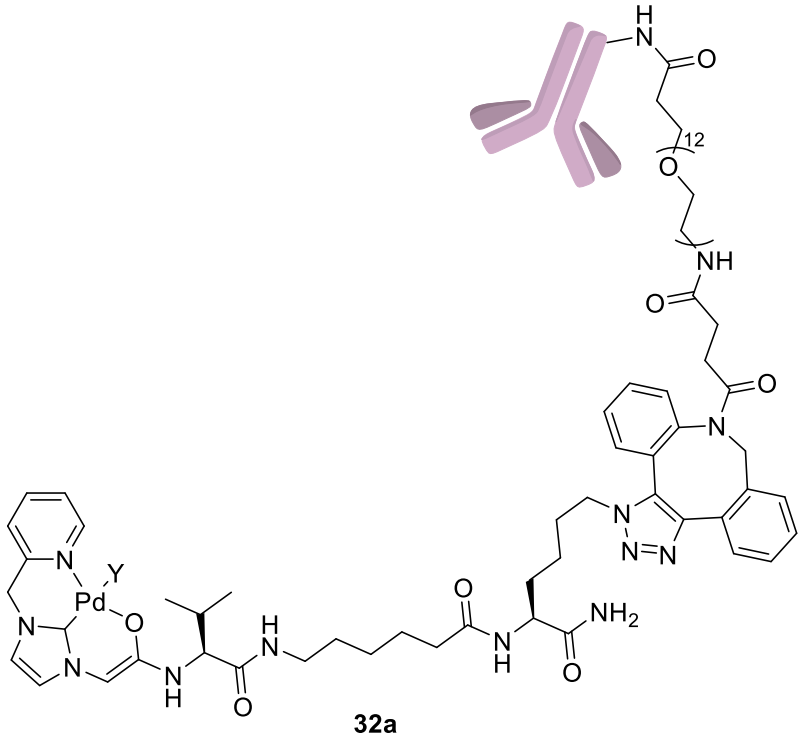

32a

To **31a** (45 µL, 20 mg/mL), a solution of **19** (3.45 µL,10 mM) was added. The solution was shaken at 37 °C for 4 h at 1000 rpm in an Eppendorf ThermoMixer®. The solution was diluted in PBS (200 µL) and purified using Amicon centrifugal spin columns (0.5 mL, MWCO 10 kDa) using a Thermo Scientific Heraeus Pico 17 benchtop centrifuge (13200 rpm, 10 min) and washed with PBS (10 × 0.5 mL) to elute unreacted **19**. The concentrated protein solution (50 µL) was collected in an Eppendorf by centrifugation (1 min, 13200 rpm).

SDS-PAGE: Bands at 25,000 and 50,000 Da; **MALDI-TOF MS**: Intensity max at 148,000 Da; **ICP-MS**: 1.02 ppm (9.6 µM); **Degree of labelling**: 2 moles of Palladium per mole of Herceptin.

Herceptin-(Peg)$_{12}$-dibenzocyclooctyne-19 32b

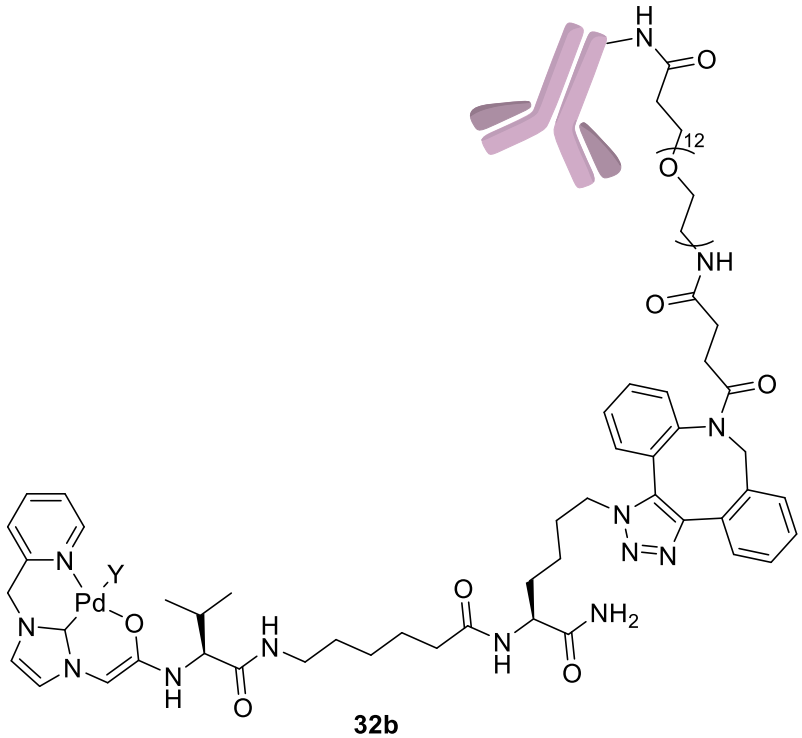

32b

32b was synthesised using the same protocol as use to synthesis **32a** except starting using **31b** as a starting molecule with a larger amount of **19** (17.3 µL,10 mM).

SDS-PAGE: Bands at 25,000 and 50,000 Da; **MALDI-TOF MS**: Intensity max at 165,000 Da; **ICP-MS**: 4.61 ppm (35.5 µM); **Degree of labelling**: 10 moles of Palladium per mole of Herceptin.

5.5 Biological experiments

Kinetic assays of fluorophore activation

Catalyst screening: Stock solutions (20 µM) of the probe dichlorofluorescein were prepared in 5 % acetonitrile with either PBS or plasma. The catalyst solutions were freshly prepared either in PBS or in plasma. The screenings were carried out on black 96-well plates. 50 µL of the probe **Pro-DCF** or **PROC-Rh 110** (to give a working concentration of 10 µM) was added per well, followed by 50 µL of the catalyst solution (0.8 mol %) and the increase in fluorescence (λex/em = 485/520 nm) at 37 °C recorded over time (4 h or 12 h) on a plate reader (n = 3). The relative increase in fluorescence was compared with the blank and the control experiment (PBS or plasma).

Stability of catalysts

Catalysts **8**, **9** and **12** (~1 mg/mL) were stored in H_2O/ACN (9:1) at 4 °C for 2 months. Following this, the samples were analysed by analytical HPLC.

Cell culture

HeLa, SK BR-3 or MCF-7 cells were cultured in Dulbecco's modified Eagle medium (DMEM) supplemented with 10 % fetal bovine serum (FBS), L-glutamine (4 mM) and antibiotics (penicillin and streptomycin, 100 units/mL). Cell culture was performed in a 5 % CO_2 atmosphere at 37 °C in 1377 Experimental a SteriCult 200 (Hucoa-Erloss) incubator. The day before the assays, the cells were washed with PBS, detached with trypsin/ethylenediaminetetraacetic acid (EDTA) (0.25 % trypsin, 1 mM EDTA), counted, and diluted with DMEM to the appropriate concentration.

Prodrug activation in MCF-7 cells

carried out by Durgadas Cherukaraveedu

MCF-7 cells (from the European Collection of Authenticated Cell Cultures (ECACC)) were grown in Dulbecco's modified eagle medium (DMEM) supplemented with 10 % FBS, 1 % penicillin/streptomycin and 200 nM L-glutamine in a humidified incubator at 37 °C with 5 % CO_2. Cells were cultured in T-75 flasks (Corning) to ≥ 80 % confluence. Cells were harvested with trypsin/EDTA (Gibco.) The MCF-7 cells (8×10^3 cells/well) were seeded on 96-well plates and grown to ~60 % confluence overnight. Control cells were treated with 100 µM of **5-FU** (with 1 % DMSO), 100 µM **Pro-5-FU** (with 1 % DMSO), and 10 µM and 50 µM of catalyst **8**. The cells for prodrug activation were treated first with 100 µM of **Pro-5-FU** for 1

day and followed by addition of 10 mol % (Pd) of catalyst **8**, and the cells were incubated for 4 days under standard cell culture conditions. The cells were washed with PBS, followed by the addition of 100 µL of 3-(4,5-dimethylthiazol-2-yl)-2,5-diphenyltetrazolium bromide (MTT) solution (1 mg/mL in PBS/DMEM, 3:7, v/v) for 3 h at 37 °C. Then, 100 µL of MTT solubilisation solution (10 % Triton-X 100 in 0.1 N HCI in isopropanol) was added to each well and the plate was shaken horizontally for 30 min to dissolve the formazan crystals. The absorbance at 570 nm was measured on a multimode plate reader and the cell viability was calculated compared to untreated cells and expressed as percentage of cell viability.

Prodrug activation in MCF-7 spheroids

carried out by Durgadas Cherukaraveedu

MCF-7 cells (ECACC) were added into black 96-well Corning Ultra low attachment surface coated microplates (~2000 cells/well) to generate the multicellular spheroids. The media was changed daily until spheroids formed (approximately 750 µm diameter). The spheroids were treated with 100 µM of **Pro-5-FU** and 10 mol % of the catalyst **8** on the well plate, and incubated for 4 days. The control spheroids were treated with catalyst **8** (10 mol %), or **5-FU** (100 µM) or **Pro-5-FU** (100 µM). The spheroids were washed thoroughly with PBS and stained for cell viability with the LIVE/DEAD™ Cell Imaging Kit (488/570) according to manufacturer's instructions and imaged with a confocal microscope.

Cell viability assay

HeLa cells were plated in a 96-well plate (10000 cells/well) and grown for 24 h. Solutions of **19**, **20**, **21** and **PROC-Rh 110** in DMEM were added to the wells at the desired concentrations and incubated with the cells for 24 h. Media was then replaced with 350 µL 3-(4,5-dimethylthiazol-2-yl)-2,5-diphenyltetrazolium bromide (MTT) solution (1 mg/mL) and the cells incubated for 3 h at 37 °C. After incubation, the resulting formazan crystals were dissolved by adding 350 µL of MTT solubilisation solution (10 % Triton-X 100 in 0.1 N HCl in isopropanol). The absorbance was measured at a wavelength of 570 nm (BioTek HT Synergy multi-mode reader) and results compared to a control of untreated cells which were normalised to 100 %.

Flow cytometry

For flow cytometry analysis, SKBR-3 and MCF-7 cells were plated in a 24-wellplate (20000 cells/well) and grown for 24 h at 37 °C. The medium was removed and a solution of **30a** (at appropriate concentrations) in DMEM was added and incubated for 18 h at 37 °C. After

incubation, cells were washed twice with PBS, harvested with trypsin/EDTA (0.25 % trypsin, 1 mM EDTA) and resuspended in DMEM. Intracellular fluorescence was analysed by flow cytometry (Becton Dickinson (BD) FACSAriaTM). A total of 10,000 events were analysed per sample.

Chapter 6 References

1 F. Bray, J. Ferlay, I. Soerjomataram, R. L. Siegel, L. A. Torre and A. Jemal, *CA. Cancer J. Clin.*, 2018, **68**, 394–424.

2 J. Ferlay, I. Soerjomataram, R. Dikshit, S. Eser, C. Mathers, M. Rebelo, D. M. Parkin, D. Forman and F. Bray, *Int. J. Cancer*, 2015, **136**, E359–E386.

3 S. Tsim, C. A. O'Dowd, R. Milroy and S. Davidson, *Respir. Med.*, 2010, **104**, 1767–1774.

4 S. A. Kenfield, E. K. Wei, M. J. Stampfer, B. A. Rosner and G. A. Colditz, *Tob. Control*, 2008, **17**, 198–204.

5 J. M. Samet, E. Avila-Tang, P. Boffetta, L. M. Hannan, S. Olivo-Marston, M. J. Thun and C. M. Rudin, *Clin. Cancer Res.*, 2009, **15**, 5626–5645.

6 M. P. Revel, M. F. Carette, M. Torrent and J. Trédaniel, *Diagn. Interv. Imaging*, 2014, **95**, 727–738.

7 V. Raman, C. F. J. Yang, J. Z. Deng and T. A. D'Amico, *J. Thorac. Dis.*, 2018, **10**, S898–S904.

8 R. Pirker, *Transl. Lung Cancer Res.*, 2014, **3**, 305–310.

9 C. Weinstock, S. Khozin, D. Suzman, L. Zhang, S. Tang, S. Wahby, K. B. Goldberg, G. Kim and R. Pazdur, *Clin. Cancer Res.*, 2017, **23**, 4534–4539.

10 A. Hessenbruch, *Endeavour*, 2002, **26**, 137–141.

11 S. Khondee and T. D. Wang, *J. Healthc. Eng.*, 2013, **4**, 1–22.

12 H. Lusic and M. W. Grinstaff, *Chem. Rev.*, 2013, **113**, 1641–1666.

13 F. Nieto, J. J. Millán, G. G. Parreira, H. Chiarini-Garcia and R. C. N. Melo, *Handb. Phys. Med. Biol.*, 2010, 40-1-40–16.

14 Y. Sone, A. Sobajima, T. Kawachi, S. Kohara, K. Kato and S. Naganawa, *Br. J. Radiol.*, 2014, **87**, 1–7.

15 L. Schrevens, *Oncologist*, 2004, **9**, 633–643.

16 G. M. Van Dam, G. Themelis, L. M. A. Crane, N. J. Harlaar, R. G. Pleijhuis, W. Kelder, A. Sarantopoulos, J. S. De Jong, H. J. G. Arts, A. G. J. Van Der Zee, J. Bart, P. S. Low and V. Ntziachristos, *Nat. Med.*, 2011, **17**, 1315–1319.

17 J. D. Predina, A. D. Newton, C. Connolly, A. Dunbar, M. Baldassari, C. Deshpande, E. Cantu, J. Stadanlick, S. A. Kularatne, P. S. Low and S. Singhal, *Mol. Ther.*, 2018, **26**, 390–403.

18 J. D. Predina, A. D. Newton, J. Keating, A. Dunbar, C. Connolly, M. Baldassari, J. Mizelle, L. Xia, C. Deshpande, J. Kucharczuk, P. S. Low and S. Singhal, *Ann. Thorac. Surg.*, 2018, **105**, 901–908.

19 J. Burggraaf, I. M. C. Kamerling, P. B. Gordon, L. Schrier, M. L. De Kam, A. J. Kales, R. Bendiksen, B. Indrevoll, R. M. Bjerke, S. A. Moestue, S. Yazdanfar, A. M. J. Langers, M. Swaerd-Nordmo, G. Torheim, M. V. Warren, H. Morreau, P. W. Voorneveld, T. Buckle, F. W. B. Van Leeuwen, L. I. Ødegårdstuen, G. T. Dalsgaard, A. Healey and J. C. H. Hardwick, *Nat. Med.*, 2015, **21**, 955–961.

20 H. Kobayashi, M. Ogawa, R. Alford, P. L. Choyke and Y. Urano, *Chem. Rev.*, 2010, **110**, 2620–2640.

21 M. Staderini, A. Megia-Fernandez, K. Dhaliwal and M. Bradley, *Bioorganic Med. Chem.*, 2018, **26**, 2816–2826.

22 G. Shay, C. C. Lynch and B. Fingleton, *Matrix Biol.*, 2015, **44**–**46**, 200–206.

23 K. Kessenbrock, V. Plaks and Z. Werb, *Cell*, 2010, **141**, 52–67.

24 J. L. Crisp, E. N. Savariar, H. L. Glasgow, L. G. Ellies, M. A. Whitney and R. Y. Tsien, *Mol. Cancer Ther.*, 2014, **13**, 1514–1525.

25 B. A. Chabner and T. G. Roberts, *Nat. Rev. Cancer*, 2005, **5**, 65–72.

26 D. Hanahan and R. A. Weinberg, *Cell*, 2011, **144**, 646–674.

27 A. M. Florea and D. Büsselberg, *Cancers (Basel).*, 2011, **3**, 1351–1371.

28 J. Rautio, H. Kumpulainen, T. Heimbach, R. Oliyai, D. Oh, T. Järvinen and J.

Savolainen, *Nat. Rev. Drug Discov.*, 2008, **7**, 255–270.

29 M. Miwa, M. Ura, M. Nishida, N. Sawada, T. Ishikawa, K. Mori, N. Shimma, I. Umeda and H. Ishitsuka, *Eur. J. Cancer*, 1998, **34**, 1274–1281.

30 N. Curado, G. Dewaele-Le Roi, S. Poty, J. S. Lewis and M. Contel, *Chem. Commun.*, 2019, **55**, 1394–1397.

31 M. F. bin Othman, E. Verger, I. Costa, M. Tanapirakgul, M. S. Cooper, C. Imberti, V. J. Lewington, P. J. Blower and S. Y. A. Terry, *Nucl. Med. Biol.*, , DOI:10.1016/j.nucmedbio.2019.12.004.

32 E. M. Sletten and C. R. Bertozzi, *Angew. Chemie - Int. Ed.*, 2009, **48**, 6974–6998.

33 J. Li and P. R. Chen, *Nat. Chem. Biol.*, 2016, **12**, 129–137.

34 K. Lang and J. W. Chin, *ACS Chem. Biol.*, 2014, **9**, 16–20.

35 H. C. Hang, C. Yu, D. L. Kato and C. R. Bertozzi, *Proc. Natl. Acad. Sci. U. S. A.*, 2003, **100**, 14846–14851.

36 P. Thirumurugan, D. Matosiuk and K. Jozwiak, *Chem. Rev.*, 2013, **113**, 4905–4979.

37 M. F. Debets, S. S. Van Berkel, J. Dommerholt, A. J. Dirks, F. P. J. T. Rutjes and F. L. Van Delft, *Acc. Chem. Res.*, 2011, **44**, 805–815.

38 C. R. Bertozzi, *Acc. Chem. Res.*, 2011, **44**, 651–653.

39 M. L. Blackman, M. Royzen and J. M. Fox, *J. Am. Chem. Soc.*, 2008, **130**, 13518–13519.

40 J. J. Soldevila-Barreda and N. Metzler-Nolte, *Chem. Rev.*, 2019, **119**, 829–869.

41 Y. Bai, J. Chen and S. C. Zimmerman, *Chem. Soc. Rev.*, 2018, **47**, 1811–1821.

42 M. Martínez-Calvo and J. L. Mascareñas, *Coord. Chem. Rev.*, 2018, **359**, 57–79.

43 J. G. Rebelein and T. R. Ward, *Curr. Opin. Biotechnol.*, 2018, **53**, 106–114.

44 P. K. Sasmal, C. N. Streu and E. Meggers, *Chem. Commun.*, 2013, **49**, 1581–1587.

45 C. Streu and E. Meggers, *Angew. Chemie - Int. Ed.*, 2006, **45**, 5645–5648.

46 T. Völker, F. Dempwolff, P. L. Graumann and E. Meggers, *Angew. Chem. Int. Ed. Engl.*, 2014, **53**, 10536–10540.

47 M. I. Sánchez, C. Penas, M. E. Vázquez and J. L. Mascareñas, *Chem. Sci.*, 2014, **5**, 1901–1907.

48 H. T. Hsu, B. M. Trantow, R. M. Waymouth and P. A. Wender, *Bioconjug. Chem.*, 2016, **27**, 376–382.

49 M. Tomás-Gamasa, M. Martínez-Calvo, J. R. Couceiro and J. L. Mascarenãs, *Nat. Commun.*, 2016, **7**, 12538.

50 Y. Bai, X. Feng, H. Xing, Y. Xu, B. K. Kim, N. Baig, T. Zhou, A. A. Gewirth, Y. Lu, E. Oldfield and S. C. Zimmerman, *J. Am. Chem. Soc.*, 2016, **138**, 11077–11080.

51 J. Clavadetscher, S. Hoffmann, A. Lilienkampf, L. Mackay, R. M. Yusop, S. A. Rider, J. J. Mullins and M. Bradley, *Angew. Chemie - Int. Ed.*, 2016, **55**, 15662–15666.

52 A. Kumar, S. Kumar, N. Kumari, S. H. Lee, J. Han, I. J. Michael, Y. K. Cho and I. S. Lee, *ACS Catal.*, 2019, **9**, 977–990.

53 C. Vidal, M. Tomás-Gamasa, P. Destito, F. López and J. L. Mascareñas, *Nat. Commun.*, 2018, **9**, 1913.

54 K. Tsubokura, K. K. H. Vong, A. R. Pradipta, A. Ogura, S. Urano, T. Tahara, S. Nozaki, H. Onoe, Y. Nakao, R. Sibgatullina, A. Kurbangalieva, Y. Watanabe and K. Tanaka, *Angew. Chemie - Int. Ed.*, 2017, **56**, 3579–3584.

55 S. Bose, A. H. Ngo and L. H. Do, *J. Am. Chem. Soc.*, 2017, **139**, 8792–8795.

56 P. K. Sasmal, S. Carregal-Romero, A. A. Han, C. N. Streu, Z. Lin, K. Namikawa, S. L. Elliott, R. W. Köster, W. J. Parak and E. Meggers, *ChemBioChem*, 2012, **13**, 1116–1120.

57 S. V. Chankeshwara, E. Indrigo and M. Bradley, *Curr. Opin. Chem. Biol.*, 2014, **21**, 128–135.

58 J. Li and P. R. Chen, *ChemBioChem*, 2012, **13**, 1728–1731.

59 R. M. Yusop, A. Unciti-Broceta, E. M. V. Johansson, R. M. Sánchez-Martín and M. Bradley, *Nat. Chem.*, 2011, **3**, 239–243.

60 J. Li, J. Yu, J. Zhao, J. Wang, S. Zheng, S. Lin, L. Chen, M. Yang, S. Jia, X. Zhang and P. R. Chen, *Nat. Chem.*, 2014, **6**, 352–361.

61 J. Clavadetscher, E. Indrigo, S. V. Chankeshwara, A. Lilienkampf and M. Bradley, *Angew. Chemie - Int. Ed.*, 2017, **56**, 6864–6868.

62 J. T. Weiss, J. C. Dawson, K. G. Macleod, W. Rybski, C. Fraser, C. Torres-Sánchez, E. E. Patton, M. Bradley, N. O. Carragher and A. Unciti-Broceta, *Nat. Commun.*, 2014, **5**, 3277.

63 T. L. Bray, M. Salji, A. Brombin, A. M. Pérez-López, B. Rubio-Ruiz, L. C. A. Galbraith, E. E. Patton, H. Y. Leung and A. Unciti-Broceta, *Chem. Sci.*, 2018, **9**, 7354–7361.

64 M. Martínez-Calvo, J. R. Couceiro, P. Destito, J. Rodríguez, J. Mosquera and J. L. Mascareñas, *ACS Catal.*, 2018, **8**, 6055–6061.

65 E. Indrigo, J. Clavadetscher, S. V. Chankeshwara, A. Megia-Fernandez, A. Lilienkampf and M. Bradley, *Chem. Commun.*, 2017, **53**, 6712–6715.

66 M. A. Miller, B. Askevold, H. Mikula, R. H. Kohler, D. Pirovich and R. Weissleder, *Nat. Commun.*, 2017, **8**, 15906.

67 F. Wang, Y. Zhang, Z. Du, J. Ren and X. Qu, *Nat. Commun.*, 2018, **9**, 1209.

68 J. T. Weiss, J. C. Dawson, C. Fraser, W. Rybski, C. Torres-Sánchez, M. Bradley, E. E. Patton, N. O. Carragher and A. Unciti-Broceta, *J. Med. Chem.*, 2014, **57**, 5395–5404.

69 P. Destito, A. Sousa-Castillo, J. R. Couceiro, F. López, M. A. Correa-Duarte and J. L. Mascareñas, *Chem. Sci.*, 2019, **10**, 2598–2603.

70 X. Ma, H. Wang and W. Chen, *J. Org. Chem.*, 2014, **79**, 8652–8658.

71 E. Indrigo, J. Clavadetscher, S. V. Chankeshwara, A. Lilienkampf and M. Bradley,

Chem. Commun., 2016, **52**, 14212–14214.

72 A. Unciti-Broceta, F. Diezmann, C. Y. Ou-Yang, M. A. Fara and M. Bradley, *Bioorganic Med. Chem.*, 2009, **17**, 959–966.

73 K. Worm-Leonhard and M. Meldal, *European J. Org. Chem.*, 2008, 5244–5253.

74 S. E. Coelho, F. S. S. Schneider, D. C. De Oliveira, G. L. Tripodi, M. N. Eberlin, G. F. Caramori, B. De Souza and J. B. Domingos, *ACS Catal.*, , DOI:10.1021/acscatal.9b00210.

75 R. N. Zuckermann, J. M. Kerr, W. H. Moosf and S. B. H. Kent, *J. Am. Chem. Soc.*, 1992, **114**, 10646–10647.

76 T. S. Burkoth, A. T. Fafarman, D. H. Charych, M. D. Connolly and R. N. Zuckermann, *J. Am. Chem. Soc.*, 2003, **125**, 8841–8845.

77 M. Santra, S. K. Ko, I. Shin and K. H. Ahn, *Chem. Commun.*, 2010, **46**, 3964–3966.

78 J. D. Sara, J. Kaur, R. Khodadadi, M. Rehman, R. Lobo, S. Chakrabarti, J. Herrmann, A. Lerman and A. Grothey, *Ther. Adv. Med. Oncol.*, 2018, **10**, 1–18.

79 Z. Liu, X. Gao and X. Long, *ICCET 2010 - 2010 Int. Conf. Comput. Eng. Technol. Proc.*, 2010, **2**, 3–13.

80 A. M. Scott, J. D. Wolchok and L. J. Old, *Nat. Rev. Cancer*, 2012, **12**, 278–287.

81 J. M. Reichert, C. J. Rosensweig, L. B. Faden and M. C. Dewitz, *Nat. Biotechnol.*, 2005, **23**, 1073–1078.

82 T. Kubota, R. Niwa, M. Satoh, S. Akinaga, K. Shitara and N. Hanai, *Cancer Sci.*, 2009, **100**, 1566–1572.

83 J. M. Lambert and R. V. J. Chari, *J. Med. Chem.*, 2014, **57**, 6949–6964.

84 B. Pro, R. Advani, P. Brice, N. L. Bartlett, J. D. Rosenblatt, T. Illidge, J. Matous, R. Ramchandren, M. Fanale, J. M. Connors, Y. Yang, E. L. Sievers, D. A. Kennedy and A. Shustov, *J. Clin. Oncol.*, 2012, **30**, 2190–2196.

85 J. Katz, J. E. Janik and A. Younes, *Clin. Cancer Res.*, 2011, **17**, 6428–6436.

86 P. D. Senter and E. L. Sievers, *Nat. Biotechnol.*, 2012, **30**, 631–637.

87 A. Beck, L. Goetsch, C. Dumontet and N. Corvaïa, *Nat. Rev. Drug Discov.*, 2017, **16**, 315–337.

88 B. E. C. G. de Goeij and J. M. Lambert, *Curr. Opin. Immunol.*, 2016, **40**, 14–23.

89 J. M. Lambert and A. Berkenblit, *Annu. Rev. Med.*, 2018, **69**, 191–207.

90 A. Thomas, B. A. Teicher and R. Hassan, *Lancet Oncol.*, 2016, **17**, e254–e262.

91 T. V. Jerjian, A. E. Glode, L. A. Thompson and C. L. O'Bryant, *Pharmacotherapy*, 2016, **36**, 99–116.

92 R. V. J. Chari, M. L. Miller and W. C. Widdison, *Angew. Chemie - Int. Ed.*, 2014, **53**, 3796–3827.

93 H. Yao, F. Jiang, A. Lu and G. Zhang, *Int. J. Mol. Sci.*, , DOI:10.3390/ijms17020194.

94 P. Akkapeddi, S. A. Azizi, A. M. Freedy, P. M. S. D. Cal, P. M. P. Gois and G. J. L. Bernardes, *Chem. Sci.*, 2016, **7**, 2954–2963.

95 V. Chudasama, A. Maruani and S. Caddick, *Nat. Chem.*, 2016, **8**, 114–119.

96 J. R. Junutula, H. Raab, S. Clark, S. Bhakta, D. D. Leipold, S. Weir, Y. Chen, M. Simpson, S. P. Tsai, M. S. Dennis, Y. Lu, Y. G. Meng, C. Ng, J. Yang, C. C. Lee, E. Duenas, J. Gorrell, V. Katta, A. Kim, K. McDorman, K. Flagella, R. Venook, S. Ross, S. D. Spencer, W. Lee Wong, H. B. Lowman, R. Vandlen, M. X. Sliwkowski, R. H. Scheller, P. Polakis and W. Mallet, *Nat. Biotechnol.*, 2008, **26**, 925–932.

97 P. F. Bross, J. Beitz, G. Chen, X. H. Chen, E. Duffy, L. Kieffer, S. Roy, R. Sridhara, A. Rahman, G. Williams and R. Pazdur, *Clin. Cancer Res.*, 2001, **7**, 1490–1496.

98 D. C. Andersen and D. E. Reilly, *Curr. Opin. Biotechnol.*, 2004, **15**, 456–462.

99 B. Q. Shen, K. Xu, L. Liu, H. Raab, S. Bhakta, M. Kenrick, K. L. Parsons-Reponte, J. Tien, S. F. Yu, E. Mai, D. Li, J. Tibbitts, J. Baudys, O. M. Saad, S. J. Scales, P. J. McDonald, P. E. Hass, C. Eigenbrot, T. Nguyen, W. A. Solis, R. N. Fuji, K. M. Flagella, D. Patel, S. D. Spencer, L. A. Khawli, A. Ebens, W. L. Wong, R. Vandlen, S. Kaur, M. X. Sliwkowski, R. H. Scheller, P. Polakis and J. R. Junutula, *Nat.*

Biotechnol., 2012, **30**, 184–189.

100 S. D. Fontaine, R. Reid, L. Robinson, G. W. Ashley and D. V. Santi, *Bioconjug. Chem.*, 2015, **26**, 145–152.

101 R. J. Christie, R. Fleming, B. Bezabeh, R. Woods, S. Mao, J. Harper, A. Joseph, Q. Wang, Z. Q. Xu, H. Wu, C. Gao and N. Dimasi, *J. Control. Release*, 2015, **220**, 660–670.

102 J. Lu, F. Jiang, A. Lu and G. Zhang, *Int. J. Mol. Sci.*, 2016, **17**, 561.

103 G. Casi and D. Neri, *J. Control. Release*, 2012, **161**, 422–428.

104 J. R. McCombs and S. C. Owen, *AAPS J.*, 2015, **17**, 339–351.

105 R. A. Firestone, D. Willner, S. J. Hofstead, H. D. King, T. Kaneko, G. R. Braslawsky, R. S. Greenfield, P. A. Trail, S. J. Lasch, A. J. Henderson, A. M. Casazza, I. Hellström and K. E. Hellström, *J. Control. Release*, 1996, **39**, 251–259.

106 M. N. Saleh, S. Sugarman, J. Murray, J. B. Ostroff, D. Healey, D. Jones, C. R. Daniel, D. LeBherz, H. Brewer, N. Onetto and A. F. LoBuglio, *J. Clin. Oncol.*, 2000, **18**, 2282–2292.

107 A. W. Tolcher, S. Sugarman, K. A. Gelmon, R. Cohen, M. Saleh, C. Isaacs, L. Young, D. Healey, N. Onetto and W. Slichenmyer, *J. Clin. Oncol.*, 1999, **17**, 478–484.

108 V. H. J. Van Der Velden, J. G. Te Marvelde, P. G. Hoogeveen, I. D. Bernstein, A. B. Houtsmuller, M. S. Berger and J. J. M. Van Dongen, *Blood*, 2001, **97**, 3197–3204.

109 G. Wu, Y.-Z. Fang, S. Yang, J. R. Lupton and N. D. Turner, *J. Nutr.*, 2004, **134**, 489–492.

110 L. Turell, S. Carballal, H. Botti, R. Radi and B. Alvarez, *Brazilian J. Med. Biol. Res.*, 2009, **42**, 305–311.

111 G. M. Dubowchik and R. A. Firestone, *Bioorganic Med. Chem. Lett.*, 1998, **8**, 3341–3346.

112 G. M. Dubowchik, R. A. Firestone, L. Padilla, D. Willner, S. J. Hofstead, K. Mosure,

J. O. Knipe, S. J. Lasch and P. A. Trail, *Bioconjug. Chem.*, 2002, **13**, 855–869.

113 M. Lopus, E. Oroudjev, L. Wilson, S. Wilhelm, W. Widdison, R. Chari and M. A. Jordan, *Mol. Cancer Ther.*, 2010, **9**, 2689–2699.

114 R. V. J. Chari, B. A. Martell, J. L. Gross, S. B. Cook, S. A. Shah, W. A. Blättler, S. J. McKenzie and V. S. Goldmacher, *Cancer Res.*, 1992, **52**, 127–131.

115 U. Vaishampayan, M. Glode, W. Du, A. Kraft, G. Hudes, J. Wright and M. Hussain, *Clin. Cancer Res.*, 2000, **6**, 4205–4208.

116 B. F. Issell and S. T. Crooke, *Cancer Treat. Rev.*, 1978, **0**, 199–207.

117 K. S. MacMillan and D. L. Boger, *J. Med. Chem.*, 2009, **52**, 5771–5780.

118 E. J. Small, R. Figlin, D. Petrylak, D. J. Vaughn, O. Sartor, I. Horak, R. Pincus, A. Kremer and C. Bowden, *Invest. New Drugs*, 2000, **18**, 193–197.

119 M. M. C. Van Der Lee, P. G. Groothuis, R. Ubink, M. A. J. Van Der Vleuten, T. A. Van Achterberg, E. M. Loosveld, D. Damming, D. C. H. Jacobs, M. Rouwette, D. F. Egging, D. Van Den Dobbelsteen, P. H. Beusker, P. Goedings, G. F. M. Verheijden, J. M. Lemmens, M. Timmers and W. H. A. Dokter, *Mol. Cancer Ther.*, 2015, **14**, 692–703.

120 C. Saura, F. Thistlethwaite, U. Banerji, S. Lord, V. Moreno, I. MacPherson, V. Boni, C. D. Rolfo, E. G. E. de Vries, C. M. L.- Van Herpen, S. Rottey, J. J. J. Geenen, F. Eskens, M. Gil Martin, E. Mommers, N. P. Koper, R. Mulder and P. G. Aftimos, *J. Clin. Oncol.*, 2018, **36**, 1014–1014.

121 J. Thorson, E. Sievers, J. Ahlert, E. Shepard, R. Whitwam, K. Onwueme and M. Ruppen, *Curr. Pharm. Des.*, 2005, **6**, 1841–1879.

122 N. K. Damle and P. Frost, *Curr. Opin. Pharmacol.*, 2003, **3**, 386–390.

123 S. C. Alley, N. M. Okeley and P. D. Senter, *Curr. Opin. Chem. Biol.*, 2010, **14**, 529–537.

124 P. Agarwal and C. R. Bertozzi, *Bioconjug. Chem.*, 2015, **26**, 176–192.

125 S. K. Sharma and K. D. Bagshawe, *Adv. Drug Deliv. Rev.*, 2017, **118**, 2–7.

126 K. D. Bagshawe, S. K. Sharma and R. H. J. Begent, *Expert Opin. Biol. Ther.*, 2004, **4**, 1777–1789.

127 I. Niculescu-Duvaz and C. J. Springer, *Adv. Drug Deliv. Rev.*, 1997, **26**, 151–172.

128 R. F. SHERWOOD, R. G. MELTON, S. M. ALWAN and P. HUGHES, *Eur. J. Biochem.*, 1985, **148**, 447–453.

129 K. D. Bagshawe and S. K. Sharma, *Transplant. Proc.*, 1996, **28**, 3156–3158.

130 S. Panowski, S. Bhakta, H. Raab, P. Polakis and J. R. Junutula, *MAbs*, 2014, **6**, 34–45.

131 C. A. Hudis, *N. Engl. J. Med.*, 2007, **357**, 39–51.

132 T. Vu and F. X. Claret, *Front. Oncol.*, , DOI:10.3389/fonc.2012.00062.

133 H. S. Cho, K. Mason, K. X. Ramyar, A. M. Stanley, S. B. Gabelli, D. W. Denney and D. J. Leahy, *Nature*, 2003, **421**, 756–760.

134 D. J. Slamon, W. Godolphin, L. A. Jones, J. A. Holt, S. G. Wong, D. E. Keith, W. J. Levin, S. G. Stuart, J. Udove, A. Ullrich and M. F. Press, *Science (80-.).*, 1989, **244**, 707–712.

135 L. Coussens, T. L. Yang-Feng, Y. C. Liao, E. Chen, A. Gray, J. McGrath, P. H. Seeburg, T. A. Libermann, J. Schlessinger, U. Francke, A. Levinson and A. Ullrich, *Science (80-.).*, 1985, **230**, 1132–1139.

136 H. Cheng, M. Q. Xiong, C. X. Cheng, H. J. Wang, Q. Lu, H. F. Liu, F. Bin Yao, C. Chen and F. Verpoort, *Chem. - An Asian J.*, 2018, **13**, 440–448.

Chapter 7 Appendices

Publications

D. Cherukaraveedu, P. T. Cowling, G. P. Birch, M. Bradley and A. Lilienkampf, *Org Biomol Chem*, 2019, **17**, 5533-5537.

With permission from the Royal Society of Chemistry

Organic & Biomolecular Chemistry

PAPER

View Article Online
View Journal | View Issue

Check for updates

Cite this: *Org. Biomol. Chem.*, 2019, **17**, 5533

Solid-phase synthesis of biocompatible N-heterocyclic carbene–Pd catalysts using a sub-monomer approach†

Durgadas Cherukaraveedu, ‡ Paul T. Cowling, ‡ Gavin P. Birch, Mark Bradley * and Annamaria Lilienkampf *

Received 28th March 2019,
Accepted 6th May 2019

DOI: 10.1039/c9ob00716d

rsc.li/obc

Taking inspiration from the assembly of so-called peptoids (*N*-alkylglycine oligomers) we present a new synthetic methodology whereby N-heterocyclic carbene (NHC) based Pd ligands were assembled using a sub-monomer approach and loaded with Pd *via* solid-phase synthesis. This allowed the rapid generation a library of NHC–palladium catalysts that were readily functionalised to allow bioconjugation. These catalysts were able to rapidly activate a caged fluorophore and 'switch-on' an anticancer prodrug in 3D cell culture.

Open Access Article. Published on 08 May 2019. Downloaded on 5/11/2020 1:08:28 PM.
This article is licensed under a Creative Commons Attribution 3.0 Unported Licence.

Introduction

Bioorthogonal reactions enable the selective visualisation and manipulation of biological processes in living systems and have been widely used in a number of applications.[1–4] Transition metal mediated bioorthogonal reactions are of particular interest as they enable an array of non-natural chemical transformations that can be used to modulate living systems.[5,6] Reactions mediated by copper,[7,8] iron,[9] gold,[10–12] ruthenium,[12–16] and iridium[17] have all found applications in living systems, although palladium is perhaps the most utilised metal in a biological setting.[18]

Palladium has gained popularity in bioorthogonal chemistry due its ability to perform catalytic cross-coupling reactions, enabling the generation of carbon–carbon and carbon–heteroatom bonds under mild, biological conditions,[19–21] and more recently *in vivo*.[22,23] Palladium catalysts have been used to initiate a range of intracellular reactions including dealkylation,[24] decaging of propargyloxycarbonyl groups,[19,24,25] as well as Suzuki–Miyaura cross-couplings.[20,26–28] Thus, palladium mediated reactions have been used to selectively activate enzymes through deprotection of modified amino acids within proteins,[21,29] to synthesise anticancer agents *in cellulo* from two benign precursors,[19] as well as activate produgs;[20–22,24] however, to date, the majority of the examples have used palladium nanoparticles entrapped within a polymeric support,[19,20,22–24,26,27,30] simple palladium salts such as $Pd(OAc)_2$,[31–33] or designed targeted palladium ligands.[34]

This is in contrast to the highly active palladium catalysts used in conventional organic synthesis that use a variety of stabilising ligands (*e.g.* phosphines) or N-heterocyclic carbenes (NHC),[35,36] but few have been used in a biological setting. Chen used an NHC–Pd catalyst (with imidazolium-based ligands bearing hydrophilic quaternary ammonium salts) to mediate the Suzuki–Miyaura coupling reaction between a boronic acid functionalised biotin and 4-iodophenylalanine modified cell surface proteins, enabling subsequent imaging of the cell surface with fluorescently labelled streptavidin.[33] Recently, we reported a water soluble NHC–Pd catalyst coupled to a cell penetrating peptide, which was able to remove a propargyloxycarbonyl group from a pro-fluorophore in cells, thus demonstrating the first intracellular application of NHC–Pd chemistry.[37] While catalyst loading was carried out on the solid-phase, the synthesis of the NHC ligand required multi-step synthesis in solution, purification, and conjugation to a solid support.

Here, we report an efficient microwave assisted solid-phase synthesis of a series of biocompatible NHC–Pd catalysts and their chemistry in cells. To the best of our knowledge, a solid phase approach to the generation of NHC–Pd catalysts has not been reported and, with our approach, these stable NHC–Pd catalysts were prepared in good yields with the majority of the catalysts showing good activity in a biological setting.

Results and discussion

A solid-phase synthetic route was developed for the NHC–Pd catalysts by adopting the 'sub-monomer' approach, originally developed by Zuckermann for the synthesis of peptoids (*N*-alkyl glycine oligomers), with sequential acylation and alkylation reactions on a resin.[38,39] The NHC ligand chosen here

EaStCHEM School of Chemistry, Joseph Black Building, University of Edinburgh, EH9 3FJ, UK. E-mail: mark.bradley@ed.ac.uk, annamaria.lilienkampf@ed.ac.uk

†Electronic supplementary information (ESI) available: Supporting figures and tables, and experimental procedures. See DOI: 10.1039/c9ob00716d

‡Equal contribution.

Open Access Article. Published on 08 May 2019. Downloaded on 5/11/2020 1:08:28 PM.
This article is licensed under a Creative Commons Attribution 3.0 Unported Licence.

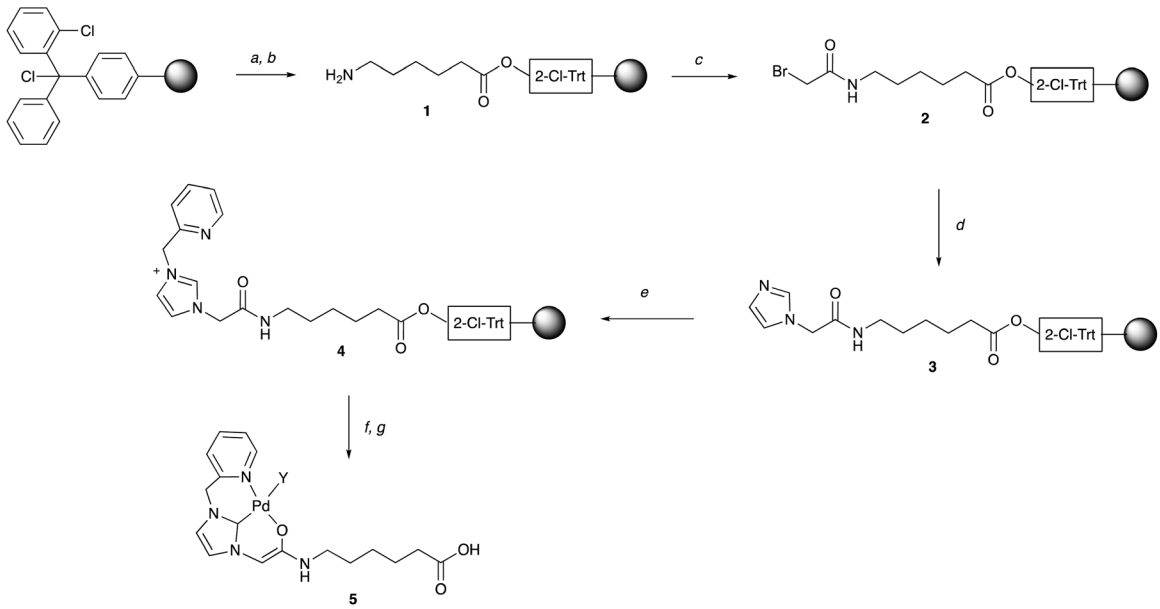

Scheme 1 The microwave assisted solid-phase synthesis of NHC–Pd catalyst **5**. (a) 0.3 M Fmoc-Ahx-OH, 0.5 M DIPEA, anhydrous DCM–DMF (9 : 1), 1 h; (b) 20% piperidine in DMF, 2 × 10 min; (c) 2 M $BrCH_2CO_2H$, 1 M DIC, anhydrous DMF, 20 min, 60 °C, μw; (d) 2 M imidazole, 0.5 M $AgNO_3$ in anhydrous DMSO, 40 min, 60 °C, μw; (e) 1 M 2-(bromomethyl)pyridine, 1 M EtN_3, 0.5 M $AgNO_3$, anhydrous DMF, 90 min, 60 °C, μw; (f) BEMP, anhydrous DMF, N_2, 45 min, then $Pd(COD)Cl_2$ overnight; (g) 30% HFIP–DCM, 1 h. All conversions were monitored by cleavage of a small sample from the resin and characterisation by HPLC and NMR. As drawn, the catalyst is Pd(II) with Y most likely formate (from the HPLC purification buffer).

was first reported by Meldal who showed that a resin-bound NHC–Pd complex (conjugated to a hydrophobic dipeptide) showed good catalytic efficiency in Suzuki–Miyaura cross-couplings in water.[40] Here, this pyridine-derivatised imidazolium ligand was attached to a range of different amino acid spacers, with the aim of providing biocompatibility, aqueous stability, as well as a handle for biomolecule conjugation.

Solid-phase synthetic route for the NHC–Pd catalysts

Fmoc-Ahx-OH was coupled to a 2-chlorotrityl chloride linker on a polystyrene resin (mesh 100–200), with subsequent removal of the Fmoc group giving **1**, which was acylated with 2-bromoacetic acid (2 M in DMF) using DIC as a coupling reagent at 60 °C under μw irradiation for 20 min (Scheme 1). The bromide in **2** was substituted by imidazole to give **3**, with optimised reaction conditions (ESI, Table S1†) allowing quantitative *N*-alkylation *via* an excess of imidazole (2 M) at 60 °C (μw heating for 40 min) in anhydrous DMSO with 0.5 M $AgNO_3$. The addition of $AgNO_3$ was required for full conversion (based on HPLC analysis, ESI, Fig. S1†). The imidazole in **3** was *N*-alkylated with 2-(bromomethyl)pyridine (1 M) to give **4** with >95% conversion using Et_3N (1 M) and $AgNO_3$ (0.5 M) at 60 °C in anhydrous DMF (for optimisation see ESI, Table S2†) giving the NHC ligand in >95% purity and 65% overall yield over 3 steps (ESI, Fig. S2 and S3†). Palladium loading of the NHC-ligand **4** on solid-phase was carried out as reported by Meldal[40] with minor modifications. In brief, the carbene was generated on the resin from the imidazolium ion with the phosphazene base 2-*tert*-butylimino-2-diethylamino-1,3-dimethylperhydro-1,3,2-diazaphosphorine (BEMP) in anhydrous DMF. $Pd(COD)Cl_2$ was added subsequently to generate the NHC–Pd catalyst **5** (Scheme 1), which was cleaved off the resin with 30% HFIP in DCM and purified by semi-preparative RP-HPLC. This allowed the rapid and efficient generation of >100 mg quantities of the catalyst **5** that could be freely stored.§

Synthesis of NHC–Pd catalyst library

This solid-phase synthesis route was used to generate an NHC–Pd catalyst library (**5–12**). Using the NHC moiety with different amino acid spacers gave a range of both hydrophilic and hydrophobic groups to compare the potential effect on catalytic activity, as well as the robustness of the synthetic method (Fig. 1). The catalysts were synthesised using the 2-chlorotrityl linker, but the methodology was also compatible with the Rink-amide linker (ESI, catalyst **13**). The ligands for catalysts **5–12** were fully characterised using NMR, HPLC, and HRMS, and after palladium loading, the catalysts were cleaved off the resin, purified by semi-preparative RP-HPLC, and characterised by ESI-MS and HPLC (ESI, Table S3†). The purity of the catalysts was confirmed by analytical HPLC (ESI, Fig. S4 and S5† – the "naked ligands" and the Pd-loaded ligands displayed different retention times) and the presence of palla-

§The solid-phase approach used here offers advantages over more traditional solution-phase methods, namely the use of mass-action to drive the chemistries and the removal of intermediary purification steps. The ligand was previously synthesised in three steps (in solution) with a combined reaction time of 7.5 h (compared to 3 h in this work) requiring both silica column chromatography and preparative RP-HPLC purification.[40]

 This journal is © The Royal Society of Chemistry 2019

Open Access Article. Published on 08 May 2019. Downloaded on 5/11/2020 1:08:28 PM.
This article is licensed under a Creative Commons Attribution 3.0 Unported Licence.

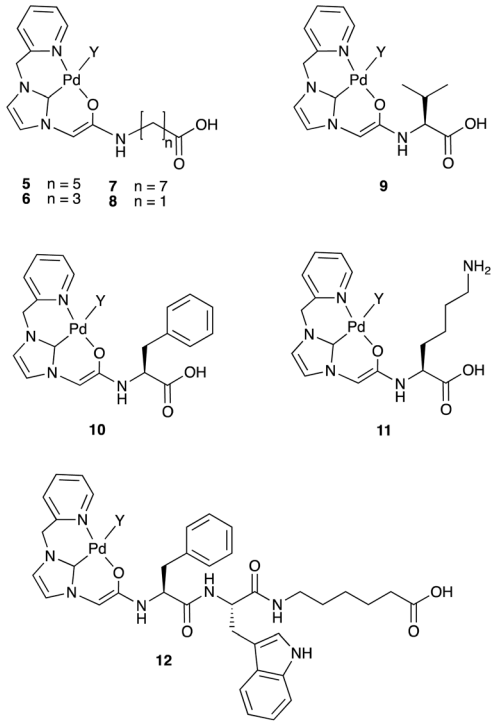

Fig. 1 The NHC–Pd catalysts **5–12** synthesised by the optimised solid-phase synthesis protocol (Scheme 1). As drawn, the catalyst is Pd(II). In the biological experiments Y can be exchanged to various species with different coordination/charge states possible.

dium also established by HRMS (ESI, Fig. S6†) (the presence of the Pd meant that the ^{1}H NMR spectra were highly broadened). These catalysts were stable for two weeks at room temperature in ACN/H_2O, and ≥8 weeks at 4 °C.

Screening of catalytic activity

The fluorogenic probe based on 2,7-dichlorofluorescein (DCF) was used to evaluate the activity of the catalysts.[41] The profluorophore *O*-propargylated **DCF-1** was converted to the fluorescent molecule **DCF-2** ($\lambda_{Ex/Em}$ 480/520 nm) upon Pd-catalysed cleavage of the propargyl group (Fig. 2A). Catalyst screening was carried out at 37 °C in PBS and in MCF-7 cell lysate to evaluate catalytic activity under biologically relevant conditions. Catalysts **5–12** (0.8 mol%) were incubated with **DCF-1** (10 μM) and the increase in fluorescence measured over 4 h with an additional measurement at 20 h (ESI, Fig. S7†). With the exception of **7** and **11**, all the catalysts were active in PBS with **8** and **9** showing comparable activity to 0.8 mol% $Pd(OAc)_2$ (Fig. 2B). The decaging reactions were notably slower in cell lysate with **8** and **9** again showing the best catalytic efficiency under these conditions and outperforming $Pd(OAc)_2$ (ESI, Fig. S8A†). Although shorter hydrophobic spacers seemed to be preferred in PBS (**8** > **9** > **10**), clear structure–activity relationships could not be established for the catalytic activity, particularly in the cell lysate, highlighting the need for methods to rapidly generate combinatorial catalyst libraries.

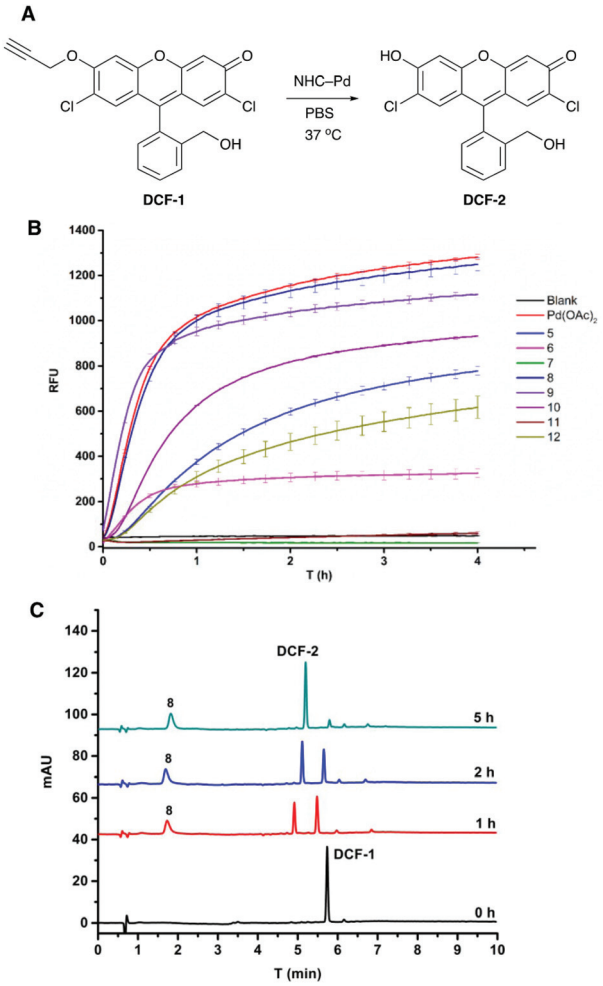

Fig. 2 (A) Pd catalysed depropargylation reaction of profluorophore **DCF-1** to give fluorescent **DCF-2** ($\lambda_{Ex/Em}$ 480/520 nm). (B) Screening of catalysts **5–12** (0.8 mol%) for the activation of **DCF-1** (10 μM) in PBS (n = 3). The reactions were monitored over 4 h and the increase in fluorescence recorded over time and compared to blank (no catalyst) and 0.8 mol% $Pd(OAc)_2$. (C) The catalytic decaging of **DCF-1** (50 μM) with catalyst **8** (2 mol%) monitored by HPLC (detection at 282 nm) over 5 h with the reaction carried out in PBS, showing >92% of **DCF-2**.

Catalyst **8** was further evaluated by monitoring the decaging of **DCF-1** (50 μM) by HPLC, with the experiments performed in PBS and in human plasma to mirror a cellular environment rich in proteins. In PBS, **8** (2 mol%) gave 92% conversion to **DCF-2** after 5 h (Fig. 2C), whereas in plasma 97% conversion was observed (ESI, Fig. S8B†).

Prodrug activation in cancer cells and in cancer cell spheroids

The catalyst **8** was evaluated for its efficiency to activate the caged anticancer drug *N*-propargyl protected 5-fluorouracil[24] (**Pro-5-FU**) (Fig. 3A). In PBS, 5 mol% of **8** was able to convert **Pro-5-FU** (100 μM) into the active drug 5-fluorouracil (**5-FU**) within 48 h, as monitored by HPLC (Fig. 3B).

The co-treatment of MCF-7 cell first with **Pro-5-FU** (100 μM) for 24 h followed by catalyst **8** (10 mol%) for 4 days resulted in

Open Access Article. Published on 08 May 2019. Downloaded on 5/11/2020 1:08:28 PM.
This article is licensed under a Creative Commons Attribution 3.0 Unported Licence.

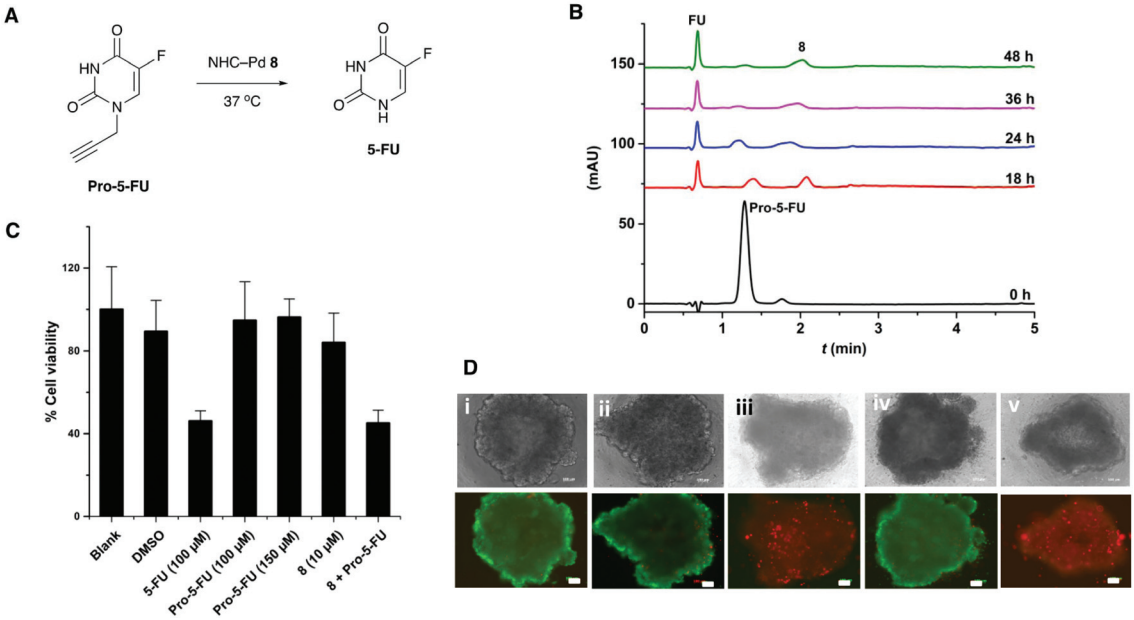

Fig. 3 (A) The Pd-catalysed decaging of prodrug 5-fluoro-1-propargyluracil **Pro-5-FU** into the active anticancer drug 5-fluorouracil **5-FU**. (B) Decaging of **Pro-5-FU** (100 μM) with catalyst **8** (5 mol%) in PBS (pH 7.4, 37 °C) monitored by HPLC with detection at 282 nm. (C) MTT cytotoxicity assay for prodrug activation in MCF-7 cells. The prodrug **Pro-5-FU** (100 μM with 1% DMSO) did not induce cytotoxicity and the NHC–Pd catalyst **8** (10 μM) only showed minor reduction in cell viability (84% viability) after 5 days incubation (untreated control cells were defined as 100% viable). Co-treatment with catalyst **8** (10 mol%, 10 μM) and **Pro-5-FU** (100 μM) for 5 days resulted in comparable cytotoxicity to **5-FU**. (D) *In situ* activation of prodrug **Pro-5-FU** by catalyst **8** in 3D MCF-7 spheroids (drug activation most likely happening extracellularly). The spheroids were imaged for live/dead status, Green cells ($\lambda_{Ex/Em}$ 495/520 nm) are live whilst the red cells ($\lambda_{Ex/Em}$ 595/615 nm) are dead. (i) Untreated spheroid (control); (ii) Spheroid treated with (10 μM) of catalyst **8**; (iii) Spheroid treated with **5-FU** (100 μM) resulting in cell death; (iv) Spheroid treated with prodrug **Pro-5-FU** (100 μM) showing good viability; (v) Spheroid co-treated with the **Pro-5-FU** (100 μM) and catalyst **8** (10 μM) suggesting cell death equivalent to that seen with 100 μM of **5-FU**. Scale bar 100 μm.

comparable cytotoxicity (MTT assay) to **5-FU** (Fig. 3C), with the drug activation likely taking place both intra- and extracellularly (**Pro-5-FU** is readily taken up by cells[30]). Catalyst **8** did not show notable cytotoxicity with 84% cell viability at 10 μM concentration.

Next, MCF-7 spheroids were treated with the prodrug **Pro-5-FU** (100 μM) and catalyst **8** (10 mol%) for 5 days, stained with the LIVE/DEAD™ Cell Imaging Kit (488/570), and analysed by fluorescence microscopy. Spheroids treated with both the prodrug and catalyst resulted in cell death comparable to cells treated with **5-FU**, whereas treatment with only the catalyst or the prodrug **Pro-5-FU** had no effect on the viability of the 3D spheroids (Fig. 3D). These results demonstrate that the catalyst was able to decage a protected prodrug in a more representative 3D cancer model, which may have applications in future anticancer prodrug therapies.

Conclusions

A highly efficient microwave assisted solid-phase synthesis of NHC–Pd catalysts, based on the 'sub monomer' approach was developed and used to generate biocompatible catalysts on scale. Catalyst **8**, comprising of the NHC–Pd moiety linked to a glycine, was the most robust catalyst in the series and was able to activate a fluorogenic probe in a biological setting and decage the protected anticancer drug (5-fluoro-1-propalgyluracil) in a 3D cancer cell culture resulting in comparable cell death to 5-fluorouracil. These robust NHC-Pd catalysts have a carboxylic acid that can be readily converted to a stable active ester thus providing a handle for bioconjugation and offering applications for both specific cell targeting ligands and bioorthogonal prodrug activations.

Conflicts of interest

There are no conflicts to declare.

Acknowledgements

We thank the European commission for the Marie Skłodowska-Curie Individual Fellowship for D. C. (MSCA-IF-2014-EF, MetalCell 659489), and the Engineering and Physical Sciences Research Council and Medical Research Council CDT Optima (grant number EP/L016559/1) and the Rosetrees Trust for funding. We also thank the SIRCAMS at University of Edinburgh for the HRMS analysis and the School of Chemistry NMR facility.

This journal is © The Royal Society of Chemistry 2019

Open Access Article. Published on 08 May 2019. Downloaded on 5/11/2020 1:08:28 PM.
This article is licensed under a Creative Commons Attribution 3.0 Unported Licence.

Notes and references

1 J. Li and P. R. Chen, *Nat. Chem. Biol.*, 2016, **12**, 129–137.
2 J. G. Rebelein and T. R. Ward, *Curr. Opin. Biotechnol.*, 2018, **53**, 106–114.
3 E. M. Sletten and C. R. Bertozzi, *Angew. Chem., Int. Ed.*, 2009, **48**, 6974–6998.
4 J. J. Soldevila-Barreda and N. Metzler-Nolte, *Chem. Rev.*, 2019, **119**, 829–869.
5 M. Martinez-Calvo and J. L. Mascarenas, *Chimia*, 2018, **72**, 791–801.
6 Y. Bai, J. Chen and S. C. Zimmerman, *Chem. Soc. Rev.*, 2018, **47**, 1811–1821.
7 J. Clavadetscher, S. Hoffmann, A. Lilienkampf, L. Mackay, R. M. Yusop, S. A. Rider, J. J. Mullins and M. Bradley, *Angew. Chem., Int. Ed.*, 2016, **55**, 15662–15666.
8 Y. Bai, X. Feng, H. Xing, Y. Xu, B. K. Kim, N. Baig, T. Zhou, A. A. Gewirth, Y. Lu, E. Oldfield and S. C. Zimmerman, *J. Am. Chem. Soc.*, 2016, **138**, 11077–11080.
9 P. K. Sasmal, S. Carregal-Romero, A. A. Han, C. N. Streu, Z. Lin, K. Namikawa, S. L. Elliott, R. W. Koster, W. J. Parak and E. Meggers, *ChemBioChem*, 2012, **13**, 1116–1120.
10 K. Tsubokura, K. K. H. Vong, A. R. Pradipta, A. Ogura, S. Urano, T. Tahara, S. Nozaki, H. Onoe, Y. Nakao, R. Sibgatullina, A. Kurbangalieva, Y. Watanabe and K. Tanaka, *Angew. Chem., Int. Ed.*, 2017, **56**, 3579–3584.
11 A. M. Perez-Lopez, B. Rubio-Ruiz, V. Sebastian, L. Hamilton, C. Adam, T. L. Bray, S. Irusta, P. M. Brennan, G. C. Lloyd-Jones, D. Sieger, J. Santamaria and A. Unciti-Broceta, *Angew. Chem., Int. Ed.*, 2017, **56**, 12548–12552.
12 C. Vidal, M. Tomas-Gamasa, P. Destito, F. Lopez and J. L. Mascarenas, *Nat. Commun.*, 2018, **9**, 1913.
13 C. Streu and E. Meggers, *Angew. Chem., Int. Ed.*, 2006, **45**, 5645–5648.
14 M. Tomas-Gamasa, M. Martinez-Calvo, J. R. Couceiro and J. L. Mascarenas, *Nat. Commun.*, 2016, **7**, 12538.
15 T. Volker, F. Dempwolff, P. L. Graumann and E. Meggers, *Angew. Chem., Int. Ed.*, 2014, **53**, 10536–10540.
16 M. I. Sanchez, C. Penas, M. E. Vazquez and J. L. Mascarenas, *Chem. Sci.*, 2014, **5**, 1901–1907.
17 S. Bose, A. H. Ngo and L. H. Do, *J. Am. Chem. Soc.*, 2017, **139**, 8792–8795.
18 S. V. Chankeshwara, E. Indrigo and M. Bradley, *Curr. Opin. Chem. Biol.*, 2014, **21**, 128–135.
19 J. Clavadetscher, E. Indrigo, S. V. Chankeshwara, A. Lilienkampf and M. Bradley, *Angew. Chem., Int. Ed.*, 2017, **56**, 6864–6868.
20 R. M. Yusop, A. Unciti-Broceta, E. M. Johansson, R. M. Sanchez-Martin and M. Bradley, *Nat. Chem.*, 2011, **3**, 239–243.
21 J. Li, J. Yu, J. Zhao, J. Wang, S. Zheng, S. Lin, L. Chen, M. Yang, S. Jia, X. Zhang and P. R. Chen, *Nat. Chem.*, 2014, **6**, 352–361.
22 M. A. Miller, B. Askevold, H. Mikula, R. H. Kohler, D. Pirovich and R. Weissleder, *Nat. Commun.*, 2017, **8**, 15906.
23 T. L. Bray, M. Salji, A. Brombin, A. M. Perez-Lopez, B. Rubio-Ruiz, L. C. A. Galbraith, E. E. Patton, H. Y. Leung and A. Unciti-Broceta, *Chem. Sci.*, 2018, **9**, 7354–7361.
24 J. T. Weiss, J. C. Dawson, K. G. Macleod, W. Rybski, C. Fraser, C. Torres-Sanchez, E. E. Patton, M. Bradley, N. O. Carragher and A. Unciti-Broceta, *Nat. Commun.*, 2014, **5**, 3277.
25 J. T. Weiss, J. C. Dawson, C. Fraser, W. Rybski, C. Torres-Sanchez, M. Bradley, E. E. Patton, N. O. Carragher and A. Unciti-Broceta, *J. Med. Chem.*, 2014, **57**, 5395–5404.
26 E. Indrigo, J. Clavadetscher, S. V. Chankeshwara, A. Lilienkampf and M. Bradley, *Chem. Commun.*, 2016, **52**, 14212–14214.
27 F. Wang, Y. Zhang, Z. Du, J. Ren and X. Qu, *Nat. Commun.*, 2018, **9**, 1209.
28 P. Destito, A. Sousa-Castillo, J. R. Couceiro, F. Lopez, M. A. Correa-Duarte and J. L. Mascarenas, *Chem. Sci.*, 2019, **10**, 2598–2603.
29 J. Wang, S. Zheng, Y. Liu, Z. Zhang, Z. Lin, J. Li, G. Zhang, X. Wang, J. Li and P. R. Chen, *J. Am. Chem. Soc.*, 2016, **138**, 15118–15121.
30 G. Y. Tonga, Y. D. Jeong, B. Duncan, T. Mizuhara, R. Mout, R. Das, S. T. Kim, Y. C. Yeh, B. Yan, S. Hou and V. M. Rotello, *Nat. Chem.*, 2015, **7**, 597–603.
31 J. Li, S. Lin, J. Wang, S. Jia, M. Yang, Z. Hao, X. Zhang and P. R. Chen, *J. Am. Chem. Soc.*, 2013, **135**, 7330–7338.
32 C. D. Spicer and B. G. Davis, *Chem. Commun.*, 2011, **47**, 1698–1700.
33 X. J. Ma, H. X. Wang and W. Z. Chen, *J. Org. Chem.*, 2014, **79**, 8652–8658.
34 M. Martinez-Calvo, J. R. Couceiro, P. Destito, J. Rodriguez, J. Mosquera and J. L. Mascarenas, *ACS Catal.*, 2018, **8**, 6055–6061.
35 G. C. Fortman and S. P. Nolan, *Chem. Soc. Rev.*, 2011, **40**, 5151–5169.
36 J. F. Jensen, K. Worm-Leonhard and M. Meldal, *Eur. J. Org. Chem.*, 2008, 3785–3797.
37 E. Indrigo, J. Clavadetscher, S. V. Chankeshwara, A. Megia-Fernandez, A. Lilienkampf and M. Bradley, *Chem. Commun.*, 2017, **53**, 6712–6715.
38 R. N. Zuckermann, J. M. Kerr, S. B. H. Kent and W. H. Moos, *J. Am. Chem. Soc.*, 1992, **114**, 10646–10647.
39 T. S. Burkoth, A. T. Fafarman, D. H. Charych, M. D. Connolly and R. N. Zuckermann, *J. Am. Chem. Soc.*, 2003, **125**, 8841–8845.
40 K. Worm-Leonhard and M. Meldal, *Eur. J. Org. Chem.*, 2008, 5244–5253.
41 M. Santra, S. K. Ko, I. Shin and K. H. Ahn, *Chem. Commun.*, 2010, **46**, 3964–3966.